THÈSE

PRÉSENTÉE A

L'UNIVERSITÉ BORDEAUX 1

ÉCOLE DOCTORALE DES SCIENCES CHIMIQUES

Par Gabriel LOGET

POUR OBTENIR LE GRADE DE

DOCTEUR

SPÉCIALITÉ : Chimie-Physique

ELECTRIC FIELD-GENERATED ASYMMETRIC REACTIVITY: FROM MATERIALS SCIENCE TO DYNAMIC SYSTEMS

Directeur de recherche : Prof. Alexander KUHN

Soutenue le : 21.09.2012

Devant la commission d'examen formée de :

Prof. CROOKS, Richard M.	Professeur, University of Texas at Austin	Rapporteur
Prof. SCHUHMANN, Wolfgang	Professeur, Ruhr-Universität Bochum	Rapporteur
Dr. LINCOT, Daniel	Directeur de recherche CNRS, Chimie Paris Tech	Examinateur
Dr. AIME, Jean-Pierre	Directeur de recherche CNRS, Université Bordeaux I	Examinateur
Prof. NESO, Sojic	Professeur, Institut Polytechnique de Bordeaux	Examinateur
Prof. KUHN, Alexander	Professeur, Institut Polytechnique de Bordeaux	Directeur de thèse

A ma famille, à qui je dois tout.

Imagination is more important than knowledge.
Knowledge is limited.
Imagination encircles the world.

Einstein, 1929

La symétrie c'est l'ennui.

Victor Hugo, 1862

Acknowledgements

I would like to thank my supervisor Pr. Alexander Kuhn for everything I learnt from him during these three years, in science and beyond. His wide scientific interest, curiosity and enthusiasm profoundly inspired me. His philosophy will keep on influencing me. Dankeschön.

I acknowledge all members of the jury committee of my defense, especially Pr. Richard M. Crooks, Pr. Wolfgang Schuhmann, Dr. Daniel Lincot and Dr. Jean-Pierre Aimé.

I also thank Pr. Neso Sojic for sharing his knowledge on ECL, for his advices and for giving me the opportunity to contribute in different projects around science.

I acknowledge Dr. Nina Hüsken for the stimulating scientific discussions as well as for correcting a great part of this thesis.

I would like to thank my friend Dr. Dodzi Zigah for his wisdom and his frankness.

A great part of this thesis has been the result of different collaborations, within the University of Bordeaux but also with Kasetsart University in Thailand and the University of Cambridge in England. These collaborations are described in detail in appendix 6.

I acknowledge especially my bipolar friends: Dr. Jérome Roche, Zahra Fattah, Jérémy Lannelongue, Guillaume Larcade, Michael Ongaro and Chawanwit Kumsapaya for all the work we did together, the discussions, the good music and the nice fireworks we had occasionally in the lab.

I would like to thank Milica Sentic for her luminescent mind.

I thank all the Cubihole's: Richard W. Taylor, Dr. Sumeet Mahajan, Dr. Tung-Chun Lee, Dr. Ollala Pérez, Dr. Ruben Esteban, Dr. Roger J. Coulston, Samuel T. Jones, as well as the Cubibosses: Pr. Jeremy J. Baumberg, Dr. O. A. Schermann and Dr. Javier Aizpurua. Being involved in this European project was a wonderful experience from a scientific and a personal point of view.

Véronique Lapeyre, Patrick Garrigue and Dr. Stéphane Arbault are acknowledged for their inputs and technical supports.

I would like to thank all the NSysA team: Dr. Matthias Heim *a.k.a.* "Der Schlächter von Bayern", Laurent le Henaff *a.k.a.* "Le Demi Breton", Dr. Milena Milutinovic *a.k.a.* "Ракија", Thomas Abadie *a.k.a.* "Lucky Luke", Suresh Vajrala *a.k.a.* "Polnareff d'Hyderābād", Salem Ben Amor *a.k.a.* "Pascal Brutal", Catherine Adam *a.k.a.* "Fifi Brindacier", Florent *a.k.a.* "Johnny Hallyday", Churalat Wattanakit *a.k.a.* "Pleu" *a.k.a.* "Beune" *a.k.a.* "Peule" *a.k.a.* "Apple", Aline Simon Lalande, Dr. Yémima Bon Saint Côme, Dr. Hélène Lalo, Dr. Jennifer Lenz, María del Pozo, Lisa Peyrard, Léa Messager, Dr. Emmanuel Suraniti, Dr. Emeline Girard, Dr. Bertrand Goudeau, Dr. Valérie Ravaine, Dr. Laurent Bouffier, Dr. Sandra Pinet and Dr. Isabelle Gosse. Merci, it was so much fun to work with you!

I finally strongly acknowledge Juliana Hack for all the support she gave me during these three years in Bordeaux and before. Obrigado.

Résumé

L'électrochimie bipolaire est un phénomène générant une réactivité asymétrique à la surface d'objets conducteurs, sans contact électrique direct. Ce concept est basé sur le fait que lorsqu'un objet conducteur est localisé dans un champ électrique, il se polarise. Par conséquent, une différence de potentiel est générée entre ses deux extrémités, et peut être utilisée pour induire des réactions redox localisées. Dans cette thèse, l'utilisation de l'électrochimie bipolaire pour la science des matériaux et pour la locomotion d'objets est présentée.

Jusqu'à présent, la plupart des méthodes ou procédés utilisés pour générer des objets asymétriques, appelés aussi objets « Janus », nécessitent l'introduction d'une interface pour briser la symétrie. Nous avons développé une nouvelle approche basée sur l'électrodéposition bipolaire pour générer ce type d'objet en grande quantité. Grace à cette technologie différents matériaux tels que des métaux, des polymères et des semi-conducteurs ont pu être déposés sur diverses particules conductrices. Il a été aussi démontré que l'électrochimie bipolaire pouvait être utilisée pour la microstructuration de substrats conducteurs.

Nous avons induit des mouvements à des objets conducteurs en exploitant le phénomène d'électrochimie bipolaire. Certains objets Janus synthétisés par l'approche précédente ont pu être utilisés comme micronageurs. La brisure de symétrie qui est générée par l'électrochimie bipolaire peut être aussi utilisée directement pour générer un mouvement de particules isotropes. En employant ce concept, nous avons pu provoquer des mouvements de translation, rotation et lévitation pour des particules de carbones ou métalliques.

Mots-clés:

Asymétrie, Electrochimie bipolaire, Electrodéposition, Particules Janus, Micromoteurs

Abstract

The phenomenon of bipolar electrochemistry generates an asymmetric reactivity on the surface of conductive objects in a wireless manner. This concept is based on the fact that when a conducing object is placed in an electric field, it gets polarized. Consequently, a potential difference appears between its two extremities, that can be used to drive localized redox reactions. In the present thesis, bipolar electrochemistry was used for material science and the locomotion of objects.

So far, the majority of methods and processes used for the generation of asymmetric objects, also called “Janus” objects, is based on using interfaces to break the symmetry. We developed a new approach based on bipolar electrodeposition for generating this type of objects in the bulk. Using this technology, various materials like metals, polymers and semiconductors could be deposited on different types of conducting particles. We also showed that bipolar electrochemistry can be used for the microstructuration of conducting substrates.

Motion generation by bipolar electrochemistry has also been demonstrated. Some of the Janus objects synthesized by the previous approach can be used as microswimmers. The asymmetric reactivity that is induced by bipolar electrochemistry can also be used directly to generate motion of non-hybrid objects. With this concept we induced translations, rotations and levitations of carbon and metal particles.

Keywords:

Asymmetry, Bipolar Electrochemistry, Electrodeposition, Janus particles, Micromotors

Table of contents

Symbols

Symbol	Meaning	Usual units
A	absorbance	none
A	amplitude	cm
C	concentration	M
D	diffusion coefficient	$cm^2\ s^{-1}$
d	diameter or length of a bipolar electrode	cm
d_{dep}	deposit length	cm
E	potential	V
E	polarization potential	V
E^0	standard potential of the redox couple	V
E_a	anode potential	V
E_c	cathode potential	V
E_{imp}	potential imposed between anode and cathode	V
E_m	mixed potential	V
$\mathscr{E}$	imposed electric field	$V\ cm^{-1}$
$\mathscr{E}_{eff}$	measured electric field	$V\ cm^{-1}$
F	Faraday constant	$C\ mol^{-1}$
F_{drive}	driving force generated on the surface of a particle	N
F_{net}	sum of the driving forces	N
f	frequency	Hz
G_{bps}	cell conductance at the bipolar electrode vicinity	S
h	height	cm
i	current	A
i_{be}	faradaic current flowing through the bipolar electrode	A
i_{bps}	by-pass current	A
i_t	total current flowing through the cell	A
j	current density	$A\ cm^{-2}$
j_0	exchange current density	$A\ cm^{-2}$
K_s	solubility constant	none
k	cell constant	cm^{-1}
k_b	Boltzmann constant	$J\ K^{-1}$
L	distance between the feeder electrodes	cm
L_m	distance between the microelectrodes	cm
n	stoichiometric number of electrons involved in a redox reaction	none
n	number of mole	mol
R	gas constant	$J\ K^{-1}\ mol^{-1}$
R_{be}	resistance of the bipolar electrode	Ω
R_{bps}	cell resistance at the bipolar electrode vicinity	Ω
R_{eq}	equivalent resistance	Ω
r	$n\,(1-\alpha)$ for oxidation reactions or $n\alpha$ for reduction reactions	none
r	radius of the bipolar electrode	cm
T	temperature	K

Symbol	Meaning	Usual units
T	period	s
t	time	s
t_0	initial time	s
t_u	time at which the swimmer is in its highest position	s
t_d	time at which the swimmer is in its lowest position	s
U	measured potential difference	V
ΔV	maximum polarization potential	V
ΔV_{min}	minimum potential value to trigger electrochemical reactions at a bipolar electrode	V
V_r	volume of the reaction compartment	mL
v	speed	bl s^{-1}
w	ring width	μm
x	position on the bipolar electrode	m
x_a	position of the anodic extremity	m
x_c	position of the cathodic extremity	m
x_0	position of the bipolar electrode where $E = E_m$	m
α	charge transfer coefficient	none
γ	faradaic current divided by the total current	none
ζ	zeta potential	mV
σ	conductivity	S cm^{-1}
Θ	angular position	rad
λ	wavelength	nm
ϕ	rotation angle	rad
ω	angular speed	rpm
χ	electric field transmission efficiency	none
Ω	virtual plane	none

Abbreviations

Abbreviation	Meaning
a.c.	alternating current
AFM	atomic force microscopy
AgNW	silver nanowire
ATP	adenosine triphosphate
AP	asymmetric particle
APP	asymmetric patchy particle
BE	bipolar electrode
BEF	bipolar electrode focusing
bl	bodylength
BODIPY	boron dipyrromethene
bp	base pair
CABED	capillary-assisted bipolar electrodeposition
CB[*n*]	cucurbit[*n*]uril
CE	capillary electrophoresis
CMT	carbon microtube
CNF	carbon nanofiber
CNP	carbon nanopipe
CNT	carbon nanotube
CP	conducting polymer
CT	carbon tube
CV	cyclic voltammetry
d.c.	direct current
DLS	dynamic light scattering
DMSO	dimethyl sulfoxide
E. coli	*Escherichia coli*
ECL	electrochemiluminescence
EDP	electrophoretic deposition paint
EDX	energy dispersive X-ray spectroscopy
EG	ethylene glycol
EOF	electroosmotic flow
e-paper	electronic paper
EPF	electrophoretic flow
EPOC	electrochemical promotion of heterogeneously catalyzed reaction
FBER	fluidized bed electrode reactor
GC	glassy carbon
HAADF	high angle annular dark field
HLB	hydrophilic-lipophilic balance
HQ	hydroquinone
HRP	horseradish peroxidase
ICP-MS	inductively coupled plasma mass spectrometry

Abbreviation	Meaning
ITO	indium-tin oxide
JP	Janus particle
LED	light emitting diode
MOON	modulated optical nanoprobe
MTMOS	methyltrimethoxysilane
MWCNT	multi-wall carbon nanotube
NEMCA	non-faradaic electrochemical modification of catalytic activity
NP	nanoparticle
NT	nanotube
NW	nanowire
ox	oxidant
PAni	polyaniline
PBS	phosphate buffer saline
PDMS	polydimethylsiloxane
PEDOT	poly(3,4-ethylenedioxythiophene)
PEG	polyethylene glycol
PEM	polyelectrolyte multilayer
PEO	poly(ethylene oxide)
PMMA	poly(methylmethacrylate)
PMT	poly(3-methylthiophene)
PP	patchy particle
PPy	polypyrrole
PS	polystyrene
PTFE	polytetrafluoroethylene
SAM	self-assembled monolayer
SC	semiconductor
SCBE	spatially coupled bipolar electrochemistry
SDP	seeded dispersion polymerization
SEM	scanning electron microscopy
SEP	seeded emulsion polymerization
SERS	surface-enhanced Raman spectroscopy
SFM	surface force microscopy
SPR	surface plasmon resonance
STEM-EDX	scanning transmission electron microscopy-energy dispersive X-ray spectroscopy
STM	scanning tunneling microscopy
SWCNT	single-wall carbon nanotube
red	reductant
TEM	transmission electron microscopy
TMAOH	tetramethylammonium hydroxide
TMP	tetramethylbenzidine
TEOS	tetraethoxysilane
TrPA	tripropylamine
TTIP	titanium(IV) tetraisopropoxide
XRD	X-ray diffraction

Preface

Bipolar electrochemistry is a phenomenon which generates an asymmetric reactivity on the surface of conductive objects in a wireless manner. Even though this concept has been known for a very long time, it has not been very popular for a few decades. Recently it has regained considerable attention, especially in the field of micro- and nanoscience. The aim of the present thesis is to introduce bipolar electrochemistry, its state of the art and to present novel applications of this phenomenon in two domains where asymmetry is crucial.

In the first chapter, a general introduction to bipolar electrochemistry will be given, exploring concepts such as thermodynamics and kinetics on bipolar electrodes. The theoretical aspects will be illustrated by experimental data.

Historical aspects of bipolar electrochemistry will be briefly presented in chapter two and recent applications in domains like analytics, electronics and material science will be reviewed.

The two following chapters, three and four, are independent and constitute the experimental part of the thesis. The third chapter concerns the use of bipolar electrochemistry for material science and especially for the bulk synthesis of asymmetric structures, so called “Janus” or asymmetric patchy particles. These objects, which are generally synthetized in a one or two dimensional reaction space, are of great importance for various applications. The interface-based synthetic approaches existing in the literature will be briefly discussed and illustrated by the example of electron beam-induced asymmetrical reduction. New bulk techniques, based on bipolar electrodeposition, will be presented. The diversity in terms of structuration and material combination offered by these new techniques will then be illustrated by different examples. Finally, we will discuss the use of bipolar electrochemistry for the micro- and nanostructuration of substrates.

The fourth chapter deals with the development of micromotors. Asymmetry is critical in this field which is currently a major research axis. After a brief discussion about biomotors present in nature and the main approaches used to mimic them by synthetic concepts, we will present two approaches

using bipolar electrochemistry. The first strategy consists in using asymmetric objects that were synthetized in chapter 3 as motors. In this strategy bipolar electrochemistry is indirectly used when compared with the second approach, which consists in using it directly to propel isotropic objects. Concerning the direct use of bipolar electrochemistry, two mechanisms have been developed. The first one relies on the generation and release of bubbles and was used for translation, rotation and levitation of bipolar electrodes. We will also present the integration of a light emitting process into this mechanism. The second mechanism is based on a dissolution/deposition mechanism and was named bipolar self-regeneration.

A general conclusion will be given in chapter five. Middle and long term perspectives going beyond the two fields developed in the two previous chapters will be also discussed in this final chapter.

Chapter 1

Introduction to bipolar electrochemistry

1.1. Bipolar electrode: definition

The term "bipolar electrode" (BE) is employed for any object exhibiting at the same time oxidation and reduction reactions, that is, being an anode and a cathode at the same time.[1,2] This is the first difference with respect to conventional electrochemical experiments, where cathodes and anodes are physically separated. BEs do not have to be mixed up with other bipolar objects that one can find in different areas of electrochemistry, such as bipolar membranes[3] (membranes composed by anion and a cation exchange parts, generally used for electrodialysis) or bipolar plates[4] (used for fuel distribution in fuel cells). BEs can be objects exhibiting a chemical anisotropy, designed in order to promote oxidation and reduction reactions at the same time under certain conditions. This concept has been widely used with bimetallic nanorods that can be used as self-propelling particles (see section 4.1.2. for more details),[5,6] or enzyme-modified carbon fibers.[7] The bipolar behavior of this kind of hybrid objects has also been used for unassisted photosplitting[8,9] or as recently reported, in fuel cells.[10] In these cases, bipolar electrochemistry originates from the hybrid composition of the objects. It is important to note that, unlike in these examples, our interest here is focused on objects which are, in most of the case chemically isotropic and exhibit a BE behavior when exposed to an external electric field. This kind of BE can also be found in the literature under the name of "floating electrodes".

1.2. Polarization of a conducting object in an open configuration

In this section, the simple case of a conducting object immersed in a homogeneous electrolytic solution and exposed to an electric field (between two feeder electrodes) will be considered. By definition it is not in contact with one or both feeder electrodes (Figure 1.1a). It is important to mention, that in this case the object is not obstructing the cell dividing it into two different distinct electrolytic compartments. This latter case, referred to "closed" configuration as defined by Ndungu,[11] differs from the considered "open" configuration and will be discussed later in section 1.5.

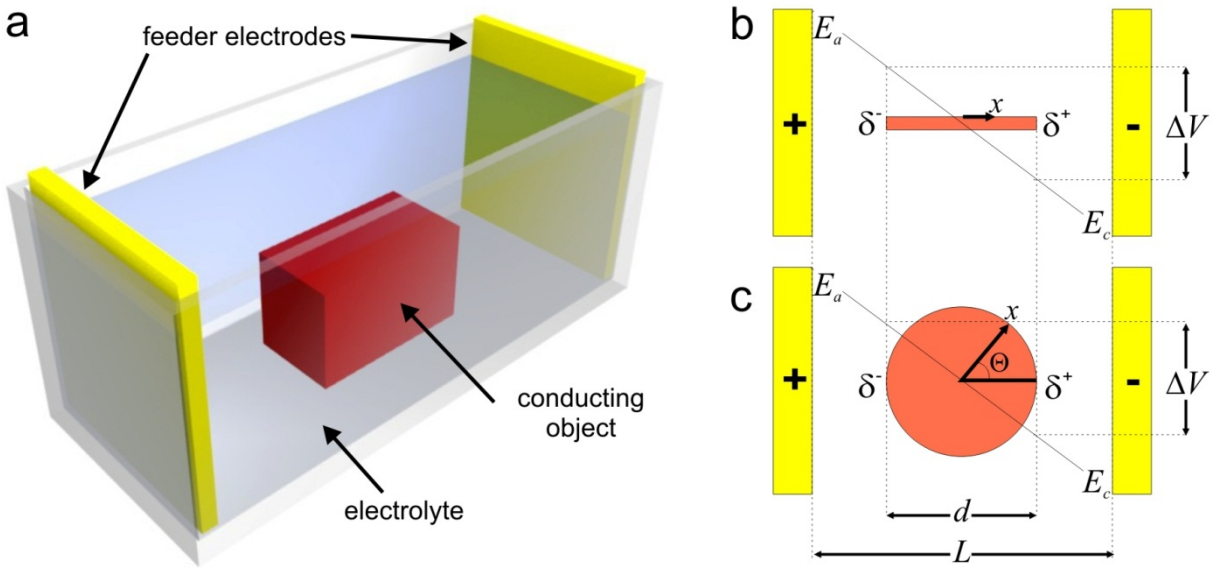

Figure 1.1 Polarization of a conducting object. a) Scheme of the considered system, a conducting object is localized between two feeder electrodes in an electrolyte solution. b) Scheme showing the polarization of a linear conducting object. c) Scheme showing the polarization on the 2D projection of a spherical conducting object.

In the absence of electric field, the immersed conducing object is at a mixed potential E_m. A potential difference $E_{imp} = E_a - E_c$ is applied between the feeder electrodes, E_a and E_c being the potential of the anode and the cathode respectively. Considering the distance between the two feeder electrodes L, the electric field value $\mathscr{E}$ is given by:

$$\mathscr{E} = \frac{E_a - E_c}{L} \tag{1.1}$$

If in a first order approximation the drop of potential, which may occur at the feeder electrode/electrolyte interfaces, and electric field distortions due to the reactions at the feeder electrodes are neglected. The imposed potential $E_a - E_c$ drops then linearly through the electrolytic solution. Figure 1.1b and c show the solution potential distribution in the cell for two object morphologies, one linear and one spherical, respectively. As a consequence of the presence of the

electric field, a polarization potential E, which is given by the difference of the solution potential value with respect to the conducing object arises. The value of E varies along the object/solution interface and can be calculated at a position x as: [2]

$$E = \mathscr{E}x \tag{1.2}$$

for a linear object (Figure 1.1b) and:

$$E = \mathscr{E}\frac{d}{2}\cos\Theta \tag{1.3}$$

for a spherical object (Figure 1.1c), d being the object diameter. As shown in Figure 1.1b and c, the maximum polarization potential difference occurs between the extremities of the object, its value, ΔV can be calculated as:

$$\Delta V = \mathscr{E}d \tag{1.4}$$

This value is directly related to the reactivity at the extremities of the polarized interface. Let us now consider the same system than previously, but in the presence of electroactive species, red 1 and ox 2, which can undergo the following reactions:

$$\text{red 1} \rightarrow \text{ox 1} + n_1\, e^- \tag{1.5}$$

and

$$\text{ox 2} + n_2\, e^- \rightarrow \text{red 2} \tag{1.6}$$

n_1 and n_2 being the number of electron involved for each electrochemical reactions and the two redox couples red 1/ox 1 and red 2/ox 2 having a standard potential E_1^0 and E_2^0, respectively. One can assume that the minimum potential value ΔV_{min}, needed to induce reaction (1.5) and (1.6) at both side of the polarized interface, has to be, in a first order approximation at least equal to the difference of standard potentials of the two involved redox couples

$$\Delta V_{min} = \left| E_1^0 - E_2^0 \right| \tag{1.7}$$

(ΔV_{min} can be considered to be proportional to the energy required for red 1 to give an electron to ox 2). Indeed, if the condition $\Delta V > \Delta V_{min}$ is fulfilled, *i.e.* $\mathscr{E}$ is important enough for a conducting object with a given size (Equation 1.4), electrochemical reactions 1.5 and 1.6 can happen simultaneously at both extremities of the object. The oxidation reaction 1.5 will occur at the anodic pole together with the reduction reaction 1.6, at the cathodic pole. This is depicted in Figure 1.2.

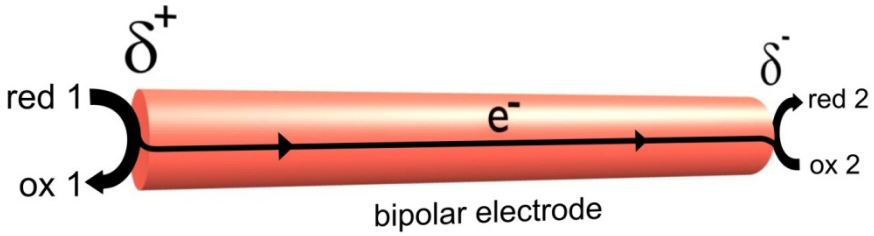

Figure 1.2. Scheme showing the bipolar electrode behavior of a cylindrical conducting object immersed in a solution containing the electroactive species red 1 and ox 2, exposed to an electric field. In this case, the thermodynamic threshold condition $\Delta V > \Delta V_{min}$ is fulfilled.

We can say that above the polarization potential threshold value ΔV_{min}, the conducing object is exhibiting a bipolar electrode behavior, promoting electrochemical reactions at localized areas on its interface in a wireless manner. We will then always refer to it as bipolar electrode (BE) in the following. The driving force of these reactions being the potential drop within the solution, that is, the applied electric field between the feeder electrode, this represents another difference compared to "conventional" electrochemistry, where the driving force of a reaction is directly controlled by the potential of an electrode linked to a potentiostat. We are now going to discuss qualitatively these thermodynamic aspects of BE reactions using experimental data.

In order to directly visualize the effects of the two key parameters that control the driving force of the BE, the electric field value $\mathscr{E}$ and the BE length d, we decided to perform a set of experiments on carbon graphite bars. The first series of experiments consisted in performing bipolar electrodeposition on different graphite rods with the same length but at different $\mathscr{E}$ values during 20 min in a 1 mM $AgNO_3$ aqueous solution. As one can see from Figure 1.3a, this led to the silver deposition at one extremity of some rods (at the cathodic pole, which faced the feeder anode). Figure 1.3b shows a plot of the silver deposit length d_{dep}, as a function of ΔV (calculated using Equation 1.4). Up to $\Delta V \approx 1.25$ V no silver deposit is observed. Above this threshold, silver deposits are formed at the cathodic pole of the BE. d_{dep} increases linearly until ≈5 V, corresponding to the polarization for which the cathodic and anodic areas reached their maximum (this aspect will be further developed in section 1.4.). The value for which the first metal deposit is observed, $\Delta V \approx 1.25$ V, should correspond to ΔV_{min} and this can be verified by changing the length of the BE at a given $\mathscr{E}$ value, as we will discuss in the following.

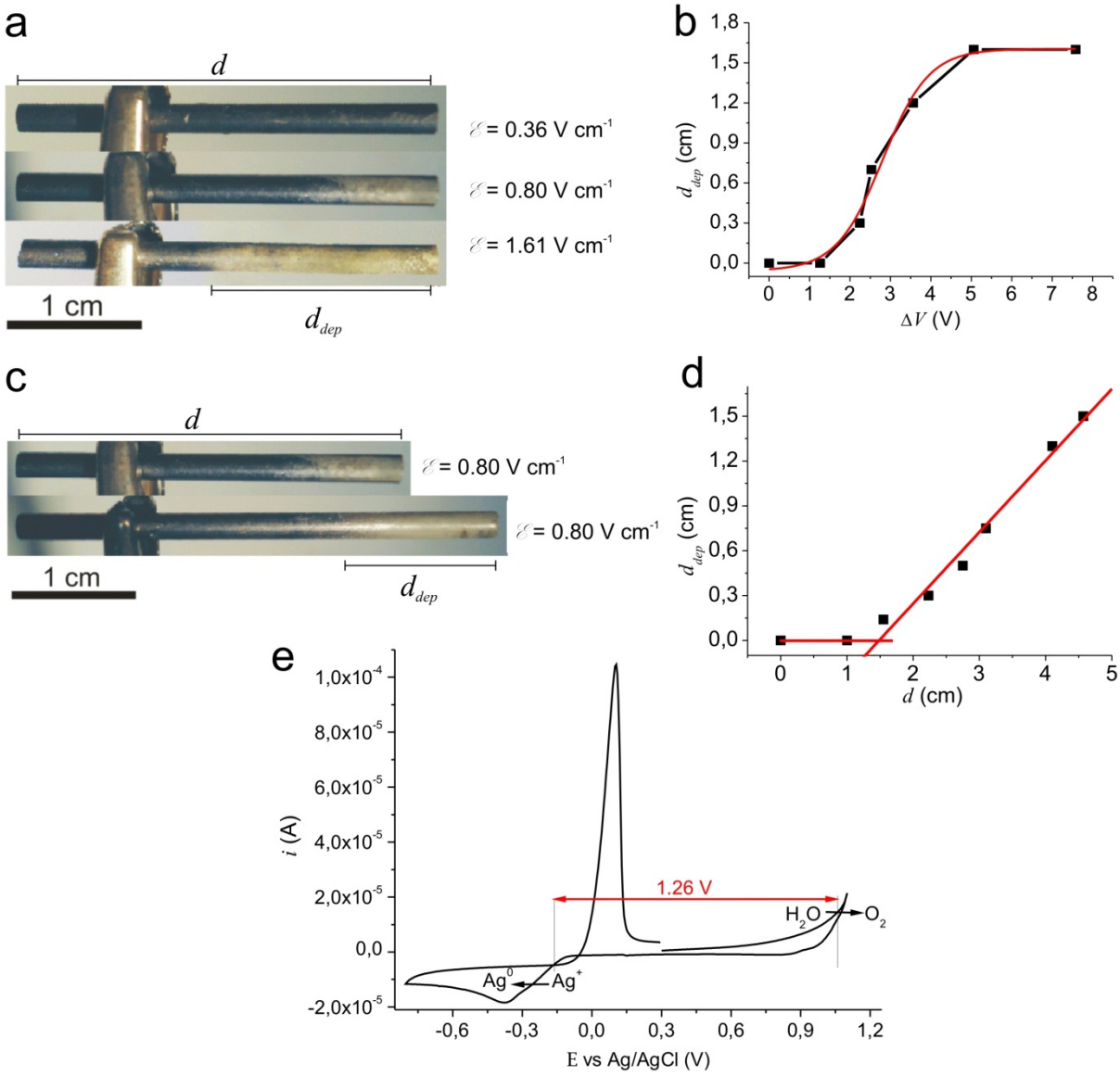

Figure 1.3. Polarization of graphite rods in silver nitrate aqueous solutions. a) Optical micrographs of carbon rods with the same length, showing in some cases a silver deposit, obtained by bipolar electrodeposition at different electric field values. b) Graph showing the length of the deposits d_{dep} as a function of the polarization potential between the object extremities ΔV. c) Optical micrographs showing carbon graphite rods of different lengths with a silver deposit, obtained by bipolar electrodeposition at the same electric field value, $\mathscr{E}$ = 0.80 V cm^{-1}. d) Plot of the deposit lengths as a function of the rod length. e) Cyclic voltammogram obtained using a glassy carbon working electrode in an $AgNO_3$ 1 mM aqueous solution at 100 mV s^{-1} (0.1 M KNO_3).

For the second set of experiments, carbon rods with different lengths d were used with the same solution than previously and $\mathscr{E}$ was set to 0.80 V cm^{-1}. This resulted, as it can be observed in Figure 1.3c, in different measurable lengths of d_{dep}. Figure 1.3d shows the evolution of d_{dep} as a function of d. Before reaching $d \approx 1.5$ cm, no silver is observable on the rod, but after this threshold is reached, d_{dep} increases linearly. Indeed, increasing the d value for the same $\mathscr{E}$ will lead to a linear increase of

ΔV, as it is shown by Equation 1.4. The threshold rod length of ≈1.5 cm should then correspond to ΔV_{min}. Application of Equation 1.4 gives the value ΔV ≈1.2 V for this length.

Equation 1.7 states that ΔV_{min} can be roughly estimated from the standard potential difference of the redox couples involved in the bipolar mechanism, but a more accurate way (in terms of experimental conditions) to determine this value, would be to perform a cyclic voltammetry (CV) experiment in the bipolar electrochemistry conditions, using as working electrode a comparable material than the one used as a BE. Even if it is difficult to reproduce exactly the bipolar electrochemistry conditions with CV measurements (mainly due to the need of supporting electrolyte), one can assume that this is the method of choice for the determination of ΔV_{min}. The obtained cyclic voltammogram is shown in Figure 1.3e, and three waves are observable corresponding from left to right to the reduction of silver nitrate into silver metal, followed by the stripping of the metallic silver previously deposited and finally, the water oxidation. The oxidation occurring at the polarized carbon rod in a BE regime is the latter one, a fact that was confirmed by the visualization of bubbles at the anodic pole (the extremity facing the feeder cathode) during the experiments. The potential difference between this reaction and the silver nitrate reduction corresponds to ΔV_{min} and can be directly determined from the CV. Its value, 1.26 V, is in very good agreement with the previously determined ΔV_{min} values.

Björefors *et al.* studied potential distributions on millimeter long gold BEs electrodes for different $\mathscr{E}$ values.[12] The authors proposed an optical characterization of the potential gradient in a solution containing a redox active probe. This characterization, based on surface plasmon resonance (SPR) measurements relies on the fact that at sufficient ΔV, redox reactions can be induced, and thus the local refractive index along the gold surface must change and lead to a different SPR answer linked to the potential value at different points.[12] Electrochemical characterizations of the potential gradient were also proposed. It consisted in measuring the potential between the bipolar electrode and a reference electrode in solution placed at different points along the BE and calculating the relative current density in the vicinity of the bipolar electrode, proportional to the potential measured between two microelectrodes positioned very close to the BE. Plotting the relative current and the solution potential as a function of the BE distance was possible, leading to results in good agreement with a simulation based on a conductivity model.[12]

As we discussed, the two main important points for bipolar reactions to occur are: *i)* the external electric field $\mathscr{E}$ and *ii)* the size of the object *d*. The electric field is an easily controllable parameter, which allows a fine control of the localization of the electrochemical reactions along a BE surface. The size aspect is clearly demonstrated by Equation 1.4. A smaller object will require a more important $\mathscr{E}$ value than a bigger object to become a BE, and this becomes a problem when trying to

achieve electrochemical reactions on nanosized objects (a topic that will be further detailed in Chapter 3). Now that we explored some thermodynamic aspects of BEs, and we discussed the possible methods for estimating ΔV_{min} with bipolar electrochemistry and a conventional electrochemical method, we will consider in the following some kinetic aspects of BEs.

1.3. Estimation and measurement of faradaic and by-pass currents

Let us consider an experiment where a BE is immersed into an electrolyte solution. As shown in Figure 1.4a, the total current flowing through the cell i_{tot} is divided into two parts in the vicinity of the BE. One fraction, i_{be}, flows through the BE via electronic conduction to ensure the bipolar electrochemical reactions that occur at both BE poles (Figure 1.2), and will be called faradaic current. The other fraction, called the by-pass current i_{bps} flows through the solution via migration of charged species. The following relation has to be fulfilled:

$$i_{tot} = i_{be} + i_{bps} \tag{1.8}$$

We define the ratio γ as the fraction of faradaic current divided by the delivered current:

$$\gamma = \frac{i_{be}}{i_{tot}} \tag{1.9}$$

Looking at the equivalent resistance circuit in Figure 1.4b, it is obvious that the resistance of the BE, R_{be}, directly influences γ. Using a high resistance solution and a very conducting BE, will minimize the by-pass current value, i_{bps}. Also the cell design, allowing a local resistivity increase around the BE can help decreasing i_{bps}.

By-pass currents have been investigated in detail, especially for the design of bipolar electrochemical reactors (see section 2.1.). Models based on equivalent circuits[13-14] or current-potential curves[15] have been developed in order to estimate them. The determination of i_{bps} can be achieved by a direct measurement of i_{be} using split BEs.[16,17] As shown in Figure 1.4c, a split BE is composed of two conducting parts, partially exposed to the electric field and electrically connected outside the cell by means of electrical wires. As an example, the set-up that we use is composed of two gold wires folded by 90° with one part inside the cell and the other outside. The separation of the two wires is ensured by fixing them with silicon paste. One can consider that the split BE experiences the same polarization than a gold wire having a length corresponding to the distance between the extremities of the metal wires immersed in the solution. This set-up allows a connection with an ampermeter in series in order to easily probe i_{be} and thus i_{bps} (Equation 1.8). This configuration can be used for the rapid screening of a set of different experimental conditions, which can be very useful to determine

the best operating conditions for bipolar electrochemistry. In order to illustrate the influence of different parameters on i_{be} and i_{bps}, the following set of experiments has been carried out.

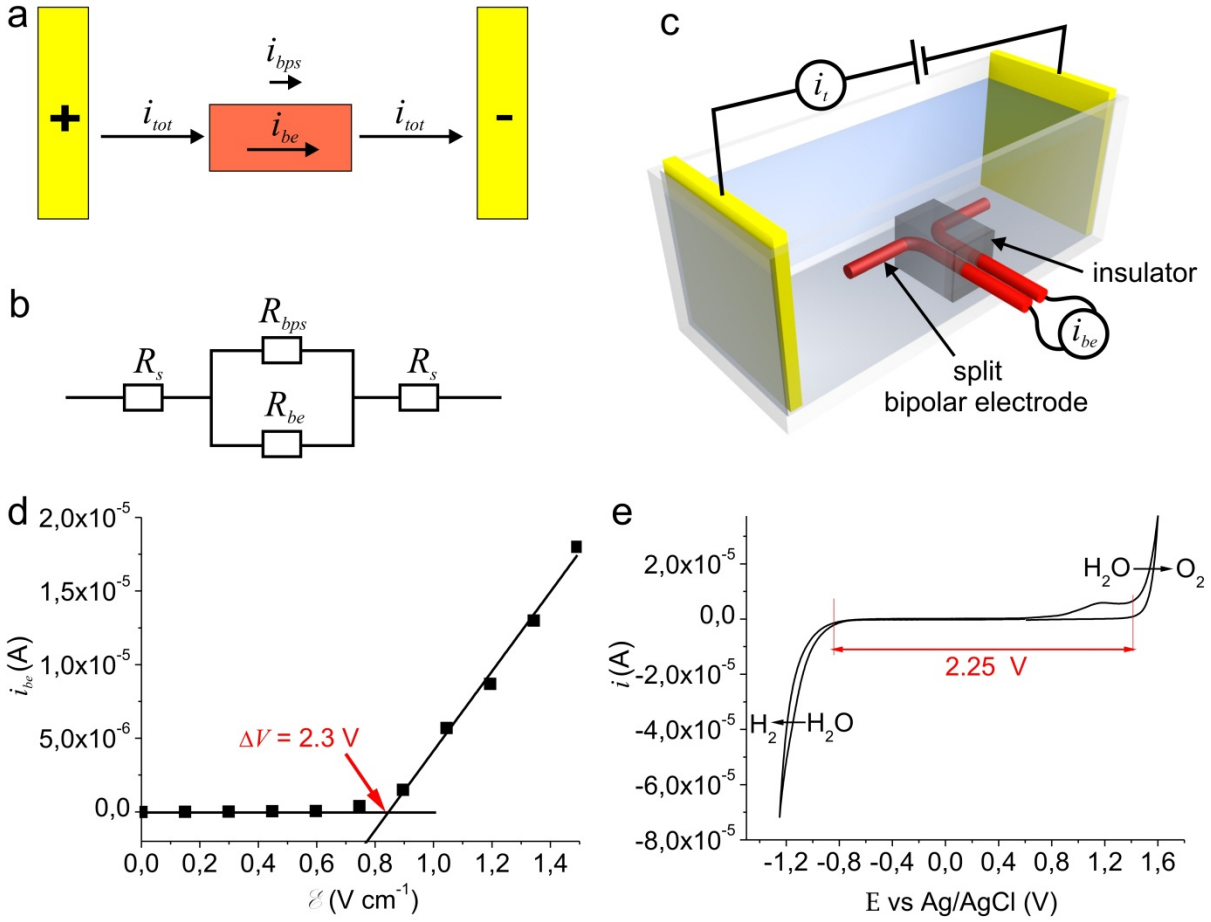

Figure 1.4. Faradaic and by-pass currents. a) Scheme of the currents flowing through the cell during a bipolar electrochemistry experiment. b) Resistance equivalent circuit for the situation depicted in figure 1.4a. c) Scheme showing the split BE set-up used for recording currents flowing through a BE. d) Plot of i_{be}, obtained using a split BE (gold wire, 1 mm diameter, d = 2.7 cm), as a function of the applied external electric field positioned in a 1 mM KNO_3 aqueous solution. e) Cyclic voltammogram obtained using a gold working electrode in a 0.1 M KNO_3 aqueous solution at 100 mV s^{-1}.

First, the electric field influence will be discussed. Figure 1.4d shows i_{be} values obtained with a gold bipolar split electrode immersed in an aqueous 1 mM KNO_3 solution as a function of applied electric field $\mathscr{E}$. Below 0.75 V cm^{-1}, no faradaic current is measured, meaning that no reaction happen at the BE poles. When the electric field is strong enough to promote the electrochemical reactions, the faradaic current, i_{be} begins to flow through the BE. After reaching 0.9 V cm^{-1}, i_{be} increases linearly with $\mathscr{E}$. A linear fit of the data obtained for $\mathscr{E}$ > 0.9 V cm^{-1} intersects i_{be}= 0 A at $\mathscr{E}$ = 0.85 V cm^{-1}, which correspond to a ΔV of 2.3 V (d = 2.7 cm) according to Equation 1.4. As it can be seen on the CV presented in Figure 1.4e, this value is in very good agreement with the threshold value ΔV_{min}

required for inducing water oxidation and water reduction at the anodic and cathodic pole respectively (see section 1.2.). The small increase in i_{be}, measured at ≈0.75V cm^{-1}, is due to the reduction of water coupled with the oxidation of the gold surface at the anodic pole, which occurs at a smaller ΔV, as it is confirmed by the shoulder-like gold oxidation wave on the CV.

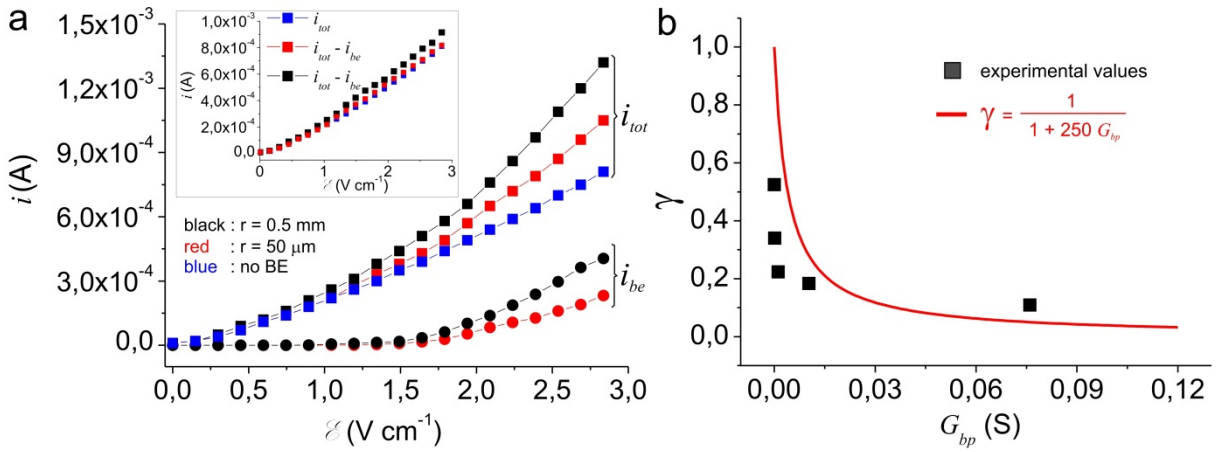

Figure 1.5. Measurements of faradaic and by-pass currents. a) Graph showing i_{tot} and i_{be} as a function of the applied electric field $\mathscr{E}$, obtained with and without split BEs (BEs are gold wires with different radius r and the same length d = 2.7 cm) in an aqueous solution of 1 mM KNO_3. Inset: graph showing i_{tot} - i_{be} (black: BE with a 1 mm diameter, red: BE with a 0.1 mm diameter) as a function of applied electric field. b) Graph showing γ as a function of the solution conductance G_{bp}.

Figure 1.5a shows polarization curves of the total current i_{tot} and the faradaic current i_{be} determined with and without BE in the cell. First we can note that i_{tot}, obtained without BE, increases linearly with $\mathscr{E}$, as it is controlled by the cell resistance. When a conducing object is in the cell, and $\mathscr{E}$ is strong enough to make it a BE, i_{tot} becomes more important.[16,18] Indeed, as the BE provides an easier current pathway, the cell conductivity is increased in the presence of a BE. In this framework, Eardley *et al.* developed a lumped parameter model for describing the effective conductivity of BEs.[19] As it is shown on the two bottom polarization curves of Figure 1.5a, less faradaic current flows through a BE having a smaller section because of its higher resistance, R_{be}. Consequently, i_{tot} values are more important when using a BE having a 1 mm section diameter compared to a 0.1 mm section diameter. From the curves obtained with BE, the by-pass current i_{bps} can be determined as the difference between i_{tot} and i_{be} (Equation 1.8). As it is shown in the inset of Figure 1.5a, i_{bps} is in the same order of magnitude for the two BE sections and matches qualitatively with i_{tot} obtained without BE.

Let us now discuss the influence of ionic strength on the current ratio γ, defined by Equation 1.9. As it was previously described, increasing the solution resistance should induce an increase of γ. In order to confirm this, using a similar set-up based on a split BE, we measured i_{be} and i_{tot} at the same

electric field value ($\mathscr{E}$ = 3 V cm^{-1}) with different concentrations of supporting electrolyte (KNO_3 from 0.1 mM to 1 M). For simplifying the model predicting the evolution of γ, we make the hypothesis that $d \approx L$ (the BE extremities are almost in contact with the feeder electrodes), in this case we can write the following relation:

$$\frac{1}{R_{eq}} = \frac{1}{R_{bps}} + \frac{1}{R_{be}} \tag{1.10}$$

Where R_{eq} is the equivalent resistance corresponding to the parallel combination of the by-pass resistance R_{bps} and the BE resistance R_{be}, as defined in Figure 1.4b. Combining Equation 1.9 with the latter one gives:

$$\gamma = \frac{1}{1 + \frac{R_{be}}{R_{bps}}} \tag{1.11}$$

Using G_{bps} as the by-pass conductance, *i.e.* the cell conductance at the BE vicinity, Equation 1.11 gives:

$$\gamma = \frac{1}{1 + R_{be} * G_{bps}} \tag{1.12}$$

Figure 1.5b shows the evolution of γ as a function of G_{bps} (calculated after measuring the electrolytic solution conductivities, σ_s using a geometrically determined cell constant, k = 1.2 cm^{-1}). As it is expected, working with a higher ionic strength (*i.e.* increasing G_{bps}) leads to an increase of by-pass current and thus a decrease of γ. Moreover, the global trend follows very roughly a fit of Equation 1.12 setting R_{eb} = 250 Ω. This resistance value, being orders of magnitude higher than that of the BE and the ampermeter impedances, can be explained by the charge transfer resistances of the anodic and cathodic reactions occurring at both extremities of the BEs.

1.4. Qualitative determination of the faradaic current profile along a bipolar electrode: the case of electron-transfer limited reaction

Kinetic aspects concerning the faradaic current that occurs along the BE are of primary importance. Many papers have been devoted to this question and different models have been developed in order to simulate the current profile along BEs. The model that will be used here is based on the one published by Duval *et al.* for describing aluminum wafer bipolar corrosion.[18] Using assumptions such as electron-transfer limited reactions, irreversible electrochemical reactions and electric field homogeneity around the BE, this model is in some cases far from the real experimental situation, especially when dealing with strong electric fields and/or big BEs, but provides a straightforward and

simple method for qualitatively understanding the faradaic current profile along the BE. Let us consider a cylindrical BE, as depicted in Figure 1.6a, with a length d and a radius r, immersed in a solution containing two electroactive species red 1 and ox 2, which can undergo the reactions 1.5 and 1.6 at the anodic and cathodic pole of the BE, respectively. We define j_1 and j_2 as the anodic and cathodic pole current densities. Assuming that these reactions are limited by the electron-transfer, Butler-Volmer should apply. We define the parameters r_1 and r_2 for reaction 1.5 and 1.6, respectively, as:

$$r_1 = n_1\,(1-\alpha_1) \tag{1.13}$$

and

$$r_2 = n_2\,\alpha_2 \tag{1.14}$$

with α_1 and α_2 being the charge transfer coefficients for reaction (1.5) and (1.6), respectively, and n_1 and n_2 the number of exchanged electrons, as defined in section 1.2. The dependence of the faradaic currents on the polarization potential E can be expressed considering the two following Tafel expressions for the anodic process (1.5) and the cathodic one (1.6),[20] respectively:

$$j_1(E) = j_{01}\,exp\left[r_1\frac{F}{RT}(E-E_1^0)\right] \tag{1.15}$$

$$j_2(E) = -j_{02}\,exp\left[-r_2\frac{F}{RT}(E-E_2^0)\right] \tag{1.16}$$

F being the Faraday constant, R the ideal gas constant, T the temperature, j_{01} and j_{02} the apparent exchange current densities for reaction 1.5 and 1.6, respectively, the other terms have been defined in section 1.2. E_m being the mixed potential of the BE, we define x_0 as the position where the net faradaic current is zero:

$$E(x_0) = E_m \tag{1.17}$$

and

$$j_1(E_m) = -\,j_2(E_m) \tag{1.18}$$

We can define now the polarization potential at x as:

$$E(x) - E(x_0) = \mathscr{E}(x-x_0) \tag{1.19}$$

Because there is no charge accumulation on the BE, the number of charges exchanged at the anodic pole has to be exchanged also at the cathodic pole. Thus the following general condition is fulfilled:

$$i_1 = -\,i_2 = i_{be} \tag{1.20}$$

i_1 and i_2 being the total anodic and cathodic pole currents, respectively. As we show in Figure 1.6b and Figure 1.6c, x_0 is the frontier between the anodic and cathodic domain of the BE. i_1 is then the integral of j_1 over the BE section from $x = x_0$ to $x = d$:

$$i_1 = \int_{x_0}^{d} 2\pi r\, j_1\big(E(x)\big)\, dx = \int_{x_0}^{d} 2\pi r j_{01}\, exp\left[r_1 \frac{F}{RT}(E_m + \mathscr{E}(x - x_0) - E_1^0)\right] dx \qquad (1.21)$$

and i_2 is the integral of j_2 over the BE section diameter from $x = 0$ to $x = x_0$:

$$\begin{aligned} i_2 &= \int_0^{x_0} 2\pi r\, j_2(E(x))\, dx \\ &= -\int_0^{x_0} 2\pi r j_{02}\, exp\left[-r_2 \frac{F}{RT}(E_m + \mathscr{E}(x - x_0) - E_2^0)\right] dx \end{aligned} \qquad (1.22)$$

The integration of Equations 1.21 and 1.22 gives:

$$i_1 = \frac{2\pi r j_{01}}{r_1 \frac{F}{RT}\mathscr{E}} \exp\left[r_1 \frac{F}{RT}(E_m - E_1^0)\right]\left(exp\left[r_1 \frac{F}{RT}\mathscr{E}(d - x_0)\right] - 1\right) \qquad (1.23)$$

and

$$i_2 = \frac{2\pi r j_{02}}{r_2 \frac{F}{RT}\mathscr{E}} \exp\left[-r_2 \frac{F}{RT}(E_m - E_2^0)\right]\left(1 - exp\left[r_2 \frac{F}{RT}\mathscr{E}x_0\right]\right) \qquad (1.24)$$

From these equations one can deduce that the position of x_0 depends among others on r_1, r_2, j_{01} and j_{02}.[18] In the special case of $r_1 = r_2$ and $j_{01} = j_{02}$ the position of x_0 will be exactly in the middle of the rod, that means at $d/2$. For every other situation, the transition from the anodic zone to the cathodic zone is shifted in one or the other direction. An illustration of such a shift can be found in the bottom part of Figure 1.3a where the silver deposit can be observed beyond the middle of the graphite bar. Even if the above model provides a first understanding of the current distribution, one has to keep in mind that it can be applied only in very rare experimental cases. Indeed, when dealing with big BEs and/or high electric fields, the current will not be controlled by electron transfer everywhere along the BE, but will rather be a competition between electron and mass transfer. Mass transfer will then play an important role and in this case diffusion and/or migration of electroactive species (depending on experimental conditions) will have to be taken in account. Finally, in practice, one has also to consider the field distribution in the vicinity of the BE, that can be influenced by the generated concentration gradients. More complicated models are required to predict the combined influence of all these parameters.

1.4. Qualitative determination of the faradaic current profile along a bipolar electrode

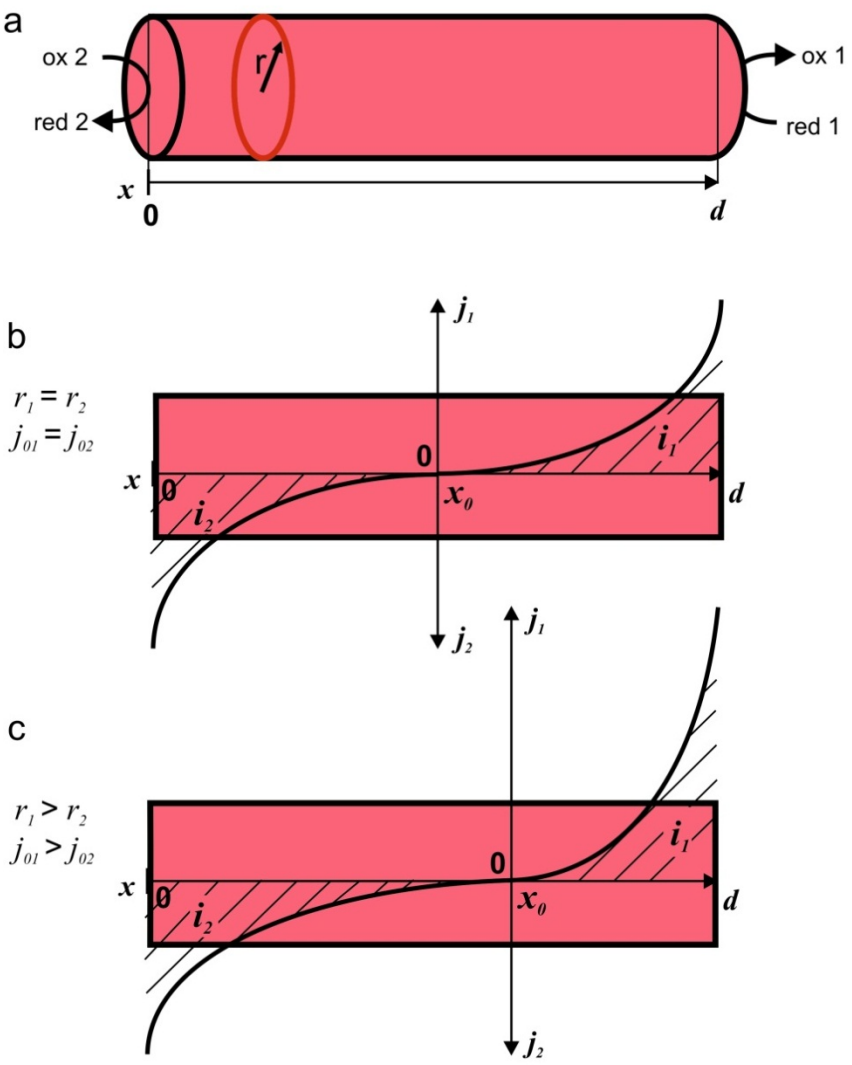

Figure 1.6. Current profiles along a cylindrical BE. a) Scheme of the cylindrical BE and the electrochemical reactions considered in section 1.2. b) Current profile along the BE for $r_1 = r_2$ and $j_{01} = j_{02}$. c) Current profile along the BE for $r_1 > r_2$ and $j_{01} > j_{02}$.

Others models than the one developed here have been proposed in the literature. Alkire reported the current study at a porous BE, for a reversible reaction, under convection and without migration of the electroactive species.[21] Yen *et al.* proposed a Butler-Volmer current distribution for a single bipolar sphere.[22] Demonstrating that the reactions at their interface are limited by the electron-transfer, Fleischmann *et al.* developed a model for diffusing bipolar spherical ultramicroelectrodes.[23,24] Duval *et al.* also developed a current model for planar BEs undergoing reversible and irreversible reactions, taking into account diffusive mass-transfer of electroactive species.[25] In the framework of electrokinetically driven bipolar electrochemistry (a topic that will be further developed in section 2.2.5.), they added the convection to this system and were able to simulate concentration profiles in the vicinity of the BE.[26] Later, a quantitative study for the analysis

of an electrophoretic conducting channel acting as a BE in the presence of a reversible redox couple was also proposed.[27] Finally, a semi-empirical method based on classic chronoamperometric measurements for determining the current density profile along a BE was proposed by Mavré *et al.*[28]

1.5. The case of closed bipolar electrochemistry

In constrast to all previously described situations, we will call "closed bipolar electrochemistry" the situation when the BE totally obstructs the cell in such a way that it is divided into two independent compartments (Figure 1.7a).[11,29] Although the situation is rarely encountered in the field of nanoscience, it differs from the "open" configuration and has several advantages. First, the fact that no by-pass current can exist is very advantageous especially in domains where high efficiencies are required. Secondly, playing with parameters such as the BE material[30] or its geometry,[29] the ratio between the polarization potential between the BE extremities, ΔV and the potential difference imposed at the feeder electrodes can be strongly increased when compared to the open configuration. In the extreme case almost the entire potential drop will occur between the BE extremities. Finally, the cell being separated into two independent compartments, the closed configuration can be used to physically separate the bipolar reduction mixture from the oxidation one if one wants to insulate reaction products or reactants.

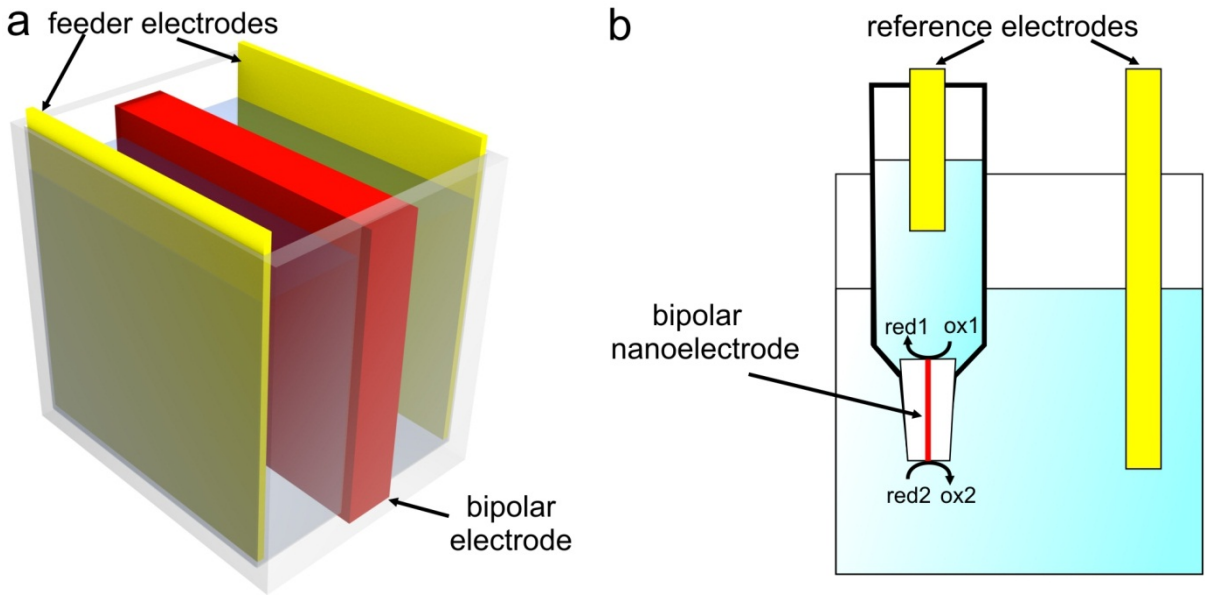

Figure 1.7. Closed bipolar electrochemistry. a) Scheme of a closed bipolar electrochemical cell. b) Scheme of the bipolar nanoelectrode used by Guerrette *et al*.in reference (29).

In the context of closed bipolar electrochemistry, Guerrette *et al.* recently described the use of bipolar micro- and nanoelectrodes for voltammetric studies.[29] As depicted in Figure 1.7b, their bipolar nanoelectrode was made of a carbon fiber sealed in a capillary tip. Different electroactive species where introduced inside the capillary and in the outside reservoir. One can consider that the total applied potential difference between the reference electrodes is restituted between the carbon BE extremities. The obtained steady-state current-potential curves have been interpreted by the coupling of reactions 1.5 and 1.6.[29] The closed configuration has also been used for probing molecular mechanisms. Indeed, this kind of cell can be used to study electron exchange between an oxidant and a reductant when physically separated and/or solubilized in different media. The current-voltage curves obtained with such a set-up coupled with a bipotentiostat was used to obtain information about electroless plating mechanisms[31,32] and interfacial electron-transfer.[33]

References

(1) Mavré, F.; Anand, R. K.; Laws, D. R.; Chow, K.-F.; Chang, B.-Y.; Crooks, J. A.; Crooks, R. M. *Anal. Chem.* **2010**, *82*, 8766.
(2) Loget, G.; Kuhn, A. *Anal. Bioanal. Chem.* **2011**, *400*, 1691.
(3) Pourcelly, G. *Russ. J. Electrochem.* **2002**, *38*, 919.
(4) Mehta, V.; Cooper, J. S. *J. Power Sources* **2003**, *114*, 32.
(5) Wang, Y.; Hernandez, R. M.; Bartlett, D. J.; Bingham, J. M.; Kline, T. R.; Sen, A.; Mallouk, T. E. *Langmuir* **2006**, *22*, 10451.
(6) Campuzano, S.; Kagan, D.; Orozco, J.; Wang, J. *Analyst* **2011**, *136*.
(7) Mano, N.; Heller, A. *J. Am. Chem. Soc.* **2005**, *127*, 11574.
(8) Smotkin, E.; Bard, A. J.; Campion, A.; Fox, M. A.; Mallouk, T.; Webber, S. E.; White, J. M. *J. Phys. Chem.* **1986**, *90*, 4604.
(9) Smotkin, E. S.; Cervera-March, S.; Bard, A. J.; Campion, A.; Fox, M. A.; Mallouk, T.; Webber, S. E.; White, J. M. *J. Phys. Chem.* **1987**, *91*, 6.
(10) Fan, C. Q.; Rivera, H.; Rao, U.; Liu, R.; Smotkin, E. S. *Electrochim. Acta* **2012**, *59*, 470.
(11) Ndungu, P. G., PhD thesis, Drexel University, **2004**.
(12) Ulrich, C.; Andersson, O.; Nyholm, L.; Björefors, F. *Anal. Chem.* **2009**, *81*, 453.
(13) King, C. J. H.; Wright, A. R. *Electrochim. Acta* **1977**, *22*, 1135.
(14) Kusakabe, K.; Morooka, S.; Kato, Y. *J. Chem. Eng. Jpn* **1986**, *19*, 43.
(15) Comninellis, C.; Plattner, E.; Bolomey, P. *J. Appl. Electrochem.* **1991**, *21*, 415.
(16) Kusakabe, K.; Morooka, S.; Kato, Y. *J. Chem. Eng. Jpn* **1982**, *15*, 45.
(17) Sudoh, M.; Kodera, T.; Hino, H.; Shimamura, H. *J. Chem. Eng. Jpn* **1988**, *21*, 198.
(18) Duval, J.; Kleijn, J. M.; van Leeuwen, H. P. *J. Electroanal. Chem.* **2001**, *505*, 1.
(19) Eardley, D. C.; Handley, D.; Andrew, S. P. S. *Electrochim. Acta* **1973**, *18*, 839.
(20) Bard, A. J.; Faulkner, L. R. *Electrochemical methods*; 2nd ed.; John Wiley & Sons, Inc., **2001**.
(21) Alkire, R. *J. Electrochem. Soc.* **1973**, *120*, 900.
(22) Yen, S.-C.; Yao, C.-Y. *J. Electrochem. Soc.* **1991**, *138*, 2697.
(23) Fleischmann, M.; Ghoroghchian, J.; Pons, S. *J. Phys. Chem.* **1985**, *89*, 5530.
(24) Fleischmann, M.; Ghoroghchian, J.; Rolison, D.; Pons, S. *J. Phys. Chem.* **1986**, *90*, 6392.
(25) Duval, J. F. L.; Minor, M.; Cecilia, J.; van Leeuwen, H. P. *J. Phys. Chem. B* **2003**, *107*, 4143.
(26) Duval, J. F. L.; van Leeuwen, H. P.; Cecilia, J.; Galceran, J. *J. Phys. Chem. B* **2003**, *107*, 6782.
(27) Qian, S.; Duval, J. F. L. *J. Colloid Interf. Sci.* **2006**, *297*, 341.
(28) Mavré, F.; Chow, K.-F.; Sheridan, E.; Chang, B.-Y.; Crooks, J. A.; Crooks, R. M. *Anal. Chem.* **2009**, *81*, 6218.
(29) Guerrette, J. P.; Oja, S. M.; Zhang, B. *Anal. Chem.* **2012**, *84*, 1609.
(30) Cattarin, S.; Musiani, M. M. *J. Electrochem. Soc.* **1995**, *142*, 3786.
(31) Plana, D.; Shul, G.; Stephenson, M. J.; Dryfe, R. A. W. *Electrochem. Commun.* **2009**, *11*, 61.
(32) Plana, D.; Jones, F. G. E.; Dryfe, R. A. W. *J. Electroanal. Chem.* **2010**, *646*, 107.
(33) Hotta, H.; Akagi, N.; Sugihara, T.; Ichikawa, S.; Osakai, T. *Electrochem. Commun.* **2002**, *4*, 472.

Chapter 2

State of the art of bipolar electrochemistry

2.1. Well-established applications of bipolar electrochemistry

2.1.1. Technologies for electrochemical reactors

Since the seventies, bipolar electrochemistry has been used intensively for designing electrochemical reactors. The development of this area generated a strong gain of knowledge in this field and is still until now the most relevant industrial application of BEs (with the bipolar batteries, see next section). Due to a number of advantages that BEs offers with respect to monopolar electrodes, many electrochemical reactors based on bipolar electrochemistry concepts have been patented. We will now explore some strategies explored for the design of such reactors.

Even if in some cases, by-pass currents can decrease the reactor efficiency, the high active area and the wireless aspect that provides bipolar electrochemistry makes bipolar electrochemical reactors powerful tools for many industrial applications. The most conventional bipolar electrochemical reactors are based on BE stacks between feeder electrodes in open or closed configurations, as shown in Figure 2.1a. A strong advantage of this configuration resides on the absence of by-pass current (see section 1.5.). Until 30 BEs can be found in industrial stacks[1] and the BE morphology can vary from simple plates,[2] and perforated plates[3] to porous conductive membranes[4]. The spatial arrangement of BEs has been adapted for specific applications such as gas-liquid electrosynthesis[5] or fused salt electrolysis.[6] These bipolar reactors have been used for different purposes, among which one can cite electrodegradation of organic compounds[3] and zinc electrowinning from chloride melts.[7]

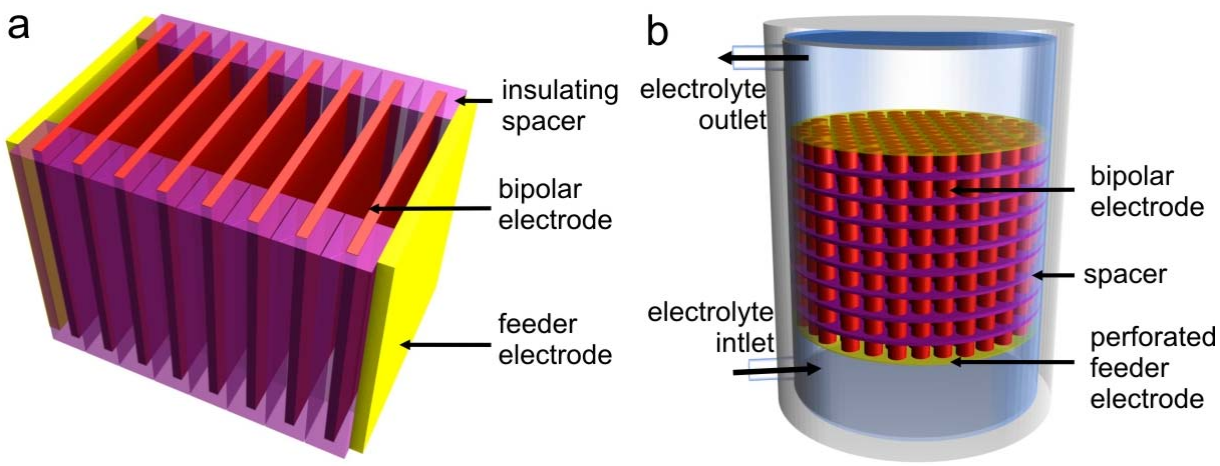

Figure 2.1. Bipolar cells. a) Scheme of a typical stack of a bipolar cell, inspired from reference (1). b) Scheme of a bipolar trickle bed, inspired from, inspired from reference (8).

In order to further increase the active surface area, bipolar packed-bed reactors, have also been developed. In this case, the BEs are usually composed of millimeter or sub-millimeter sized conducting objects packed in an arranged or a random manner.[9] These "packs" are most of the time electrically insulated from each other, as shown in Figure 2.1b, by using insulating spacers such as polymer nets for example.[8,10] The individual bipolar particles themselves can also be insulated one from another by covering them partially with an insulating material (Figure 2.2a) or totally covered by an insulating mesh (Figure 2.2b). Another interesting approach, illustrated in Figure 2.2c, is based on the use of a bed of conducting spherical particles separated with insulating ones.[11] It has been shown that in some cases, bipolar electrochemical effects can arise for single packed particles when in physical contact with each other and with the feeder electrodes,[12] this has been shown for example with manganese alloy particle stacks.[12] Most likely the high electrical resistance at interparticle contacts is the cause of their bipolarity. The reactors using this technology, combined with circulating fluid, such as the one depicted in Figure 2.1b, are called bipolar trickle bed reactors. Their use for applications such as production of potassium permanganate,[12] epoxydation of propylene,[13,14] furan methoxylation[8] and removal of metal cations from water[15] have been reported.

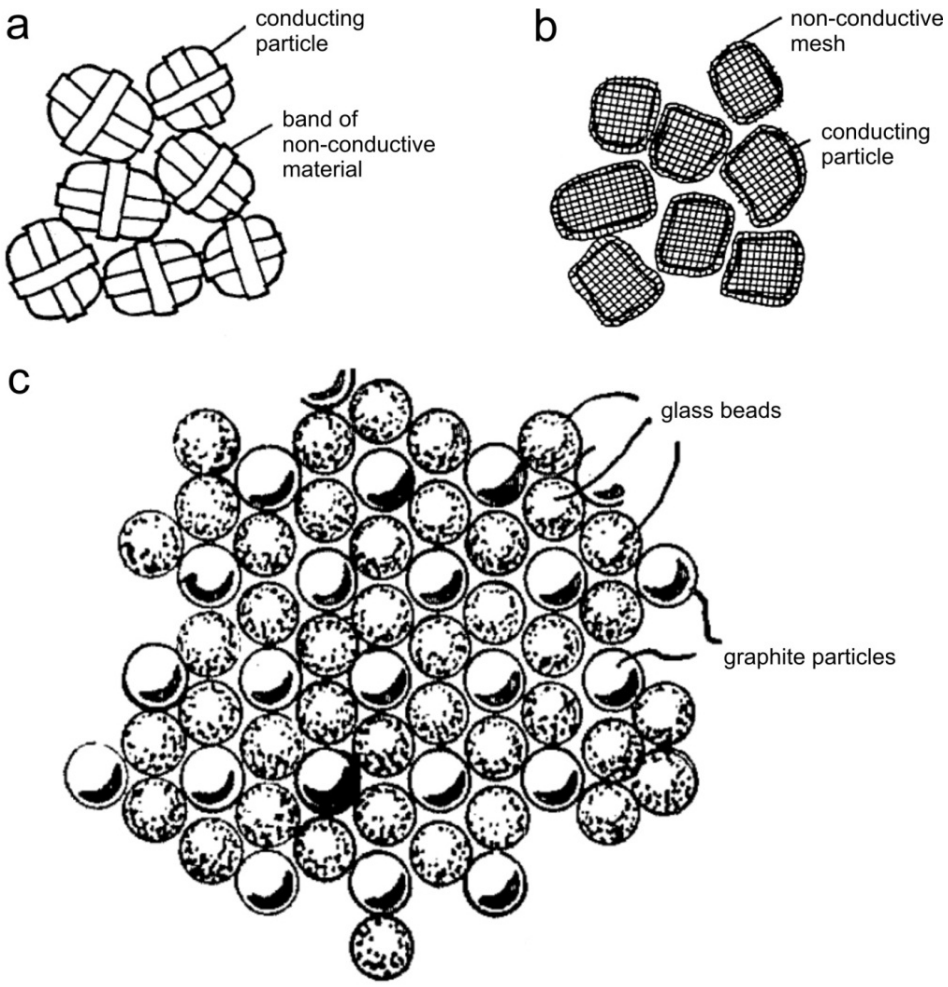

Figure 2.2. Bipolar beds. a) Bipolar particles insulated from each other using a band of non-conductive material. Adapted from an original drawing of patent (10). b) Bipolar particles insulated from each other using a non-conductive mesh. Adapted from an original drawing of patent (10). c) Graphite conductive beads separated by insulating glass beads. Adapted from an original drawing of patent (11).

The example of fluidized bed reactors (FBERs) is very interesting within the context of bipolar electrochemistry. Those beds are suspensions of particles (usually conductive) in motion, as shown in Figure 2.3b. The particles are then in intermittent contact with the feeder electrodes and with each other. Research on this reactor type has been widely developed in the seventies, since their use provides advantages for several industrial electrochemical processes,[16] such as electrodeposition on powders (see Figure 2.3a).[17] Plimley and Wright studied theoretically and experimentally the bipolar mechanism for FBERs,[18] which were previously mainly considered as monopolar reactors. This mechanism allowed to explain anomalous results, and was experimentally confirmed by Lee *et al.*[19] Before those reports, Fleishmann *et al.* already took advantage of bed bipolarity for designing bipolar FBERs.[20,21] It is interesting to note that one of the special features of this system is that due to the BE rotation, the anodic poles become cathodic and *vice versa*, leading to a self-cleaning action[22,23] that

could be very useful for certain uses in electrosynthesis. Applications of bipolar FBERs can be found in sea water electrolysis for hypochlorite production,[20,24] hypobromite production,[20,24] dimethyl secabate synthesis,[24] and copper deposition.[25]

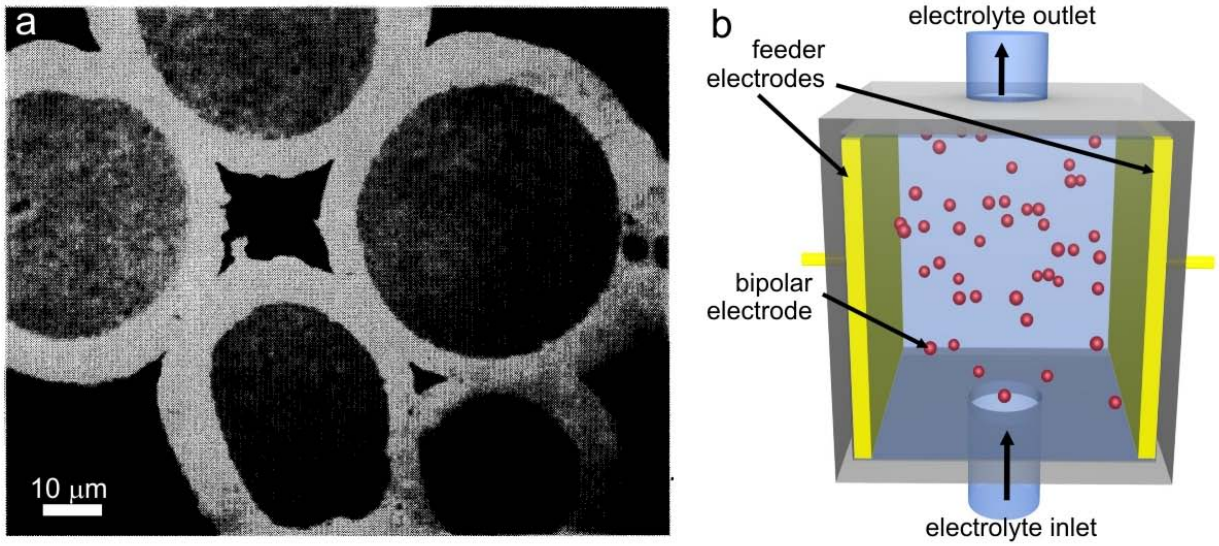

Figure 2.3. Fluidized bed electrochemical reactor. a) Optical micrograph of $AgSn_3$ particles coated with silver in a monopolar FBER, reprinted from reference (17). b) Scheme of a bipolar FBER.

It seems interesting to note that, unlike in all the previously reported applications where BEs are just a way to increase the active surface, BEs can act in some cases as an important part of the process from a chemical or a physical point of view. This is the case in applications such as defluorination of water by electrocoagulation using aluminum BEs in a bipolar reactor,[26,27] copper dissolution in a bipolar FBER[28] and dissolution of packed nuclear fuels.[29]

The last part of this section differs fundamentally from the previous ones from a purely mechanistic point of view. Non-faradaic electrochemical modification of catalytic activity (NEMCA),[30] also called electrochemical promotion of heterogeneously catalyzed reaction (EPOC)[31] is a process involving a solid electrolyte (usually yttria-stabilized zirconia or β-Al_2O_3) modified at one extremity by one catalyst metal layer and a non-catalyst metal layer at the opposite extremity. In conventional NEMCA processes, the metal layers are connected to a generator which makes the catalyst layer a working electrode and the non-catalyst layer a counter-electrode. In the presence of adequate reactants, it has been shown that the catalytic efficiency could be enhanced several hundred times, when compared with the open circuit one,[31] which cannot be explained by the faradaic currents. Up to now, NEMCA has been tested on hundreds of reactions, and even if the mechanism is still under investigation, it seems mainly due to the electrochemically induced spillover of the transported ionic

species from the solid electrolyte to the catalyst interface.[30,31] The NEMCA protocol has been transposed to bipolar electrochemistry, where isolated metal catalysts disposed on solid electrolytes act as BEs. The NEMCA effect in a bipolar configuration was first observed for the oxidation of ethylene using a single Pt bipolar catalyst.[32] Several spatial configurations were then tested to use several bipolar catalysts at the same time.[33] The same reaction was also achieved with dispersed RuO_2 bipolar catalysts.[34] More recently, Xia *et al.* reported the use of Pt nanoparticles (NPs) dispersed on yttria-stabilized zirconia as bipolar catalysts for the promotion of CO combustion.[35,36]

2.1.2. Bipolar batteries

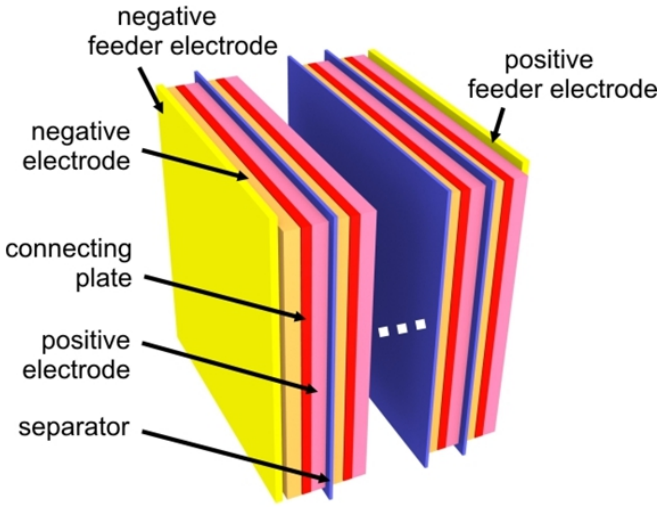

Figure 2.4. Scheme of the electrode arrangement in a bipolar battery.

Decreasing the number of electrical connections in batteries by using BE stacks instead of using monopolar electrodes allows minimizing power losses due to ohmic drop (especially in a closed configuration, see section 1.5.). In this context, many battery technologies have been adapted to the bipolar configuration. This has been the case for lead-acid,[37,38] nickel-metal hybrid,[39-40] Li-ion,[41] Li-polymer,[42] metal-H_2,[43,44] Zn-polyaniline[45] and metal-air[46] technologies. As it is shown in Figure 2.4, the BEs are generally composed by sandwiching a negative electrode plate, an electrically conductor plate and a positive electrode plate, and are electrically insulated from each other using separators. Many battery designs, BE morphologies and spatial arrangements have been proposed, as it can be seen in several patents.[47-48]

2.2. Recent applications of bipolar electrochemistry

2.2.1. Corrosion and bipolar electrochemistry

The anodic pole of a metal BE can obviously be oxidized, leading to its localized dissolution, especially for a non-noble metal. Duval *et al.* studied this phenomenon on centimeter-sized and few hundred nm thick aluminum wafers submitted to external electric fields.[49] The reported polarization curves exhibited two regimes corresponding to two different behaviors of the aluminum wafers. Indeed, similar to our data reported in section 1.3. (Figure 1.5), for the lowest $\mathscr{E}$ values, the currents were found to be proportional to the electric field, showing the ohmic contribution of the cell. Above a certain threshold value the current increased exponentially with $\mathscr{E}$ due to the apparition of the faradaic current flowing through the BEs. This threshold value of $\mathscr{E}$ corresponds to a ΔV of approximately 1.5 V between the poles of the bipolar electrode, which is in good agreement with the ΔV_{min} for water reduction at one side and the aluminum oxidation at the other side. Of course, because of this dissolution, ΔV, that is dependent on the length of the bipolar electrode (see section 1.2., Equation 1.4) decreases with time, leading to a logarithmic decrease of the wafer length as a function of time.[49] Direct industrial applications of this metal-dissolution process induced by bipolar electrochemistry have already been proposed for copper[28] and nuclear fuels[29] a few decades ago, and have been used recently for optical sensing (see section 2.2.3.2. for description and related references).

Instead of being directly used for the dissolution of BEs, the polarization of metal objects can give very useful information about their intrinsic resistance towards corrosion. The polarization resistance method is a commonly used technique for measuring the resistance of a metal towards corrosion but it requires a direct electrical contact of the studied object. Andrade *et al.* reported the contactless determination of the polarization resistance of a centimeter-sized metal BE immersed in an electrolyte under *d.c.* conditions.[50] Their proposed resistance equivalent circuit allowed extracting this value from chronopotentiometric measurements in a four electrode cell.[50] More recently, Keddam *et al.* reported the simulation of potential and current fields for a bipolar piece of metal in an *a.c.* regime and demonstrated experimentally the utility of impedance spectroscopy measurements for extracting corrosion characteristic data in a wireless manner.[51] The technique was used to probe the polarization resistance of carbon steel in different media with various ionic strengths including mortar,[51,52] and gave results close to those obtained with the classic three-electrode method where the metal was electrically connected. This new technique might be of

primary importance for building new-generation probes for the non-contact sensing of steel-bar corrosion in concrete.

2.2.2. Concentration and separation in miniaturized devices

Separation, preconcentration or concentration enrichment techniques are often required for increasing the sensitivity of detection systems. One of the most used separation system, electrophoresis, requires the use of high electric fields, so provides a good environment for performing bipolar electrochemistry. In electrophoresis, the solution containing a mixture of charged species is submitted to an electric field within a capillary or a microchannel, (see section 3.5.1. for more details). The ion motion is controlled by the synergetic action of two forces, one being due to the electrophoretic flow (EPF) and the other due to the electroosmotic flow (EOF). Their combination drive the separation of the species. Applications of BE in such miniaturized systems for concentrating and separating analytes have been the subject of numerous recent papers that are discussed in the following.

Concentrating analytes using a BE in a capillary electrophoresis (CE) set-up was first reported by Wei *et al.*[53] In their process, Pt wires were inserted in a CE fused silica capillary and CE experiments using fluorescence detection were carried out either with cationic or anionic analytes. The presence of the Pt wire led to a concentration increase of the analyte and improved the fluorescence detection signal intensity. On-capillary fluorescence imaging experiments were performed in the vicinity of the Pt wire. It has been shown that the flow of a neutral species such as coumarin 334 was not influenced at the Pt wire. In contrast, the flow of a negatively charged fluorophore was very much affected at the wire, leading to an increase of its concentration. This phenomenon was explained by a mechanism based on the pH variation caused by water electrolysis half-reactions occuring at the Pt wire extremities.[53] Consequently, an acid gradient at the anodic pole appears, simultaneously with a hydroxide gradient at the cathodic pole (see section 3.6.4. for more details about the mechanism). The analyte charges being strongly affected by pH, their electrophoretic mobility is influenced by these gradients at the bipolar electrode edges, leading to their accumulation.[53] Because this method strongly depends on parameters such as the analyte's pK_a and the pH of the medium, its versatility is limited.[54]

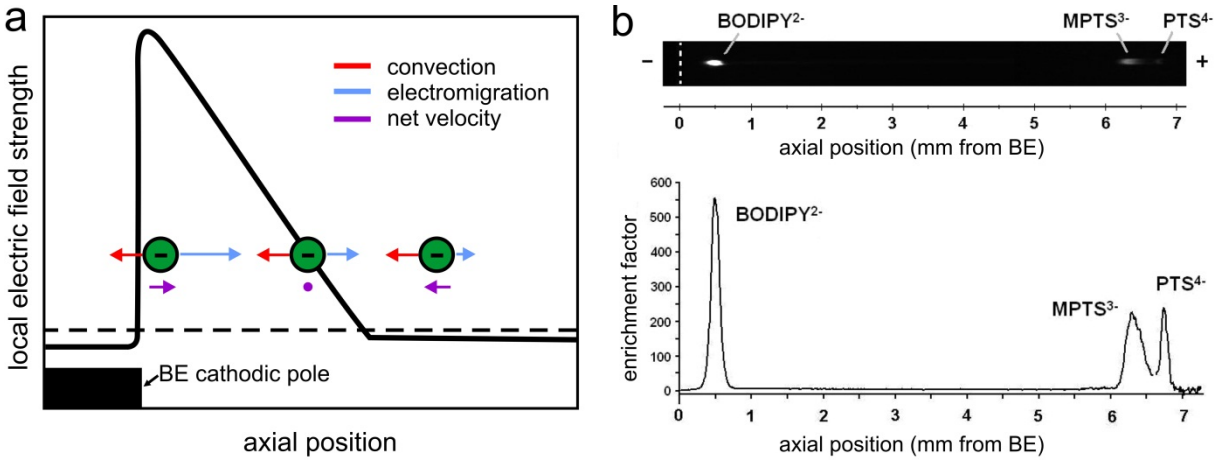

Figure 2.5. Bipolar electrode focusing. a) Schematic representation of the local axial electric field adjacent to the BE cathodic pole when the BE is active (solid line) and when inactive (dashed line). The net velocity vectors are shown at three locations for an anionic species under the combined force of electromigration and convection, adapted from reference (55). b) Top: fluorescent micrograph showing the separation of three anionic species, BODIPY disulfonate ($BODIPY^{2-}$), 8-methoxypyrene-1,3,6-trisulfonic acid ($MPTS^{3-}$) and 1,3,6,8-pyrene tetrasulfonic acid (PTS^{4-}), in 5 mM TRIS buffer within a pluronic acid-modified channel. Bottom: Plot of enrichment factor *vs* axial location corresponding to the top picture; reprinted from reference (56).

Another concentration and separation method based on the use of a BE has been recently reported and intensively developed by Crooks' group.[57,54-58] In this technique, namely bipolar electrode focusing (BEF), a gold BE or a split-BE (see section 1.3.) is located in a glass-polydimethylsiloxane (PDMS) microchannel filled with a low-concentrated buffer solution of the analyte. The first experiments were performed with boron dipyrromethenedisulfonate (BODIPY disulfonate) in Tris–HCl buffer. Electric fields were applied between two external compartments and the BODIPY disulfonate flow along the microchannel was recorded, revealing its concentration close to the BE's cathodic pole.[54] The latter molecule being highly acidic, Wei's[53] mechanism could not explain this phenomenon, which was rather rationalized in terms of electric field redistribution at the BE vicinity. Indeed, neutralization of $TrisH^+$ ions close to the cathodic pole by the OH^- produced by water reduction leads to a conductivity decrease and thus a local electric field increase at the cathodic pole as demonstrated by simulation.[59] The tracer flow, which is initially dominated by the EOF, driving it from the reservoir containing the anode to the cathode, will be strongly influenced at the cathodic side of the bipolar electrode due to the locally increased electric field. As it is represented in Figure 2.5a, in this microchannel region, the EPF will increase, which decreases the BODIPY mobility, until stopping it at the point where the EOF is fully balanced by the EPF.[59] The effect of parameters such as applied electric field, flow rate, buffer concentration, tracer concentration and surface treatment of the microchannel walls, on the local electric field profile, the enrichment position and the

amplification factor have been studied in detail.[55] As shown in Figure 2.5b, using this technique, three anionic dyes having different electrophoretic mobilities could be separated from a mixture.[56]

This concept has also been adapted for the filtration of charged species.[58] In this application, no buffer is used, which results in an increase of the conductivity at the BE edges. The resulting electric field gradient has been used to deplete anions and is expected to be effective for any charged species: molecules, biomolecules or NPs.[58] Concentrating and separating analytes with BEs is a new concept, and due to its efficiency and simplicity, this process seems very competitive compared to other classic separation and concentration procedures, especially for applications in microfluidic devices. Moreover, it has been shown that electrochemical monitoring of the enrichment can directly be coupled to BEF, which makes it even more attractive.[60] Indeed, the conductivity depletion at the BE cathodic pole during BEF, directly increases the polarization voltage ΔE between the BE extremities. This driving force amplification, which corresponds to the enrichment process, leads to an increase of the faradaic current i_{be} that can be directly measured using a split BE connected to an amperemeter (see section 1.3.).[60]

2.2.3. Sensing with bipolar electrochemistry

2.2.3.1. Electrochemical detection

As discussed above, due to the intrinsic requirement of high electric fields, electrophoresis provides very favorable conditions for bipolar electrochemistry, and in addition to the applications concerning analytes separation, it can also be used for their detection. Amperometric detection of redox active molecules under CE conditions has been shown by Klett *et al.*[61] They used two 10 μm-spaced gold microbands located at the capillary outlet, positioned perpendicular to the field direction and set in a split BE configuration. The influence of the applied electric field on ΔE was studied. It was found that electric fields superior to 3 kV m^{-1} were sufficient to reach mass-transport controlled conditions for K_4FeCN_6 oxidation and simultaneous K_3FeCN_6 reduction at the microband extremities in a solution containing these two analytes. At this electric field, the measured currents were found to be proportional to the redox couple concentration for solutions having the same conductivity. A 100 μM detection limit was reached using this set-up.[61]

Ordeig *et al.* reported a similar technique using a microfluidic channel.[62] The set-up consisted in a PDMS microchannel, that was positioned on an array of several 20 μm wide microbands. The microbands could be set as split BEs by a connecting two of them. The liquid flow within the microchannel was controlled by a syringe pump and the electric field was imposed between two external feeder electrodes. Simulations and preliminary studies of the influence of flow rate on the

current were performed and the procedure was tested with analytes such as ferrocyanide, ferricyanide and ascorbic acid. For the same ascorbic acid concentration, similar limiting currents were observed for distances between the electrodes ranging from 50 to 260 μm, which leads to the conclusion that in these three configurations, the current value is driven by the electroactive species concentration. These limiting currents were found to increase with increasing the ascorbic acid concentration and the electrochemical detection was possible for concentrations down to at least 50 μM.[62]

2.2.3.2. Optical detection based on dissolution

Crooks' team reported an original optical sensing method based on BEs.[63,64] The concept is based on the indirect detection of an electrochemical reaction based on the dissolution of the anodic pole of a BE. As previously discussed in section 1.4., the faradaic cathodic and anodic rates must be equal. Estimating the electrodissolution of a metallic anodic pole of a BE, one can then detect an analyte that is reduced at the cathodic pole.[63,64] First, the Ag dissolution caused by the reduction of a sacrificial oxidant, p-benzoquinone was studied using a split bipolar electrode configuration (see section 1.3.). The charge passing through it could be measured and was found to be correlated to the remaining length of the bipolar electrode.[63] As shown in Figure 2.6a, a more complex DNA sensing platform has then been set up. The cathodic pole of a Au/Ag BE was modified with an oligonucleotide exposed to the complementary biotin-modified oligonucleotide tagged with an avidin-functionnalized horseradish peroxidase (HRP). In presence of H_2O_2 and tetramethylbenzidine (TMB), the HRP catalyses the H_2O_2 conversion, while simultaneously oxidizing the reduced form of TMB. Under the influence of a sufficient external electric field, the oxidized TMB can be reduced at the BE cathodic pole while Ag gets oxidized at the anodic pole, probing the hybridization step (Figure 2.6b).[63]

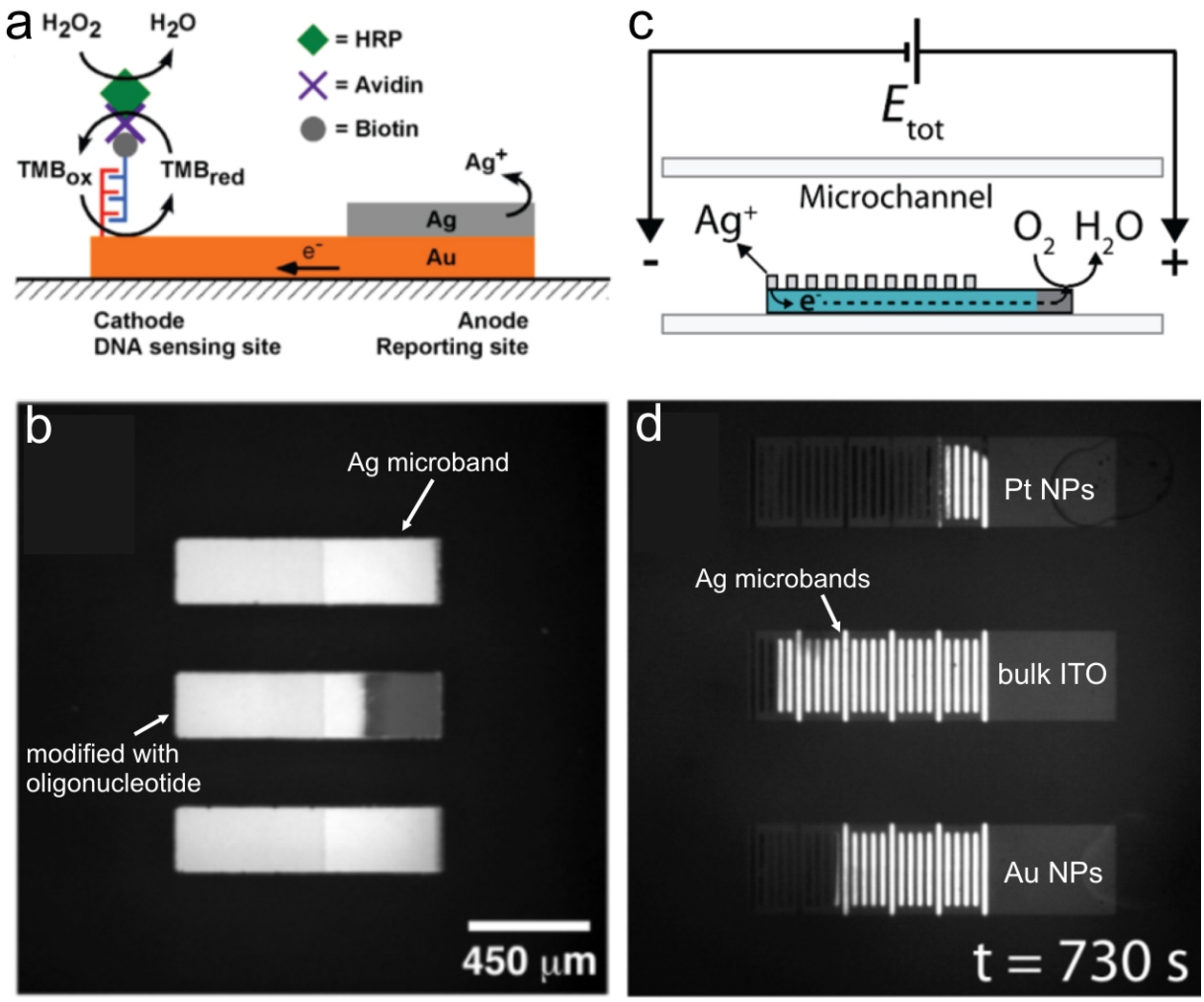

Figure 2.6. Dissolution for detection. a) Scheme of the DNA sensing platform using silver at the anodic pole of a BE. Adapted from reference (63). b) Optical micrograph showing the sensing platform composed by a set of three BEs after 90 s in the electric field: only the middle one has been modified with the oligonucleotide, while the two others are covered with 6-mercaptohexanol. Adapted from reference (63). c) Scheme of the sensing platform used for screening oxygen reduction electrocatalysts. Adapted from reference (64). d) Optical micrograph showing the sensing platform composed by a set of three BEs that contain different electrocatalysts at their cathodic poles (right side) after 730 s under the electric field. The width of each silver microband is 15 μm. Adapted from reference (64).

As depicted in Figure 2.6c, the technique can also be adapted for screening electracatalysts as it was very recently reported for oxygen reduction reaction.[64] In these experiments, the sensing platforms were composed of three indium-tin oxide (ITO)-based BEs, containing at their respective cathodic poles different electrocatalysts of interest, and their anodic poles were composed of silver microbands physically separated but electrically connected. The catalytic activity of dendrimer-encapsulated Au and Pt particles and bulk ITO were compared using this platform. After exposure for a certain time to the electric field, the efficiencies can be compared just by counting the number of

remaining silver microbands (Figure 2.6d). The results were found to be in very good agreement with data obtained by CV experiments and the number of dissolved microbands was found to be proportional to ΔV_{min} (see section 1.2.).[64] This simple technique provides an efficient way for detecting electrochemical events visually and because no special optical readout is required, very simple and cheap equipment can be used. Moreover, the sensitivity can be easily tuned by playing with the silver layer thickness.[63]

2.2.3.3. Optical detection based on electrogenerated electrochemiluminescence

Electrochemiluminescence (ECL) is a light emitting process generated by electrochemical means. ECL systems often use ruthenium trisbipyridyl ($Ru(bpy)_3^{2+}$) as the light-emitting species and an amine, such as tripropylamine (TrPA), as a co-reactant. ECL is based on the following mechanism: at approximately 1.1 V *vs* Ag/AgCl, $Ru(bpy)_3^{2+}$ and TrPA get oxidized to form $Ru(bpy)_3^{3+}$ and $TrPA^{\cdot+}$. $TrPA^{\cdot+}$ deprotonates and a subsequent electron transfer from $TrPA^{\cdot}$ to $Ru(bpy)_3^{3+}$ causes the formation of the excited state $Ru(bpy)_3^{2+*}$. Its high specificity, sensitivity and the fact the direct optical readout can be performed with a CCD camera, makes this technique a tool of choice for analytical detection. ECL is generally performed in conventional, three-electrode electrochemical cells, but its convenience makes it powerful for collecting information on processes occurring at BEs. ECL BEs have been employed for electric field mapping,[65] microfluidic integrated circuits[66] (see section 2.2.4.), and analytics as described below. It has also been used in the framework of this thesis, as it will be presented in section 4.4.

The first report of an ECL-detection technique based on bipolar electrochemistry was presented by Arora *et al*.[67] As shown in Figure 2.7a, their approach consisted in integrating an U-shaped platinum BE in the separation channel of a glass chip for electrokinetic chromatography. During the separation process, that occurred with electric fields in the kV m^{-1} range, one leg of the Pt BE was the cathodic pole where reactions such as O_2 or H_2O reduction occurred, while the other leg was the anodic pole where the ECL took place. The detection of two ECL-active ruthenium complexes was achieved by observing the emitted light at the BE anodic pole. Detection limits in the μM range could be obtained. Another experiment consisted in separating and detecting three amino acids (ECL co-reactants, as discussed previously) from a mixture.[67] Wu *et al.* used similar systems for cell analysis.[68,69] They demonstrated the inhibition of ECL by folic acid, which was explained by a quenching of $Ru(bpy)_3^{2+*}$.[68] As a consequence, ECL signal at the cathodic poles of BEs could be used for the study of folate receptors on cell membranes.[68] More recently, DNA strands tagged with silica NPs containing $Ru(bpy)_3^{2+}$ were covalently attached to the anodic pole of a bipolar electrode that was

used for the detection of a specific gene in breast cancer cells.[69] In this system, the reporter DNA strands which are released in the presence of the specific analyte gene, conjugates with the DNA strands of the BE, moving away the ECL active tag from the BE surface which resulted in a decrease of the ECL signal.[69]

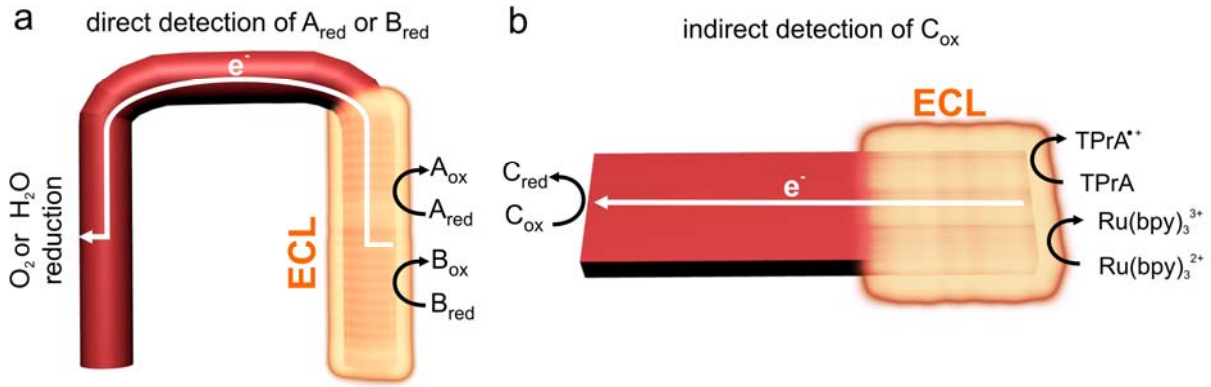

Figure 2.7. ECL for detection. a) Direct detection of analytes participating in ECL mechanism, using an ECL BE, as reported by Manz' group. b) Indirect detection of an oxidant, as reported by Crooks' group.

The latter approach consists in a direct use of ECL mechanism for detection, which limits the panel of potential analytes to the range of molecules which can actively participate in the light emitting mechanism. Indirect detection based on ECL emission at BEs has been proposed by Crooks' team. In this case the ECL generated at the anodic pole of individual BEs or BE arrays located in microfluidic systems is used to probe the reduction that occurs at the cathodic pole, as shown in Figure 2.7b. Indeed, similar to the optical detection (section 2.3.3.2.), there is a direct correlation between number of electrons involved in the reduction and the ECL photon flux. The first report concerned the detection of benzyl viologen using a ECL BE.[70] The effects of the length and the geometry of the bipolar electrode were studied and the reported detection limit was in the nM range. As shown in Figure 2.8a and b, the process was then adapted to a BE array and it has been shown that ECL could be generated simultaneously at the cathodic poles of 1000 BEs.[71] A DNA sensing plateform, based on a 1 mm long gold microband covered with a specific oligonucleotide, was designed using this concept.[72] The hybridization with the Pt NP-labelled complementary oligonucleotide led to O_2 reduction at the cathodic pole of the bipolar electrode and simultaneous ECL emission at the opposite side (Figure 2.8c). Under the same experimental conditions, no ECL emission was observed without hybridization.[72] A theoretical framework for further understanding ECL generation at bipolar electrodes has been reported by Mavré *et al*.[73]

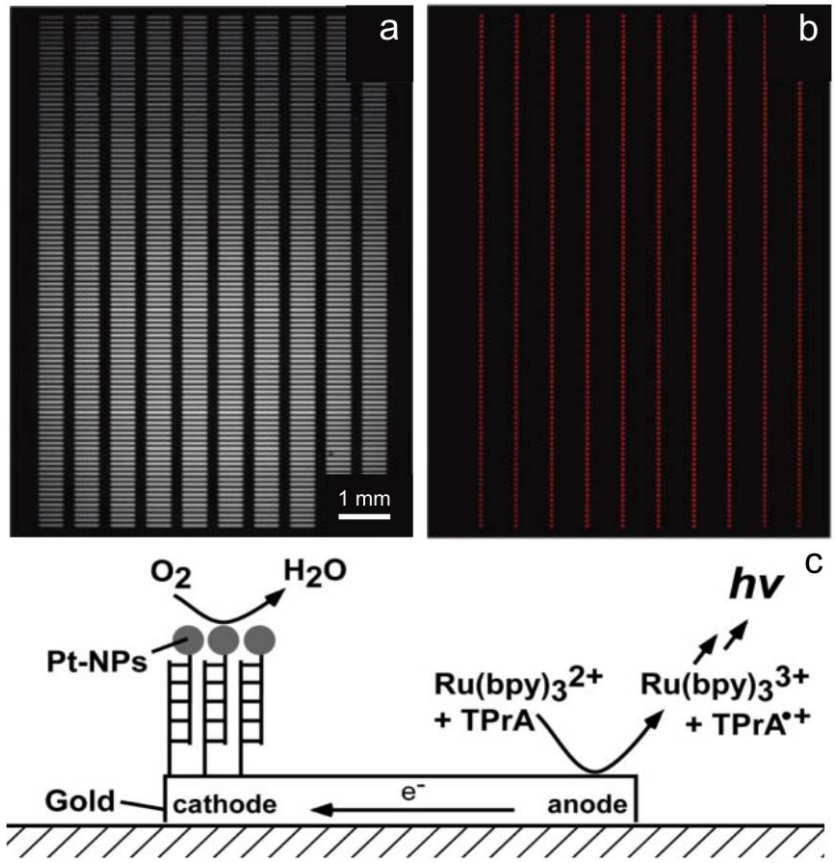

Figure 2.8. Indirect ECL detection. a) Optical micrograph of a BE array. Adapted from reference (71). b) ECL intensity emitted at 4 kV m^{-1}. Adapted from reference (71). c) Scheme of a bipolar electrochemical DNA sensor. Adapted from reference (72).

Another very original analytical concept, so called "Snapshot voltammetry", based on a ECL BE has been developed by Chang et *al*.[74] The technique consists in using a triangular-shaped bipolar electrode, the BE's tip being the anodic pole where ECL can be visualized, while the opposite edge is the cathodic pole. This BE geometry was chosen in order to make sure that ECL is not limited by the reduction (equivalent to using a bigger counter electrode in conventional voltammetry) and to minimize shifting of the frontier between the anodic and cathodic sections (x_0,see section 1.4.) that could happen when increasing the electric field. After being determined experimentally by varying the electric field values, this position can be used as a reference point for evaluating the potential gradient along the electrode. It has been demonstrated that half wave potentials and number of transferred electrons can be extracted from the measurement of the ECL intensity.[74] The authors showed that values obtained with snapshot voltammetry are in good agreement with those obtained using a classic three-electrode set-up.[74]

2.2.4. Elaboration of integrated circuits and electronic devices

Bradley *et al.* reported the generation of electrical contacts and electronic devices based on the use of BEs.[75-81] Indeed, making contacts using bipolar electrochemistry instead of classical industrial processes such as photolithography is an interesting alternative, especially when dealing with the conception of three-dimensional microcircuits. The principle of the technique consists in applying electric fields in a parallel fashion with respect to the alignment of two millimeter-sized copper particles immersed in pure water.[75] As depicted in Figure 2.9a, the copper particles act as BEs where reduction of water occurs at the cathodic poles and copper dissolution takes place at the anodic poles leading to a local enrichment of copper ions in the solution. These ions migrate towards the cathodic pole of the neighboring particle where they undergo subsequent reduction into metallic copper. The metal growth, directed by the electric field direction leads to dendritic electric wires connecting the two particles (Figure 2.9b).[77] This technique was named spatially coupled bipolar electrochemistry (SCBE).[76] Due to their larger electrochemical windows, the replacement of water by organic solvents allowed increasing the range of accessible electric fields.[78] It was also shown that the wire's solidity can be increased using an electroless plating procedure after the SCBE. The generation of connections on commercial circuit boards with this technique allowed the illumination of light emitting diodes.[80] The process has been downscaled using micrometer-sized Cu particles[78] and a study at the sub-micrometer scale with silver revealed that, due to a lack of driving force, the SCBE process reaches a practical limit for particles in the range of few hundreds of nanometer.[82] In a more recent publication, SCBE was employed to create diodes when allowing the electric connection between two external copper rings with a central *n*- or *p*-doped silicon chip.[81]

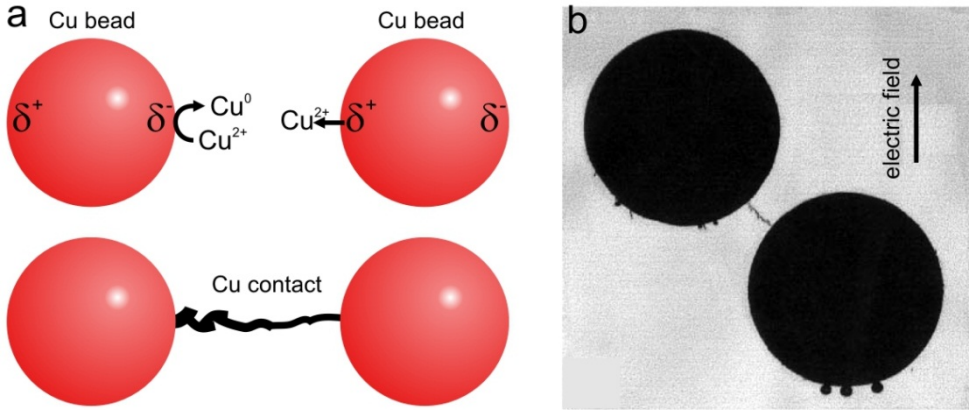

Figure 2.9. Spatially coupled bipolar electrochemistry. a) Schematic illustration of the SCBE mechanism on copper particles. b) Optical micrograph showing the electric contact between copper particles created by SCBE. Adapted from reference (77).

Due to the increasing interest in microfluidic systems, signal processing in such devices is an attractive research area and adapting classic logic-gates in a chemical way is generating a lot of attention. After having shown that BEs could be used for coupling reactions occurring in two different fluid channels in order to design microelectrochemical logic circuits,[83] Crooks' team developed bipolar electrochemistry-based micro-electrochemical gates and integrated circuits.[66] In this work the new notion of "active BEs" was introduced. In fact, a split BE, connected to a power supply, allows to shift the polarization potential between the extremities of the object with respect to the initial ΔV value (that is, the potential between the BE when in a "passive mode"). Considering the generator potential as an input parameter and the ECL (see section 2.2.3.3. and 4.4.) as an output parameter, OR, AND, NAND, and NOR logic gates have been designed.[66] Because of the use of very low voltages as input parameters, this approach might find attractive applications in lab-on-chip devices.

2.2.5. Pressure-driven bipolar electrochemistry

This section differs from all the others in this chapter in a fundamental aspect: here the electric field necessary for the generation of a BE is not induced by external feeder electrodes, but by an electrokinetic phenomenon. The so-called "streaming potential" can be seen as the opposite of electroosmotic flow (EOF). Indeed, a liquid driven through a thin layer cell or a microfluidic device having charged walls induces a counter ion motion in the electric double layer which generates this potential.[84] Under classic conditions, the streaming potential is given by the Smoluchowski equation.[84]

Duval *et al.* studied intensively electrokinetic phenomena arising at the interface of conducting objects from a theoretical and an experimental point of view.[85-87] It was shown that in presence of a reversible redox couple, the streaming potentials expected from the Smoluchowski relation are far from those experimentally determined.[86] This has been explained by the electrochemical behavior of the metal substrate which, by being a BE, develops a current that flows in the opposite direction with respect to the liquid flow. Thus, the Smoluchowski equation cannot be employed to predict streaming potentials under such conditions.[85] The nonlinear relationship between the streaming potential and the applied pressure was quantitatively interpreted by a modified Smoluchowski expression.[85,86] Using this new relation with streaming potential measurements allows getting information about the zeta potential ζ of the metal surface.[85] This has been experimentally achieved using pyrite grains with different surface coverages of humic acid.[87] Recently, using a similar concept, Dumitrescu *et al.* reported the pressure-driven dissolution of the anodic silver pole of a BE immersed in a microfluidic channel.[88]

2.2.6. Macroscopic bipolar electrodes for synthetizing material gradients

Material and molecular gradients are important in applications such as biosensors, spectroscopy and optics. Taking advantage of the polarization potentials gradient along a BE, the easy and wireless generation of material or molecular gradients on a BE surface is straightforward. Different examples that have been recently reported will be discussed now.

2.2.6.1. Formation of solid-state gradients

Shannon's group developed the concept of synthesizing solid-state gradient libraries on BEs. Their first work showed bipolar deposition of Cd, CdS and S gradients on a gold wire.[89] Since the deposition potentials of Cd, CdS and S are very different, their deposition takes place at different locations on the wire surface, in a solution containing Cd^{2+} and $S_2O_4^{2-}$ ions. The surface was then characterized by Raman spectroscopy and Auger electron spectroscopy. The reduction of Cd^{2+} to Cd^0 started at the cathodic pole, followed by the deposition of a stoichiometric CdS layer when moving towards the anodic pole and finishing with an elemental S layer at even more positive anodic overpotentials.[89] Using a similar mechanism, they also reported the formation of Ag-Au alloy gradients on stainless steel substrates.[90] The surfaces were investigated by scanning electron microscopy (SEM) and energy dispersive X-ray (EDX) spectroscopy, which revealed that the Ag content in atom percent at the cathodic pole varied from 55 to 100. After the formation of a benzene thiol monolayer, surface-enhanced Raman scattering (SERS) was evaluated along the BE, revealing its maximum effect for an Ag atom percent of about 70, using an excitation wavelength of 514.5 nm.[90]

2.2.6.2. Gradients on conducting polymers

Conducting polymers (CPs, see section 3.5.3. for more information) have usually a high conductivity, and their oxidation or reduction (coupled with the integration of counter ions present in the medium) affect the material band gap, changing significantly their color. Inagi *et al.* reported the gradient doping of CP films.[91,92] In the first publication, centimeter-long films of poly(3-methylthiophene) (PMT) were used as BEs, resulting in their asymmetric doping that could be followed visually (see Figure 2.10a) and spectroscopically by probing the counter ions by EDX measurements at different position on the film.[91] The reversibility of the process on the same polymer was demonstrated and, as shown in Figure 2.10a, the process was extended to two other polymers, poly(3,4-ethylenedioxythiophene) (PEDOT) and poly(aniline) (PAni).[92] The local application of the electric field on CP films was then used for their patterning.[93] It was recently shown that azide-functionalized CP BEs can be gradually modified by "click" chemistry in the presence of Cu^{2+} and an alkine.[94] As shown in Figure 2.10b, the local generation of Cu^+ at the cathodic pole catalyzes the

grafting. This strategy was used for the production of polymer films with hydrophobicity and fluorescence gradients.[94]

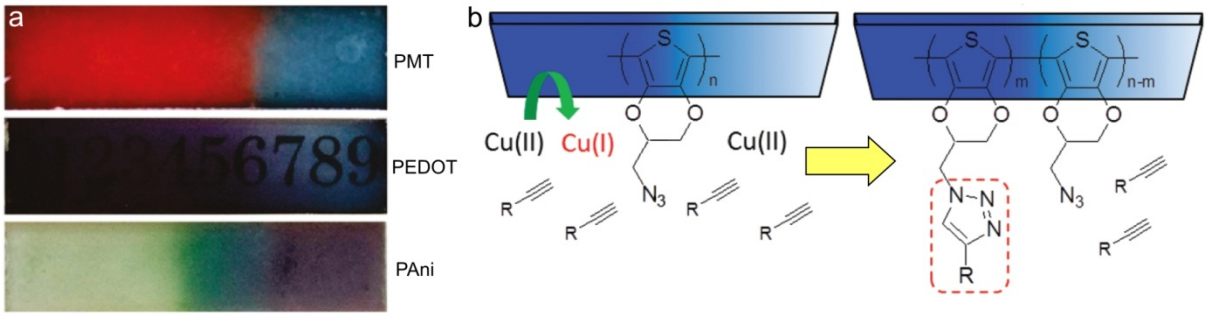

Figure 2.10. a) Optical micrographs showing different conducting polymers that were asymmetrically doped by bipolar electrochemistry. Reprinted from reference (92). b) Sheme showing the "electro-click" reaction of PEDOT-N_3 film and alkyne using cathodically generated Cu^+ species. Adapted from reference (94).

2.2.6.3. Formation of molecular gradients

Björefors *et al.* used the polarization potential gradients at BEs for creating self-assembled monolayer (SAM) gradients that were post-functionalized with proteins.[95,96]

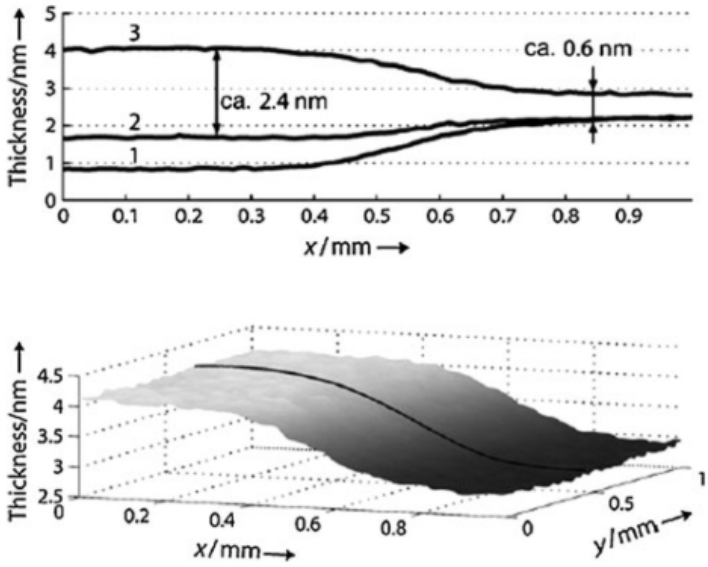

Figure 2.11. Top: line profiles obtained by ellipsometry measurements, showing the thickness of molecular gradients obtained by bipolar electrochemistry. Line 1 shows the result of the first desorption, line 2 is obtained after backfilling with a PEG, and line 3 represents the resulting protein gradient. Bottom: thickness map of the protein gradient. Reprinted from reference (96).

Millimeter long gold wafers, functionalized with thiolated mPEG SAMs were used as BEs. Under the influence of the electric field, the SAM was toposelectively desorbed from the cathodic pole, leading to a molecular gradient at the gold surface, which was characterized by ellipsometry. The naked gold surface was then backfilled with another functionalized PEG, which promoted the formation of a lysozyme gradient. As depicted in Figure 2.11, the thickness gradient values were measured by ellipsometry and the values obtained were found to be in good agreement with the theoretical values of the thiol and protein SAM thickness.[96]

2.3. Asymmetric electrodeposition on micro- and nanoparticles

2.3.1. Monopolar electrodeposition on microparticles

One important research axis of this thesis that will be developed in the following chapter is devoted to bipolar electrodeposition on micro and nano-particles for the generation of asymmetric particles. The asymmetric deposition on particulate BEs was not envisaged in the early developments of bipolar electrochemistry. Even if Lashmore *et al.* used a vibrating FBER for achieving metal electrodeposition on powders[17] (section 2.1.1.) it seems that the bipolarity that could be offered by such a system was not considered. Indeed, in this case, the reactor being mainly monopolar (the bed being in contact with the cathode), with high particle convection rates, core shell particles were obtained (see Figure 2.3a).

The only technique allowing the production of asymmetric particles, based on a monopolar mechanism has been recently reported by Gong *et al.*[97] As shown in Figure 2.12, this technique is based on the immobilization of Sn^{2+}-modified SiO_2 beads on an ITO electrode surface. After a partial masking of the bead with a conducting polymer, ZnO wires were grown electrochemically on the unprotected part and the asymmetric particle could be recovered after the polymer dissolution (inset of Figure 2.12).[97]

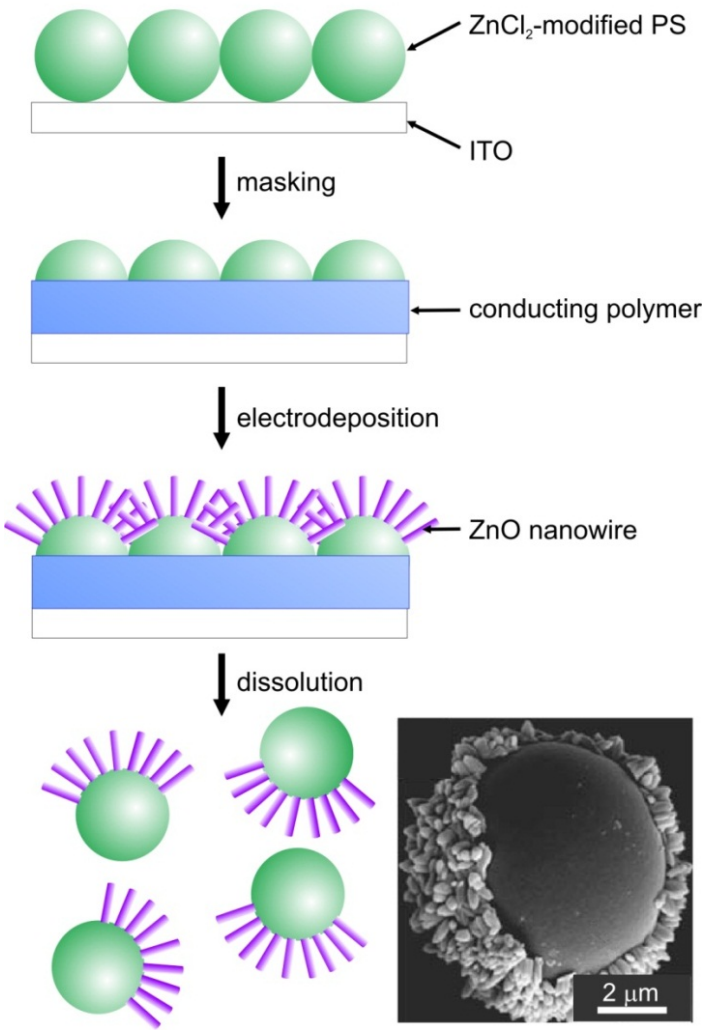

Figure 2.12. Scheme showing the synthesis of PS microspheres with ZnO nanowires by an electrochemical method. Inset: SEM picture of a PS/ZnO asymmetric particle, reprinted from reference (97).

2.3.2. Earlier works on bipolar electrodeposition with micro- and nanoelectrodes

2.3.2.1. Interfacial bipolar electrodeposition

Prior to this thesis, several publications concerning the asymmetric bipolar electrodeposition on micro- and nanoelectrodes have been published. It seems important to discuss those reports in order to clearly position the work of this thesis in the context of the literature.

As discussed previously, the asymmetric reactivity that is offered BEs is a unique feature. Using it at small scales, can allow the regioselective modification on micro- and nanoparticles, leading to the generation of asymmetric particles. Asymmetric bipolar electrodeposition on microparticles has been first reported by Bradley's group, in 1999.[98] As shown in Figure 2.13a, their concept consists in applying an electric field perpendicular to track etched membranes or cellulose papers with one layer of adsorbed particles. These surfaces being used to ensure the particle immobilization during the bipolar electrodeposition. The first publication reported the modification of micrometer-sized amorphous graphite particles with Pd.[98] In this case a Pd salt was reduced at the cathodic pole and the solvent oxidized at the anodic pole of the particulate BEs. The modified particles exhibited a higher catalytic activity when previously modified which a higher electric field. The same technique has also been used to create hybrid Au/carbon/Pd micro-objects (Figure 2.13b) by exposing the membranes to two different plating baths for two bipolar electrodeposition runs.[98] Pulsed bipolar electrodeposition was also performed for depositing Pd onto graphite powders. Field magnitudes from 50 to 300 kV m^{-1} and with frequencies varying from 0.5 to 10 kHz were used.[99] The Pd percentage and the average surface area per gram of Pd on the modified particles was determined; the amount of deposited Pd increased with the $\mathscr{E}$ value, but no significant correlation between the amount of Pd and the frequency was obtained. The particles were observed by transmission electron microscopy (TEM) showing different types of growth.

This team also focused their attention on the modification of anisotropic carbon substrates[101] such as carbon nanofibers (CNFs), carbon nanotubes (CNTs) and carbon nanopipes (CNPs). A similar set-up was used, but, in this case, the cellulose paper was placed parallel with respect to the electric field. Commercial CNFs and CNTs were modified at one end with Pd using electric field values of 300 and 1000 kV m^{-1} respectively with *d.c.* or pulsed fields.[102] In a more recent publication, CNPs were modified with *d.c.* fields leading to CNPs modified with polypyrrole (PPy) at both sides, as shown in Figure 2.13c.[100]

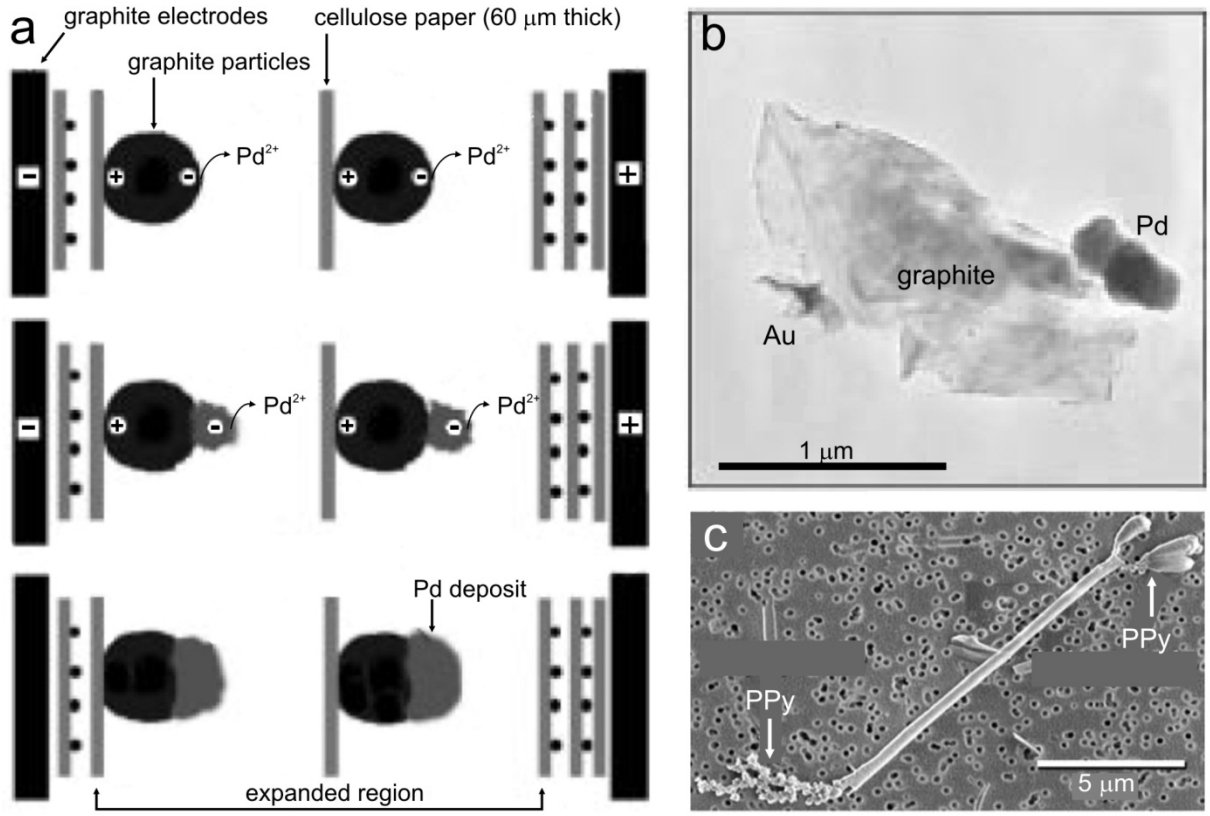

Figure 2.13. Interfacial bipolar electrodeposition. a) Schematic representation of the setup used for bipolar electrodeposition of Pd on graphite particles. Adapted from reference (98). b) TEM of an isolated graphite particle with Pd and Au introduced sequentially at opposite ends by bipolar electrodeposition with opposite field directions for each metal. Adapted from reference (98). c) Environmental SEM image of a CNP modified at both extremities with PPy by bipolar electrodeposition. Adapted from reference (100).

2.3.2.2. Bipolar electrodeposition in a capillary

Bradley's work has been of major importance for the development of the technology; however, the process had a couple of disadvantages, such as the use of organic solvents and especially the fact that the particles had to be immobilized on a surface. As a direct consequence of this latter aspect, the process can only lead to monolayer equivalents of modified objects, thus making an upscale to an industrial level very difficult. Another bipolar electrodeposition technique developed by Kuhn's group, has been reported by Warakulwit *et al.* in 2008.[103,104] This technique is based on a capillary electrophoresis (CE) equipment and is called capillary assisted bipolar electrodeposition (CABED). As this work was used as a starting point in the early stage of this thesis, the technique will be fully described in section 3.5. The first reported experiments were achieved at the macroscopic level and showed that using this technology, it was possible to selectively deposit gold at one end of a carbon

fiber, as shown in Figure 2.14a. Bubble formation coming from water oxidation was observed at the opposite end.[104]

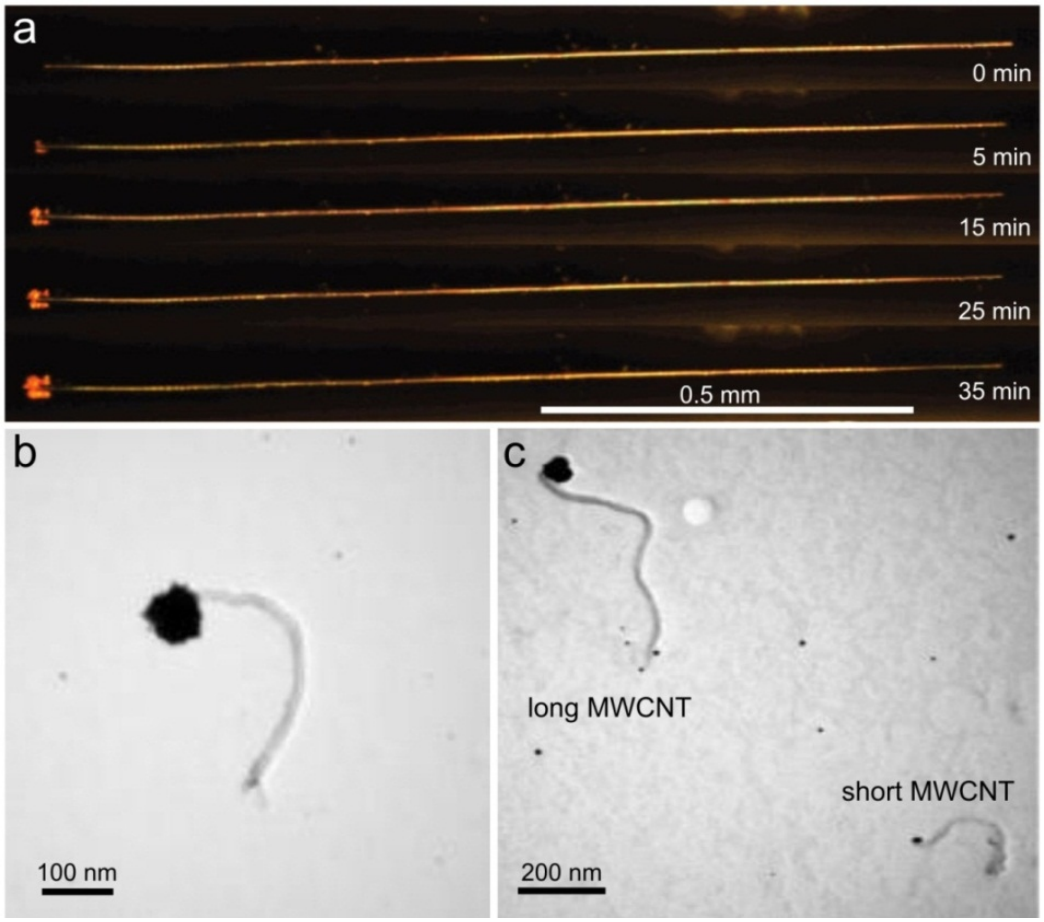

Figure 2.14. Capillary assisted bipolar electrodeposition. a) Optical micrographs of a carbon fiber inside a glass capillary during asymmetric deposition of gold by bipolar electrochemistry. Adapted from reference (104). b,c) TEM pictures of MWCNTs modified by CABED with gold. Adapted from reference (104).

Similar experiments were carried out successfully using multi-wall carbon nanotubes (MWCNTs).[104] As shown in Figure 2.14b and c, the gold-modified asymmetric objects were observed by TEM and characterized by EDX spectroscopy. The sizes of the deposit were in the order of 10 nm and increased with the length of the MWCNT (Figure 2.14c), confirming that the deposits are due to bipolar electrochemistry (indeed a long tube will experience a higher ΔV than a shorter tube, resulting in different driving forces for the deposition). In this experiment, the MWCNTs were not immobilized; this constituted the first bulk bipolar electrodeposition method, effective at the nanoscale, leading to high value-added asymmetric particles.

References

(1) Comninellis, C.; Plattner, E.; Bolomey, P. *J. Appl. Electrochem.* **1991**, *21*, 415.
(2) Hänni, W.; Perret, A.; Comninellis, C., **2001**, US patent 6306270 B1.
(3) Sudoh, M.; Kodera, T.; Hino, H.; Shimamura, H. *J. Chem. Eng. Jpn* **1988**, *21*, 198.
(4) Alkire, R. C.; Engelmaier, W.; Kessler, T. J., **1977**, US patent 4043891.
(5) Goodridge, F.; Plimley, R. E., **1981**, US patent 4270995.
(6) Beck, T.; Rousar, I.; Thonstad, J. *Metall. Mater. Trans. B* **1994**, *25*, 661.
(7) Zhao, G. *Trans. Nonferrous Met. Soc. China* **1995**, *5*, 45.
(8) Kusakabe, K.; Morooka, S.; Kato, Y. *J. Chem. Eng. Jpn* **1986**, *19*, 43.
(9) Kusakabe, K.; Morooka, S.; Kato, Y. *J. Chem. Eng. Jpn* **1982**, *15*, 45.
(10) Byerley, J. J.; Enns, K., **1985**, US patent 4517067.
(11) Backhurst, J. R.; Goodridge, F.; Fleischmann, M.; Oldfield, J. W., **1973**, US patent 3761383.
(12) Agladze, R. I.; Manukov, E. A.; Agladze, G. R., **1981**, US patent 4269689.
(13) Ellis, K. G.; Jansson, R. E. W. *J. Appl. Electrochem.* **1981**, *11*, 531.
(14) Manji, A.; Oloman, C. W. *J. Appl. Electrochem.* **1987**, *17*, 532.
(15) Kusakabe, K.; Kimura, T.; Morooka, S.; Kato, Y. *J. Appl. Electrochem.* **1987**, *17*, 724.
(16) Kazdobin, K.; Shvab, N.; Tsapakh, S. *Chem. Eng. J.* **2000**, *79*, 203.
(17) Lashmore, D. S.; Beane, G. L.; Kelley, D. R.; Johnson, C. E., **1997**, US patent 5603815.
(18) Plimley, R. E.; Wright, A. R. *Chem. Eng. Sci.* **1984**, *39*, 395.
(19) Lee, J. K.; Shemilt, L. W.; Chun, H. S. *J. Appl. Electrochem.* **1989**, *19*, 877.
(20) Fleischmann, M.; Goodridge, F.; King, C. J. H., **1978**, US patent 4124453.
(21) Backhurst, J. R.; Fleischmann, M.; Goodridge, F.; Plimley, R. E., **1980**, US patent 4206020.
(22) Goodridge, F. *Electrochim. Acta* **1977**, *22*, 929.
(23) Nadebaum, P. R.; Fahidy, T. Z. *Electrochim. Acta* **1975**, *20*, 715.
(24) Goodridge, F.; King, C. J. H.; Wright, A. R. *Electrochim. Acta* **1977**, *22*, 1087.
(25) Hutin, D.; Coeuret, F. *J. Appl. Electrochem.* **1977**, *7*, 463.
(26) Mameri, N.; Yeddou, A. R.; Lounici, H.; Belhocine, D.; Grib, H.; Bariou, B. *Water. Res.* **1998**, *32*, 1604.
(27) Mameri, N.; Lounici, H.; Belhocine, D.; Grib, H.; Piron, D. L.; Yahiat, Y. *Sep. Purif. Technol.* **2001**, *24*, 113.
(28) Bareau, J. Y.; Coeuret, F. *J. Appl. Electrochem.* **1979**, *9*, 737.
(29) Hartland, S.; Spencer, A. J. M. *Trans. Instn. Chem. Engrs.* **1963**, *41*, 328.
(30) Vayenas, C. G.; Bebelis, S.; Ladas, S. *Nature* **1990**, *343*, 625.
(31) Imbihl, R. *Prog. Surf. Sci.* **2010**, *85*, 241.
(32) Marwood, M.; Vayenas, C. G. *J. Cat.* **1997**, *168*, 538.
(33) Marwood, M.; Balomenou, S.; Tsiliras, A.; Cavalca, C.; Pliangos, C.; Vayenas, C. *Ionics* **1998**, *4*, 207.
(34) Wodiunig, S.; Bokeloh, F.; Nicole, J.; Comninellis, C. *Electrochem. Solid-State Lett.* **1999**, *2*, 281.
(35) Xia, C.; Hugentobler, M.; Yongdan, L.; Comninellis, C.; Harbich, W. *Electrochem. Commun.* **2010**, *12*, 1551.
(36) Xia, C.; Hugentobler, M.; Li, Y.; Foti, G.; Comninellis, C.; Harbich, W. *Electrochem. Commun.* **2010**, *13*, 99.
(37) Saakes, M.; Woortmeijer, R.; Schmal, D. *J. Power Sources* **2005**, *144*, 536.
(38) Loyns, A. C.; Hill, A.; Ellis, K. G.; Partington, T. J.; Hill, J. M. *J. Power Sources* **2005**, *144*, 329.
(39) Wiesener, K.; Ohms, D.; Benczúr-Ürmössy, G.; Berthold, M.; Haschka, F. *J. Power Sources* **1999**, *84*, 248.
(40) Ohms, D.; Kohlhase, M.; Benczúr-Ürmössy, G.; Wiesener, K.; Harmel, J. *J. Power Sources* **2002**, *105*, 120.
(41) Marsh, R. A.; Russell, P. G.; Reddy, T. B. *J. Power Sources* **1997**, *65*, 133.

(42) Livshits, V.; Blum, A.; Strauss, E.; Ardel, G.; Golodnitsky, D.; Peled, E. *J. Power Sources* **2001**, *97–98*, 782.
(43) van Ommering, G.; Koehler, C. W., **1984**, US patent 4565749.
(44) Lim, H. S., **1984**, US patent 4567119.
(45) Karami, H.; Mousavi, M. F.; Shamsipur, M.; Riahi, S. *J. Power Sources* **2006**, *154*, 298.
(46) Turley, H. L.; Niksa, M. J.; Pohto, G. R.; Niksa, A. J., **1989**, US patent 4927717.
(47) Einstein, H., **1978**, US patent 4211833.
(48) Kelley, K. C., **2009**, US patent 0053601A1.
(49) Duval, J.; Kleijn, J. M.; van Leeuwen, H. P. *J. Electroanal. Chem.* **2001**, *505*, 1.
(50) Andrade, C.; Martínez, I.; Castellote, M. *J. Appl. Electrochem.* **2008**, *38*, 1467.
(51) Keddam, M.; Nóvoa, X. R.; Vivier, V. *Corros. Sci.* **2009**, *51*, 1795.
(52) Keddam, M.; Nóvoa, X. R.; Puga, B.; Vivier, V. *Eur. J. Env. Civil Eng.* **2011**, *15*, 1097.
(53) Wei; Xue, G.; Yeung, E. S. *Anal. Chem.* **2002**, *74*, 934.
(54) Dhopeshwarkar, R.; Hlushkou, D.; Nguyen, M.; Tallarek, U.; Crooks, R. M. *J. Am. Chem. Soc.* **2008**, *130*, 10480.
(55) Anand, R. K.; Sheridan, E.; Hlushkou, D.; Tallarek, U.; Crooks, R. M. *Lab. Chip* **2011**, *11*, 518.
(56) Laws, D. R.; Hlushkou, D.; Perdue, R. K.; Tallarek, U.; Crooks, R. M. *Anal. Chem.* **2009**, *81*, 8923.
(57) Mavré, F.; Anand, R. K.; Laws, D. R.; Chow, K.-F.; Chang, B.-Y.; Crooks, J. A.; Crooks, R. M. *Anal. Chem.* **2010**, *82*, 8766.
(58) Sheridan, E.; Knust, K. N.; Crooks, R. M. *Analyst* **2011**, *136*.
(59) Hlushkou, D.; Perdue, R. K.; Dhopeshwarkar, R.; Crooks, R. M.; Tallarek, U. *Lab. Chip* **2009**, *9*.
(60) Sheridan, E.; Hlushkou, D.; Anand, R. K.; Laws, D. R.; Tallarek, U.; Crooks, R. M. *Anal. Chem.* **2011**, *83*, 6746.
(61) Klett, O.; Nyholm, L. *Anal. Chem.* **2003**, *75*, 1245.
(62) Ordeig, O.; Godino, N.; del Campo, J.; Muñoz, F. X.; Nikolajeff, F.; Nyholm, L. *Anal. Chem.* **2008**, *80*, 3622.
(63) Chow, K.-F.; Chang, B.-Y.; Zaccheo, B. A.; Mavré, F.; Crooks, R. M. *J. Am. Chem. Soc.* **2010**, *132*, 9228.
(64) Fosdick, S. E.; Crooks, R. M. *J. Am. Chem. Soc.* **2012**, *134*, 863.
(65) Fosdick, S. E.; Crooks, J. A.; Chang, B.-Y.; Crooks, R. M. *J. Am. Chem. Soc.* **2010**, *132*, 9226.
(66) Chang, B.-Y.; Crooks, J. A.; Chow, K.-F.; Mavré, F.; Crooks, R. M. *J. Am. Chem. Soc.* **2010**, *132*, 15404.
(67) Arora, A.; Eijkel, J. C. T.; Morf, W. E.; Manz, A. *Anal. Chem.* **2001**, *73*, 3282.
(68) Wu, M.-S.; Xu, B.-Y.; Shi, H.-W.; Xu, J.-J.; Chen, H.-Y. *Lab. Chip* **2011**, *11*, 2720.
(69) Wu, M.-S.; Qian, G.-s.; Xu, J.-J.; Chen, H.-Y. *Anal. Chem.* **2012**, *84*, 5407.
(70) Zhan, W.; Alvarez, J.; Crooks, R. M. *J. Am. Chem. Soc.* **2002**, *124*, 13265.
(71) Chow, K.-F.; Mavré, F.; Crooks, J. A.; Chang, B.-Y.; Crooks, R. M. *J. Am. Chem. Soc.* **2009**, *131*, 8364.
(72) Chow, K.-F.; Mavré, F.; Crooks, R. M. *J. Am. Chem. Soc.* **2008**, *130*, 7544.
(73) Mavré, F.; Chow, K.-F.; Sheridan, E.; Chang, B.-Y.; Crooks, J. A.; Crooks, R. M. *Anal. Chem.* **2009**, *81*, 6218.
(74) Chang, B.-Y.; Mavré, F.; Chow, K.-F.; Crooks, J. A.; Crooks, R. M. *Anal. Chem.* **2010**, *82*, 5317.
(75) Bradley, J.-C.; Chen, H.-M.; Crawford, J.; Eckert, J.; Ernazarova, K.; Kurzeja, T.; Lin, M.; McGee, M.; Nadler, W.; Stephens, S. G. *Nature* **1997**, *389*, 268.
(76) Bradley, J.-C.; Crawford, J.; Ernazarova, K.; McGee, M.; Stephens, S. G. *Adv. Mater.* **1997**, *9*, 1168.
(77) Bradley, J.-C.; Dengra, S.; Gonzalez, G. A.; Marshall, G.; Molina, F. V. *J. Electroanal. Chem.* **1999**, *478*, 128.
(78) Bradley, J.-C.; Crawford, J.; McGee, M.; Stephens, S. G. *J. Electrochem. Soc.* **1998**, *145*, L45.
(79) Bradley, J.-C., **2000**, US patent 6120669.

(80) Bradley, J.-C.; Ma, Z.; Clark, E.; Crawford, J.; Stephens, S. G. *J. Electrochem. Soc.* **1999**, *146*, 194.
(81) Bradley, J.-C.; Ma, Z.; Stephens, S. G. *Adv. Mater.* **1999**, *11*, 374.
(82) Bradley, J.-C.; Babu, S.; Carroll, B.; Mittal, A. *J. Electroanal. Chem.* **2002**, *522*, 75.
(83) Zhan, W.; Crooks, R. M. *J. Am. Chem. Soc.* **2003**, *125*, 9934.
(84) Delgado, A. V.; González-Caballero, F.; Hunter, R. J.; Koopal, L. K.; Lyklema, J. *J. Colloid Interf. Sci.* **2007**, *309*, 194.
(85) Duval, J. F. L.; van Leeuwen, H. P.; Cecilia, J.; Galceran, J. *J. Phys. Chem. B* **2003**, *107*, 6782.
(86) Duval, J. F. L.; Huijs, G. K.; Threels, W. F.; Lyklema, J.; van Leeuwen, H. P. *J. Colloid Interf. Sci.* **2003**, *260*, 95.
(87) Duval, J. F. L.; Sorrenti, E.; Waldvogel, Y.; Gorner, T.; De Donato, P. *Phys. Chem. Chem. Phys.* **2007**, *9*.
(88) Dumitrescu, I.; Anand, R. K.; Fosdick, S. E.; Crooks, R. M. *J. Am. Chem. Soc.* **2011**, *133*, 4687.
(89) Ramakrishnan, S.; Shannon, C. *Langmuir* **2010**, *26*, 4602.
(90) Ramaswamy, R.; Shannon, C. *Langmuir* **2010**, *27*, 878.
(91) Inagi, S.; Ishiguro, Y.; Atobe, M.; Fuchigami, T. *Angew. Chem. Int. Ed.* **2010**, *49*, 10136.
(92) Ishiguro, Y.; Inagi, S.; Fuchigami, T. *Langmuir* **2011**, *27*, 7158.
(93) Ishiguro, Y.; Inagi, S.; Fuchigami, T. *J. Am. Chem. Soc.* **2012**, *134*, 4034.
(94) Shida, N.; Ishiguro, Y.; Atobe, M.; Fuchigami, T.; Inagi, S. *ACS Macro Lett.* **2012**, *1*, 656.
(95) Ulrich, C.; Andersson, O.; Nyholm, L.; Björefors, F. *Anal. Chem.* **2009**, *81*, 453.
(96) Ulrich, C.; Andersson, O.; Nyholm, L.; Björefors, F. *Angew. Chem. Int. Ed.* **2008**, *47*, 3034.
(97) Gong, J.; Zu, X.; Li, Y.; Mu, W.; Deng, Y. *J. Mater. Chem.* **2011**, *21*, 2067.
(98) Bradley, J.-C.; Ma, Z. *Angew. Chem. Int. Ed.* **1999**, *38*, 1663.
(99) Bradley, J.-C.; Babu, S.; Mittal, A.; Ndungu, P.; Carroll, B.; Samuel, B. *J. Electrochem. Soc.* **2001**, *148*, C647.
(100) Babu, S.; Ndungu, P.; Bradley, J.-C.; Rossi, M. P.; Gogotsi, Y. *Microfluid. Nanofluid.* **2005**, *1*, 284.
(101) Ndungu, P. G., PhD thesis, Drexel University, **2004**.
(102) Bradley, J.-C.; Babu, S.; Ndungu, P. *Fullerenes Nanotubes Carbon Nanostruct.* **2005**, *13*, 227.
(103) Warakulwit, C., PhD thesis, Bordeaux University and Kasetsart University, **2007**.
(104) Warakulwit, C.; Nguyen, T.; Majimel, J.; Delville, M.-H.; Lapeyre, V.; Garrigue, P.; Ravaine, V.; Limtrakul, J.; Kuhn, A. *Nano Lett.* **2008**, *8*, 500.

Chapter 3

Bipolar electrodeposition for material science: Janus particle synthesis, micro- and nanostructuration

3.1. Asymmetric particles: definitions

Janus was one of the major roman gods and was usually represented with two faces looking in opposite directions (Figure 3.1). Being the god of time, beginnings, endings and transitions, he was also the god of gates and doors, hence we can still find his presence in the words "*January*" or "*janitor*" (gatekeeper). In reference to the god's facial features, De Gennes coined in the late eighties the term "Janus grains".[1,2] He used it for describing particles that, similarly to amphiphilic molecules, were composed of two different parts, one being hydrophilic and the other being hydrophobic. After De Gennes' introduction, the term "Janus particle" was usually employed for describing objects with sizes ranging from the micro- to the nanoscale owing two different chemistries or polarities and thus, structures exhibiting a chemical break of symmetry.[3,4] As shown in Figure 3.2a, the scientific interest for these structures has been exponentially growing in the last decade. Asymmetry at the nanoscale can be found in nature, a good example being hydrophobins. These proteins that are produced by filamentous Fungi, possess a hydrophobic patch composed by chain residues of leucine, valine and analine which occupy 20 % of their surface.[5] As a result of this chemical asymmetry, these proteins exhibit a surfactant behavior which can induce their self-assembly at the water/air interface.[6] This property has already been exploited for stabilizing emulsions.[7] In the last few years the term Janus is increasingly employed beyond the frontiers of micro- and nanochemistry. One can find in the recent literature publications dealing for example with "Janus macro-molecules" such as dendrimers[8] and fullerenes.[9] As the following chapter is focused on asymmetric particles at the micro- and nanoscale, this topic will not be developed.

Figure 3.1. Several representations of the roman god Janus. a) Janus on a roman coin. b) Engraving of a bust of Janus. c) Stain glass window from Notre Dame de Paris cathedral, showing Janus. d) Statue of Janus and Bellona in Schönbrunn palace, Vienna.

A very wide range of particles owning different chemistries and shapes are now available and their complexity is increasing due to the variety of synthetic procedures that emerge as nanotechnology is developing. It therefore becomes necessary to establish a precise classification that is likely to be accepted by the scientific community.[10] In this context, even if the term "Janus particle" was widely used, Du *et al.* recently clarified the description of asymmetric particles.[11] Based on their definitions, we will distinguish between "Janus" and "patchy" particles. "Janus particles" (JPs) will be employed when the object is composed of equally separated domains Figure 3.2b) in contrast to "asymmetric patchy particles" (APPs) for systems with non-equally separated domains (Figure 3.2c). The generic term "asymmetric particles" (APs) will be used when describing both of them.

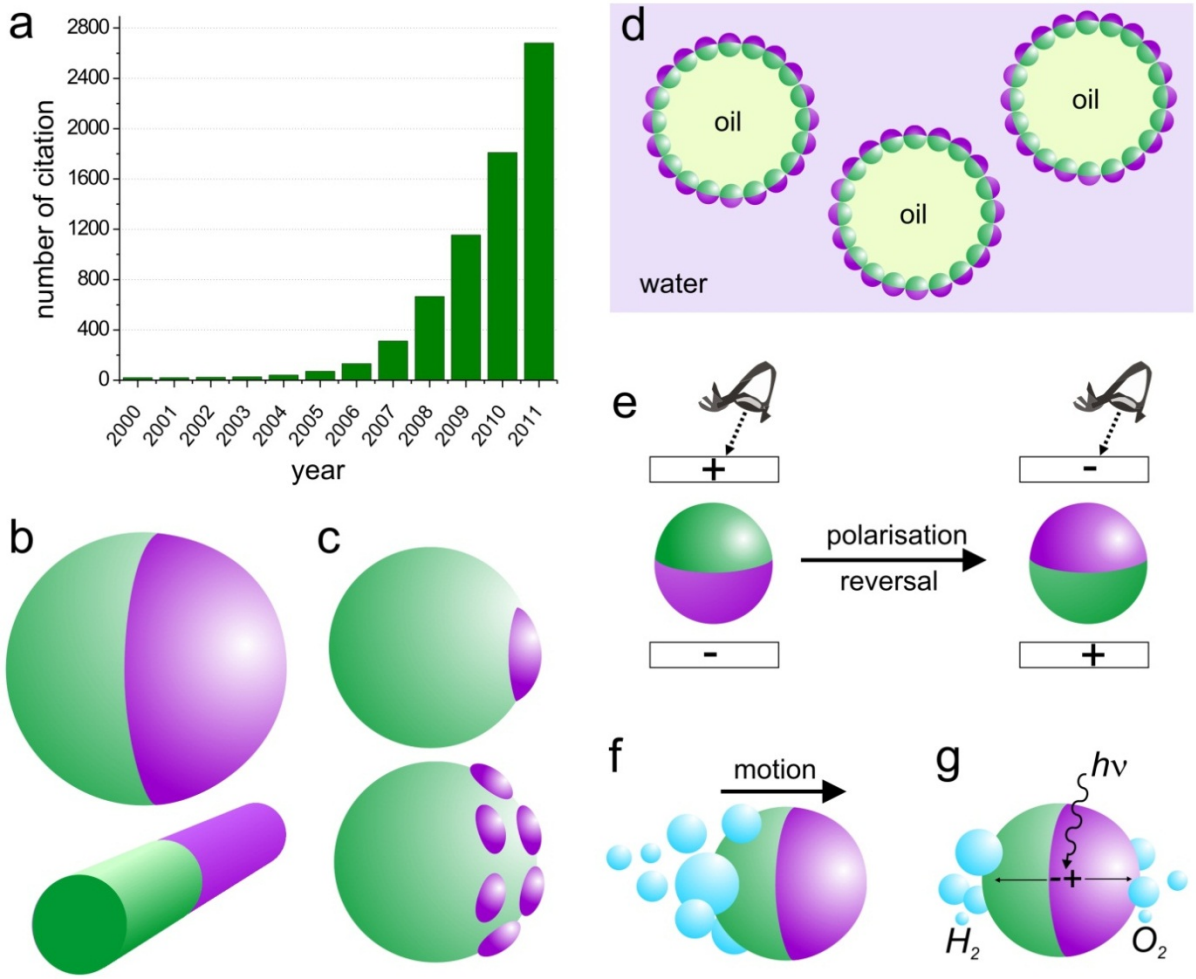

Figure 3.2. Janus particles and their applications. a) Histogram showing the evolution of the number of citations concerning Janus particles during the past twelve years (data extracted from ISI web of knowledge). b) Janus particles (JPs), isotropic (top) and anisotropic (bottom). c) Asymmetric patchy particles (APPs). d) JPs as emulsion stabilizers. e) Electrophoretical rotation of a JP between two transparent electrodes. f) Janus swimmer propelled by bubble generation at one side of the object. g) Electron-hole photogeneration at a metal-semiconductor Janus interface for water splitting. Adapted from reference (12).

Although increasing efforts are made to create different types of patchy particles (PPs),[11,13,14] symmetrical patchy particles will not be discussed, as the main focus of the present chapter is the physico-chemical asymmetry of the particles. JPs and APPs can be isotropic or anisotropic (Figure 3.2b), they can have plenty of different shapes and be constituted of many materials, that can be either hard or soft. A straightforward approach for producing APs, introduced by Casagrande in 1988,[1] that is still used in many laboratories consists in immobilizing particles at an interface for breaking the symmetry. Even if these interface-based techniques allow a very good regularity in functionalization, they make the preparation of large quantities rather difficult because they usually lead to monolayer equivalents of material as the modification occurs in a two-dimensional reaction

space. In its 1992 Nobel prize lecture, De Gennes already mentioned the importance of scaling-up the production of assymmetric objects[2]. Obviously, for their commercialization and their use at an "industrial scale", bulk techniques for producing APs need to be developed. Consequently, one can notice in the recent literature intensive efforts made in this direction.[4,3,10-12,15-26] In the second section of this chapter, the properties and applications of APs will be discussed. The synthetic techniques reported in the literature will be briefly presented in section 3.3. The experimental results will be reported in the following sections.

3.2. Applications of asymmetric particles

3.2.1. Adsorption at interfaces and self-assembly

Because of their intrinsic heterogeneities, one of the first properties of Janus and asymmetric patchy particles that naturally comes into one's mind is their assembly at interfaces, and intensive work has been carried out to observe and understand this phenomenon. De Gennes illustrated the assembly of JPs at interfaces using the expression: "*The skin can breathe*", imagining a monolayer of "*Janus grains*" like a membrane with "*pores*" between the grains, allowing the exchanges between the two separated media.[2] Organization of poly(methyl methacrylate) (PMMA) and polystyrene (PS) JPs at the water-air interface has been observed by Xu *et al*.[27] and several theoretical studies have been performed for predicting JP behavior at liquid-liquid interfaces. Binks *et al.* performed calculations in order to compare the adsorption of homogeneous spherical silica particles to asymmetric ones at the oil-water interface. It was found that by maximizing the amphiphilicity of particles, desorption energies can be increased by a factor of three.[28] Nonomura *et al.* estimated the adsorption energy for ≈10 μm diameter Janus disks at a liquid-liquid interface as about 10^8-10^9 k_BT.[29] Considering these data, in addition to the Pickering effect, which generally is related to particles in emulsions, the strong potential for APs to be used as particulate surfactants becomes obvious (Figure 3.2d).[30] Comparable to the hydrophilic-lipophilic balance (HLB) for amphiphilic molecules, the notion of "Janus balance" was introduced by Jiang *et al.* as the ratio of work to transfer a JP from the oil-water interface into the oil phase and the work needed to move it into the water phase.[31] This value (that can also be applied to homogeneous particles) is calculated with simple parameters and gives information about the particle adsorption which can help designing efficient asymmetric particle emulsifiers. Hirose *et al.* studied theoretically the adsorption of spherical submicron APs at curved interfaces, and concluded that liquid droplets surrounded by Janus particles may be stable and can be considered as a soft solid.[32] Ruhland *et al.* measured interfacial tensions at liquid-liquid interfaces using submicrometer and micrometer-sized PMMA/PS Janus disk stabilizers.[33] A very nice practical

study of micrometer-sized spherical JPs at the oil-water interface was carried out by Park *et al.*[34] It has been shown that, in contrast to homogeneous particles, JPs were attracted to each other due to capillary interactions generated by the irregular shape of the Janus boundary. A control of the inter-particle interactions based on electrostatic repulsions was also demonstrated.[34] Adams *et al.* also insisted on the importance of the quality of the Janus boundary as well as its roughness for the adsorption at air-water and water-oil interfaces.[35] Cheung *et al.* used Monte-Carlo simulations with nanometer-sized JPs and emphasized the fact that at these scales, the particles get more affected by Brownian motion, and one has to carefully consider their orientational freedom.[36] Glaser *et al.* measured a considerable decrease of water-hexane interfacial tension using ≈10 nm APPs compared to homogeneous particles of similar size and chemical nature.[37] The binding of Pt/Fe_3O_4 asymmetric nanodumbbells to WS_2 nanotubes was recently studied.[38] Sahoo *et al.* showed that the soft Pt block has a higher sulfur affinity than the harder magnetite face, driving the binding proceeds preferentially through the Pt face. This binding preference can be reversed by masking the Pt face with an organic protecting group.[38]

3.2.1.1. Particulate surfactants

Several groups used Janus and APPs as particulate surfactants. Polymeric and silica micrometer and submicrometer-sized APPs with different morphologies were used for stabilizing emulsions (Figure 3.2d).[39,40] Recently, more complex and very interesting systems were developed. Firstly, Tanaka *et al.* showed the control of the Janus balance on mushroom-like asymmetric particles upon stimuli such as temperature and pH, resulting in stabilization/destabilization of emulsions.[41] Secondly, Liang *et al.* used tailored Janus nanosheets as particulate surfactants; modification of one side of the sheets with paramagnetic particles allowed manipulation of the droplets with a magnetic field.[42] Particulate surfactants owning catalytic parts make them very attractive catalysts for reactions where reactants and products are soluble in different phases.[43] Such a system was elegantly presented by Crossley *et al.* for improving biofuel upgrade reactions.[44]

3.2.1.2. Stabilizers in polymer systems

Advanced materials can be obtained by blending non-miscible polymers. In order to be successful, the blending requires the use of compatibilizing agents, often block copolymers, which generates several problems such as micellisation and non-specific adsorption of the agent.[45] In order to overcome the problems, Walter *et al.* demonstrated the use of JPs as very efficient stabilizers for PMMA and PS blends.[45] Simulations were also recently performed in order to predict the incorporation of JPs into macroscopically oriented structures of diblock copolymers.[46] Interestingly, it

was recently observed that JPs can be spontaneously generated in quaternary polymer blends.[47] In a similar way JPs have been used for emulsion polymerization of PS, styrene and *n*-butylacrylate without additives.[45] The size of the monodisperse PS latexes that can be obtained are controlled by the amount of added JPs.[45]

3.2.1.3. Water repellent

Morphologies and wetting properties of silica wafers coated with micrometer-sized spherical asymmetric polymeric particles (hydrophilic/hydrophobic) were recently studied and compared to the one obtained with homogeneous particles.[48] Surfaces coated with homogeneous particles showed a hydrophobic behavior, while, due to APs self-assembly into aggregates, surfaces coated with them were super-hydrophobic.[48] Kim *et al.* prepared microstructured JPs that were used for conceiving flexible hydrophobic surfaces and liquid marble that can be manipulated with tweezers.[49] The possibility to use JPs for making water repellent textiles has also been demonstrated recently.[50]

3.2.1.4. Janus particles for membranes

Based on computer simulations, Axeleev *et al.* predicted that combining a lipid membrane and APs could lead to a new kind of membrane.[51] When the membrane is stretched, pores can open, that close again when the tension is released. As shown in Figure 3.3, In the presence of APs, which will locate at the inner pore wall, the pore is stabilized letting an “open door” for exchanges through the membrane.[51]

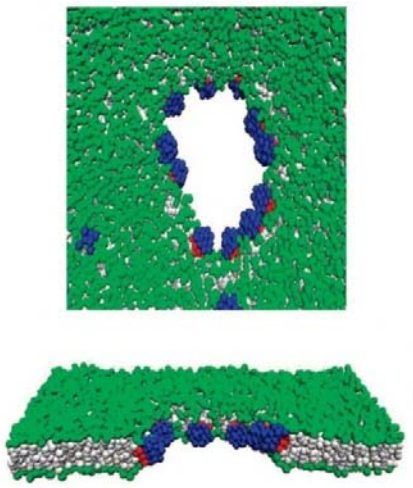

Figure 3.3. Simulated snapshots of a lipid bilayer membrane in the presence of JPs, showing the top (top) and the side view (bottom) of a pore that was formed by stretching a membrane. Adapted from reference (51).

3.2.1.5. Self-assembly of asymmetric particles

APs, like amphiphilic molecules, have the ability to self-assemble into superstructures. This phenomenon is very interesting from an intellectual as well as from a practical point of view and could be used to mimic molecular behavior.[10,22] Experimentally, Park *et al.* showed that micrometer-long gold/polypyrrole (PPy) nanorods arrange themselves in solution, giving rise to fascinating structures (from bundles to core-shell hollow spheres) that can be controlled by tailoring the rod morphology.[52] Walter *et al.* studied the assembly of PMMA/PS Janus cylinders, showing that above a certain critical concentration or in certain solvents fiber-like superstructures constituted of cylinders with a PS domain at the centre are formed.[53] Theoretically, first simulations of the patterns that can be formed by the self-assembly of JPs were performed using a very simplified 2D model.[54] Granick's team carried out very important work based on simulations and experimental observations to further understand JPs assembly.[23] Simulations and experiments revealed that dipolar spherical JPs form clusters with a preserved charge anisotropy (in the case where the particle diameter is higher than the electrostatic screening length).[55] A second approach, based on experiments and a model considering charged/hydrophobic spherical JPs, also predicted the formation of small clusters.[56] A very interesting element revealed in this case is that the size of the cluster can be controlled by the salt concentration. At low ionic strength, the electrostatic repulsion between JPs will dominate the hydrophobic interactions, leading to small clusters. Increasing the salt concentration will lead to bigger clusters with very interesting morphologies such as worm-like structures or a chiral triple helix.[56,57] The self-assembly of Janus ellipsoids has also been recently predicted with a primitive model using Monte Carlo simulations.[58]

3.2.2. Dynamics in magnetic and electromagnetic fields

3.2.2.1. Orientation control of Janus particles in *d.c.* electric and magnetic fields-towards pixels for e-paper

Electronic paper (e-paper) is a display technology designed to imitate the paper appearance for objects such as mobile phones and e-book readers. The majority of e-paper technologies are based on electrophoretic screens. The display is constituted of vesicles, acting as pixels, which are filled with black and white particles owning opposite charges. Each vesicles being sandwiched between transparent electrodes, switching their polarity results in attracting particles with different charge and colour towards the reader's eye.[59] One can easily imagine that JPs are very suitable objects to increase the performance of such a technology. This would avoid the use of vesicles and allow to increase the display resolution since in this case each JP can act as a pixel (Figure 3.2e). Indeed,

dipolar JPs will orientate in *d.c.* electric fields as it has been demonstrated with gold/latex JPs[60] and with gyricon balls.[61] This phenomenon has been already used for conceiving electrophoretic screens with electrically anisotropic 100 μm black/white[62] and 300 μm black/green[63] Janus beads. Very recently, colored magneto-driven displays have been introduced, with Janus beads containing magnetic nanoparticles (NPs) at one side and fluorescent quantum dots[64] or a colloidal photonic crystal at the opposite side.[65]

3.2.2.2. Motion and assembly in *a.c.* electric fields and magnetic fields

Velev's group carried out pioneering work by studying experimentally the behavior of JPs in external fields.[66] As it was predicted by Bazant and Squires,[67,68] APs composed of materials with different polarisability move in homogeneous *a.c.* electric fields.[69] Micrometer-sized PS/gold JPs have been studied in low-frequency *a.c.* electric fields. First, due to the largest induced dipole orientation in the field direction, they orientate with the boundary being parallel with respect to the ACEF direction. Then, submitted to induced charge electrophoresis,[67,68] they move normal to the electric field towards the PS part (Figure 3.4a). In fact, the induced double layer of the metal part being composed of much more counter-ions than at the insulating part, the ions will move tangentially to the electric field direction, dragging liquid and thus generating the motion (Figure 3.4a, inset).[69] Due to the electric-field-induced dipole interactions between the same JPs, at higher field frequencies, they assemble in staggered chains, 3D bundles or 2D crystals (Figure 3.4b and c) and disassemble when the field is switched off.[70] Micrometer-sized PS/iron JPs can assemble in *a.c.* electric fields as well as in magnetic fields.[71] Depending on the coating thickness, different JP chain morphologies can be formed, which persist when the magnetic field is removed and can be disassembled by demagnetisation.[71] APs containing a *p*-type material/metal junction exhibit a diode like behavior.[72] Chang *et al.* have shown that diodes can be moved in a controlled way an *a.c.* electric fields.[73] Indeed, the rectifying effect of the diode generates an electroosmotic flow in the electric double layer which directs the motion.[73] Recently, Calvo-Marzal *et al.* propelled cadmium-polypyrrole APs in *a.c.* electric fields at a micrometer-scale.[74]

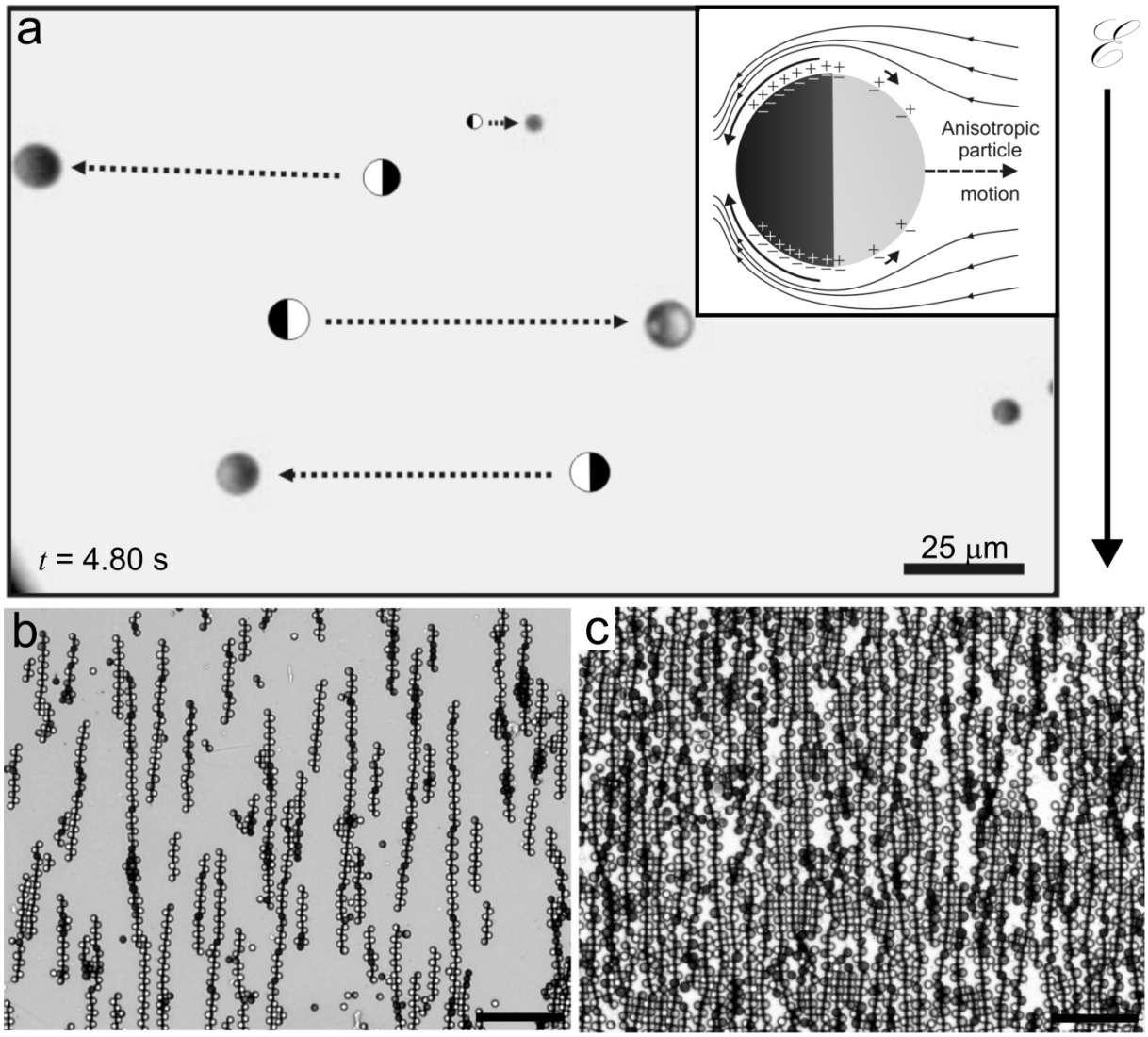

Figure 3.4. Janus particle dynamics in *a.c.* electric fields. a) Optical images illustrating motion of PS/gold JPs in an *a.c.* field of 140 V.cm^{-1} and 1 kHz frequency, JP positions at t = 0 s are represented by drawings. Inset: induced charge electrophoresis scheme responsible for the motion. Adapted from reference (69). b) Optical micrograph of staggered chains of PS/gold JPs formed at 56 V cm^{-1} at 40 kHz; the scale bar equals 70 μm. Reprinted from reference (70). c) Optical micrograph of a metallodielectric 2D lattice of confined staggered chains formed at 27 V cm^{-1} at 40 kHz with a higher JP concentration; the scale bar equals 50 μm. Reprinted from reference (70). The field direction for the three figures is indicated by the upright arrow.

3.2.2.3. Manipulation with optical, optomagnetic traps and motion in a laser beam

In contrast to dielectric micro/nanoparticles and metallic NPs that can be manipulated in three dimensions in optical traps, metallic microparticles and micro JPs owning a metal part can be only controlled in two dimensions due to the inhibition of the light transmission by the metal coating.[75]

This lowers their spatial control in optical traps, but can also provide an original way to generate a JP rotational motion above a certain laser power.[76] Erb *et al.* showed for the first time that micrometer-sized spherical APPs with a metal patch can be controlled in three dimensions by optical tweezers.[75] Using a cobalt patch, they were able to control two additional degrees of freedom in an optomagnetic trap.[75] Besides the context of the optical tweezers, Jiang *et al.* used a defocused laser beam to propel silica/gold micrometer-sized Janus beads by self-thermolysis, the motion being directed by the temperature gradient generated due to the laser absorption by the gold.[77]

3.2.3. Chemically and magnetically-driven micro- and nanoswimmers

Autonomous microswimmers are of enormous interest for practical applications such as drug delivery,[78] DNA detection,[79] isolation of cancer cells[80] and writing of microstructures.[81] The swimmers are APPs with patches that can be used to generate a linear motion. Several strategies have been developed and the motion can be generated using magnetically and/or chemically active patches containing a ferromagnetic material,[82-84] enzymes[85] or enzyme mimics.[86] The most developed strategy consists in using the hydrogen peroxide decomposition reaction at a metal catalyst patch for generating the motion by self-electrophoresis[87] or a bubble propulsion mechanisms[88,89] (Figure 3.2f). This research area becomes very attractive and a lot of efforts are made by different groups,[90-95] among which one can cite Wang *et al.*,[96-99] Mallouk *et al.*,[100,101] Sen *et al.*[102,103] and Ozin *et al.*[104,105]. Since Chapter 4 is dedicated to dynamic systems, this area will be further developed in section 4.1.

3.2.4. Asymmetric particles for sensing

As it was discussed previously, APs orientate in a *d.c.* electric field. As this orientation ability depends on the surfaces charges, one can use APs functionalized on one part with a pH dependent charged molecule to make a pH sensor.[60] 5 nm magnetic APPs owing pH or temperature sensitive polymer patches have been synthesized. Since these parameters affect the agglomeration state of the PPs by hydrophobic forces and electrostatic repulsions, their precipitation can be considered as an output signal.[106] Himmelhaus *et al.* conceived an optical detector with arrays of ≈100 nm spherical PS/gold JPs having a homogeneous alignment (the PS half facing the substrate).[107] The maximum wavelength of the array's extinction peak depending on the refractive index of the media and on the compounds binding to the gold half spheres, these systems can be used for *in situ* sensing of self-assembled monolayer (SAM) formation and binding of biomolecules.[107] Microsized fluorescent/metal JPs spheres in suspension exhibit fluorescent patterns, looking like the moon phases, from which information about the four degrees of freedom can be deduced.[108] Magnetic fluorescent metal JPs (MagMOONs) rotating in an external magnetic field, can be very useful for detection in biological

environments, since the periodic blinking of the JPs allows an easy *in situ* background subtraction.[109-113] The free motion, due to Brownian motion, of similar systems in solution can be used for conceiving modulated optical nanoprobes (MOONs). The autocorrelation function of the fluorescence fluctuation of the blinking MOONs allows precise detection of parameters such as temperature, pressure, viscosity, chemical interactions and influences of the environment.[114,115,116]

3.2.5. Interaction with light: plasmon materials, anti-reflecting surfaces and photocatalytic applications

Wang *et al.* studied experimentally plasmonic properties of arrays made of ≈200 nm dumbbell-like gold nanoshell APs.[117] The polyvinylpyridine coated parts of the AP are embedded into PDMS, so that each AP side faces different dielectric environments, leading to non-similar plasmon modes that hybridize.[117] In another context, it was reported that PS snowman-like AP arrays on glass show a transmittance increase compared to glass with a single layer of spherical PS particles, this so-called motheye effect can be very useful for designing anti-reflective coatings.[118] Photogeneration of electron-hole pairs upon photoexcitation of semiconducting (SC) material can be used for exciting applications such as depollution, synthesis, particle modification (see section 3.3.) and water splitting. However, photocatalytic activity of sole SC particles is usually poor and leads to high charge recombination rates. Adding a metal junction to the SC particles is a strategy that can be used to increase the photocatalytic yields. Indeed, because the metal part generally acts as an “electron sink”, due to its larger electric double layer capacitance compared to the SC one, a SC/metal junction decreases the probability of charge recombination.[119] Gold/TiO_2 snowman-shaped APs with sizes around 10 nm have been studied for photocatalytic applications. This system showed an increased activity for methanol oxidation compared to TiO_2 NPs.[119] AP arrays were also more active for methylene blue degradation compared to TiO_2 and gold/TiO_2 composite NPs.[120] These results suggest that SC/metal APs can be photocatalysts of primary importance. This was recently confirmed by Seh *et al.* who reported the first use of nanosized APs (gold/TiO_2) for hydrogen photogeneration.[121] The proposed mechanism for this system, used in isopropyl alcohol, involves the surface plasmon resonance (SPR) generation on the gold part under visible light that is converted into electron-hole pairs at the metal/SC interface, driving alcohol oxidation at the gold surface and proton reduction at the TiO_2 surface.[121] Based on these results, one can imagine that photon-induced water splitting may be achieved in a near future by engineering the JPs components (Figure 3.2g).

3.2.6. Medical applications

Even if, to the best of our knowledge, no *in vivo* medical application has already been developed, it is straightforward to imagine the strong potential of APs for *in vivo* drug delivery since one part of the particle can play the role of the recognition unit (targeting the part of the body affected by the disease) whereas the other part being the drug carrier. Hu *et al*. recently reported the imaging and the magnetolytic therapy using JPs.[122] Fluorescent magnetic APPs of 100 nm have been magnetically directed for staining cells. Once the cells are stained, they can be imaged and destroyed under the action of a rotating magnetic field.[122] Recently, biocompatible hydrophilic/hydrophobic submicrometer JPs have been used to encapsulate a hydrophilic drug on one side and a hydrophobic drug on the other side.[123] Hu *et al.* also have shown that a magnetically-induced DNA release from polymeric asymmetric nanocapsules containing magnetic NPs could be achieved without affecting cell viability.[124]

Nanosized Ag/Ag_2S APs were shown to be efficient photocatalysts for the inactivation of *E Coli* cells.[125,126] The experimental evidence that this activity came from a synergetic effect of the two compounds, allowed a mechanism to be postulated. UV-lighting of the APs anchored to the cell creates an intracellular circuit loop due to separation, transport and recombination of the photogenerated charges. This generates oxidative free radicals on the surface of the bacteria, leading to the improvement of the antibacterial efficiency.[125]

3.3. Synthetic procedures for breaking the symmetry

Many techniques for the production of APs can be found in the literature. Because of the diversity of the employed techniques, a full description of them goes beyond the scope of the present thesis, and only a brief overview will be given here. For more information, we refer the interested reader to recent reviews.[4,3,11,12,17-26] The classic approaches involves the use of a single interface and, as a consequence, the synthesis is carried out in a one or two dimensional reaction space which strongly limit the production by low space-time yields. Even if they usually lead to APs with a good homogeneity with sufficient quantities for a use at the laboratory scale, up-scaling these processes to an industrial level is quite difficult to imagine. A straightforward technique that is depicted in Figure 3.5a consists in modifying objects that are immobilized at an interface, so that a part of the objects is screened and cannot be modified.[1,127-145] Other two dimensional approaches are based on the use of templates,[52,104,146-150] colloidal crystallization[151,152] or droplet coalescence.[153,154] Microfluidics devices based on hydrodynamic channels (Figure 3.5d),[62-65,123,155-158] multi barreled capillaries[159] or electrospinning setup[160-162] have also been used to generate APs.[163] During this thesis, a two

dimensional *in situ* transmission electron microscopy (TEM) technique, allowing at the same time to break the symmetry on NPs and to visualize the formation of AP formation was developed. Even if this process does not involve bipolar electrochemistry, it is directly related to the scope of this chapter and will be developed in the next section. Few low-dimensional methods seem to be quite attractive since they show that in some cases the inherent disadvantages can be balanced by high turnovers, leading to higher production rates.[61,164-167]

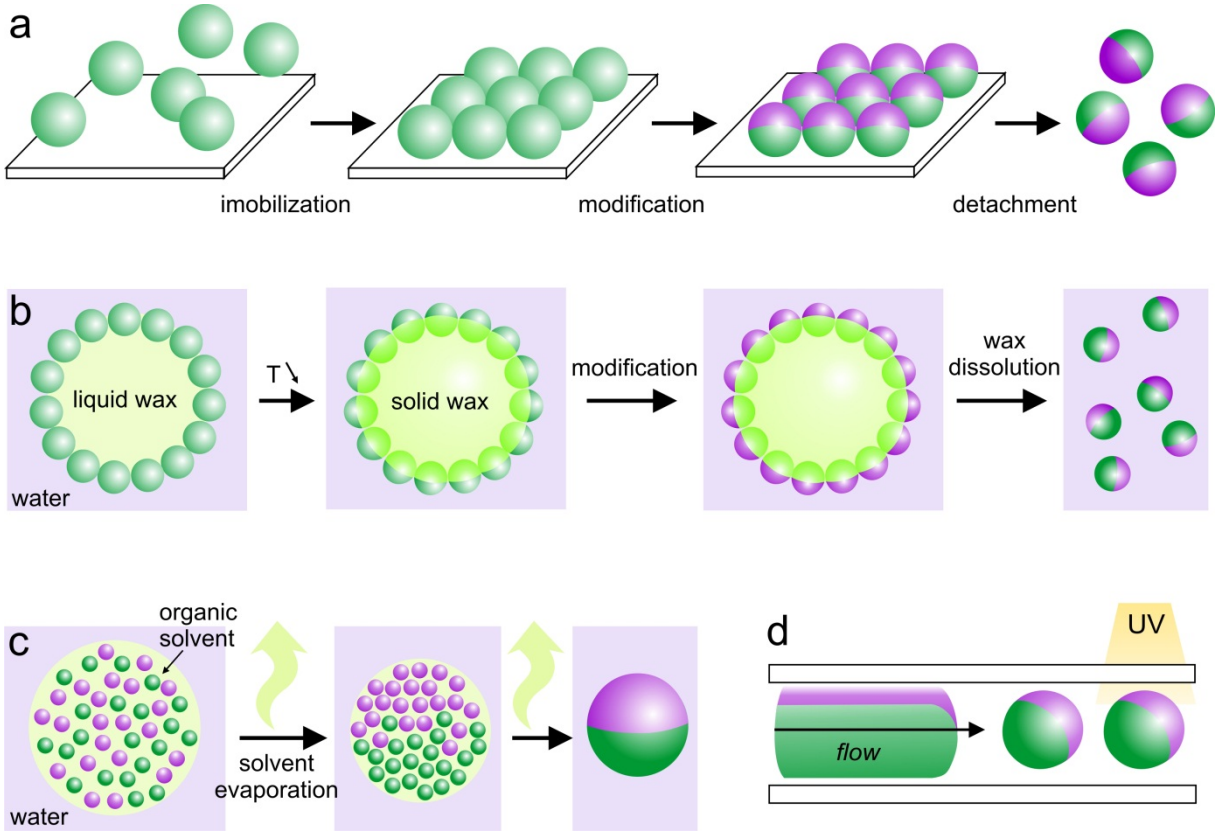

Figure 3.5. Synthesis of asymmetric particles. a) Janus particle synthesis by modification of immobilized spherical particles. b) Scheme of the wax-based Pickering emulsion method. c) Scheme of the solvent evaporation in emulsion droplets. d) Formation of Janus particles based on microfluidics. Adapted from reference (12).

Bulk methods for the generation of APs have also been reported. The interfaces in Pickering emulsions (Figure 3.5b)[168-182] or in suspensions[183-188] have also been used for breaking the symmetry. Other processes such as seeded emulsion polymerization (SEP),[189-194] seeded dispersion polymerization (SDP)[195-201] or solvent evaporation in droplets (Figure 3.5c)[122,202-208] use emulsions as bulk templates. Several techniques that does not involve interfaces also exists among which we can cite copolymer self-assembly,[209-215] crystalline transformation of the core part of core-shell particles,[216,217] crushing of core-shell particles,[2,42,218,219] ligand segregation[220-222] or preferential deposition on NPs.[223-247]

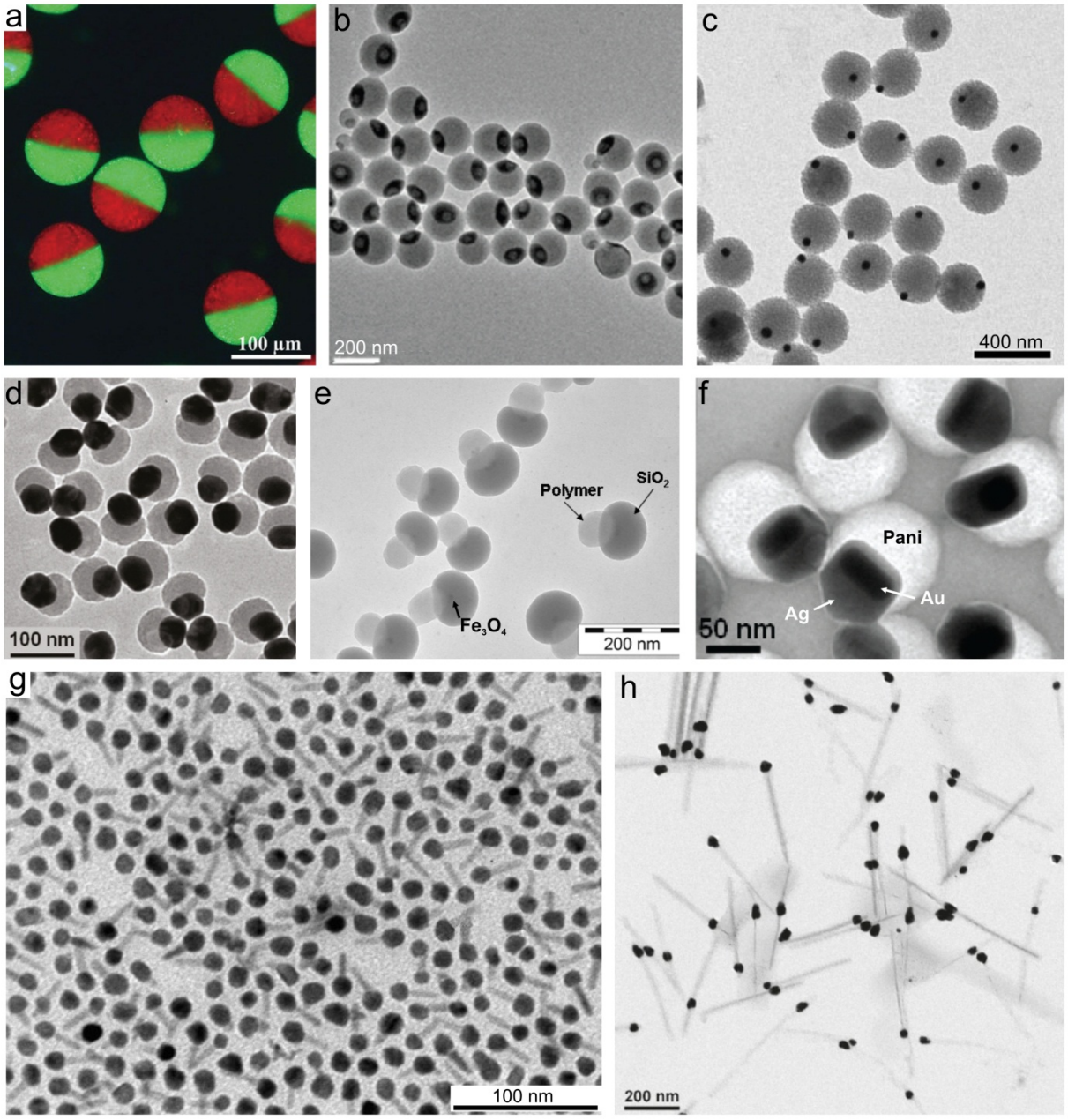

Figure 3.6. Asymmetric particles. a) Fluorescence microscopy picture showing JPs containing fluorescent beads, obtained by a microfluidic process. Adapted from reference (159). b) TEM micrograph of magnetic spherical APs obtained by solvent evaporation in emulsion droplets. Reprinted from reference (122). c) SEM image of PS-gold PPs obtained by polymerization in the presence of gold NPs. d) TEM picture of gold/SiO_2 APs obtained by ligand segregation. Reprinted from reference (220). e) TEM picture of mushroom-like PS/SiO_2 APs with an embedded Fe_3O_4 NP. Reprinted from reference (248). f) TEM micrograph of APs containing a gold-silver core shell particle and a spherical polyaniline part obtained by aniline polymerization with $AgNO_3$ in the presence of gold nanorods. Reprinted from reference (249). g) TEM picture of Co-tipped CdS nanorods. Reprinted from reference (225). h) TEM image of Te nanowires with gold tips. Reprinted from reference (231).

Besides electricity, other electromagnetic fields such as radio-frequencies,[250] micro-waves[251] and light[250] can be used to polarize SC or conducting objects and trigger their toposelective modification. Moreover, the light-induced electron-hole pair generation on SCs can be used for their modification. Light adsorption by SC materials can promote electrons from their valence band to the conduction band. Even if the recombination rate is most of the time very important, the photogenerated hole and electron can react with electron donors and acceptors respectively. Some cases of localized deposition on SC particles upon irradiation with light leading to APs can be found in literature. Reiche *et al.* showed that dark areas of illuminated TiO_2 particles can be the place for Cu^{2+} reduction while the light exposed area is an oxidation site.[252] SC nanorods were also selectively modified with metals upon light exposure. Single tip modification of ZnO nanorods with silver,[253] and CdS nanorods with gold has been reported.[254,255] Even if the single-tip modification mechanism is still unclear it has been suggested that once a metal nuclei is created at one of the tips (usually the nucleation occurs preferentially here because of a higher surface energy compared to the rest of the nanorod surface), the metal due to its large capacitance attracts the photoinduced electrons for the growth of the rest of the metal NP. Duque *et al.* deposited metals at the tips of surfactant-coated single wall carbon nanotube (SWCNTs) by exposing them, in the presence of metal salts, to microwaves[251] and radio-frequencies.[250] Indeed, similar to the bipolar electrochemistry approach, under the influence of these fields, the SWCNTs are affected by polarization which causes their modification. This approach seems also very attractive for the bulk formation of APs, even if a precise control of the obtained particle morphology has not been clearly demonstrated.

3.4. Electron beam-induced asymmetrical reduction

During this thesis, an *in situ* transmission electron microscopy (TEM) technique, allowing at the same time to break the symmetry of NPs and to visualize the formation of AP formation was developed. Even if this process does not involve bipolar electrochemistry, it is directly related to the scope of this chapter and will be developed in this section.

As discussed in section 3.2.5., metal/SC APs are of importance for photocatalysis and Au/TiO_2 APs have been already used for the photogeneration of hydrogen.[121] Because it has been recently reported that silver-silver halides (Ag-AgX) are very efficient plasmonic photocatalysts,[256,257] one can also expect Ag/AgX APs to show important efficiencies. Moreover, on account of the antimicrobial properties of Ag NPs, AgX NPs[258] and the remarkable synergetic effect observed with silver-based nanometer-sized APs for the photo-inhibition of *E Coli* (see section 3.2.6.), Ag/AgX APs are very promising for therapeutics. Only one publication reports the synthesis of such asymmetric NPs. In

this work, Banin *et al.* synthetized surfactant-capped Ag/AgBr dimer nanocrystals in the presence of methanol.[259]

The colloidal stability of suspension of NPs is most of the time induced by a stabilizing agent, usually a charged molecule or a polymer, which, by coating the NPs promote their steric or electrostatic stabilization. In this work, an original type of organic molecules, cucurbit[*n*]urils (CB[*n*]s),[260] was used as stabilizing agents. CB[*n*]s are pumpkin-shaped symmetric macrocycles composed of glycoluril sub-units (Figure 3.7a). The molecular construct of CB[*n*]s consists of a highly symmetric hydrophobic cavity with two tighter carbonyl portals. CB[*n*]s can act as supramolecular hosts that selectively form inclusion complexes with a wide variety of small organic guest molecules.[260] Recently, native CB[*n*]s were shown to have significant binding interactions with the surfaces of noble metals.[261,262] Meanwhile, CB[*n*]s have been utilized as stabilizing ligands for noble metal nanoparticles (NPs), such as that of gold,[263-266] silver,[267,268] and palladium.[269]

Visualizing chemical transformation on NPs is of first interest. Events at the nanoscale such as the growth of carbon nanofibers[270] or graphene[271] formation and isomerization[272] has been reported previously, however direct visualization of Janus NPs formation has never been demonstrated. Mulvaney and coworkers reported a TEM evidence for a spontaneous symmetry breaking induced through the generation of AgI by I_2 penetration in silver-silica core-shell particles.[216] In their work, the JP formation is not induced by exposure to an electron beam and therefore cannot be monitored in real-time by the electron microscope.

3.4.1. Synthesis of monodisperse CB[*n*]-capped nanoparticles

Precipitation from aqueous solution of $AgNO_3$ and CB[5] takes place over 24 hours in the dark with the $n_{AgNO3}/n_{CB[5]}$ molar ratio equal to one (experimental details are given in appendix 1), and leads to stable suspensions exhibiting white reflection and orange transmission (Figure 3.7c).

The white color is typical for silver-halide NP suspensions and is attributed to the presence of a small amount of bromide ions present in CB[5] batches reminiscent of the CB[5] purification process, which involves an ionic liquid containing bromide.[274] The total bromine amount in CB[5] was determined by ICP-MS analysis to be 3.01 x10^{-4} % wt. A typical UV-visible spectrum of this suspension ($C_{CB[5]} = C_{AgNO3}$ = 0.34 x10^{-4} M) can be seen in Figure 3.7b (red line). The strong peak around λ = 200 nm corresponds to $AgNO_3$ absorption, while the shoulder-like absorption in the visible region is attributed to that of silver halide NPs, as previously reported for AgBr NPs by Ray *et al.*[275] The assignment of these peaks to silver-halide NPs was further confirmed by a decrease of the absorption upon addition of ammonia to the quartz cuvette, which leads to the dissolution of the silver halide (Figure 3.7b). No

characteristic Ag^0 NP plasmon peak (around 400 nm) is observed before or after the dissolution by ammonia, which suggests the absence of Ag^0 NPs in solution. Atomic force microscopy (AFM) measurements shown in Figure 3.7d revealed the shape of the AgBr NPs to be spherical with a diameter of 47 ±3 nm. The bromide content in solution was governed by the CB[5] batch employed, but even when using different CB[5] batches, similar NPs were obtained in every case. It is noteworthy that addition of sodium bromide to the solution (from 5 to 50 mM) did not affect the shape and size of the NPs. No NPs were obtained when using a specific CB[7] batch that did not contain any Br^-. However, addition of potassium bromide at concentrations as low as 1.2 $x10^{-5}$ M in this CB[7]-$AgNO_3$ mixture induced the formation of CB[7]-capped AgBr NPs.

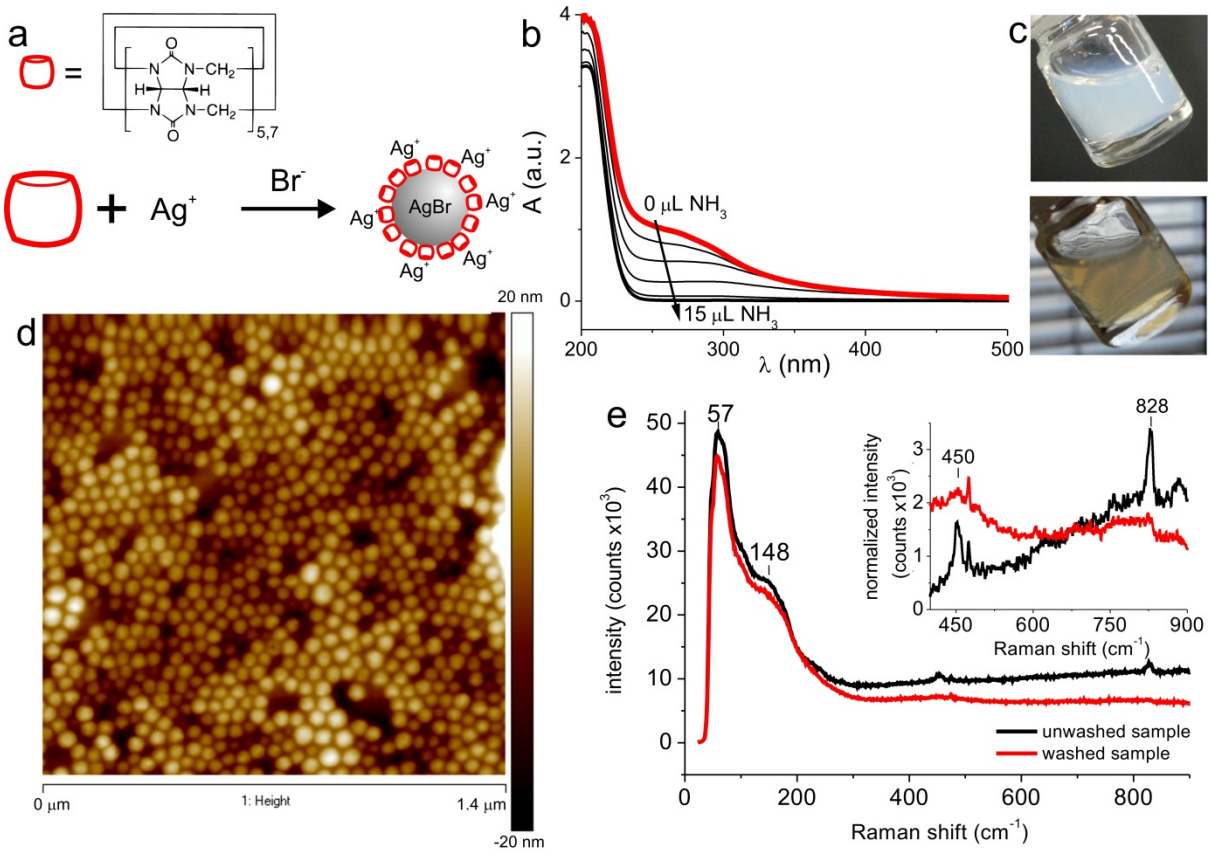

Figure 3.7. Characterization of CB[5] capped AgBr NPs. a) Scheme of AgBr NP precipitation in CB[5,7] presence. b) UV-visible absorption spectrum of AgBr NPs (red spectrum) and sequential particle dissolution with ammonia (black spectra). c) Reflection (left) and transmission (right) images of a CB[5]-capped AgBr suspension. d) AFM height image of the CB[5]-capped AgBr NPs. e) Raman spectra of unwashed (black) and washed (red) CB[5]-capped AgBr suspensions. Inset: enlargement of the normalized CB[5] Raman signal. Reprinted from reference (273).

In order to investigate the NP composition in more detail, liquid phase Raman spectroscopy was also performed with the initial and the centrifuged suspensions (Figure 3.7e). The presence of a silver halide is observed with a characteristic Raman fingerprint below 300 cm^{-1},[276] the presence of CB[5] is also confirmed by its characteristic Raman peaks at 450 and 828 cm^{-1} in both spectra.[262] The centrifugation/washing process, which allows the isolation of AgBr NPs by removal of soluble compounds, results in a significant decrease in the intensity of the CB[5] peaks in the Raman spectrum compared to the unwashed sample. This means that CB[5] is not a component of the bulk NPs, but rather acts as a stabilizing ligand on the surface of AgBr NPs. A further confirmation of this is the fact that without CB[*n*] in solution, AgBr precipitation leads to the formation of big particles, that settle at the bottom of the vial (Figure 3.9d, Inset).

This control experiment indicates that CB[5] promotes the formation of monodisperse and stable AgBr NPs by binding to their surface. Because it is well documented that CB[*n*] macrocycles have a strong affinity to cations,[277] Ag^+ should bind the portal carbonyls by electrostatic interactions (see Figure 3.7a). This is consistent with Zeta potential measurements of the colloidal suspensions, which revealed a surface potential of +43 mV for the NPs. The hydrodynamic diameter of the colloidal particles, determined by DLS, was found to be 90.6 ±0.2 nm, which correspond to an aggregate containing three to four nanoparticles based on the NP diameters obtained from AFM data. The colloidal diameter value does not vary significantly when the sample is diluted by a factor of up to 20, meaning that the observed aggregates are not a result of the non-specific aggregation of charged colloids, which typically is concentration-dependent. The result suggests that the aggregates are bridged by CB[5], similar to what has been shown for CB-gold NP aggregates in previous publications,[263,264] confirming the capping role of CB[5]. CB[*n*]s are already known to have an affinity for certain metals,[261,262] and the synthesis of CB[*n*]-capped metal nanoparticles has been previously reported.[263-269] Our finding constitute the first example of CB[*n*]-stabilized metal halide NPs, which may be extended in the near future to a larger family of hybrid NPs.

3.4.2. *In-situ* TEM synthesis of AgBr/Ag⁰ asymmetric particles

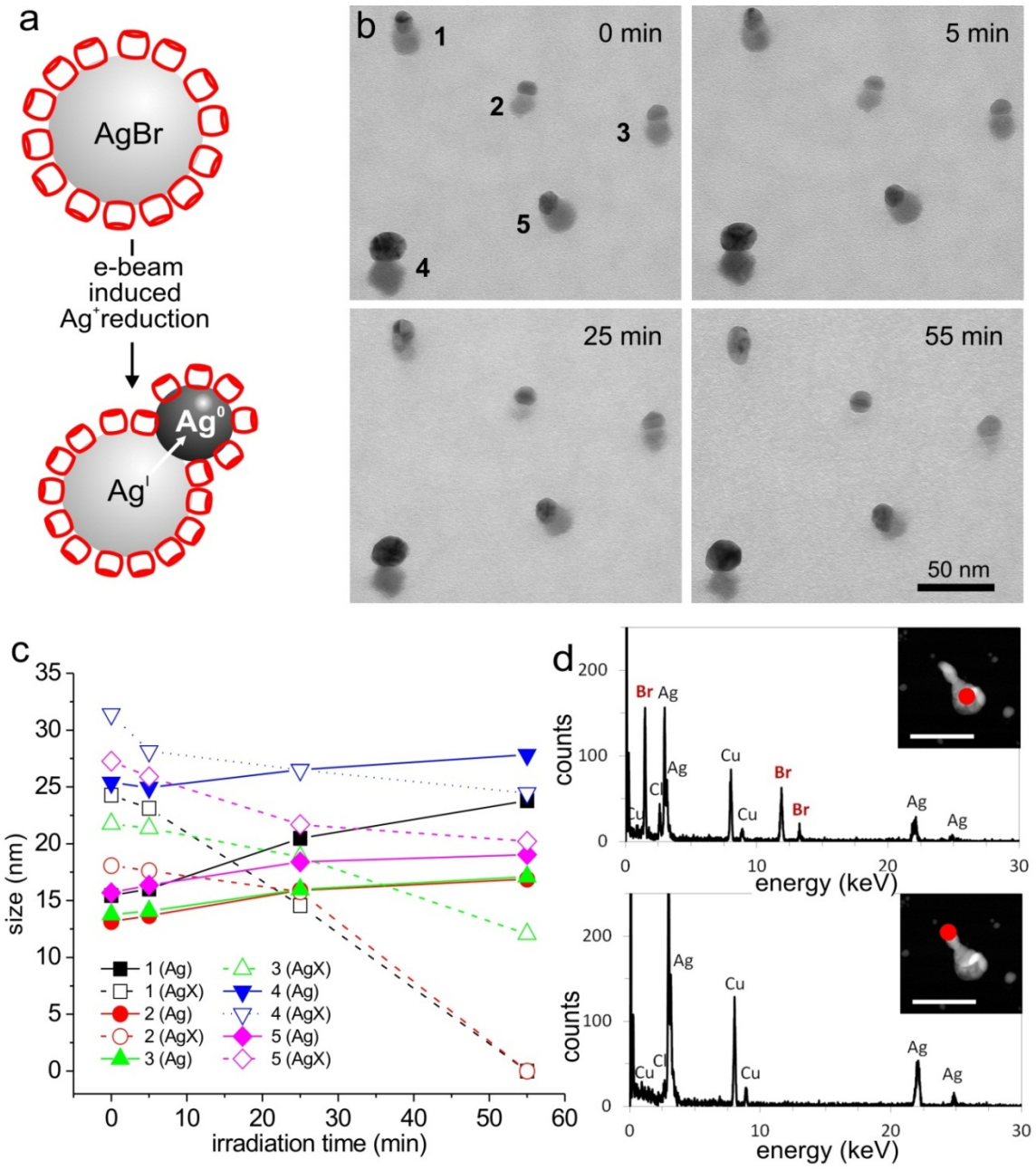

Figure 3.8. Direct visualization of the symmetry breaking of AgBr/Ag^0 NPs. a) Scheme of the mechanism. b) TEM pictures showing the morphological evolution of CB[5]-capped AgBr/Ag^0 NPs as a function of time. c) Kinetics data showing the size evolution of the Ag^0 and AgBr parts for each particle numbered in Figure 3.8b. d) STEM-EDX analysis of the different parts of a AgBr/Ag^0 NP. Top, STEM-EDX analysis of the AgBr feeder part. Bottom, STEM-EDX analysis of the Ag^0 bulb part. Insets: HAADF images of the analyzed NP, the red spot shows the area analyzed by EDX analysis, the scale bars equal 200 nm. The Cu signal originates from the Cu grid support. Reprinted from reference (273).

The obtained NPs exhibit a high reactivity when visualized in the TEM. Indeed, when exposed to the electron beam, they demonstrate a clear asymmetric evolution of their composition and morphology, which resulted in APs composed of a black and a grey part (Figure 3.8b). Scanning transmission electron microscopy-energy dispersive X-ray spectroscopy (STEM-EDX) analysis, carried out on an untypically big object, revealed the black part to be silver and the grey part to be AgBr (Figure 3.8b). We attributed this evolution to the direct reduction of the AgBr component by the electron beam as shown in Figure 3.8a. The generation of a black seed occurs very quickly so that it was impossible to record a TEM micrograph of the AgBr NP without any Ag^0. It has been therefore necessary to employ AFM to image the initial AgBr NPs and then follow the subsequent seed growth in real time under the e-beam, which is used simultaneously for imaging and to deliver the electrons for Ag^+ reduction (Figure 3.8b). It is important to note that the phenomenon was more pronounced in parts of the samples where the beam was focused, but was also effective on a much larger area of the TEM grids. For instance, imaging a grid area at magnification of 49,000 x induced the generation of black silver seeds over at least a 100 μm x 100 μm square of the grid mesh. Similar results were observed using two different TEM instruments (FEI Tecnai 12 and Technai G2), confirming clearly that the phenomenon is related to an inherent property of the NP material. Analyzing the growth process in more details (shown in Figure 3.8c), one can clearly note that the grey AgBr is the "feeder" part for the Ag^0 seed, which grows while the AgBr decreases in size until its complete consumption (55 min for the NPs with a typical size around 30 nm). Therefore, the Ag^0 component can grow by more than 5 nm in size, while the AgBr is being consumed (Figure 3.8c).

In order to investigate the mechanism, we also studied nanoparticles of AgCl and AgBr synthesized without any CB[*n*], (experimental details are given in appendix 2). Although the AgCl NPs showed an observable reactivity on account of TEM-induced reduction, no symmetry breaking could be observed. On the other hand, an asymmetric growth of a silver component was observed for the unstabilized AgBr NPs leading to APs, but with a less well-defined morphology (Figure 3.9d). Owing to the absence of the CB[*n*] stabilizing agent during the AgBr precipitation, most of the material settled at the bottom of the vial (Figure 3.9d, inset), and only a few AgBr NPs with ill-defined shape were observed. The size distribution was estimated by measuring the length of the particles from one extremity of the metal bulb to the opposite extremity of the AgBr component. As shown in Figure 3.9e, the particles obtained without CB[*n*] are significantly larger compared to those that are CB[*n*]-capped. The silver growth observed on these larger particles is also very different since the AgBr component appears to be darker than the AgBr of the CB[5]-capped NPs, suggesting the formation of a Ag^0 layer all around the AgBr. The silver components grown under the influence of the electron beam can still be identified and are indicated by arrows in Figure 3.9d. While the silver, grown on the

CB[5]-capped AgBr NPs, is spherical in nature, the silver growth of the uncapped NPs appears much less defined, and in some cases multiple bulbs can grow on a single AgBr particle (Figure 3.9d, left bottom). We conclude that the asymmetric growth of Ag^0 is a phenomenon related to the presence of AgBr, which is strongly enhanced by the presence of CB[5] on the AgBr NPs surfaces. Beyond promoting the monodispersity of the AgBr NPs, the CB[5] layer protects the AgBr part from a complete, TEM-induced reduction.

It was found that the $n_{AgNO3}/n_{CB[n]}$ molar ratio strongly influences the AgBr NP morphology and shape, which in turn has an impact on the final appearance of the resulting APs. We illustrate this structural versatility in Figure 3.9. As already discussed above, when the $n_{AgNO3}/n_{CB[5]}$ molar ratio is 1, the AgBr NPs are spherical. Figure 3.9b shows a picture of well separated AgBr/Ag^0 NPs. The yield of conversion of NPs into APs was found to be superior to 75 %. The average JP size is around 25 nm (Figure 3.9e). Using a smaller relative CB[5] concentration in solution favours the formation of bigger NPs, since fewer CBs are available for surface stabilisation, as shown for the case of $n_{AgNO3}/n_{CB[5]} = 2$ in Figure 3.9c. Interestingly, most of these NPs prepared from ratios greater than one exhibit cubic or rectangular morphologies, and a majority of the resulting JPs are about 45 nm across. The Ag^0 patch grows in some cases at an AgBr NP face and in other cases at a NP edge. This suggests that the nucleation mechanism of the reduction does not necessarily happen at energetically favoured sites. Probably due to its larger outer diameter compared to CB[5],[278] the use of CB[7] with a molar ratio of 1 leads to smaller AgBr NPs, as shown in Figure 3.9a and Figure 3.9e. When CB[7] is used, APs of about 10 nm size are observed with a very good synthetic yield. Notably, in all cases where CB[*n*] is present as a capping agent, the Ag^0 bulbs have a similar spherical morphology.

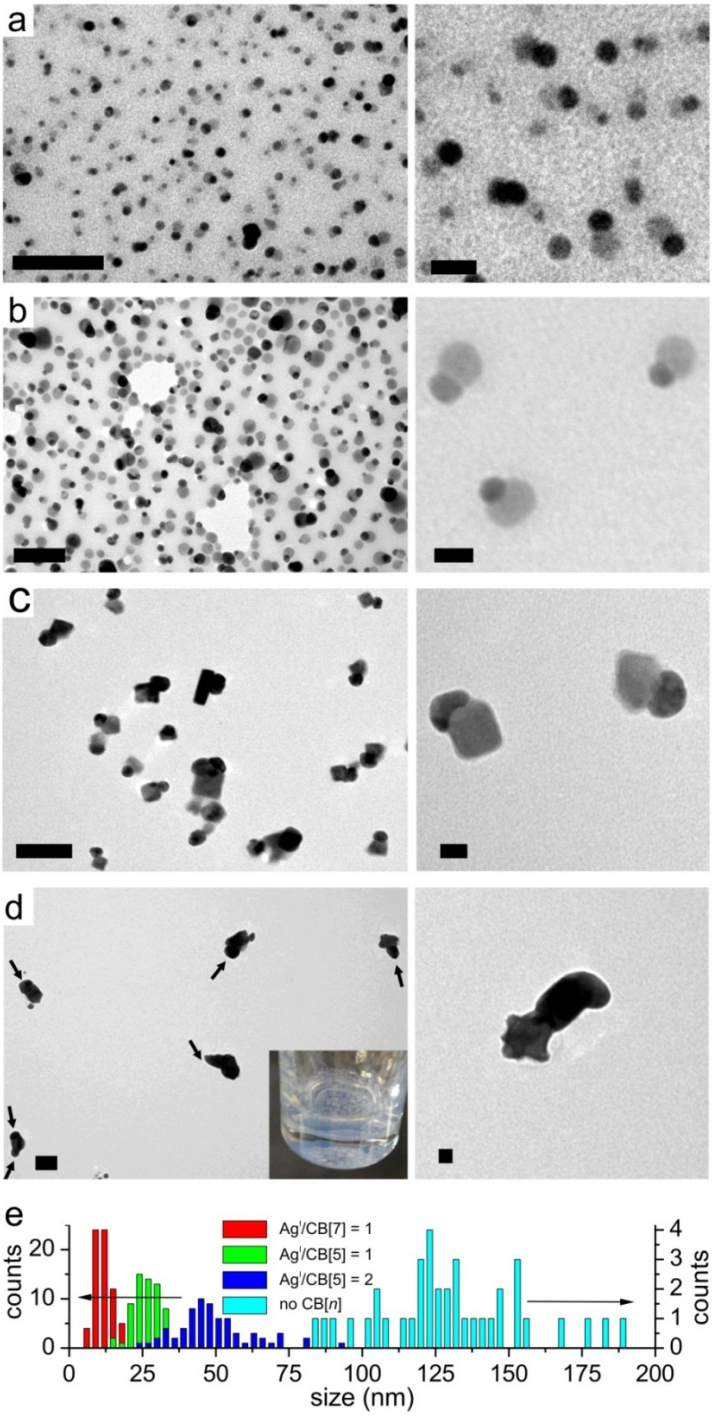

Figure 3.9. TEM pictures of AgBr/Ag^0 asymmetric particles. a) Particles obtained using $n_{AgNO3}/n_{CB[7]}$ = 1 (the left scale bar equals 100 nm, the right one equals 20 nm). b) Particles obtained using $n_{AgNO3}/n_{CB[5]}$= 1 (the left scale bar equals 100 nm, the right one equals 20 nm). c) Particles obtained using $n_{AgNO3}/n_{CB[5]}$ = 2 (the left scale bar equals 100 nm, the right one equals 20 nm). d) Particles obtained without CB[*n*] (the left scale bar equals 100 nm, the right one equals 20 nm). e) Size distributions of the JPs obtained with the different mixtures. Reprinted from reference (273).

As a conclusion of this section, we presented for the first time the straightforward aqueous-phase synthesis of CB[*n*]-stabilized AgBr NPs with a narrow size distribution. CB[*n*]s, acting as stabilizing agents, promote the formation of monodisperse AgBr NP suspensions, which are stable for over a month. The $AgNO_3$/CB[*n*] molar ratios and the CB[*n*] type were found to be key parameters for controlling the NP morphologies and sizes. Most importantly, we showed that the asymmetric reduction of these NPs, leading to the growth of Ag^0 patches, can be achieved and directly observed under the influence of electron irradiation. Depending on the shape of the AgBr particles, the generated AP morphology can be tuned.

3.5. Capillary-assisted bipolar electrodeposition

As mentioned in section 2.3.2., thanks to the asymmetric reactivity that it provides, bipolar electrodeposition is a powerful technique for the bulk generation of APs and JPs, as illustrated in Figure 3.10. The use of bipolar electrochemistry in an electrophoresis set-up has already been reported several times but mainly for analytical purposes (section 2.2.2. and 2.2.3.). The Capillary-Assisted Bipolar ElectroDeposition (CABED) technology, developed by Warakulwit *et al.*[279,280] prior to this thesis (see section 2.3.2.2.), is the first technique using an electrophoresis set-up for bipolar electrodeposition and constitutes the first example of bipolar electrodeposition in the bulk. As this process was used at the early stage of the present thesis for synthesizing asymmetric CTs, the technology will now be described and the obtained results will be presented in the following sections.

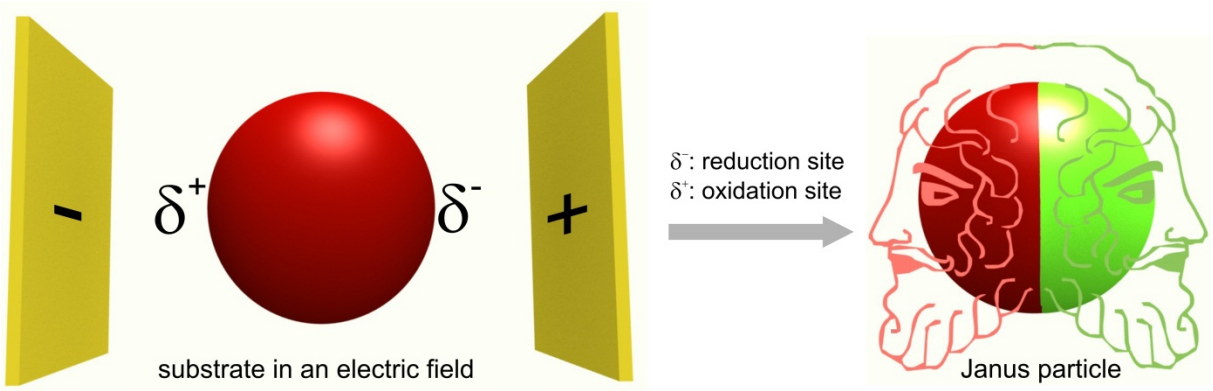

Figure 3.10. Scheme of principle of the bipolar electrodeposition used for the generation of Janus particles. Adapted from reference (281).

3.5.1. Technology description

Capillary electrophoresis (CE) is a commonly used technology for separating chemicals. The separation phenomenon is driven by the difference of the charge and hydrodynamic radius of the species. The operating principle consists in submitting to an electric field a solution containing charged entities that can be ions, DNA or NPs in a capillary. The motion of the charged species is directed by the competition of two forces. The first force is induced by the electrophoretic flow (EPF), which is the attraction of a charge to the electrode of the opposite charge. The second force is generated by the electroosmotic flow (EOF), induced by the motion of charges along the electric double layer of the capillary wall. In our case, the capillary material being glass (owning silanol surface groups), the proton flow at this interface directs the EOF towards the cathode. A photograph of the CE equipment used during our experiments is given in Figure 3.11a. In a classical CE experiment, after being filled with a solution of interest, the capillary is inserted into the capillary chamber where its two extremities are dipped into the electrode compartments containing the solvent. The electrodes, Pt wires, are located outside the capillary in such a way that the bubbles generated by the solvent cannot enter it. The maximum voltage that can be applied with our apparatus is 30 kV, which gives for typical capillaries with a length of around 20 cm, electric field in the order of 150 kV m^{-1}. A UV-vis detection system, in the capillary chamber allows monitoring the characteristics of the flow leaving the capillary at the cathodic compartment.

The CE equipment provides several important advantages for bipolar electrodeposition on suspensions of particles. The first one resides in the very high values of electric field that it provides, which is a crucial parameter for the polarization of small objects (see section 1.2.). A second very attractive point is the presence of the liquid flow, generated by the EOF within the capillary. This flow automatically drives the substrates from one compartment to another in a “continuous” way. Finally, using a capillary as a reaction compartment also provides a high surface area for heat dissipation and a resistive current pathway which is useful for decreasing by-pass currents (see section 1.3.). As shown in Figure 3.11b and c, the CABED concept is based on the modification of particles during their journey through the capillary. A suspension of conducting particles (to be modified), CTs in our case, together with electrodeposable compounds (typically a metal salt) is inserted into the anodic compartment or directly into the capillary. As depicted in Figure 3.11b, when the electric field is applied, the water flow, generated by the EOF drives the CTs towards the cathodic compartment. The bipolar electrodeposition occurs during the residence in the capillary with the cathodic pole of the BE being the place for the metal deposition and the anodic pole the place of solvent oxidation. The CT flow can be monitored at the capillary outlet using the UV-vis detector. After the experiment,

the modified CTs can be collected directly at the outlet or in the cathodic compartment for further characterization.

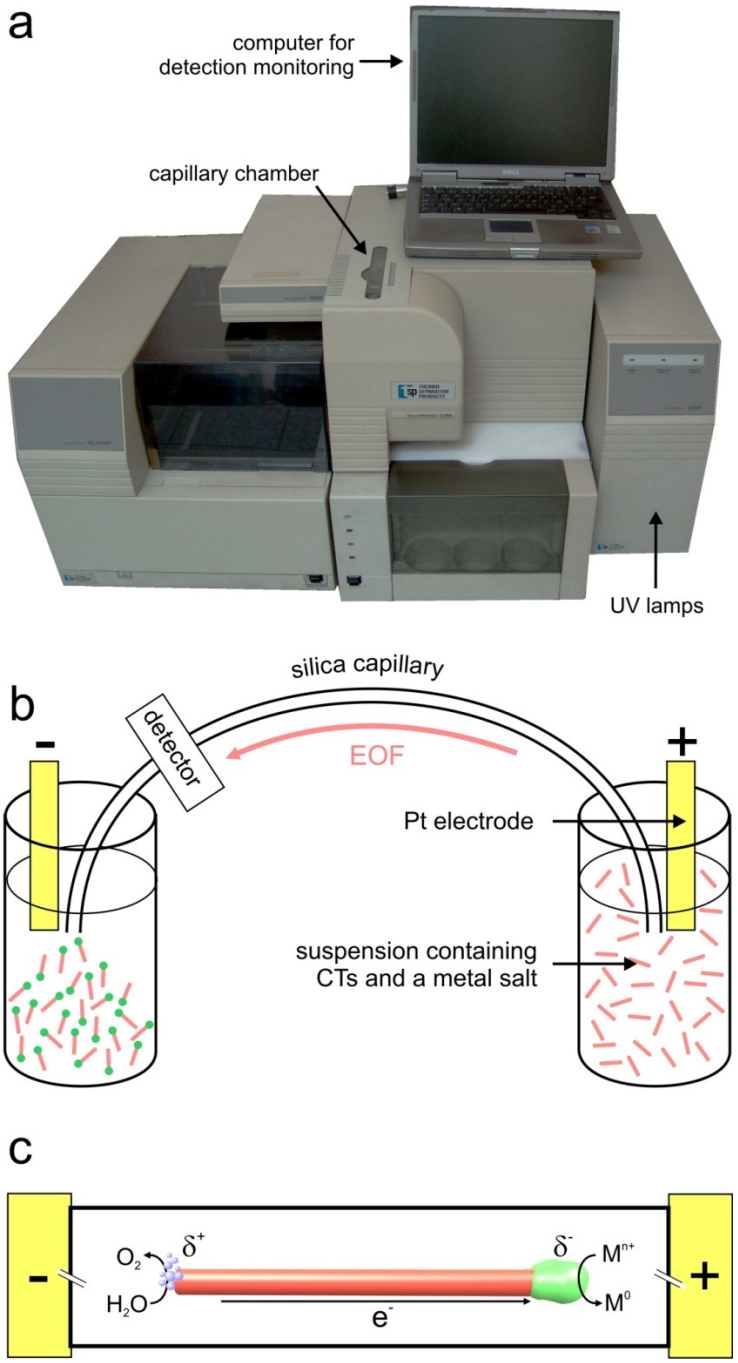

Figure 3.11. Capillary-assisted bipolar electrodeposition technology. a) Photograph of the CE set-up (SpectraPHORESIS ULTRA, TSP). b) Schematic illustration of the CE set-up (only the capillary and the electrode compartments are represented) during the CABED process. c) Schematic illustration of a CT in the capillary, being asymmetrically modified by a metal during CABED.

3.5.2. Metal deposition on carbon microtubes

3.5.2.1. Single point metal electrodeposition

In order to demonstrate the versatility of the CABED process, we decided to use it for synthesizing other APs than MWCNT/Au hybrids (section 2.3.2.2.).[279,280] The choice of carbon microtubes (CMTs) as substrate was driven by the fact that due to their length, in the range of few tenth of μm, and their width of a few hundreds of nm (Figure 3.12b), these objects are easily observable individually by optical microscopy and SEM.

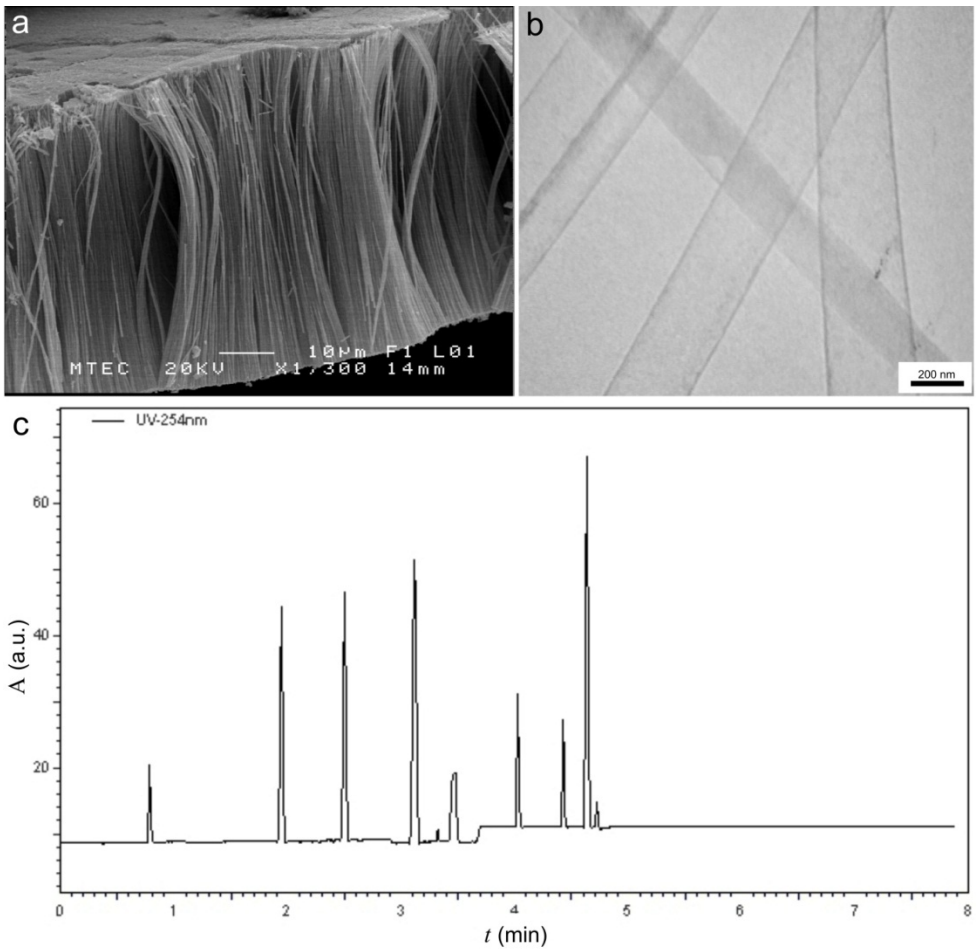

Figure 3.12. Carbon microtubes. a) SEM picture of the CMT sample after dissolution of the Al_2O_3 template. Reprinted from reference (282). b) TEM picture of typical tubes obtained after suspension in water. Reprinted from reference (282). c) UV detection of the CMTs leaving the capillary at the cathodic compartment using an electric field of 125 kV m^{-1}, the absorbance peaks are attributed to the passage of CMT aggregates in front of the detector, (the polarization is stopped at 5 min).

These CMTs are produced by chemical vapor deposition with a porous aluminum oxide membrane serving as a template.[279] After the acid digestion of the template (Figure 3.12a) the quite

homogeneous tubes were recovered as a powder. Suspensions of CMTs were produced by adding ≈0.1 mg of CMTs to absolute ethanol (1.5 mL). In order to accelerate the formation of a suspension, the mixture was sonicated, but only for a short time (1 min) to avoid excessive breaking of the tubes. After 3 h of sedimentation, 0.5 mL of the supernatant containing well dispersed CMTs were taken and added to an aqueous solution containing a metal salt with a concentration in the mM range.

Because the addition of salt increases the ionic strength, it can result in the aggregation of the CMTs, and therefore the suspensions were sonicated for a short time in an ultrasound bath before introduction into the capillary. The capillary used was a fused silica capillary with a length of 24 cm and an inner diameter of 100 µm. For typical CABED experiments, the solutions or suspensions were introduced into the capillary by filling it manually with a syringe. The applied voltage was 30 kV for 5 min. For the employed salt concentrations, the typical currents delivered by the electrophoresis setup were around 1 µA. The CMT flow can be monitored by the UV-vis detector at the capillary outlet, as shown in Figure 3.12c, which presents the absorption of the solution leaving the capillary as a function of time. The peaks are attributed to the passage of CMT aggregates in front of the detector, a phenomenon which directly stops after the electric field is switched off at t = 5 min. The sample leaving the capillary at the cathodic side was collected at the outlet and transferred onto a metal plate, rinsed, and dried. The objects were then characterized by optical microscopy and SEM.

	redox couples	metal salt	E^0 (V *vs* NHE)	ΔV_{min} (V)	C (mM)
cathodic pole	Au^0 / $[Au^{III}Cl_4]^-$	$HAu^{III}Cl_4$	+ 0.99	0.24	5
	Cu^0 / Cu^I	$Cu^{I}I$	+ 0.52	0.36	10
	Ni^0 / Ni^{II}	$Ni^{II}SO_4$	- 0.26	1.49	5
anodic pole	Cu^I / Cu^{II}	$Cu^{I}I$	+ 0.16	-	10
	H_2O / O_2	-	+ 1.23	-	solvent

Table 3.1. Characteristics of the redox couples involved during CABED experiments for the modification of CMTs. The standard potentials of the redox couples E^0,[283] the minimum potential value to trigger the electrodeposition reaction at a BE ΔV_{min} and the concentrations C are given.

The deposition of three metals, copper, gold and nickel was tested on CMTs. Table 3.1 shows some characteristics of the redox couples employed for the bipolar electrodeposition processes. In this table, a separation is made between the processes happening at the cathodic pole (the reductions of the metal salt) and at the anodic poles (the oxidation of solvent or another molecule). The theoretical minimum potential value to trigger the electrodeposition reaction at a BE, ΔV_{min}, was calculated as the difference between E^0 values of the individual reactions, as described in section 1.2. For solubility

reasons, the modification with copper by the reduction of Cu^{I} was carried out in acetonitrile. The reactions that occur at the CMT extremities in this case are:

$$Cu^{I}(l) + e^{-} \rightarrow Cu^{0}(s) \quad (3.1)$$

at the cathodic pole and:

$$Cu^{I}(l) \rightarrow Cu^{II}(l) + e^{-} \quad (3.2)$$

at the anodic pole. The E^{0} values of the two processes given in Table 3.1, reveals that the overall reaction resulting from a combination of reactions 3.1 and 3.2 should occur spontaneously via the following dismutation reaction:

$$2\ Cu^{I}(l) \rightarrow Cu^{II}(l) + Cu^{0}(s) \quad (3.3)$$

However, the CuI species is sufficiently stabilized because of the presence of I^{-} ions so that no spontaneous reaction was observed, showing that a potential difference is still needed between the two ends of the tube to drive the reaction.

Gold deposition was carried out in aqueous solution, involving the following reactions:

$$[Au^{III}Cl_4]^{-}(l) + 3\ e^{-} \rightarrow Au^{0}(s) + 4\ Cl^{-}(l) \quad (3.4)$$

at the cathodic pole and:

$$H_2O(l) \rightarrow 2\ H^{+}(l) + ½\ O_2(g) + 2e^{-} \quad (3.5)$$

at the opposite extremity of the CMT. Table 3.1 indicates that in this case the combination of (3.4) and (3.5) is not a spontaneous reaction and therefore a minimum potential difference ΔV_{min} = 0.24 V between the two tube ends has to be generated in order to achieve an asymmetric deposition. CABED experiments for the deposition of nickel were also achieved in water and also involve half-reaction (3.5) at the anodic pole. Nickel is deposited at the cathodic pole by the following reduction reaction:

$$Ni^{II}(l) + 2\ e^{-} \rightarrow Ni^{0}(s) \quad (3.6)$$

In this case, ΔV_{min} = 1.49 V (Table 3.1), showing that the nickel modification requires the highest driving force. Obviously, because the experiments are carried out in far from standard conditions in terms of pH, concentrations, and partial gas pressures, deviations from the theoretical values of the potential threshold ΔV_{min} are expected. For all these experiments the same external electric field value $\mathscr{E}$ = 125 kV m^{-1} was applied, which gives typically for an object with a length of 30 µm a ΔV of

3.75 V. This value is definitely high enough, compared to the theoretical ΔV_{min} values previously calculated, to drive all these redox reactions.

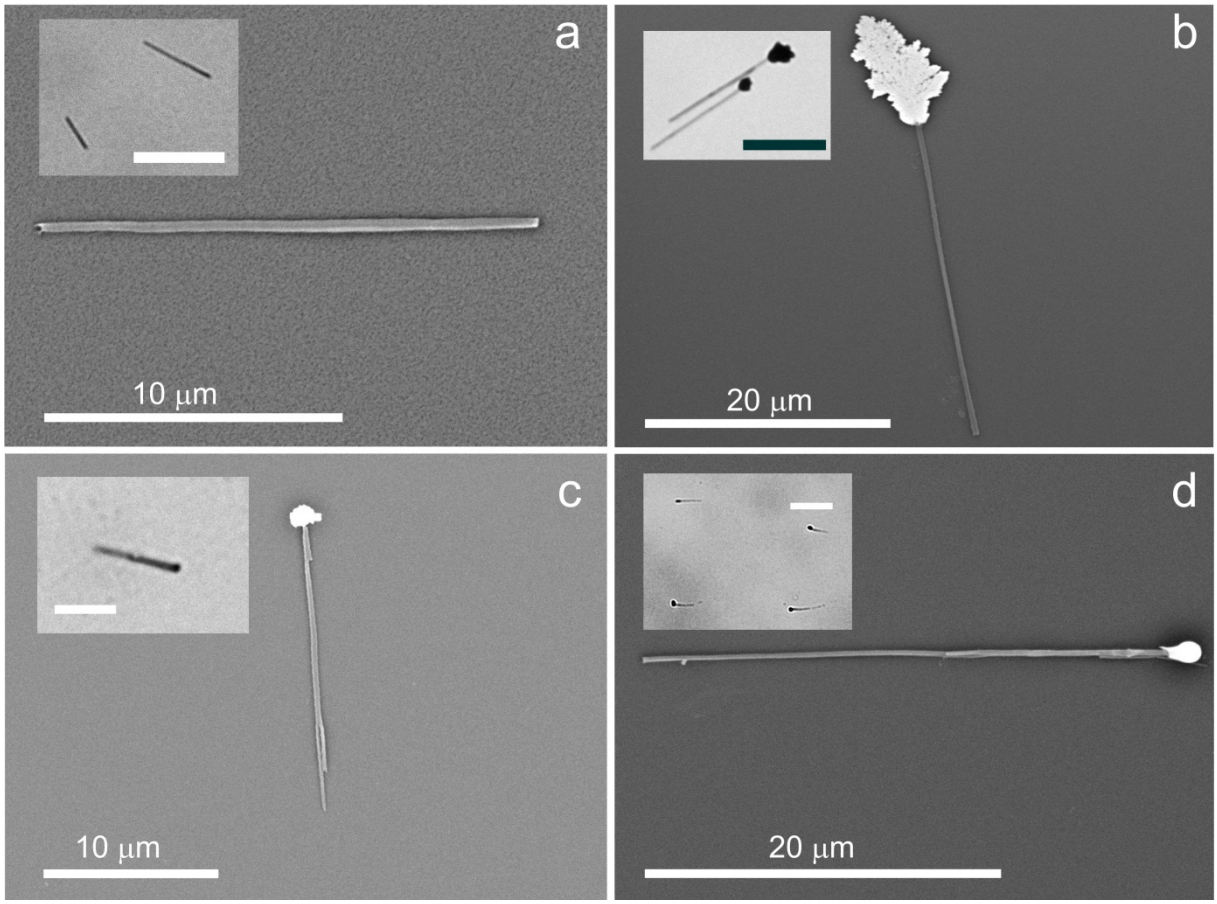

Figure 3.13. Single point-modified carbon microtubes. SEM micrographs of CMTs: a) without modification; modified at one side with b) copper, c) gold, and d) nickel. Inset: optical microscope pictures of the modified CMTs. The scale bars for a), b), and d) equal 20 μm; the scale bar for c) equals 10 μm. Reprinted from reference (284).

Looking at the SEM pictures of the CMTs collected at the capillary outlet presented in Figure 3.13 it is obvious that the corresponding metal has been deposited. Because we used the same $\mathscr{E}$ value for all the experiments, the same capillary length, and an identical experiment time, the variation in deposit size can be roughly understood via the different kinetics of growth which depends essentially on *i)* the required ΔV_{min} and *ii)* the salt concentration. Nickel modification, which requires the highest driving force, results in the smallest deposit size because for the given overall electric field the driving force is smaller and therefore the reaction proceeds more slowly. As stated above, copper deposition should occur almost spontaneously and therefore the required minimum voltage is the smallest one compared to the other metals. This means that in this case the external field generates the highest driving force and leads to the biggest deposit. Another parameter that is important for the apparent

deposit size is the growth morphology and its density. Copper is growing in a much more ramified structure, which leads for the same amount of reduced metal to a much bigger deposit compared to what is obtained for nickel and gold.

This new family of monofunctionalized asymmetric particles could be locally functionalized with organic molecules (for instance using a thiol-based chemistry), the metal patch might be also employed for binding the CMTs to a surface. A direct application of such materials can imagined in the field of micromotors, because the orientation of tubes modified with a ferromagnetic material (such as nickel) can be controlled with a magnetic field, [282] and a decomposition reaction producing bubbles can be driven by a catalytically active metal present at one tube end (see sections 4.2.1. and 4.2.2. for application of these concepts).[89]

3.5.2.2. Synthesis of dumbbell-like structures

During these bipolar electrodeposition experiments, the end of the tube opposite to the one where the metal deposition takes place is positively polarized and therefore cannot be a site for a reduction. If one wants to modify in a single experiment both ends with the same metal, polarization has to be reversed after the first deposition step so that the side that was the oxidation site becomes the reduction site. Since a classic CE set-up does not allow reversal of the polarization between the electrodes, we employed another approach consisting in the introduction of a relaxation time (without applied potential) after a first polarization to induce a statistical reversal of the CMTs in the capillary, as shown in Figure 3.14a. The optical microscope pictures in Figure 3.15 were obtained with the same dispersions of CMTs and the same value of electric field as for the previous asymmetric deposition of copper, but with a regular interruption of the potential. When the potential is continuously applied or when the relaxation time between the pulses is short (Figure 3.15 (2) and (4)), the CMTs do not have the possibility to turn around in the capillary. Actually, once these anisotropic objects are polarized in the electric field, it would cost too much energy for them to flip in the opposite direction. This means that the tubes are all aligned parallel to the electric field and will not tumble or turn during their journey through the capillary.

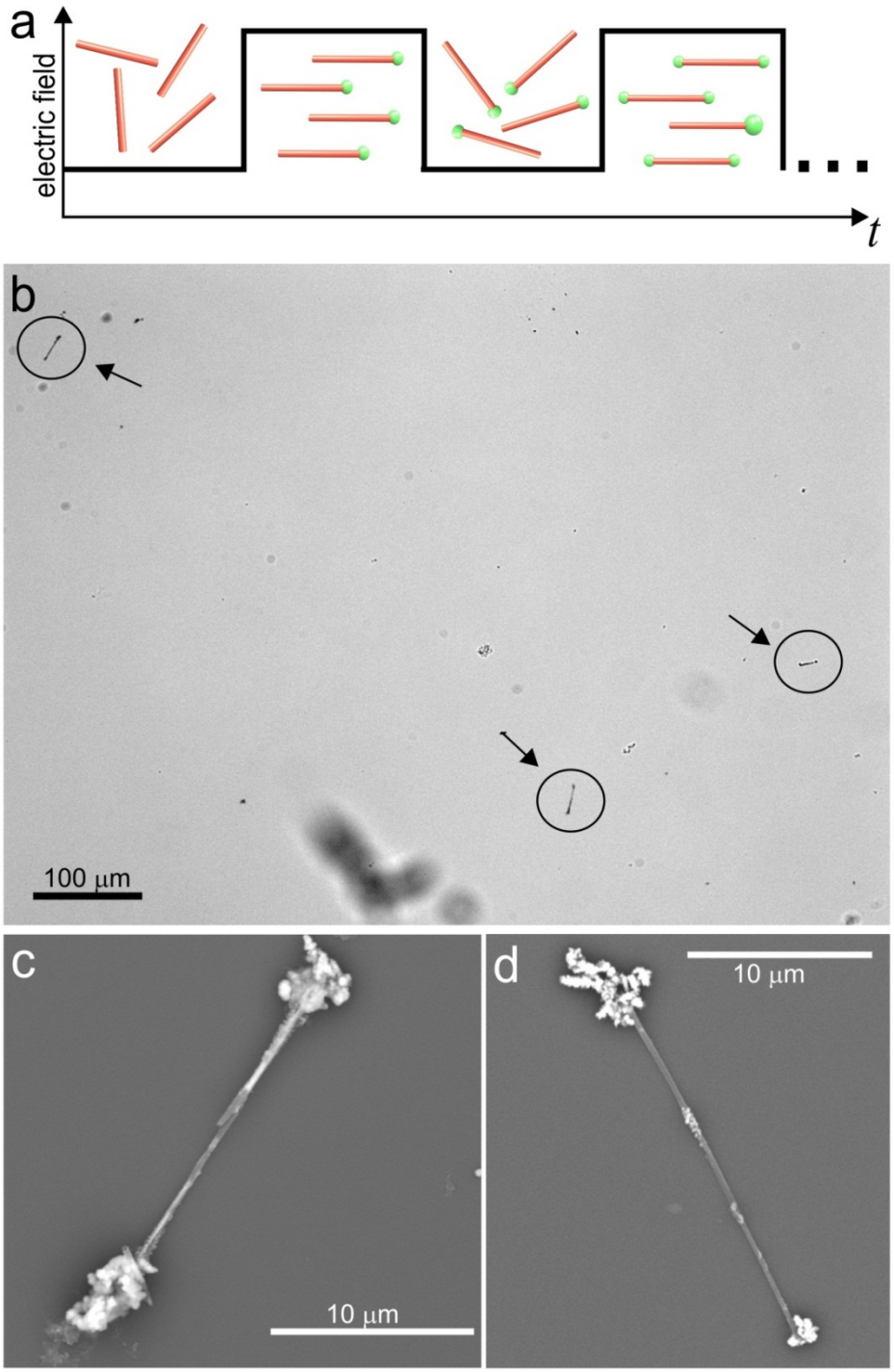

Figure 3.14. Pulsed CABED for the synthesis of dumbbell-like structures. a) Scheme showing the principle: when the electric field is off, the CMTs are affected by Brownian motion and when the electric field is on, the CMTs are oriented and acts as BEs. The schematic orientation of the CMTs at different times is depicted on the graph. b) Optical micrograph showing three dumbbell-like structures (indicated by the arrows and circles). c) and d) SEM micrographs showing two types of Cu/CMT/Cu dumbbell-like structure.

Therefore, this results in obtaining exclusively objects with deposits at one extremity. In contrast, when the pulses are sufficiently separated in time (Figure 3.14, Figure 3.15 (1) and (3)), the tubes are no longer polarized during the relaxation period and therefore have time to statistically change their orientation, which leads to a deposition at both sides of the CMTs. In this case, after the first pulse, only one end of the tube is modified with copper, but during the 5 min without polarization the tubes are allowed to reorientate in the capillary. Statistically, half of them will do so. Therefore, when the second pulse is applied, for half of the tubes the end where previously the oxidation of Cu^{I} into Cu^{II} took place becomes the reduction site where metal is formed. For these tubes, the counter reaction, which is the oxidation of Cu^{I} into Cu^{II}, now takes place at the end of the tube that had been already modified with copper during the first potential pulse. Another possible counter reaction could be the oxidation of the already present copper deposit. However, it is more difficult to oxidize Cu^{0} than Cu^{I} because the oxidation potential is more positive (Table 3.1) and therefore the dominating counter reaction is reaction 3.2, which preserves the already existing metal deposit. If this long relaxation is repeated many times, statistically all tubes have turned around several times and consequently are modified on both sides. Striking evidence for the symmetric deposition of copper at both ends of the CT is shown in the optical picture of Figure 3.14b and the SEM micrograph of Figure 3.14c. The pulse time also directly influence the deposit size. As clearly shown in Figure 3.15, 12 s pulses gives deposits that are much smaller (d_{dep} ≈1.2 μm in (1) and d_{dep} ≈2.3 μm in (2)) than when using 30 s pulses (d_{dep} ≈2.4 μm in (3) d_{dep} ≈4.4 μm in (4)). For an experiment having an even number of pulses, a given extremity of a CMT should statistically act the same number of times as cathodic pole and anodic pole but this is not 100 % true. For example, in an experiment with four pulses, one extremity of a CMT might act only once as a cathodic pole so the other extremity will act three times as a cathodic pole. This leads to a small percentage of dumbbell-like structures owning deposits with different sizes, as shown in Figure 3.14d. As a conclusion, the morphology can be controlled by the relaxation times and the deposit size by the pulse time. These proof-of-concept experiments were achieved with copper, but the bipolar symmetric functionalization can be extended to other deposable materials and substrates to generate new particles that could find applications for self-assembly.[234]

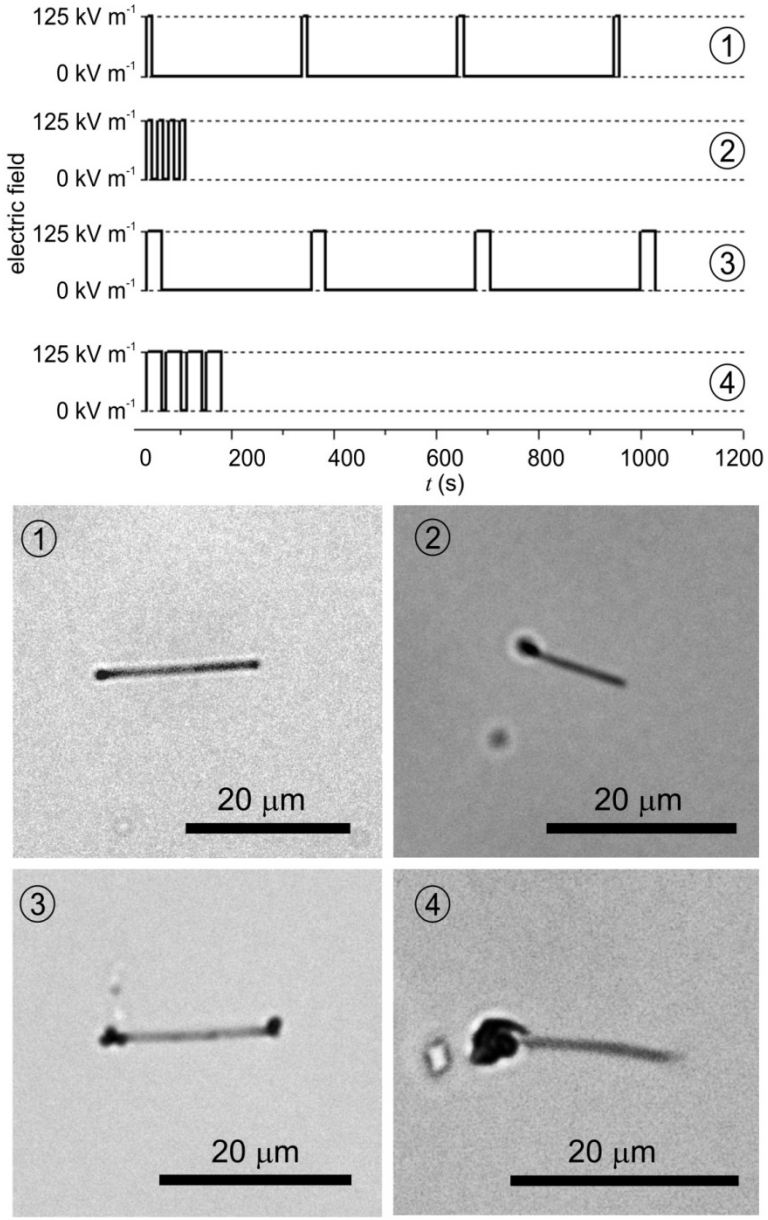

Figure 3.15. Effect of pulse and relaxation times on the structures obtained using 10 mM CuI in acetonitrile. The electric signal imposed between the electrodes is reported at the top and the corresponding optical microscope images of the modified CMTs at the bottom. The potential pulses are 12 s (1 and 2) and 30 s (3 and 4); the time between the pulses is 5 min (1 and 3) and 10 s (2 and 4). Reprinted from reference (284).

3.5.3. Deposition of conducting polymers

Conducting polymers (CPs) are organic polymers that conduct electricity. Since their discovery by A. MacDiarmid, A. Heeger, and H. Shirakawain in 1970 (awarded by a Nobel prize in 2000 for this discovery), CPs have been a hot research area either for academic topics or for the industrial sector. Electrochemical polymerization of such materials has been widely investigated[285,286] and is used for

many applications, such as the elaboration of electrochromic or sensing devices.[287] The most usual CPs, such as polypyrrole (PPy), polyaniline (PAni) or polythiophenes, are commonly deposited using classical monopolar electrochemistry at an electrode surface via the anodic oxidation of the soluble monomer. Due to its good water solubility, its biocompatibility and a good conductivity, PPy appeared as the most extensively studied CP over the past thirty years. A scheme of its electrodeposition mechanism is shown in Figure 3.16a. We studied the deposition of PPy by bipolar electrochemistry. Using electric fields of 7.3 kV m^{-1}, we synthetized Au/PPy JPs by PPy electrodeposition at the anodic pole of a gold micrometric bead, in acetonitrile. The photograph of such a JP is shown in Figure 3.16b, the color difference between the two materials is clearly observable demonstrating that the modification has been successfully achieved.

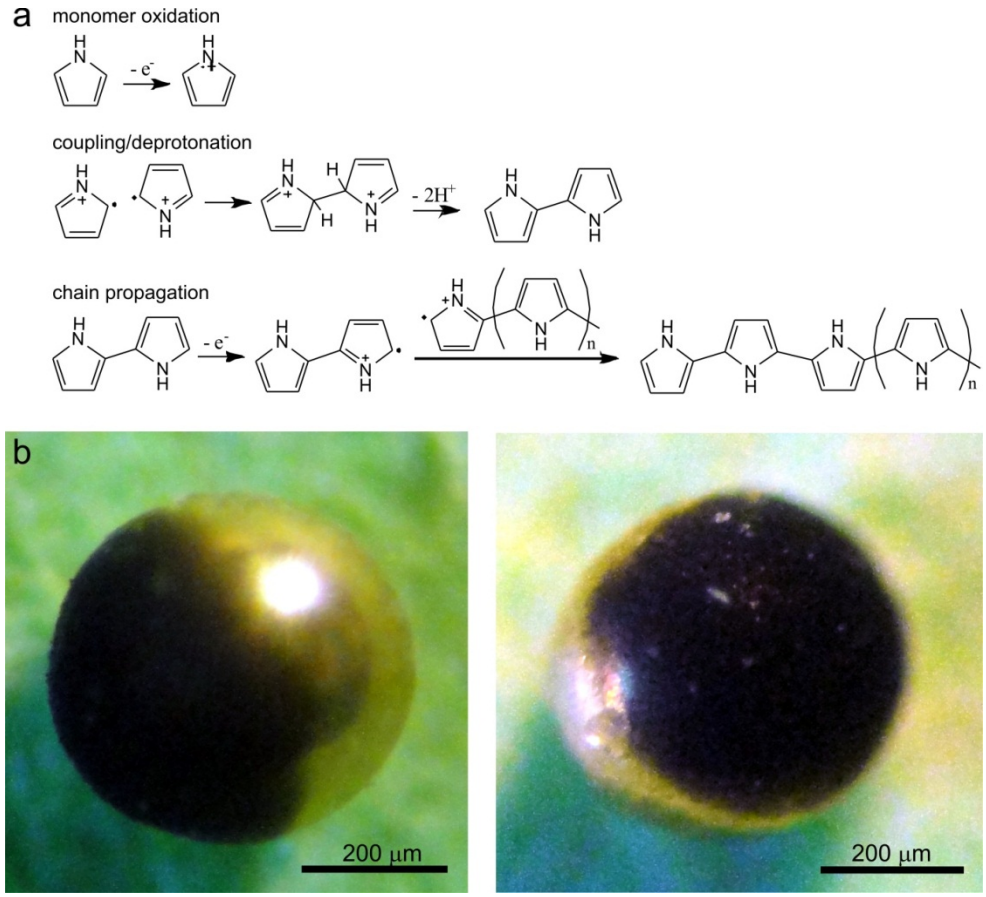

Figure 3.16. Electropolymerization of polypyrrole. a) Mechanism of PPy electropolymerization. Adapted from reference (288). b) Optical micrographs showing a Au/PPy Janus bead obtained by bipolar electropolymerization in two different orientations.

In the experiments described in section 3.5.2., the oxidation that occurs at the anodic end of the CMTs produces gas or other oxidation products, but the involved reactions do not lead to a modification. We were therefore looking for an additional strategy, which would make use of this

oxidation reaction to deposit also a material on the positively polarized side, concomitant with the reductive metal deposition on the negatively polarized side. Because of their intrinsic reactivity, the metal salt and the monomer have to be chosen carefully. A mixture of Cu^{I} and pyrrole was found to be stable in acetonitrile for at least 12 h. For longer times a brownish color, that is due to the spontaneous polymerization of pyrrole appeared. CMTs were added to this fresh solution and the bipolar electrodeposition was achieved using exactly the same parameters that were applied for the asymmetric deposition of Cu^{0} except the fact that a pyrrole concentration of 50 mM was also present. A SEM picture of a typical modified CMT is shown in Figure 3.17a, the metallic end being clearly visible due to the very high color contrast between the metal and the CMT. The PPy end is less conductive than copper and thus exhibits a weaker contrast with respect to the CMT. In order to get a second evidence of the composition the objet we performed in addition EDX experiments. The analysis has been carried out at the two opposite ends of the CMT. Figure 3.17b shows that the upper left end of the tube is characterized by a strong Cu signal around 1 keV compared to a much weaker carbon signal which originates most likely from the underlying CMT and the supporting grid. At the other end of the tube the carbon signal is much more prominent due to the presence of the CP. When both peaks are compared to the background oxygen signal, it becomes clear that their ratio is significantly different for the two ends of the tube, demonstrating the presence of the two different materials. However, on the PPy side there is still a small contribution of Cu. This signal can be assigned to ionic copper species that get trapped in the polymer matrix during the pyrrole oxidation, as it is known that copper forms stable complexes with PPy, based on Cu-N bonds.[289] This result opens up the way to a new family of bifunctional APs that can be created by bipolar electrodeposition. Indeed, one can easily imagine that various material combinations can be generated at both ends of a conducting particle, leading to structures that could show interesting features for different applications such as photocatalysis or micromotors.[85]

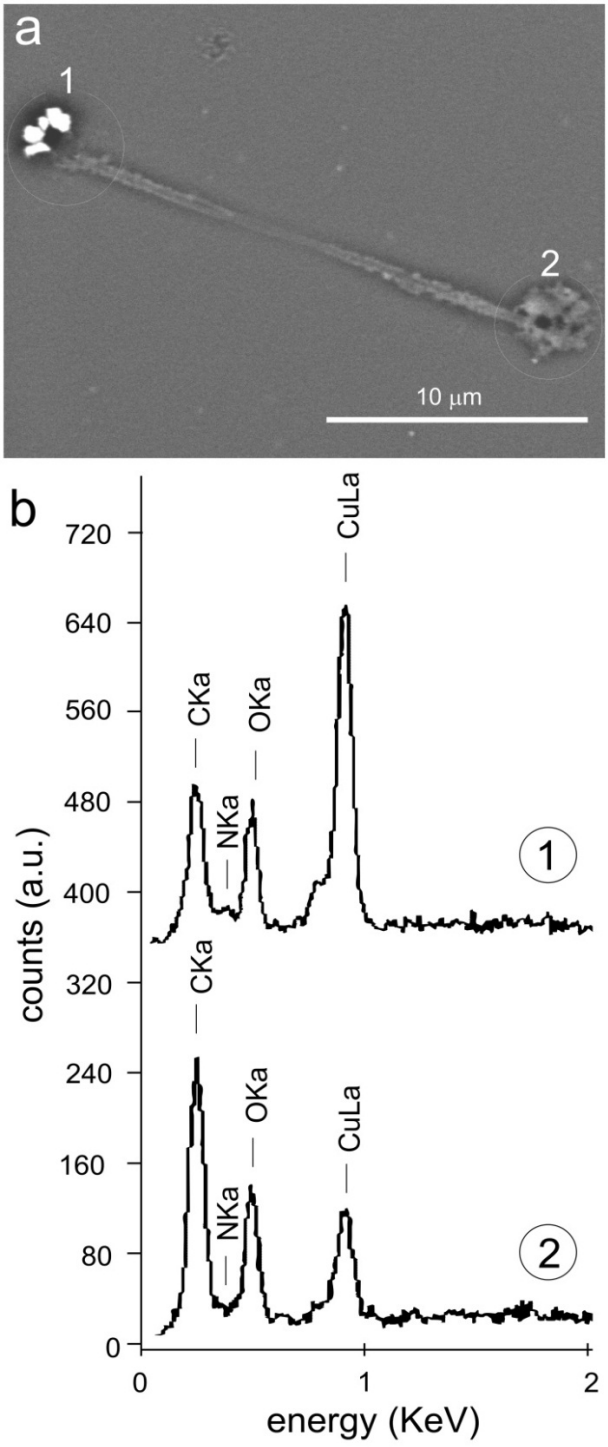

Figure 3.17. Copper/carbon microtube/polypyrrole asymmetric particle. a) Asymmetric dumbbell-like object with one copper end (circle 1) and one PPy end (circle 2). b) EDX spectra recorded for the copper end (1) and for the PPy end (2). Reprinted from reference (284).

3.6. Upscaling the production with a new cell design

Even if the CABED is a bulk process which allows the production of sufficient quantities of APs for a lab scale use, it has several disadvantages. First, an unattractive aspect of the CABED resides in the necessity of using a CE equipment that is usually expensive and cumbersome (see Figure 3.11a). Secondly, the use of this equipment has the strong disadvantage that field reversal is not possible, which eliminates some attractive openings for bipolar electrochemistry. Finally, the strongest restriction of the CABED technology is due to the fact that the modification takes place in a capillary with an inner diameter in the range of 100 μm. This parameter makes the process not well suited for a scaling-up of the production to amounts that might be interesting for industrial applications. One main objective of this thesis was thus to develop a new technology allowing a scale-up of the production of AP by bipolar electrochemistry.

3.6.1. Technology description

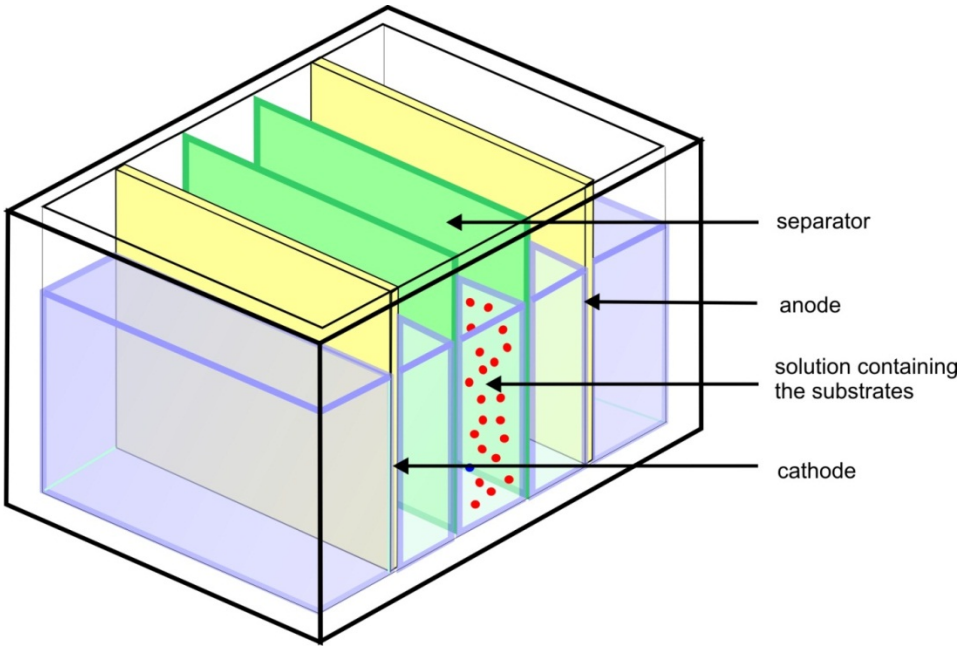

Figure 3.18. Scheme showing the bipolar electrodeposition cell. Adapted from reference (281) and reference (290).

The present technology consists in using a cell composed of one reaction compartment, in which the substrates and the reagents are located, separated by two membranes from the two electrode compartments (Figure 3.18).[290] The feeder electrodes, which are immersed in solvent containing no reactants or only supporting electrolyte, are connected to a high voltage power supply. Gold, platinum or carbon plates were used as electrodes. Two different classes of materials, polymer and

sintered glass membranes, were tested as separators due to their different properties in terms of mechanical stability, permeability and conductivity. These separators are needed in order to limit problems that might occur when using intense electric fields (bubble formation, solvent evaporation and convection due to ohmic heating). As a consequence the electrodes are separated from the reaction chamber, containing the reactants and the objects that should be modified, and their compartments are filled with cold ethanol. Using this configuration, the electric field can be imposed for relatively long periods of time (in the order of few minutes) before observing the first bubbles at the electrode surfaces.

The bipolar electrodeposition experiments that will be described in the following sections were achieved in different cells. Various sets of materials for cell and separator with different dimensions were employed. Many cells were conceived in the framework of this thesis, illustrative examples are given in Figure 3.19. In order to ensure the visualization of important phenomena that can happen during the experiment such as bubble production in the electrode compartments or the variation of the solution levels caused by the electrokinetic flows, transparent materials such as glass, PMMA or PDMS were used. Glass cells with sintered glass separators (thickness 3 mm, porosity 2), such as the one of Figure 3.19a, gave a good insulation between the different compartments since the separators were directly welded to the cell's body, but showed usually the highest EOFs. The design of PMMA/polypropylene cells, like the one shown in Figure 3.19b allows to change easily the position of electrodes and/or the separators, which allows a certain versatility in terms of volume of the reaction compartment and electric field tuning (by changing the distance between electrodes). Due to its malleability, PDMS was found to be very convenient for making cells with a small reaction compartment (see appendix 3 for details about fabrication), an important factor when the modification has to be achieved with a very small amount of substrate. The polymer membrane separators were fixed to the cell body using polytetrafluoroethylene (PTFE) tape (Figure 3.19b) or silicon paste (Figure 3.19c). Membranes were always stored in mQ water in order to avoid their shrinkage, which could induce their detachment. Prior to the experiments, the solutions were inserted into the compartments, the feeder electrodes were connected via crocodile clips to the high power supply (Consort E 862 6000 V – 150 mA or Heinzinger PNC 30,000 – 20 ump), and the electric field was applied for a certain time.

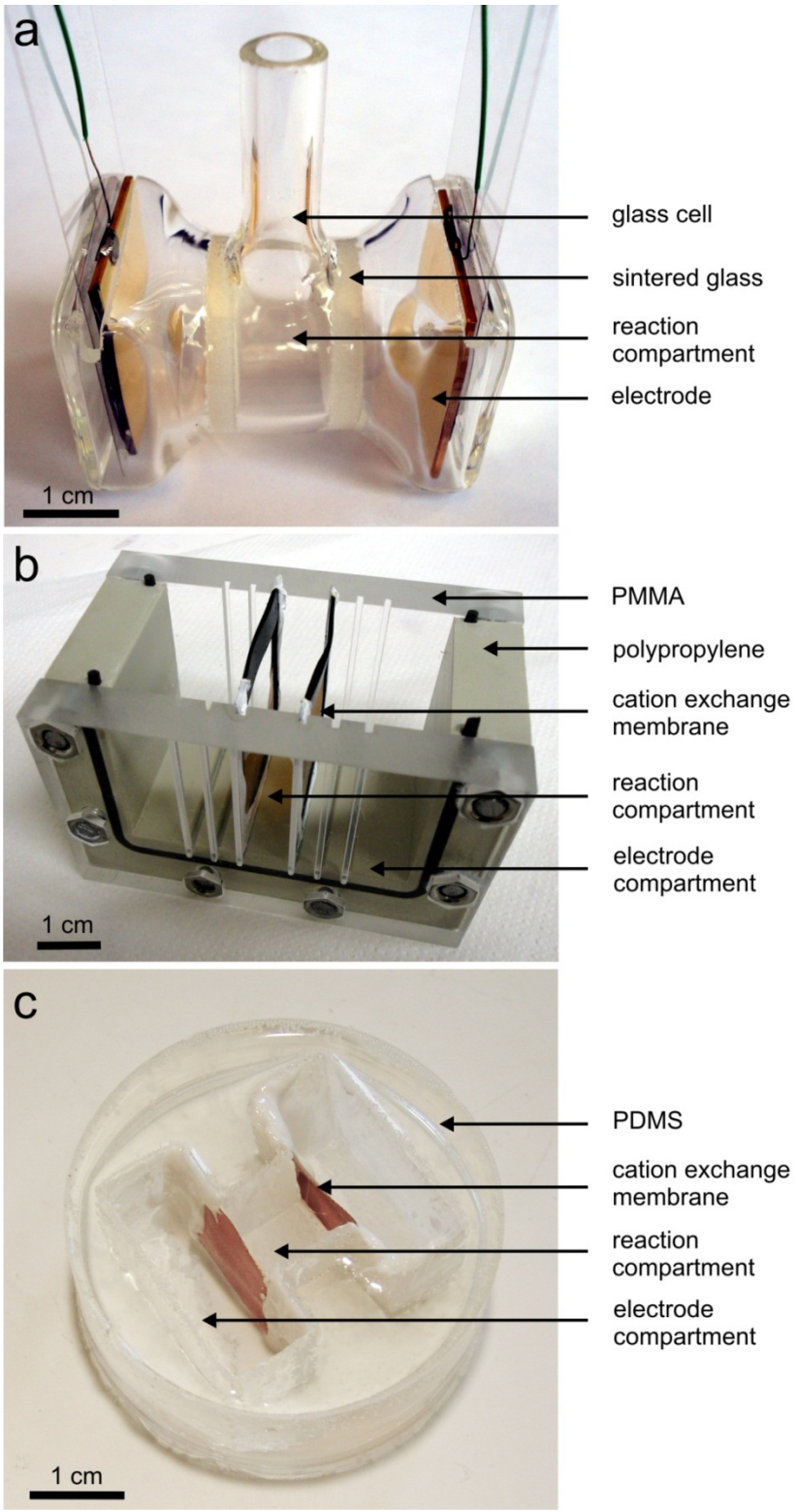

Figure 3.19. Cells used for bipolar electrodeposition. a) Glass cell. b) PMMA/polypropylene cell. c) PDMS cell.

In order to get useful information about the electric field losses within different cell configurations, we decided to evaluate the total potential drop at the compartment interfaces. The electric field inside the reaction compartment was measured in deionized water as shown in Figure 3.20a. Measurements of electric field values were performed with two microelectrodes (platinum wires with a diameter of 100 μm sealed in glass pipettes) connected to an electrometer (Keithley, 6517B). The measuring electrodes were placed at an equal distance from the outer electrodes (see Figure 3.20a) and various measurements were performed using different distances between them. Measurements were performed at room temperature, in mQ water, by applying 120 V between the external feeder electrodes with the power supply. The external electrodes were platinum and gold plates for anode and cathode, respectively. Reinforced cation exchange membranes are Nafion® perfluorinated membranes (N115) with a thickness of 0.13 mm. and the sintered porous glass has a thickness of 3 mm and a porosity of 2. The distance between the feeder electrodes was 3 cm for measurements without separators, 6.7 cm with reinforced cation exchange membranes and 4.2 cm with sintered glass separators. The fixed electric field $\mathscr{E}$ is given by the following equation:

$$\mathscr{E} = \frac{E_{imp}}{L} \tag{3.7}$$

with E_{imp} being the imposed potential between the anode and the cathode and L the distance between the feeder electrodes (see section 1.2.). The potential difference U between two microelectrodes connected to an electrometer was measured for various distances between the two microelectrodes L_m. The electric field transmission efficiency, χ, a dimensionless ratio that allows defining the efficiency of the set-up for the restitution of the imposed external electric field in the reaction compartment is given by:

$$\chi = \frac{\mathscr{E}_{eff}}{\mathscr{E}} \tag{3.8}$$

with $\mathscr{E}_{eff}$ being the electric field measured in the compartment between the separators. It follows that:

$$\chi = \frac{U\,L}{L_m\,E_{imp}} \tag{3.9}$$

and

$$U = \chi \frac{L_m\,E_{imp}}{L} \tag{3.10}$$

Equation 3.10 shows that when plotting U as a function of $\frac{L_m E_{imp}}{L}$ one can extract a value for χ from the slope of the curve. Figure 3.20b presents results obtained for three cell configurations. The separatorless configuration leads to a χ of 0.99, this means that particles in solution would be exposed to 99 % of the applied external electric field during the bipolar electrodeposition experiment. The two other cell configurations show clearly that the separators have an impact on the electric field. Indeed, χ values of 0.65 and 0.62 were obtained in pure water when using a reinforced proton exchange membrane (Nafion®) or sintered porous glass membranes as separators respectively.

However, in the electrodeposition experiment the solution in the reaction compartment contains the metal salt and therefore has a higher conductivity compared to the electrode compartments, which leads to a major potential drop in the latter ones. In order to avoid this situation, inert salt needs therefore to be added to the electrode compartments. In this case χ values around 0.5 can be maintained during a certain time, typically in the order of minutes, as presented in Figure 3.20c which shows the variation of χ as a function of time for an electric field $\mathscr{E}$ = 26.2 kV m^{-1} in a cell containing sintered porous glass membranes (E_{imp} = 1.1 kV, L = 4.2 cm). This is sufficient to generate the potential difference in the reaction compartment required for the modification of particles with dimensions in the micrometer and sub-micrometer range. For longer periods, χ is changing due to the migration and consumption of ions as well as the formation of bubbles at the feeder electrodes. However this does not affect the result of the experiment, as the modification is usually accomplished in shorter periods of time. Depending on the electric field value, the cell and the separator material, a more or less important EOF might be generated, affecting the filling levels of the different compartments. Because of the material porosity, this flow is more pronounced when using sintered glass separators. Having a slightly more filled anodic compartment allows circumventing this problem. These optimizations in terms of restitution of electric field in the reaction chamber allowed imposing a bias voltage of up to several kV with few centimeters of separation between the feeder electrodes, leading to electric fields of more than 100 kV m^{-1} during the bipolar electrodeposition experiments.

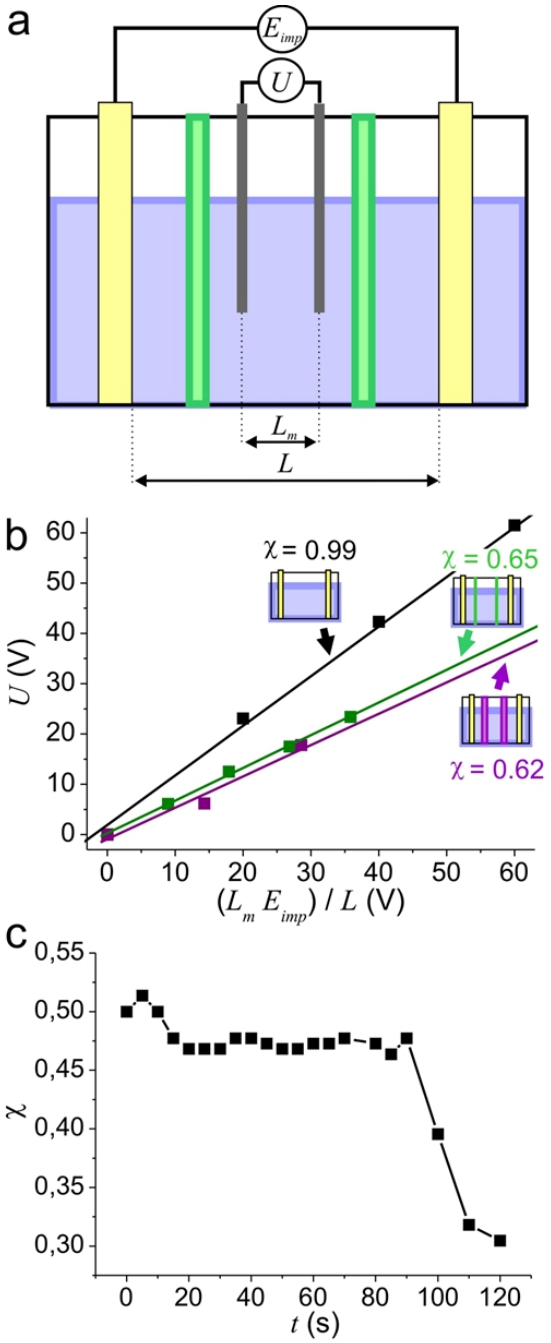

Figure 3.20. Study of different cell configurations. a) Scheme showing the measurement of the electric field inside the reaction compartment. b) Graph showing the evolution of the measured potential between the sensing electrodes as a function of the imposed electric field between the feeder electrodes and the distance between the measurement electrodes. The three curves correspond to three different cell configurations (black: without separators, green: with reinforced Nafion® membranes, purple: sintered glass membranes). c) Time evolution of the electric field transmission efficiency χ for a cell containing an ethyl cellulose gel with 0.5 mM $HAuCl_4$ in the reaction compartment and a 1 mM NH_4Cl ethanol solution in the two electrode compartments, $\mathscr{E}$= 26.2 kV m^{-1}. Adapted from reference (281).

3.6.2. Metal deposition

3.6.2.1. Metal deposition on anisotropic structures

At first we decided to perform similar experiments to those previously achieved with CABED (see section 3.5.2.1.) to test our technology, and therefore studied the metal deposition on CMTs. Due to their anisotropic nature, these substrates are preferred to isotropic ones (the latter case will be presented in section 3.8.2.2.), since in this case, they will orientate in the field (their longitudinal axis aligned parallel to the field lines). This means that no experimental precautions have to be taken in order to ensure their orientation and/or immobilization during the bipolar electrodeposition run. These experiments were achieved with gold and platinum. About 0.1 mg of the CMT powder was added to a $HAuCl_4$ solution in EtOH:H_2O, 95:5 % vol. or H_2PtCl_2 in mQ water (the metal salt concentration being in the mM range). The resulting mixture was sonicated for 1 min. A cell similar to the one shown in Figure 3.19a, with sintered-glass separators spaced by 1.4 cm and feeder gold electrodes separated by 4 cm was used (the volume of the reaction compartment V_r is about 2.2 mL). The reaction compartment of the cell was filled with the prepared mixture and the electrode compartments with absolute ethanol. Voltage biases were imposed during more than one minute. After the modification, the solution in the reaction compartment was recovered; a drop of it was evaporated and rinsed on a conductive substrate for SEM characterization.

Figure 3.21a shows optical pictures of CMTs recovered after the bipolar electrodeposition of gold using 37.5 kV m^{-1} and 1 mM $HAuCl_4$. The gold particles at one extremity of the CMTs very clearly shown in Figure 3.21b and c, that the asymmetric modification has been successfully performed. Furthermore, these CMT/Au APs have a similar shape to those obtained by CABED (Figure 3.13c). Careful examination of the samples with SEM highlights two slightly different topologies. The tube shown in Figure 3.21b is modified in a symmetrical way with the Au particle being centered with respect to the long axis of the tube. On the other hand, the tube shown in Figure 3.21c has been modified in a non-symmetrical fashion as the particle is positioned slightly off the longitudinal axis of the tube.

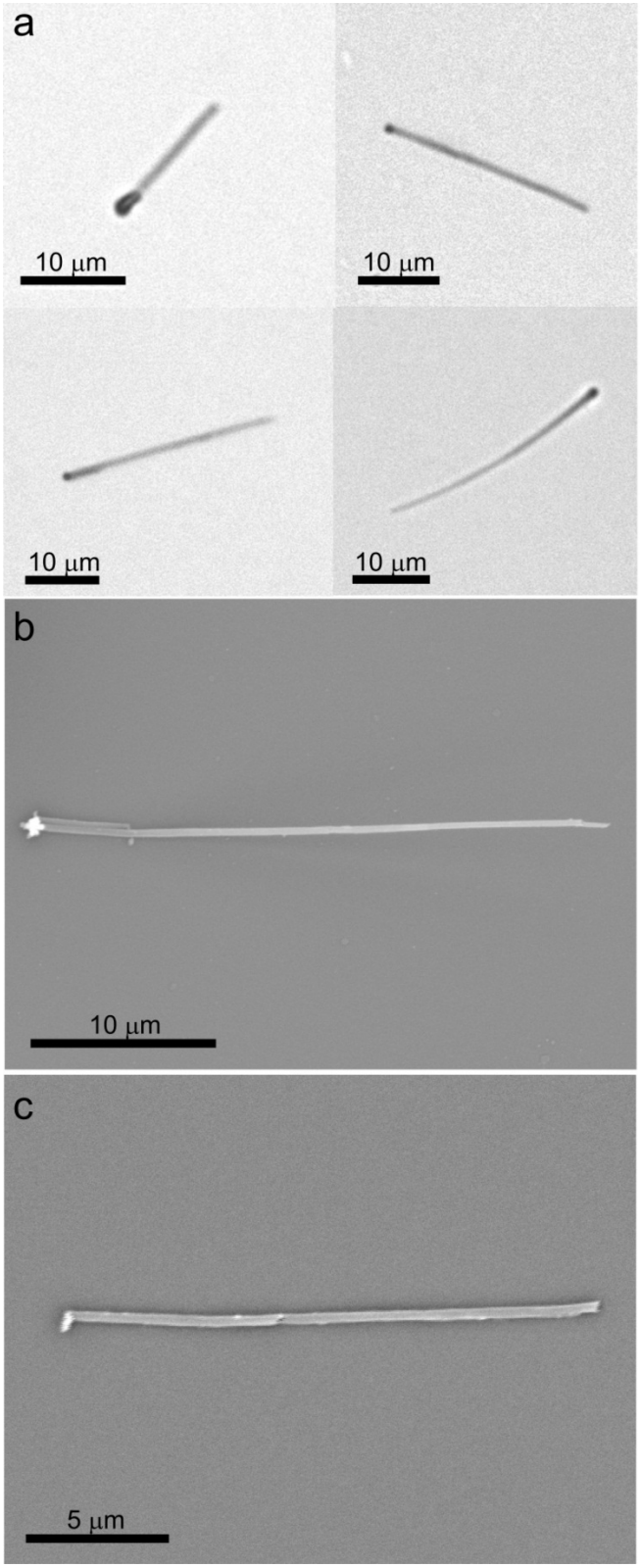

Figure 3.21. Carbon microtubes asymmetrically modified with gold. a) Series of optical micrographs showing CMT/Au APs recovered after bipolar electrodeposition experiments. b) SEM picture of a CMT/Au AP with a centered deposit. c) SEM picture of a CMT/Au AP with a non-centered deposit.

Analog experiments were performed with platinum. In this case, the bipolar electrodeposition was carried-out under identical conditions but with a $PtCl_6^{2-}$ concentration of 10 mM. The following reaction is supposed to occur at the CMT cathodic pole:

$$Pt^{IV}Cl_6^{2-}(l) + 4\ e^- \rightarrow Pt^0(s) + 6\ Cl^-(l) \quad E^0 = 0.73\ V\ vs\ NHE \tag{3.11}$$

As shown in Figure 3.22 the metal deposits are also clearly observable by optical and electronic microscopy. Due to the salt concentration, being one order of magnitude higher than the one used for the gold modification, the platinum deposits are significantly bigger than the ones obtained for gold. As an example, the Au deposit size presented in Figure 3.21b is around 950 nm while for the Pt modification, shown in Figure 3.22c, the size is about 3.5 μm (3.7 times larger). As it was the case for gold, the observation of the deposit also revealed the presence of two types of objects. Figure 3.22a shows a CMT with a centered Pt deposit whereas in Figure 3.22b the Pt deposit is non-centered, a detail of a non-centered platinum particle can also be seen on the inset of in Figure 3.22c.

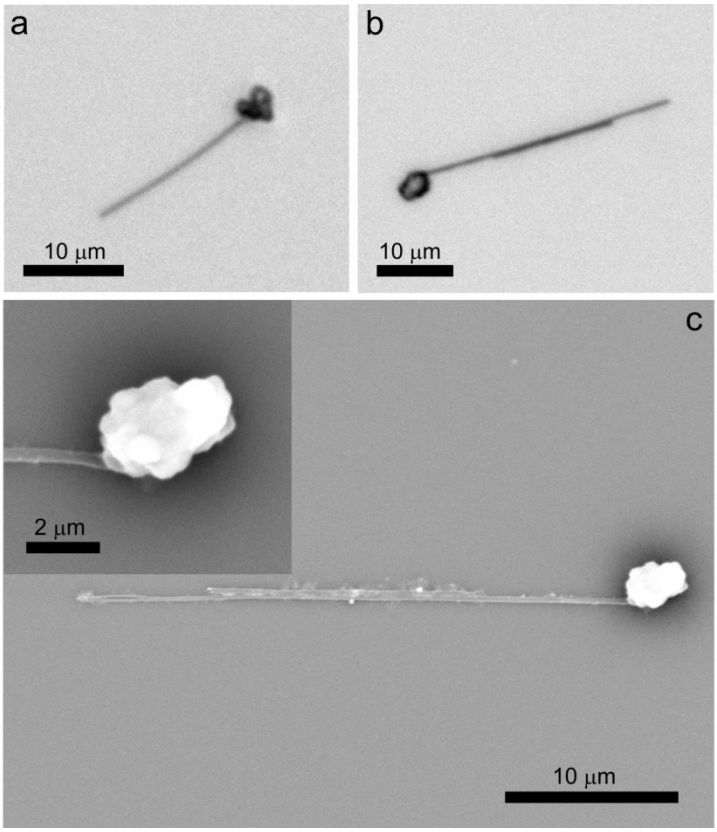

Figure 3.22. Carbon microtubes asymmetrically modified with platinum. a) Optical micrograph showing a CMT/Pt AP with a centered deposit. b) Optical micrograph showing a CMT/Pt AP with an non-centered deposit. c) SEM picture of a CMT/Pt AP with a non-centered deposit. Inset: detail on the Pt deposit.

As we will discuss in section 4.2.2., the latter APs can be used as micromotors in the presence of a chemical fuel. It was found that the AP morphology plays a crucial role in this application; thus it seems important to understand the mechanism leading to a centered or a non-centered deposit location. As shown in Figure 3.23, this difference might be explained on the basis of a mixed influence of two competing parameters, which are the time needed for the electromechanical alignment compared to the activation of the bipolar reaction. Indeed, a linear potential sweep is applied in order to reach the electric field value where $\Delta V > \Delta V_{min}$, and thus the CMTs behave as BEs (see section 1.2.). Theoretically, this potential ramp should last for a time long enough to allow an alignment of the tubes along the direction of the electric field before reaching the threshold value where the bipolar reaction starts to occur. In this case the experiment should lead theoretically to the formation of a centered electrodeposit of the metal (Figure 3.23a) with respect to the longitudinal axis of the tube, because the nucleation point is located at the point of maximum polarization. But the reality is more complicated and the alignment of a CMT at the moment where the electrodeposition starts depends on several parameters such as its initial orientation, its length, its diameter and the solvent viscosity. For some CMTs, the condition $\Delta V > \Delta V_{min}$ is fulfilled before the tube is perfectly aligned parallel to the electric field lines. In this case, the deposition also occurs at the point of highest polarization, which in this case is not located at the center of the tube end, but at the edge. Consequently the metal deposits at the most favorable nucleation site and generates a non-centered metal particle, as illustrated in Figure 3.23b. The interesting aspect of this is that these experimental conditions can be adjusted in order to tune the electrodeposition morphology. For example, one can easily imagine applying a very quick and high potential sweep for inducing almost instantaneously the deposition and thus obtaining non-centered deposits on CMTs with quantitative yields. Also, imposing first an electric field that is lower than the one required to induce the metal deposition but sufficient enough to align the CMTs followed by an increase of the electric field to a sufficient value for achieving metal deposition could allow to get quantitatively CMTs with centered deposits. Although non-centered deposition may exist in the CABED technology (see section 3.5.) this morphology has not been observed. This is surely due to the use of the capillary which, because of its shape and the electrokinetic flow induces a more efficient orientation of the CMTs parallel to the electric field lines.

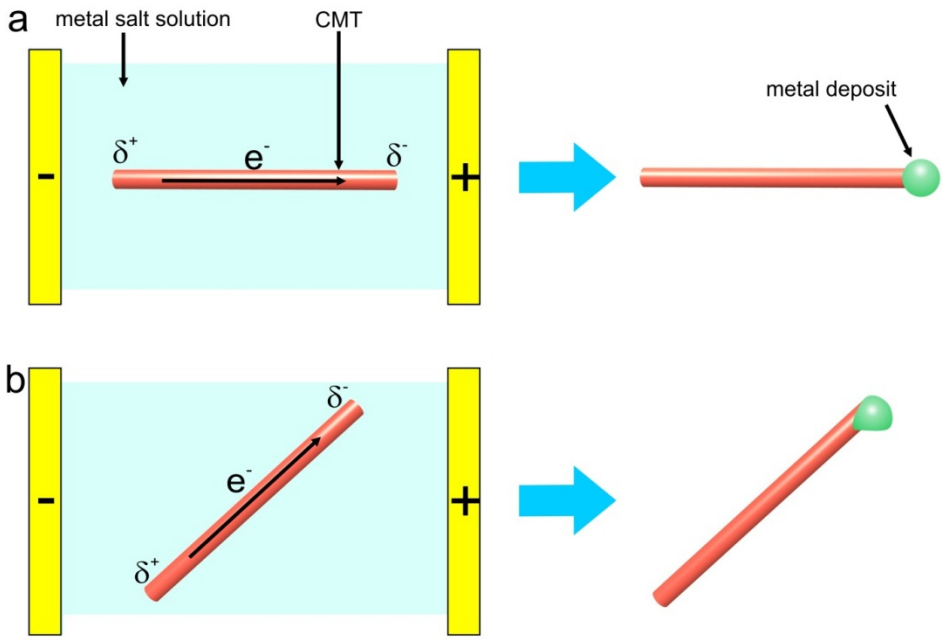

Figure 3.23. Schematic illustration explaining the origin of the different deposit locations obtained for CMTs as a function of their orientation in the electric field at the beginning of the electrodeposition process. a) CMT aligned parallel to the electric field. b) CMT non-aligned with the electric field. Adapted from reference (89).

3.6.2.2. Metal deposition on isotropic structures

Spherical JPs are of primary importance for different applications such as e-paper (section 3.2.2.1.) or particulate surfactants (section 3.2.1.1.). One can easily imagine their synthesis to be achieved at a large scale by bipolar electrodeposition of a material on one side of a conducting bead. In practice, one important issue for these experiments is the possible rotation of the objects, while exposed to the electric field. Unlike CTs, because of the isotropic nature of these objects, no preferential orientation in the electric field is expected. Electrodeposition on moving particles can be an efficient way to produce core shell particles (see section 2.1.1., Figure 2.3a),[291] but this is not the topic of interest in this chapter. As in the present technology no interfaces are involved, which could allow immobilizing the particles, another way had to be used in order to avoid or at least slow down this rotational movement. This has been achieved here by increasing the viscosity of the solution in the reaction compartment via the addition of gelling agents. Experiments were carried out with various kinds of carbon beads with sizes covering two orders of magnitude. Because of the presence of gelling agent, the resulting modified particles have to be extracted from the gel by a washing process. Two different kinds of gels were used in the reaction medium. With agarose as a gelling agent, the modification can be performed in water. Although this approach seems attractive from an industrial point of view, in this case the washing process requires a heating step to recover the APs, which can

lead to an undesired spontaneous reduction of strong oxidants like tetrachloroaurate. For this reason, agarose can be replaced by an ethanol-based gel using ethyl-cellulose. Besides avoiding the heating step for recovering the particles, working with this gel reduces osmosis effects between the cell compartments, since usually ethanol is used in the electrode compartments.

For the modification of the biggest glassy carbon (GC) beads, an ethanol based gel was first prepared by dissolving ethyl cellulose in absolute ethanol at a concentration of 200 $g.L^{-1}$. The mixture was sonicated for at least an hour until a homogenous gel was obtained. 30 mg of 200-400 µm GC beads (inset of Figure 3.24a), previously washed and sonicated in absolute ethanol, were then added to 6 ml of the ethyl cellulose gel. 1 mM $HAuCl_4$ was added and the mixture was stirred until a well dispersed suspension was obtained. 2 ml of the resulting mixture were introduced into the reaction compartment of a glass cell (similar to the one shown in Figure 3.19a) with two sintered-glass separators having a thickness of 3 mm and a porosity of 2. These separators were spaced by 1 cm and the outer gold electrodes were separated by 3.5 cm (V_r ≈2 ml). Ethanol, containing in this case 1 mM NH_4Cl as supporting electrolyte in order to limit the potential drop in the electrode compartments, was cooled for 1 min in liquid nitrogen and then added to the electrode compartments. A voltage bias of 1.5 kV was imposed for one minute. After the modification, the gel was taken out from the reaction compartment in order to isolate the modified beads. For this step, the gel containing the modified beads was dissolved in 50 ml of absolute ethanol under stirring. The resulting solution was then centrifuged at 3000 rpm for 2 min. The supernatant was removed and this washing process was repeated 3 times. Finally, the modified beads were kept in a small volume of ethanol for conservation.

Figure 3.24 a and b show GC beads recovered after a bipolar electrodeposition run. The modification with gold is clearly observable under the SEM due to the high electronic contrast of the different materials. The polydispersity of the commercial beads allows illustrating the consequences of Equation 1.4., which describes the maximum potential polarization arising between the two sides of a particle with a given characteristic size. Indeed, since the biggest ones experience a higher polarization, they have bigger deposits compared to smaller beads. Modification yields of up to 80 % were achieved (Figure 3.24a). This value has been determined as the ratio between the number of Janus beads and the total number of beads by simply counting them on SEM pictures. Because beads are sometimes positioned in a way that their deposit is hidden (facing the substrate) this can be considered as a lower limit of the estimated yield.

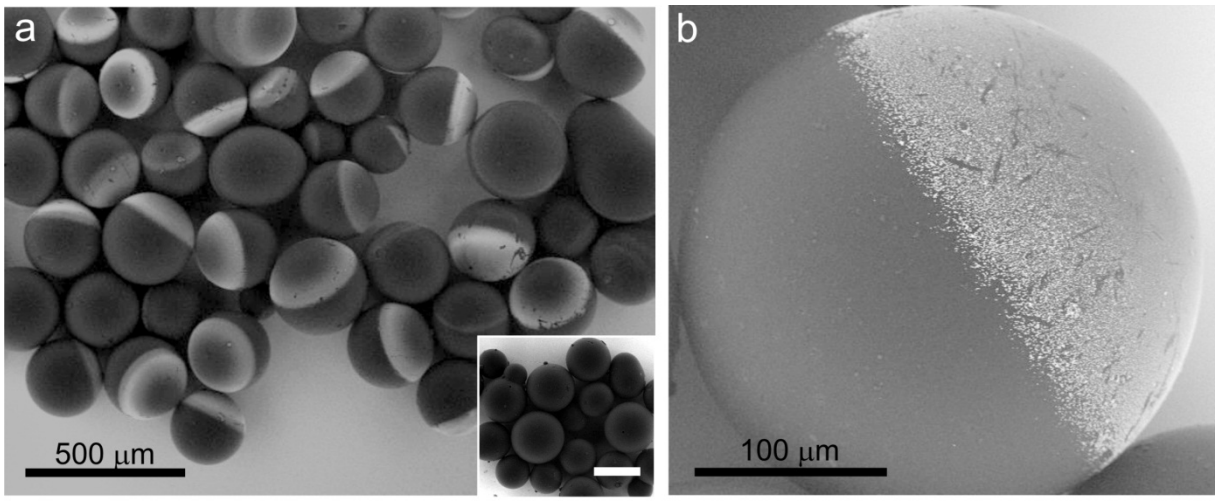

Figure 3.24. Sub-millimeteric carbon/gold Janus beads synthesized by bipolar electrodeposition. a) SEM picture of GC beads with diameters ranging from 200 to 400 μm asymmetrically modified with gold. Inset: unmodified GC beads with diameters ranging from 200 to 400 μm (the scale bar equals 200 μm). b) SEM picture showing a detailed view of one Janus bead.

For the synthesis of Janus beads with intermediate sizes, first, an agarose-based hydrogel was prepared by mixing 20 mg of agar and 5 mL of a 1 mM $HAuCl_4$ aqueous solution or 5 mL of a 1 mM $AgNO_3$ aqueous solution in a glass tube. The glass tube was quickly heated at the bottom with a heat gun until the first gas bubbles appeared on the glass walls. 6 mg (for gold modification) or 1.5 mg (for silver modification) of spherical GC powder (20 -50 μm, inset of Figure 3.25a) were incorporated into the hot gel. The gel was then rapidly cooled down by putting the glass tube in room-temperature water while stirring and sonicating it regularly during the cooling process to prevent the particle agglomeration during the gelling process. When room temperature was reached, the gel was added to the reaction compartment of the cell. The same cell than the one used for the CMT modification was used for the modification with gold (see section 3.6.2.1.). For modification with silver, a PMMA cell (similar to the one shown in Figure 3.19c) containing cation exchange membranes as separators. The separators were spaced by 1 cm and the outer gold electrodes were separated by 2 cm (V_r ≈3 mL). Ethanol cooled for 1 min in liquid nitrogen was then added to the electrode compartments. A voltage bias of 1 kV (for gold modification) or 1.5 kV (for silver modification) was imposed for more than two minutes. After the polarization, the gel was removed from the reaction compartment for the isolation step. The gel containing the modified beads was inserted in an Erlenmeyer flask and diluted with 50 mL of mQ water. It was then heated from below with a heat gun until bubbles on the glass walls were seen and the black particles settled at the bottom of the flask. The hot mixture is then centrifuged at 3000 rpm for 2 min. After centrifugation, almost all the supernatant is taken out and the beads were redispersed in 50 mL mQ water, sonicated and centrifuged again for 2 min at the

same speed. This step was repeated once again and the modified beads were finally dispersed in a small volume of water for conservation.

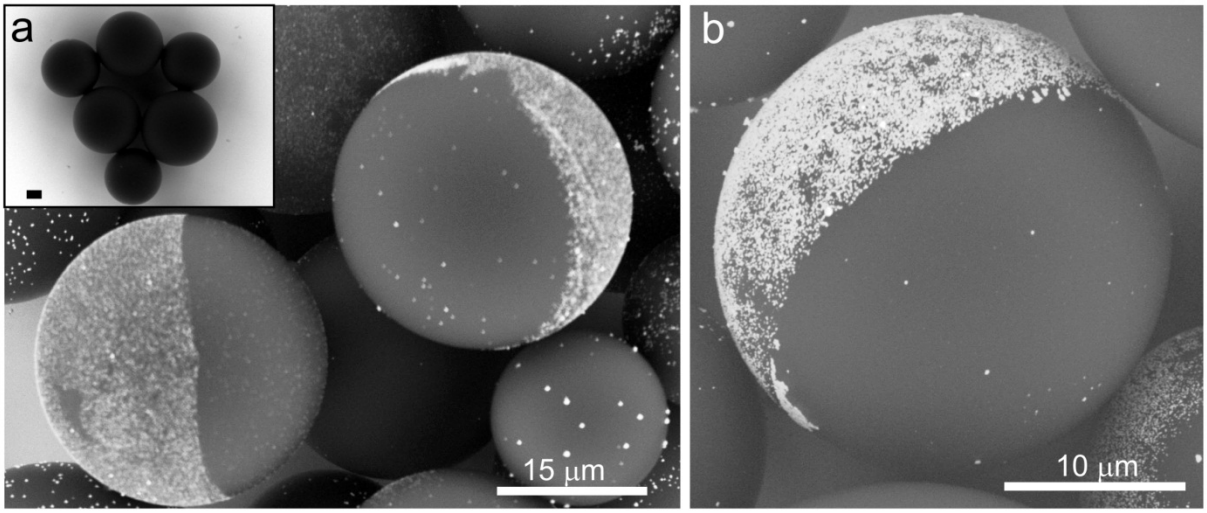

Figure 3.25. Micrometric carbon/gold Janus beads synthesized by bipolar electrodeposition. a) SEM picture of GC beads with diameters ranging from 20 to 50 μm modified asymmetrically with gold. Inset: unmodified GC beads with diameters ranging from 20 to 50 μm (the scale bar equals 5 μm). b) SEM picture showing a detailed view of one Janus bead.

Since the overvoltage needed for the gold deposition is rather low, an electric field of 25 kV m^{-1} leads to a sufficient polarization for electrodeposition on the total half sphere, as clearly proved by Figure 3.25. Theoretically, the deposit can be more or less dense depending on the gold concentration and the electric field value. As previously mentioned, the use of an agarose gel can lead to the spontaneous reduction of tetrachloroaurate, this explains the unspecific deposition of small gold dots on areas of the particles that were not modified by bipolar electrodeposition (Figure 3.25).

Silver deposition can be achieved at the cathodic pole of the GC bead through the following reaction:

$$Ag^{I}NO_3(l) + e^- \rightarrow Ag^0 \quad E^0 = 0.80 \text{ V } vs \text{ NHE} \tag{3.12}$$

In contrast to gold, the silver reduction reaction needs a higher ΔV_{min} (section 1.2.), because silver is a less noble metal with a more negative E^0. Thus, higher electric field values (75 kV m^{-1}) are needed to trigger electrodeposition. In the case illustrated in Figure 3.26, only the extremity of the beads was sufficiently polarized to allow the reduction of silver ions, leading to single point modified particles. The silver coverage could be in principle increased by using higher electric field values.

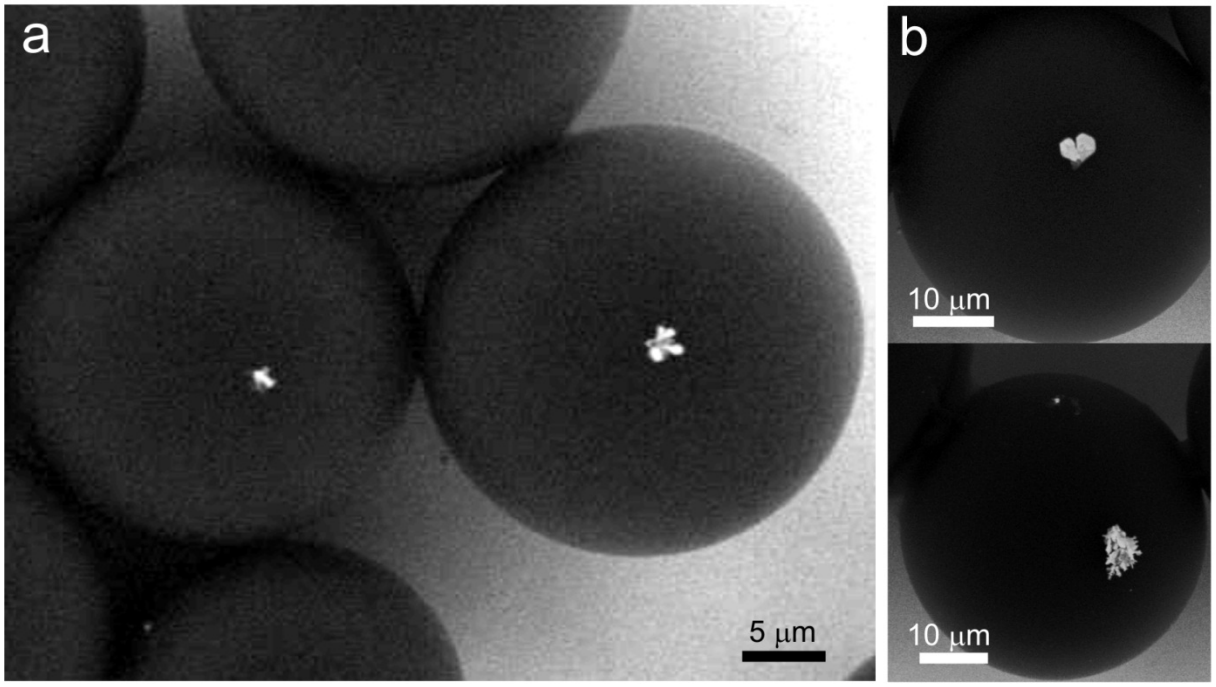

Figure 3.26. Micrometric carbon/silver asymmetric beads synthesized by bipolar electrodeposition. a) SEM picture of GC beads with diameters ranging from 20 to 50 μm modified with silver. b) SEM pictures showing detailed views of one asymmetric bead.

The bipolar modification has also been tested on particles with sizes around 1 μm. First a separation procedure was used in order to isolate the smallest GC beads (Inset of Figure 3.27a) from a spherical GC powder containing beads with diameters ranging from 0.4 to 12 μm. For this, 0.2 g of powder was then inserted into a vial containing 4 mL of mQ water, stirred and sedimented. When a black aggregate is seen at the bottom of the vial, 1 mL of the supernatant is taken and dispersed into 4 mL mQ water. The sedimentation step was repeated for 10 min and 0.2 mL of the supernatant is added to 2.3 mL of a 1 mM $HAuCl_4$ solution, 1 mL of water and 30 mg of agar. The gel and the modification is obtained in a similar way as described previously for 20-50 μm GC beads, in the same cell, imposing a voltage bias higher than 1 kV for two minutes**.** After modification, the gel was removed from the reaction compartment and the same washing procedure was performed.

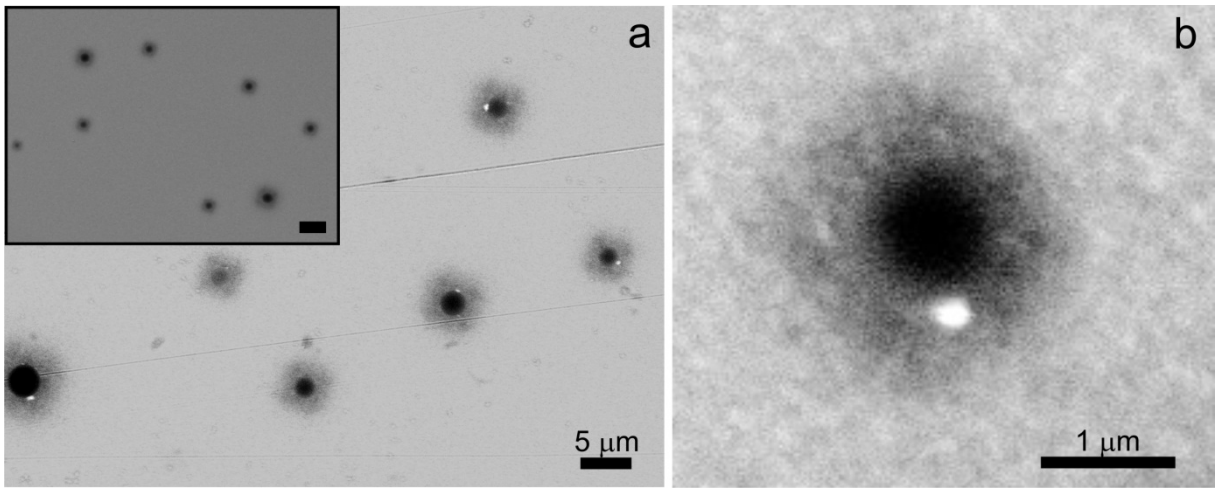

Figure 3.27. Micrometer and submicrometer-sized carbon/gold assymetric beads synthesized by bipolar electrodeposition. a) SEM picture of GC beads with diameters around 1 μm modified with gold. Inset: unmodified GC beads with diameters around 1 μm (the scale bar equals 5 μm). b) SEM picture showing a detailed view of one asymmetric bead.

Figure 3.27 shows the evidence that the modification of micrometer (Figure 3.27a) and submicrometer-sized (Figure 3.27b) is also possible with this technology. Because of the typical size of these objects, using the same electric field values than for the previous ones (25 kV m^{-1}), leads now to a modification that is smaller and localized at the very extremity of the particles. As an example, the gold patch present on the GC bead of Figure 3.27b (d ≈750 nm) is about 200 nm. This demonstrates that when playing with the two crucial parameters that control the maximum polarization potential ΔV (Equation 1.4), namely the characteristic dimensions of the objects and the applied external voltage, one can control the portion modified by the metal on the particles, from metal hemispheres (Figure 3.25b) to single points (Figure 3.27b).

JPs or PPs offer the possibility to use two different surface chemistries on the same particle. Due to their reactivity difference, each material can be selectively functionalized. As a proof-of-principle experiment, we decided to use a thiol-based chemistry in order to selectively tag the gold surface of 20-50 μm GC/Au JPs previously synthesized by bipolar electrodeposition. In these experiments the JPs were prepared as previously described and analyzed with SEM, showing similar features than the one of Figure 3.25. The functionalization protocol is shown in Figure 3.27a. Basically, 100 μL of the JP suspension was inserted in a vial containing 0.5 mL of an aqueous solution of cysteamine (10 mM). Thiol groups having a strong affinity for bare gold,[292] it is then expected that a cysteamine SAM is formed after the incubation, which was carried out for 24 H. The JPs were then washed 4 times by centrifugation with mQ water. After the washing step, the supernatant was removed and 80 μL of a water/dimethyl sulfoxide (DMSO) (50:50 % vol.) together with 0.4 mg of bis(2,2'-bipyridine)-4'-

methyl-4-carboxybipyridine-ruthenium N-succinimidyl ester-bis(hexafluorophosphate) was added and let react overnight. The succinimidyl moiety activating the ester, a peptide coupling is obtained with the surface-bonded cysteamine, grafting the Ru^{II} complex on gold moiety of the JPs.

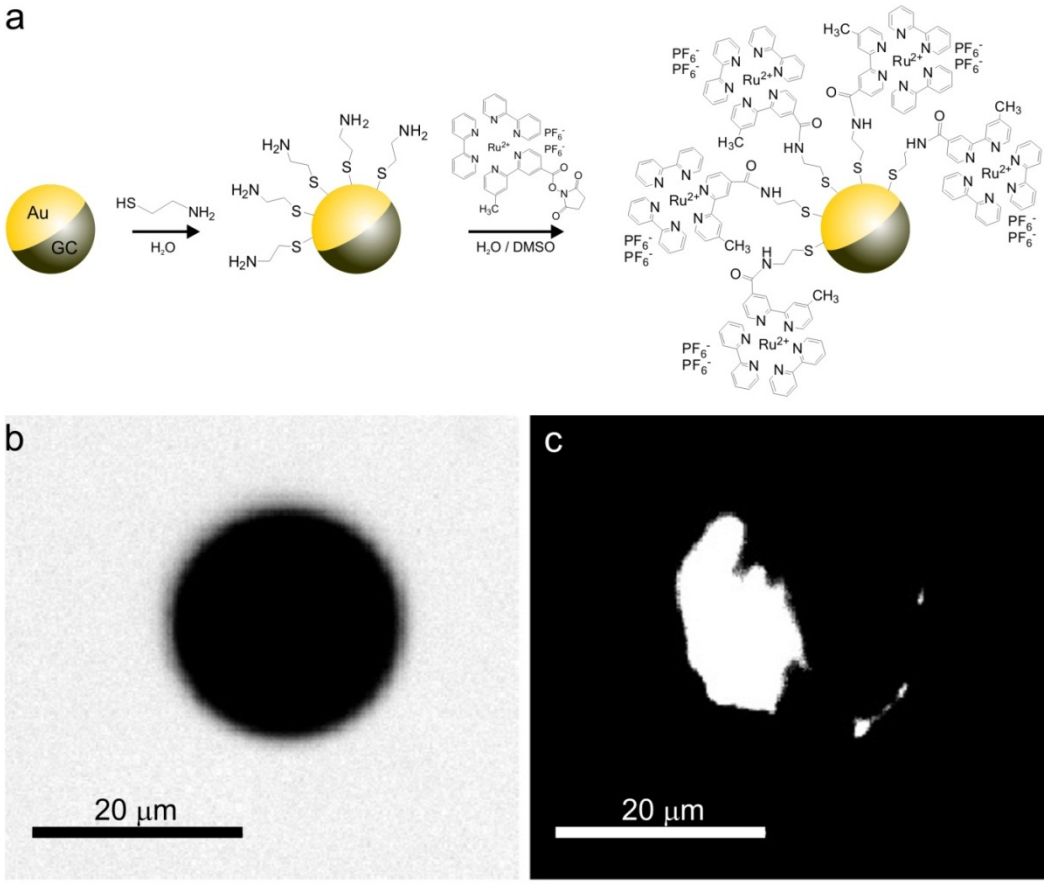

Figure 3.28. Selective fluorescent tagging of a carbon/gold Janus particle. a) Scheme showing the functionalization steps for tagging the gold surface of a GC/Au JP. b) Optical micrograph obtained by transmission microscopy, showing an individual GC/Au JP after its functionalization. c) Fluorescence micrograph showing the same GC/Au JP that was presented in Figure 3.34b.

Ru^{II} complexes, such as ruthenium(II)tris(2,2-bipyridine) ($Ru(bpy)_3^{2+}$), own very interesting optical properties[293] like photoluminescence, chemiluminescence and ECL (see section 3.2.2.2. and 4.4., for more information about ECL). We have chosen to use this fluorophore, because of these optical characteristics as well as the commercial availability of the activated ester variant, but many other molecules might be selectively grafted following the same principle. The JPs, in suspension with DMSO, were characterized by transmission (Figure 3.28b) and fluorescence microscopy (Figure 3.28c) after the functionalization. The fluorescence of the Ru^{II} complex can be clearly seen on only one half of the particle shown in Figure 3.28c, demonstrating that the asymmetric grafting has been successfully achieved. In our case, the GC surface remains naked, but one can easily imagine its subsequent functionalization using, for instance, a chemistry based on diazonium salts[294] in order to

get two different properties at each hemisphere of the particles. We here demonstrated the selective molecular functionalization on APs, that could be of importance in applications such as drug delivery (section 3.2.6.), e-paper (section 3.2.2.1.) or sensing (section 3.2.4.).

3.6.3. Single point precipitation of a metal halide

In addition to bipolar electrodeposition which involves a direct electron transfer like metal electroreduction or electropolymerization (section 3.5.3.), we have also explored other concepts that could be used for the bulk generation of Janus nanoobjects. These deposition mechanisms could be grouped under the name of "indirect bipolar electrodeposition" since, in these cases, the deposition is not achieved by a direct electron transfer from the BE to a soluble precursor. The deposits are triggered indirectly by local reactions occuring at one reactive pole of a BE. They can be the consequence of a local pH change (see section 3.6.4.) or induced by the dissolution of the BE itself, as we will now describe. This section presents proof-of-concept experiments for generating silver-silver halide Janus objects by bipolar electrochemistry, that involve the use of silver nanowires (AgNWs) as BEs.

AgNWs were synthesized by a modified polyol process[295] inspired by the one reported by Zhang *et al.*[296] In a double necked round bottom flask equipped with a reflux system, 15 mL of ethylene glycol (EG) were heated at 170 °C for 2 hours under stirring. Then, 4.5 mL of a 0.1 mM Na_2PtCl_6 solution in EG was injected into the flask. The reduction of $PtCl_6^{2-}$ by EG generates Pt^0 seeds in the solution. 5 min later, 18 mL of an EG solution containing 0.05 M $AgNO_3$ and 0.1 M polyvinylpyrrolidone (in terms of repeating units), was added dropwise with a syringe pump at a rate of 0.5 mL min^{-1}. This reaction mixture was then heated up to 170 °C for 40 min, during which silver nucleates exclusively on certain favored facets of the Pt^0 seeds, which induces the AgNW growth, stabilized by PVP. The suspension was collected and washed two times with ethanol and once with mQ water by centrifugation for 10 min at 3000 rpm in order to isolate the AgNWs from other NPs present in the initial mixture. A TEM picture with representative AgNWs as well as a photograph of a dispersion are shown in Figure 3.29.

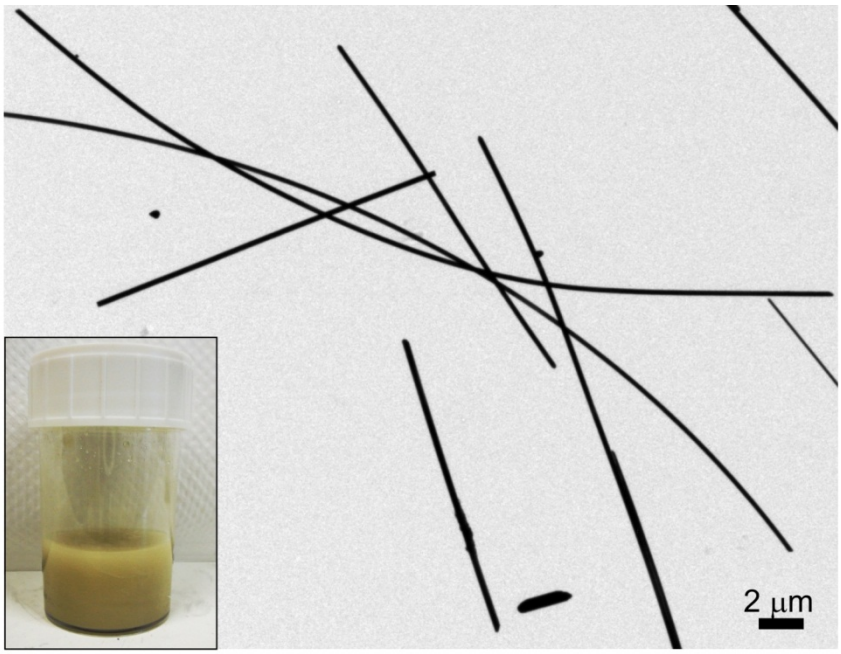

Figure 3.29. TEM image of silver nanowires. Inset: photograph showing a suspension of silver nanowires.

For the bipolar modification of AgNWs, 0.1 mL of the NW suspension, 0.1 mL of an aqueous solution of hexaaammineruthenium(III) chloride (5 mM) and 0.15 mL of mQ water, were mixed and inserted into the reaction compartment of a PDMS cell (similar to the one shown in Figure 3.19c). The cell owns two membrane separators, which are spaced by 1 cm and feeder platinum electrodes, separated by 2 cm (V_r ≈0.5 mL). Few milliliters of cold ethanol (dipped for 2 min in liquid nitrogen), were added to the electrode compartment. During these experiments, electric field values of 75 kV m^{-1} were imposed for 30 s. After the modification, the middle compartment suspension was recovered for further TEM characterizations. Figure 3.30a describes the mechanism of the modification: at the cathodic pole of the AgNW, hexaaammineruthenium(III) is reduced to hexaaammineruthenium(II), and simultaneously, Ag^0 is oxidized to Ag^+ at the anodic pole. The presence of the chloride counterions in the medium and the weak solubility of AgCl (K_s = 1.6 10^{-10} at 25 °C) causes therefore AgCl precipitation at the positively polarized extremity of the NW. Figure 3.29 shows the AgNWs before the modification and Figure 3.30b and c show typical modified AgNWs. The modification is clearly visible in the form of AgCl deposits located only at one end of the wire. Due to the partial reduction of AgCl under the electron beam during imaging, the deposits are covered by a silver layer, which makes them appear black.[273]

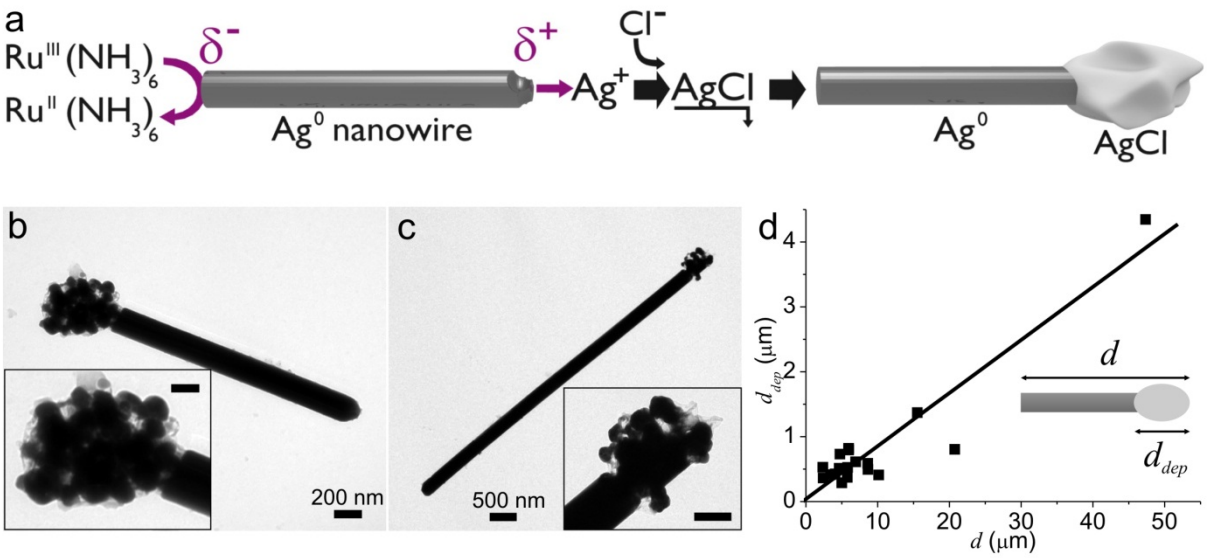

Figure 3.30. Precipitation of silver chloride at one tip of silver nanowires by bipolar electrochemistry. a) Deposition mechanism. b,c) TEM pictures of typical AgNWs/AgCl APs. Inset: detail of the AgCl deposit (the scale bars equal 100 nm and 200 nm respectively). d) Plot of the deposit length d_{dep} as a function of the nanowire length d. Reprinted from reference (281).

The employed AgNW suspensions were mainly composed of wires with lengths below 10 µm, but some were also much longer (Figure 3.29). This allowed us to study the AgCl deposit size d_{dep} as a function of the nanowire lengths d. Figure 3.30d indicates that the correlation is roughly linear, which is in agreement with the theoretically expected variation of the driving force for the modification. As can it be concluded from Equation 1.4, the length of the substrate directly influences the object polarization and thus the kinetics of the Ag^0 dissolution and the size of the AgCl deposit. The proof-of-principle experiment was carried-out with AgNWs and AgCl, but this concept can be used theoretically to generate a wide range of Ag/AgX APs with many shapes that could have interesting properties for photocatalysis[256,257] and medical applications.[258]

3.6.4. Deposition of semiconducting and insulating layers

Attractive materials can also be deposited by mechanisms involving their precipitation triggered by a local pH change at the electrode surface. Deposition of organic layers such as electrophoretic deposition paints (EDPs),[297] or inorganic layers can be performed electrochemically using precipitation of soluble polymers[298,299] or sol-gel procedures. Besides being attractive due to their electrical insulating properties, these materials are biocompatible and porous so they can be used as encapsulating matrices and consequently trap a wide variety of species such as dyes[300] or biomolecules.[301,302] In this section, we report the local modification with silica, silicone, titanate, titanium dioxide, and EDP by means of indirect bipolar electrodeposition and we finally exploit the

encapsulating properties of these materials in section 3.6.5. for the generation of functional Janus objects.

The half-reactions involved in water electrolysis:

$$H_2O \rightarrow ½\ O_2 + 2\ e^- + 2\ H^+ \quad E^0 = 1.23\ V\ vs\ NHE \tag{3.13}$$

and

$$H_2O + e^- \rightarrow ½\ H_2 + OH^- \quad E^0 = -\ 0.83\ V\ vs\ NHE \tag{3.14}$$

can be induced at both extremities of a conducting object by bipolar electrochemistry if, in a first approximation, the applied electric field induces a polarization potential ΔV between the two extremities of the object that is superior to the difference of the formal potentials of the involved redox couples, ΔV_{min} = 2.06 V (see section 1.2.). As shown by Equations 3.13 and 3.14, these reactions involve pH changes, the oxidation of water produces an acidic gradient whereas water reduction produces an alkaline gradient. In order to directly visualize the phenomenon, we carried out a proof-of-principle experiment in a cell containing a pH indicator, as it was proposed by Arora *et al.*[303] The cell was composed of two feeding electrodes and one carbon disc in the center, which acted as a BE. In this experiment the carbon disc diameter d is 6 mm and the electric field value $\mathscr{E}$ is equal to 8.1 V cm^{-1}. Figure 3.31b shows the pH gradients at the vicinity of the feeder electrodes and the BE. The color changes at the feeding anode and cathode, are due to reactions 3.13 and 3.14, respectively, which are expected to occur at this potential value (E_{imp} = 19 V). Using Equation 1.4, ΔV is found to be equal to 4.9 V, a value that is superior to the thermodynamic threshold of 2.06 V and thus allows half-reactions 3.13 and 3.14 to occur at both extremities of the BE. Strong pH variations are also observed at the extremity the BE. These pH changes are due to water oxidation (reaction 3.13) at the anodic pole and the simultaneous water reduction (reaction 3.14) at the cathodic pole that generate acid (pink color) and alkaline (purple color) gradients, respectively. Based on this experiment, which shows clearly that pH can be controlled at the reactive pole of BEs, the indirect bipolar electrodeposition triggered by pH changes becomes straightforward, as depicted in Figure 3.31a.

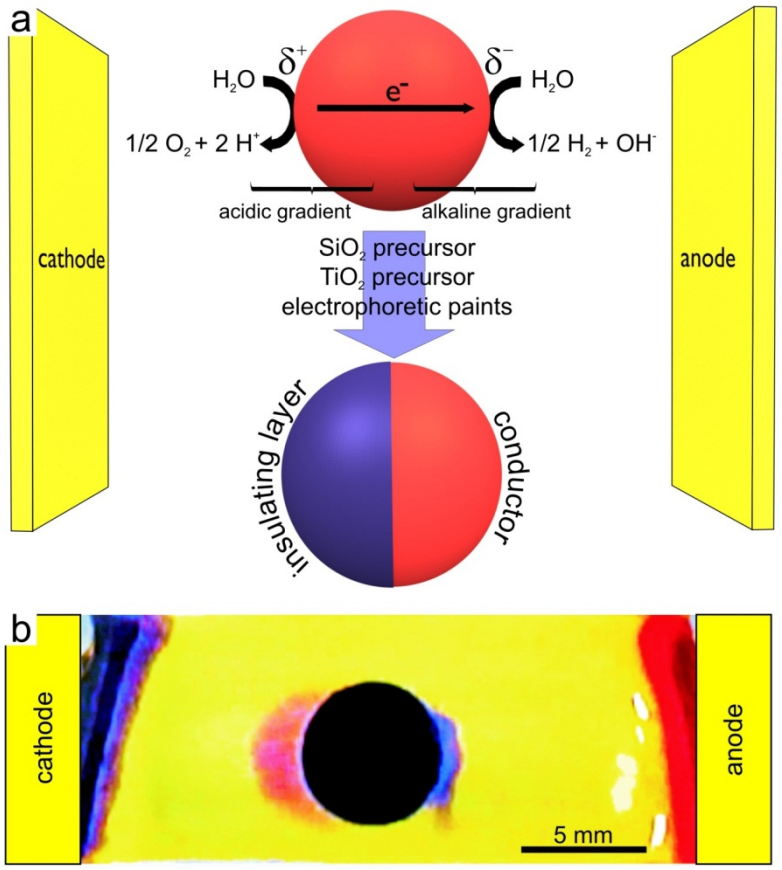

Figure 3.31. Principle of the pH-triggered bipolar electrodeposition. a) Scheme of the reactions. b) pH evolution in the vicinity of a BE visualized by using a universal pH indicator. Blue corresponds to a basic pH and pink corresponds to acid pH.

3.6.4.1. Deposition of silica and silicone

The "sol-gel" terminology is commonly used to describe a class of processes in which a solid phase is formed through gelation of a colloidal suspension (sol).[304] The first developed and probably the most used sol-gel processes are based on the polymerization of silicon monomers. In such procedures, a sol is first formed by the hydrolysis of an alkoxysilane precursor (n = 1-3, R is a general organic group and R' an alkyl group):

$$R_nSi(OR')_{4-n} + 4\text{-}n\ H_2O \rightarrow R_nSi(OH)_{4-n} + 4\text{-}n\ R'OH \quad (3.15)$$

Polycondensation of the hydrolyzed precursor, catalyzed by hydroxyl ions, can then be achieved by increasing the pH:

$$2\ R_nSi(OH)_{4-n} \rightarrow R_n(OH)_{3-n}Si\text{-}O\text{-}Si(OH)_{3-n}R_n + H_2O \quad (3.16)$$

This polymerization leads to the final polysiloxane material. Changing the functional groups R and their number allows controlling the reticulation degree and the material properties. Working with

various precursors at the same time is also possible and allows to the synthesis of a large variety of polysiloxane materials ranging from silica, using a precursor like tetraethoxysilane (TEOS), to much more sophisticated materials which can possess very different chemical and physical properties.

For these experiments, two sols were used. The first one was composed of 1 g of TEOS (see top of Figure 3.32a), 6 mL of ethanol, 6 mL of an aqueous solution of 0.1 M $NaNO_3$ and 72 μL of 0.1 M HCl. The second one was composed of 1 g of methyltrimethoxysilane (MTMOS) (see bottom of Figure 3.32a), 10 mL of methanol, 10 mL of an aqueous solution of 0.1 M $NaNO_3$ and 120 μL of 0.1 M HCl. They were stirred for few hours for the hydrolysis to occur (reaction 3.15), and were used directly as deposition bathes. Several GC particles (with diameters ranging from 630 to 1000 μm, see inset of Figure 3.32b) were placed in the reaction compartment of a PDMS cell similar to the one shown in Figure 3.19c. The two membranes are spaced by 2 cm and the outer electrodes are separated by 2.8 cm (V_r ≈2 mL). The electrode compartments were filled with mQ water. 300 V during 40 s and 400 V during 1 min were imposed for the modification with TEOS and MTMOS respectively. After the modification the beads were carefully taken out with tweezers and rinsed.

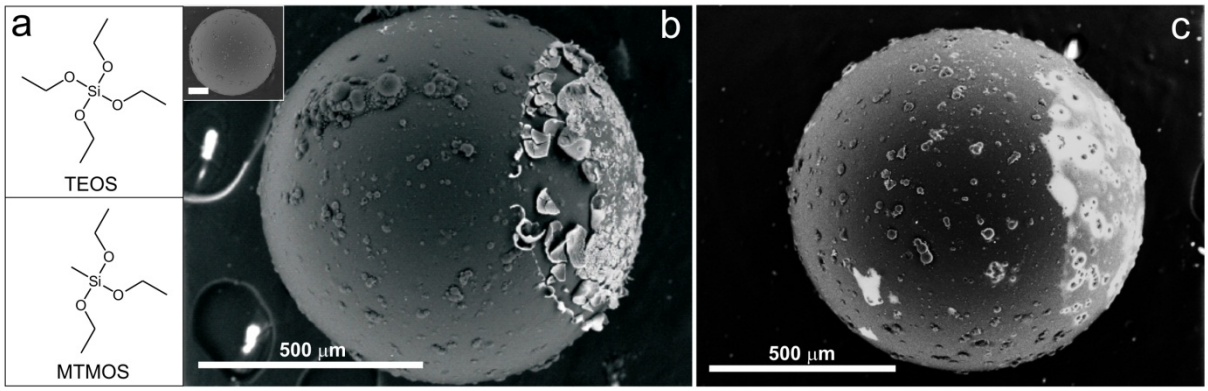

Figure 3.32. Bipolar electrodeposition of silica and silicone on glassy carbon beads. a) Molecular structure of the two sol-gel precursors used. Top: tetraethoxysilane (TEOS) and bottom: methyltrimethoxysilane (MTMOS). b) SEM picture of a GC bead modified with silica using a TEOS based sol-gel. Inset: SEM picture of an unmodified GC bead (the scale bar equals 200 μm). c) SEM picture of a GC bead modified with a silicone using a MTMOS based sol-gel.

Polycondensation occurs at the cathodic pole of the bipolar electrode, where the pH at the interface is strongly increased. The SEM micrograph in Figure 3.32b, shows a sub-millimeter carbon bead which has been modified using an electric field of 107 V cm^{-1} and a sol containing the TEOS precursor. The silica modification is clearly visible as the brightest part of the Janus object. The cracks present on the deposit are due to the bad adherence and poor flexibility of the silica material on such a surface. As mentioned above, these properties that can be tuned by controlling the polysiloxane reticulation degree (by adding functional groups R to the precursor, see reaction 3.16). Figure 3.32b

shows a similar bead modified in the same conditions than previously but using a methyltrimethoxysilane (MTMOS) precursor. The methyl group on the silicon restricts the polycondensation, which leads to a less reticulated polysiloxane with a higher flexibility than silica that covers the substrate more smoothly (Figure 3.32c).

3.6.4.2. Deposition of titanate and titanium dioxide

Other types of materials than those based on silicon can be electrodeposited by a mechanism involving a pH change. Because of the importance of TiO_2 in major fields such as photovoltaics[305] or water splitting[306] we chose to work on the bipolar electrochemical preparation of Janus objects containing a TiO_2 part. Ohya *et al.* reported the preparation of a stable transparent titanate colloidal solution by mixing Ti(IV) tetraisopropoxide (TTIP) and tetramethylammonium hydroxide (TMAOH).[307] This solution contains colloids of layered poly-Ti(IV)oxoacid species stabilized by the TMA^+ bulky counter ions. The solution remains clear and stable and can be stored at room temperature for long periods of time. It forms amorphous precipitates when alkali ions such as Na^+ and K^+ are added or when the pH of the solution is lowered. This solution can be used as a bath for the anodic deposition of titanate films.[308]

For the preparation of the titanate bath, 0.355 g of TTIP was added to 25 mL mQ water. The hydrolysis of TTIP instantaneously occurs, following the reaction:[307]

$$m\ Ti(OPr^i)_4 + (2m+1)\ H_2O \rightarrow H_2Ti_mO_{2m+1} + 4m\ Pr^iOH \qquad (3.17)$$

generating white precipitates of polymeric titanic acids. 0.453 g of TMAOH was then added to the mixture for the following acid-base reaction to occur:[307]

$$H_2Ti_mO_{2m+1} + 2\ Me_4N^+OH^- \rightarrow [Me_4N^+]_2\ [Ti_mO_{2m+1}{}^{2-}] + H_2O \qquad (3.17)$$

which generates the colloidal layered poly-Ti(IV)oxoacid species. The solution was sonicated for 30 min and stirred during hours until it became fully transparent. This bath was directly used for bipolar electrodeposition, with a similar cell and procedure than the one used for silica modification (section 3.6.4.1.). During bipolar electrodeposition, the decrease of pH produced by the water oxidation at the BE anodic pole (reaction 3.13) induces the following cation exchange for the poly-Ti(IV)oxoacids:

$$[Me_4N^+]_2\ [Ti_mO_{2m+1}{}^{2-}] + 2\ H^+ \rightarrow [H^+]_2\ [Ti_mO_{2m+1}{}^{2-}] + 2\ Me_4N^+ \qquad (3.18)$$

leading to the precipitation of the titanate film at the surface of the anodic pole.

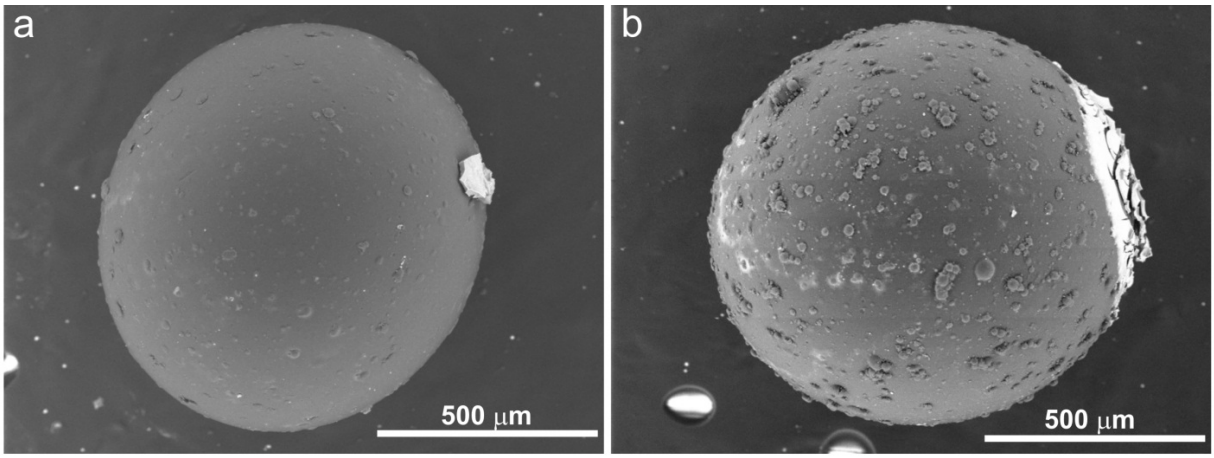

Figure 3.33. Bipolar electrodeposition of titanate on carbon beads. a) SEM picture of a GC bead modified with titanate using an electric field of 71 V cm^{-1}. b) SEM picture of a GC bead modified with titanate using an electric field of 214 V cm^{-1}.

The bipolar electrodeposition was carried out using two electric field values $\mathscr{E}$. First experiments were carried out with $\mathscr{E}$= 71 V cm^{-1}, a typical resulting asymmetric object is shown in Figure 3.33a, which shows a small titanate deposit at one extremity of the particle. As it is clearly demonstrated in Figure 3.33b, the use of a higher electric field value, in this case $\mathscr{E}$= 214 V cm^{-1}, leads to bigger deposits which cover a more important area on the GC particle. This demonstrates again that when playing with the two crucial parameters of Equation (1.4), *i.e.* the characteristic dimensions of the objects and the applied external voltage, one can control the portion of the modified area on the particles.

Since it is known that amorphous titanate can be converted into crystalline TiO_2 by calcination,[309] we tested this on our deposits. In order to collect as much powder as possible for the X-ray diffraction (XRD) analysis, the bipolar electrodeposition was carried out as previously described on 1 cm long carbon-doped polycarbonate sheets in a PDMS cell (similar to the one shown in Figure 3.19c) with two membranes spaced by 2 cm and imposing 22 V between the outer electrodes, separated by 2.8 cm, during 12 min. The deposits present on two modified sheets were recovered as a powder by scratching, and were heated at 450 °C during 4 hours. After the calcination, the powder was collected for XRD analysis. Figure 3.34 presents the obtained diffractogram. The characteristic TiO_2 anatase peaks are clearly present, demonstrating that the calcination of the titanate deposit leads to TiO_2 with an anatase crystalline structure. A XRD control analysis on an unmodified polycarbonate sheet revealed the unattributed peak at 28° to be a crystalline component coming from the substrate. These preliminary results are promising since they open the way for the bulk synthesis of APs modified with crystalline TiO_2.

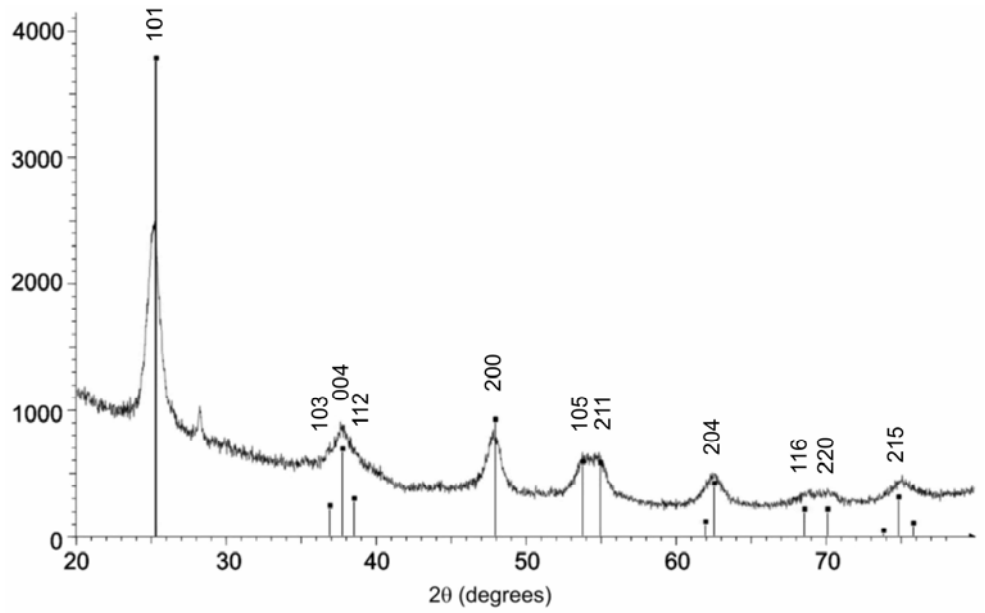

Figure 3.34. X-ray diffraction spectrum of TiO_2 after calcination. The positions of TiO_2 anatase peaks are shown by vertical lines.

3.6.4.3. Deposition of electrophoretic deposition paints

Even though EDPs have been widely used for a long time in car,[297] tin and can industries[310] as corrosion protection layers, a new type of application emerged recently, because they can be used as efficient matrices for the encapsulation of biomolecules.[301-312] The anodic EDP that was used in this work (Resydrol AY498w/35WA), is a mixture of micellar polyacrylates. Due to the presence of carboxylate groups, the water-soluble form of the polymer is negatively charged. As shown by Figure 3.35a, a pH drop induced by water oxidation at the anodic pole of the BE (reaction 3.13) leads to neutralization of the carboxylate groups and precipitation of the polymer on the surface of the bead.

Prior to use, Resydrol was diluted ten times in mQ water and used for bipolar electrochemistry as is. The bipolar electrodeposition was realized with the same cell and a similar procedure than the one used for silica modification (section 3.6.4.1.) with E_{imp} = 600 V ($\mathscr{E}$ = 71 V cm^{-1}) during 20 s. Figure 3.35b shows a SEM picture of the swowman-like asymmetric structure obtained by modifying a GC bead with EDP. The reflectivity contrast between the two materials is revealed by the optical micrograph presented in Figure 3.35c. In all these proof-of principle experiments, modifications triggered by pH were achieved at the macro- and sub-millimeter scale. We show now that this strategy can be transposed to much smaller particles using our new technology (see section 3.6.1.).

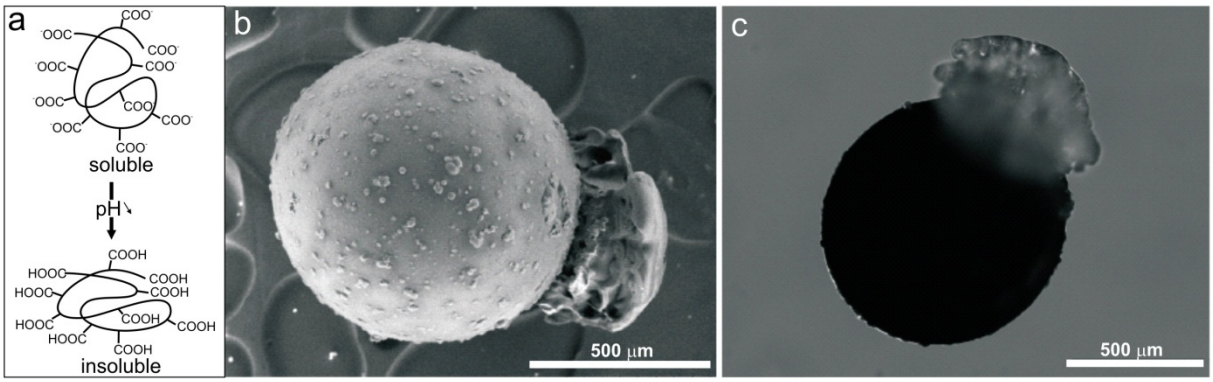

Figure 3.35. Bipolar electrodeposition of an electrophoretic deposition paint on carbon beads. a) Deposition mechanism of Resydrol EDP. b) SEM picture of a GC bead asymmetrically modified by EDP. c) Optical micrograph of a GC bead asymmetrically modified by EDP.

Two types of metal particles, amorphous Pt (Figure 3.36a) and spherical Ni (Figure 3.36c), were used. In order to ensure a good dispersion and to avoid the motion of the particles during the experiment, the dispersion viscosity was increased using a water-based gel. First, the agarose-based hydrogel was prepared by mixing 10 mg of agar, 250 mL of Resydrol, 2.25 mL of water and 5 mg of Pt or 9 mg of Ni micropowders in a glass tube and following the procedure used for the modification of 20-50 μm GC beads described in section 3.6.2.2. The gel was inserted into the reaction compartment of a PMMA/polypropylene cell similar to the one shown in Figure 3.19b, with two membranes spaced by 1 cm and the outer electrodes separated by 2 cm (V_r ≈3 mL). Ethanol cooled for 1 min in liquid nitrogen was then added to the electrode compartments. Voltage biases of 2 kV (for Pt particles) or 2.5 kV (for Ni particles) were imposed for one minute. After modification, the gel was removed from the reaction compartment, inserted in an Erlenmeyer flask and diluted with 50 mL of mQ water. It was then heated from below with a heat gun until bubbles on the glass walls developed and particles sedimentated at the bottom of the flask. The hot mixture is then centrifuged at 3000 rpm for 2 min. After centrifugation, almost all the supernatant is taken out and the beads are redispersed in 50 mL of mQ water, sonicated and centrifuged again for 2 min at the same speed. The modified particles were finally dispersed in a small volume of water for conservation.

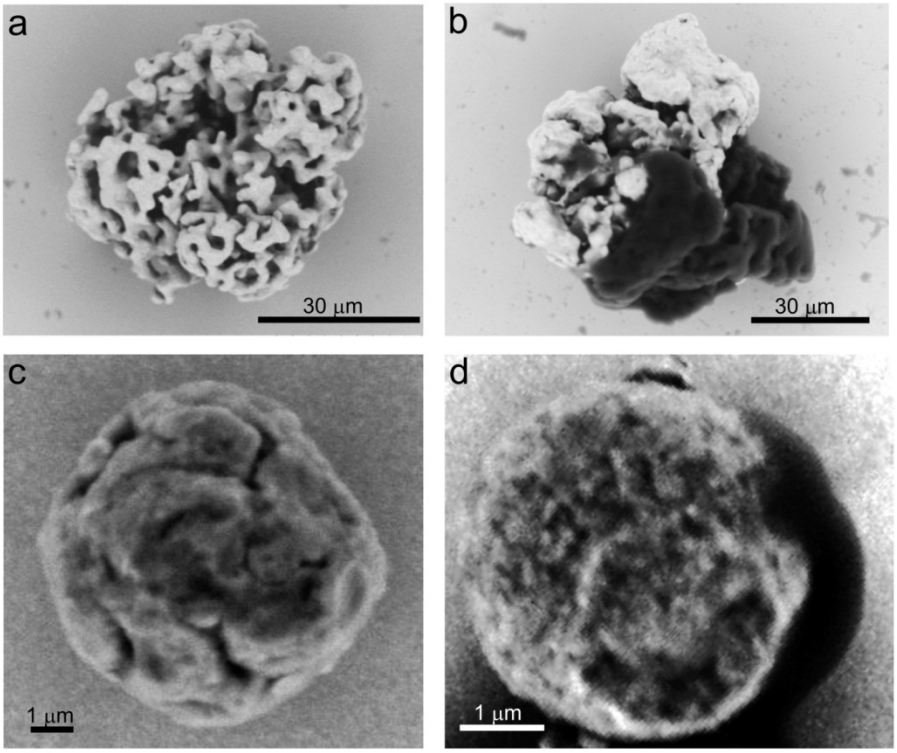

Figure 3.36. Metal microparticles asymmetrically modified with electrophoretic deposition paint by bipolar electrochemistry. a) SEM picture of an unmodified amorphous Pt particle. b) SEM picture of an amorphous Pt particle modified with EDP. c) SEM picture of an unmodified spherical Ni particle. d) SEM picture of a spherical Ni particle modified with EDP.

The modification of Pt particles (Figure 3.36a) leads to Janus-type Pt particles with an EDP part as it is shown in Figure 3.36b, where the darkest part is the EDP deposit capping the Pt particle. One can easily imagine interesting applications for these particles in heterogeneous catalysis in double phase systems.[44,43] Finally, Ni spherical particles with a diameter of a few micrometers (Figure 3.36c) were also modified with EDP to generate magnetic JPs, as it is demonstrated Figure 3.36d. As expected from Equation 1.4., the EDP deposit is much smaller in this case. A possible application for these objects is to use them as magnetic swimmers that could be used for drug delivery or cargo transport in microfluidic chips (see section 4.1.3.).

3.6.5. Trapping matrices

The bulk production of bicolored JPs is attracting a huge interest since these objects could be used as pixels for new technologies of colored electrophoretic screens (see section 3.2.2.1.) or sensors.[60] Due to their porosity, the previously deposited materials (silica, titanate and EDP, see section 3.6.4.) are also known to be very efficient for trapping various types of substrates.[300-302] Optically, the as-deposited silica and titanate layers were found to be transparent whereas EDP deposits exhibited a

grey color. In order to obtain a series of bicolored Janus objects, we decided to use the encapsulating properties of silica, titanate and EDP deposited by bipolar electrochemistry for trapping pigments, dyes and NPs. The two pathways shown in Figure 3.37 were used to trap colored compounds within the porous matrices. The first strategy involves two steps and consists in *i)* deposing the entrapping layer on the conducting particle and *ii)* infiltrating the layer with the colored compound. The second approach only requires one step as it consists in trapping the colored compound while the matrix grows during bipolar electrodeposition.

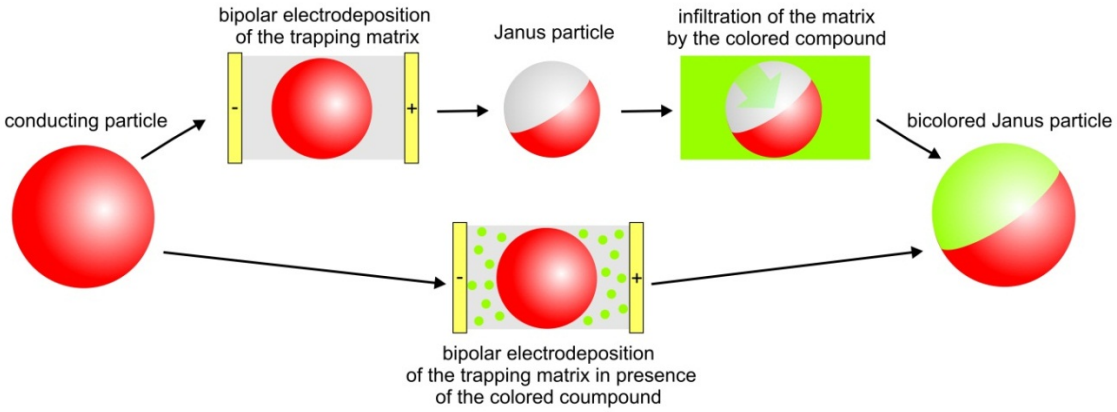

Figure 3.37. Scheme showing two possible pathways for synthesizing bicolored Janus particles, using spherical particles as an example.

First, black/white Janus objects were obtained by bipolar electrodeposition of titanate on carbon rods in the presence of alumina NPs having an average size of 50 nm. In a typical experiment, 1.8 g of alumina NPs were added to 1.5 mL of the titanate bath (see section 3.6.4.2. for the bath preparation). This mixture was inserted between the two membranes of a PDMS cell (similar to the one shown in Figure 3.19c) spaced by 2 cm, the feeder electrodes being separated by 2.5 cm. The graphite rod was located at the bottom of this compartment and mQ water was then added into the electrode compartments. 300 V were applied for 2 min and the rod was then extracted from the cell and washed with mQ water. The photograph a of Table 3.2 shows that this procedure yields graphite rods with a strongly opaque white color at the anodic pole, which is due to the encapsulation of the Al_2O_3 NPs into the transparent titanate layer. A dye infiltration step can be used to color the hybrid titanate-Al_2O_3 coating. This was achieved by dipping the modified rod for three minutes into a solution of rhodamine 101 in EtOH and washing it several times with water and ethanol. The resulting black/purple Janus object is shown in the photograph b of Table 3.2. The colored part revealed a strong fluorescence under a UV-lamp, which is clearly observable in the inset of this picture.

coating composition		photograph
matrix	colored compounds	
titanate	Al_2O_3 NPs	
titanate	Al_2O_3 NPs + rhodamine 101	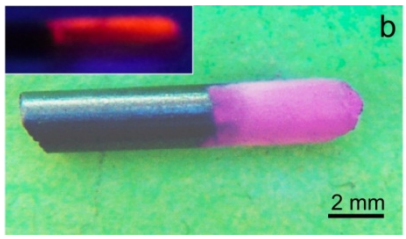
silica	fluorescein	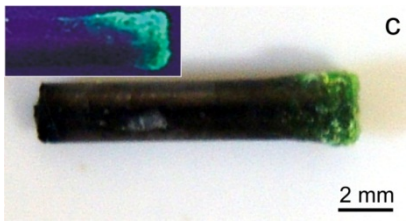
EDP	AuNPs	

Table 3.2. Bicolored Janus rods obtained by entrapping colored compounds into matrices by bipolar electrodeposition. The insets of the photographs b and c show the fluorescence of the rod extremities revealed under the UV-lamp.

Instead of using a chromophore infiltration step, the molecule can be directly trapped inside the matrix during the bipolar electrodeposition, following the bottom scheme of Figure 3.37. We illustrated this possibility with fluorescein entrapped in a silica coating. For these experiments, 1 mL of the TEOS-based sol (see section 3.6.4.1.) and 100 µL of a fluorescent solution (3 mg of fluorescein in 1 mL of water) were introduced into a plastic cell without membranes (the outer electrodes being separated by 2.5 cm). The graphite rod was located at the bottom of the cell between the electrodes and a potential of 22 V was applied. After the experiment, the rod was taken out and washed several times with water. The resulting black/green Janus object, as well as its fluorescence are shown in the photographs c of Table 3.2.

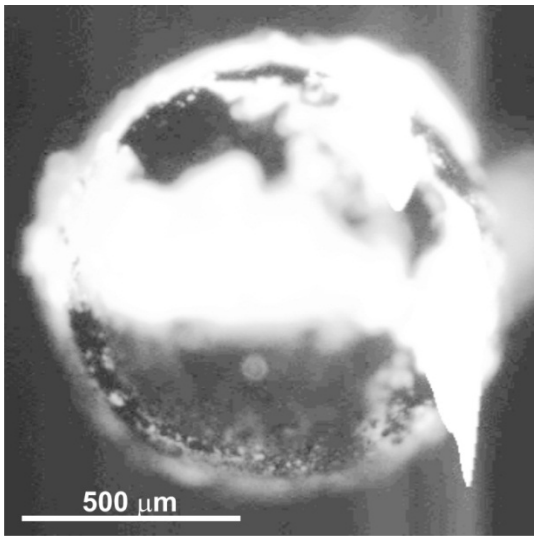

Figure 3.38. Fluorescence micrograph of a sub-millimeter glassy carbon bead modified with a silica matrix trapping TiO_2 NPs and rhodamine 101.

Anisotropic sub-millimeter sized JPs with one fluorescent part were also synthesized (Figure 3.38). In these experiments, TiO_2 NPs were first trapped in a silica matrix, which was finally infiltrated by a fluorophore. In a typical experiment, 0.2 g of TiO_2 powder (anatase, < 25 nm), were added to 2 mL of the TEOS-based sol (see section 3.6.4.1.). The reaction compartment of the cell (the same like the one used for the synthesis of black/white Janus rods) was filled with this mixture and few GC beads were placed at the bottom of this compartment. The electrode compartments were filled with water and a potential of 400 V was imposed. After modification, the beads were carefully taken out with tweezers and rinsed with mQ water. For the chromophore infiltration, the beads were dipped for a few minutes in a rhodamine 101 solution in ethanol. Figure 3.38 shows a fluorescence micrograph of the GC bead modified by the described procedure. Even if the fluorescent area is clearly localized on one half of the bead, some parts in this area do not show luminescence. This fact is surely due to cracks present in the silica matrix, as previously discussed in section 3.6.4.1.

Finally, AuNPs were encapsulated in EDP by deposing the polymer from a mixture containing AuNPs (Figure 3.39a), synthesized by the Turkevich method (experimental details are given in appendix 4). For these experiments, 0.2 mL of the AuNPs colloidal solution and 1 mL of the EDP bath (see section 3.6.4.3.) were mixed and inserted into the cell (the same like the one used for synthesizing black/green Janus rods). The graphite rod was placed at the bottom of the cell between the electrodes and a potential of 22 V was applied. After the experiment, the rod was removed and washed several times with water. One typical substrate is shown in the photograph d of Table 3.2. The pink color at one extremity of the rod is attributed to the plasmon absorption of the ≈15 nm

AuNPs (λ around 600 nm) incorporated in the matrix. AuNP aggregates located at the outer surface of the matrix are observable by SEM as it is shown in Figure 3.39b.

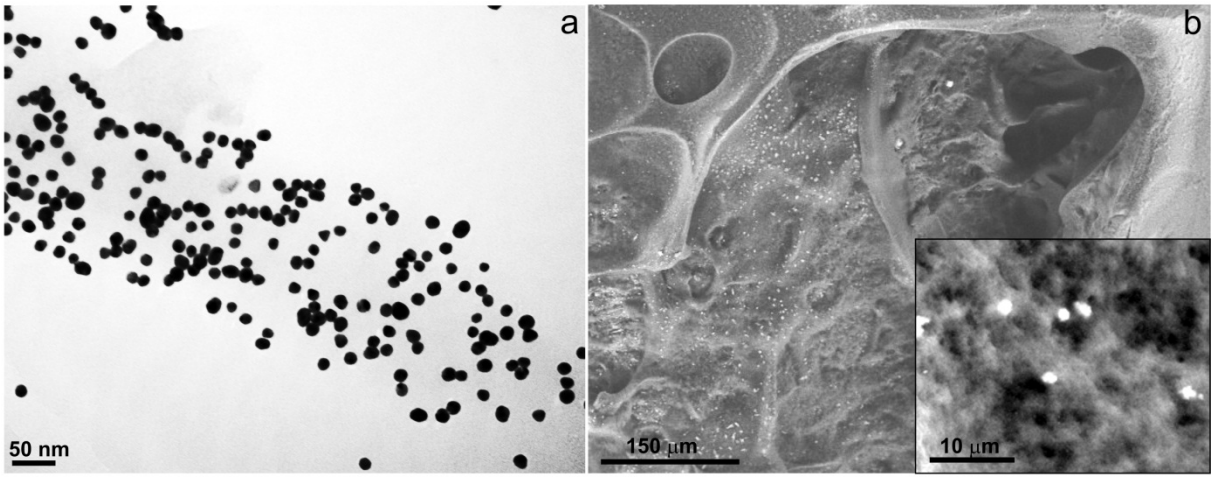

Figure 3.39. Gold nanoparticles in electrophoretic deposition paint. a) TEM picture of the AuNPs before their encapsulation in EDP. b) SEM picture showing the EDP deposit on the object presented in the photograph d of Table 3.2. Inset: SEM picture showing a detailed view of the material.

These experiments demonstrate the utility of bipolar electrodeposition for encapsulation purposes and open the way for the synthesis of a large family of anisotropically-colored and/or fluorescent JPs, which may be of strong interest for creating e-paper pixels and for biosensing technologies. A drawback of this process lies in the weak bonding between the colored compounds at the surface when compared to SAMs, based for example on Au-S bonds (see Figure 3.28). Nevertheless high color intensities can be achieved due to the occupation of a large quantity of the colored species into the porous structures as compared to a classical SAM.

3.7. Micro- and nanostructuration

Micro- and nanostructuration of surfaces are of importance in many domains ranging from electronics to detection systems. Substrate patterning is in the majority of the cases realized by means of costly technologies and time-consuming procedures such as photolithography, scanning probe lithography,[313] soft lithography[314] or electrodeposition through templates.[315,316] In all previous sections of this chapter we discussed in detail the use of bipolar electrodeposition for the partial coating of particles. We will demonstrate now that bipolar electrodeposition can be used for the straightforward micro- and nanostructuration of conductive substrates of different sizes.

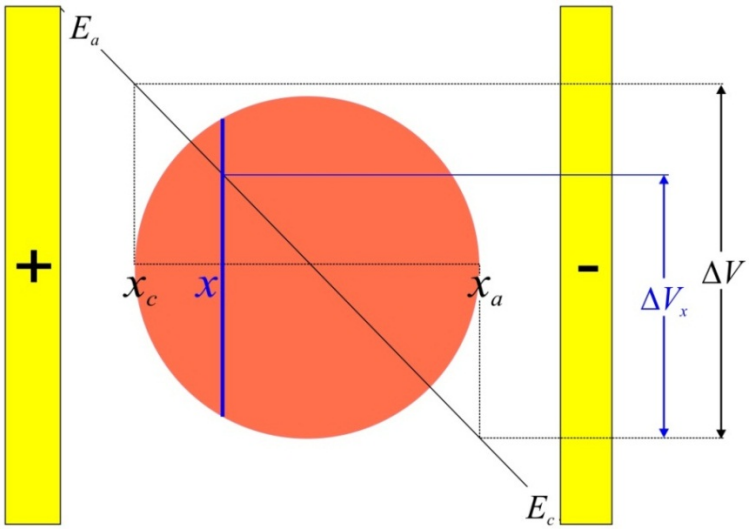

Figure 3.40. Scheme of the 2D projection of a bipolar electrode, showing the polarization potential ΔV_x arising between the points of the surface located on the vertical plane comprising x and the anodic extremity, x_a.

The polarization potential ΔV_x, represented in Figure 3.40, is related to the reactivity of the BE surface points defined by the vertical plane passing at the position x, located on the BE equatorial plane between x_a and x_c (the positions of the anodic and cathodic extremities, respectively).

The BEs of Figure 3.41 are in solutions which only contains a charged metal species which can undergo electrodeposition at its cathodic pole. The ΔV_x gradient along the BE divides its surface into two distinct areas separated by a vertical plane. In the red area of Figure 3.41a $\Delta V_x < \Delta V_{min}$ which makes the deposition of the metal impossible. For the green area, $\Delta V_x > \Delta V_{min}$ which implies that thermodynamically the metal can be deposited in this zone. The boundary between these two areas can be controlled by varying the applied electric field $\mathscr{E}$ (see section 1.2). Considering the conventional experimental conditions of bipolar electrochemistry, *i.e.* working at room temperature, no external stirring, very high electric fields, and low ionic strength in the solutions, the migration of

metal ions becomes and important component of the mass-transfer. The simplest case, depicted in Figure 3.41a, describes the deposition of metal cations such as Ag^+. The ions migrate towards the feeder cathode, and arrive "in front" of the cathodic pole of the BE, directly reaching the area where $\Delta V_x > \Delta V_{min}$. Therefore electrodeposition occurs and leads to the generation of a spherical JP.

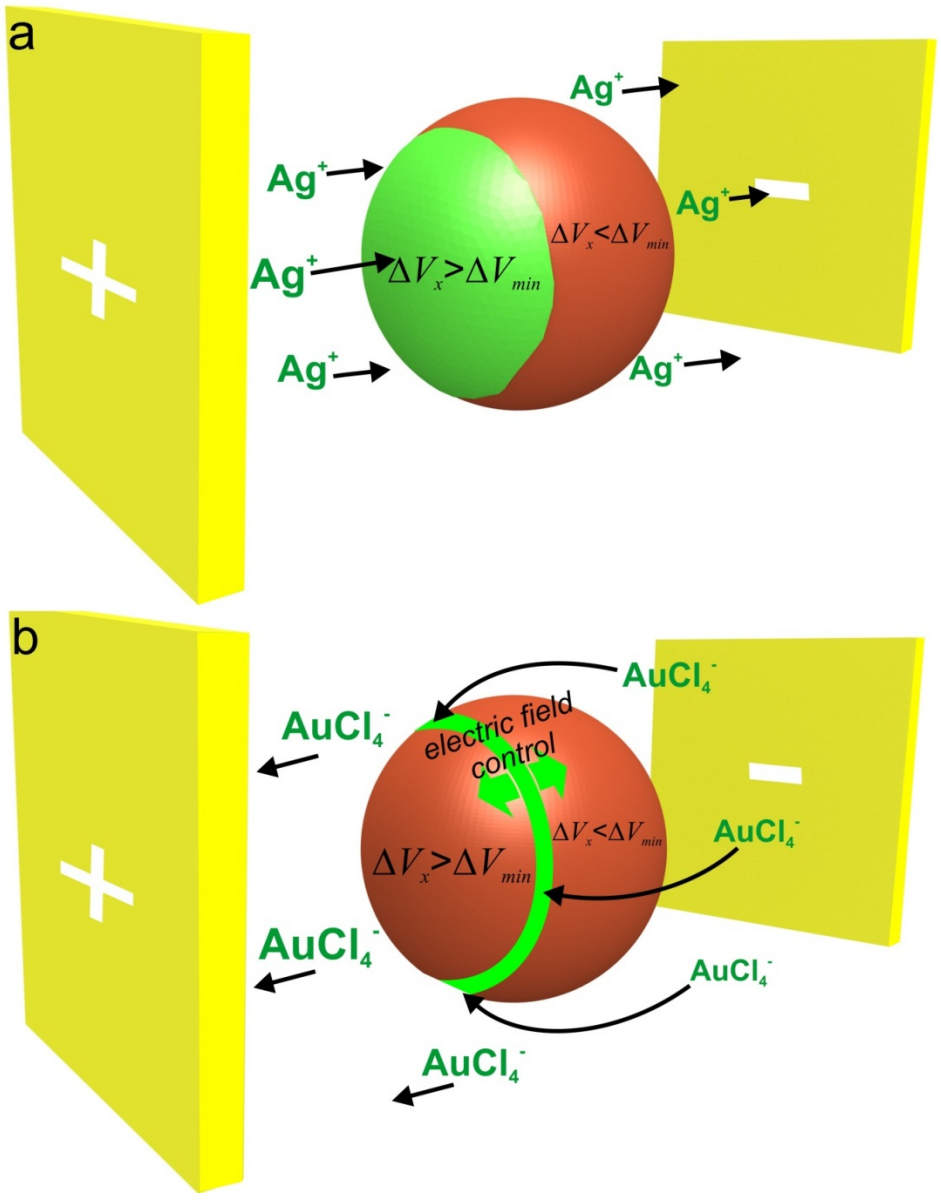

Figure 3.41. Bipolar electrodeposition of metal cations and anions on spherical bipolar electrodes, the arrows represent the migration of ions and the green surface represents the area where the reduction takes place. a) Scheme showing the reduction of Ag^+. b) Scheme showing the reduction of $AuCl_4^-$.

The case of a negatively charged metal complexes such as $AuCl_4^-$ is more complicated since in this case the direction of migration is reversed, as shown in Figure 3.41b. The metal anions migrate towards the feeder anode, pass the anodic pole of the BE and reach the cathodic pole of the particle

"from the backside". As a consequence, instead of reaching the extremity of the cathodic pole, their first contact where reduction can occur is the boundary between the cathodic and anodic zone. Depending on the overall concentration of electroactive species they are consumed in a more or less large band at this boundary. Metal ions that were present in the pole region of the cathodic area are rapidly depleted and can't be replaced because the supply is impossible due to a shadow effect. This leads to the generation of a metal ring at the boundary location. In order to qualitatively confirm this mechanism, simulations showing the hot-spots on a spherical BE during electrodeposition of a metal cation and an anion, respectively, were performed by a collaborator using Comsol Multiphysics 3.4 (see appendix 5) This will be experimentally confirmed and used in the following for the microstructuration on macroscopic and microscopic BEs.

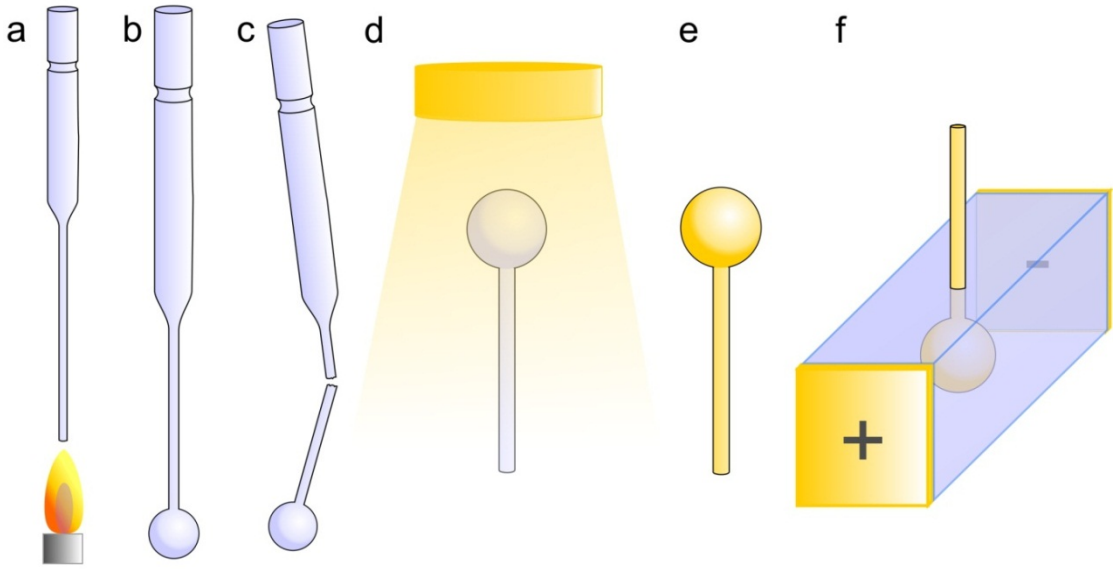

Figure 3.42. Scheme showing the process used to fabricate the gold spheres, which were used for microstructuration.

This mechanism was experimentally first tested on home-made macroscopic gold BEs, produced following the steps depicted in Figure 3.42. First, the tip of a Pasteur pipette was melted until a glass bead with a diameter of $d \approx 3$ mm was formed (step a and b in Figure 3.42). After the solidification of the bead and its separation from the rest of the pipette (step c), gold was sputtered on it by cathodic pulverization (step d and e) and the bead was directly used for the bipolar electrochemistry experiment. The bead was positioned by its shank in the middle of a cell with two feeder electrodes spaced by 2.3 cm (step f) and containing a solution of the metal salt (from 5 to 2 mM). Bipolar electrodeposition was performed for several minutes (typically five minutes) until the metal deposit could be observed with naked eyes. Photographs of various metal deposits, obtained using different experimental conditions are shown in Figure 3.43. The photographs of the beads were taken with

their shanks at the back, in such a way that it does not appear on the final picture. In order to avoid reflection effects on the gold surface as much as possible, the photographs were taken in a white box. The black spots in the middle of each picture correspond to the camera reflection on the bead, a phenomenon that cannot be avoided.

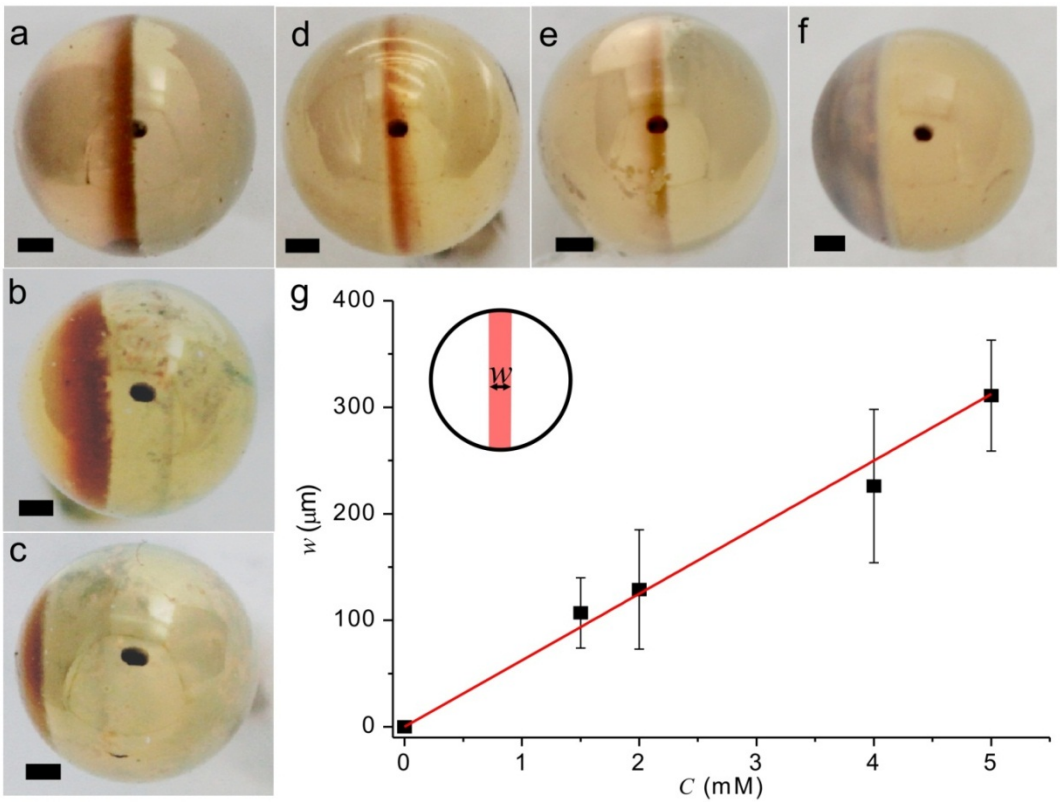

Figure 3.43. Controlled electrogeneration of Au rings on spherical bipolar electrodes (d ≈3 mm). a-f) Photographs of Au beads modified by bipolar electrodeposition using different sets of experimental conditions (the scale bars equal 500 µm). a) 5 mM $HAuCl_4$, 12 V. b) 5 mM $HAuCl_4$, 8 V. c) 5 mM $HAuCl_4$, 7 V. d) 4 mM $HAuCl_4$, 12 V. e) 2 mM $HAuCl_4$, 12 V. f) 5 mM $AgNO_3$, 9 V. g) graph showing the variation of the gold ring width w as a function of $HAuCl_4$ concentration C.

The two oppositely charged metal salts $AuCl_4^-$ and Ag^+ were used in these experiments. Apparently, the use of $AuCl_4^-$ induces the formation of a gold ring around the sphere (Figure 3.43 a-e) while Ag^+ produces a hemispherical deposit (Figure 3.43 f). This observation presents an experimental support of the hypothesis shown in Figure 3.41, which was furthermore confirmed by the simulation presented in appendix 5. Figure 3.43 a-c were obtained using exactly the same conditions (5 mM $HAuCl_4$), but using three different electric field strengths $\mathscr{E}$, by applying 12, 8 and 7 V, respectively, between the feeder electrodes. One can clearly see that the potential decrease leads to a displacement of the generated gold from the center of the BE (for high $\mathscr{E}$) towards the extremity of the cathodic pole (for the small $\mathscr{E}$). This is directly related to a decrease of the cathodic pole area

with decreasing polarization (see section 1.2.). This phenomenon allows to control the location of the ring on the BE and in the following we furthermore show that the ring width *w* can be tailored. The deposition time was found not to influence significantly *w*, but an intensification of the ring color was observed as a function of time which suggests an increase of the deposit thickness. The photographs of Figure 3.43a, d and e show gold beads obtained applying 12 V and using decreasing $AuCl_4^-$ concentrations, from 5 mM to 2 mM. One can clearly see a decrease of *w* with decreasing $AuCl_4^-$ concentration, the two parameters being proportional, as demonstrated by the graph in Figure 3.43. These results show for the first time that bipolar electrodeposition of negatively-charged metal species can be used for the controlled micro-structuration of conductive substrates. In Figure 3.44, this phenomenon is used for the generation of more complex structures.

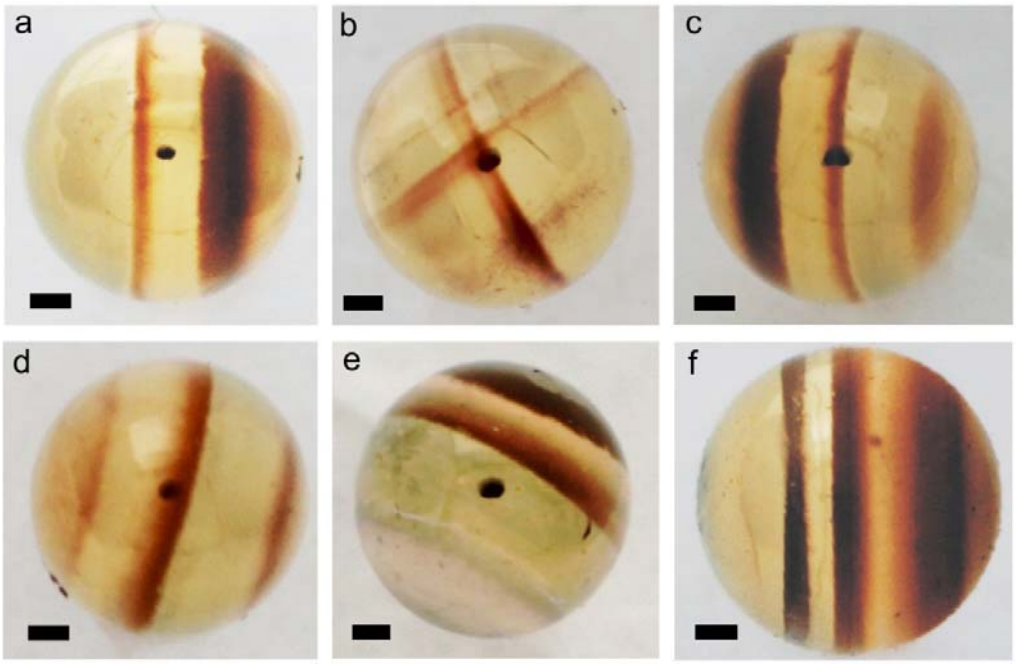

Figure 3.44. Microstructured gold beads. a-f) Photographs of gold beads modified by one or several bipolar electrodeposition runs (the scale bars equal 500 μm). a) 5 mM $HAuCl_4$, 7 V and 15 V. b) 5 mM $HAuCl_4$, 12 V and 12 V, the bead has been turned with an angle $\phi \approx 90°$ between the two runs. c) 5 mM $HAuCl_4$, 8 V, 15 V and 7 V, the bead has been turned with an angle $\phi \approx 180°$ between the second and the third run. d) 5 mM $HAuCl_4$, 12 V, 8 V and 7 V, the bead has been turned with an angle $\phi \approx 180°$ between the second and the third run. e) 5 mM $HAuCl_4$, 8 V , 12 V and 5 mM $AgNO_3$ 9 V, the bead has been turned with an angle $\phi \approx 180°$ between the second and the third run. f) 20 mM $HAuCl_4$, 15 V.

The series of photographs shown in Figure 3.50 has been obtained by modifying the experimental conditions, namely the electric field strength and the number of electrodeposition runs. Typically, two gold rings can be produced on the cathodic pole by two runs with different values of potential (Figure 3.44a). The ring can be generated at any place on the bead and turning the bead around its

shank between two runs allows the generation of rating gold crosses (Figure 3.44b) or more complex structures. In an analogue manner, three runs were used for creating three gold rings (Figure 3.44 c and d). For generating the structure shown in Figure 3.44e, which has two gold rings at one extremity and one silver hemispherical coating at the other one, both mechanisms of Figure 3.41 were employed. The two gold rings were obtained by performing two runs in the $HAuCl_4$ solution and the silver coating with one run in the $AgNO_3$ solution. The barcode structure shown in Figure 3.44f is the only one that has been obtained in just one run. This experiment was performed with a concentration of gold salt four times higher than in all the other experiments (C = 20 mM) and in this case, the mechanism which produces the rings is different from the one previously discussed. Since such a salt concentration is high enough to partially screen migration phenomena, the mechanism of Figure 3.41b is not any more valuable and the deposition of gold occurs over the whole cathodic pole, certainly controlled by the diffusion of $AuCl_4^-$ species. It is well known that metal gold electrodeposits can have different colors depending on different parameters such as their surface oxidation state, the layer porosity as well as its thickness. The existence of colored rings at the cathodic pole (right half of the bead) is a direct consequence of the porosity and thickness gradients of the deposit. The dark ring at the anodic pole is in contrast attributed to the generation of specific gold oxides which are known to have strong colors.[317] The complexity level which has been achieved in the presented experiments demonstrates strong application potential of bipolar electrodeposition for structuring conductive substrates at the microscale.

We demonstrated in section 3.6.2.2. that instead of gold rings, gold hemispheres were obtained on sub-millimeter and micrometer-sized GC beads by bipolar electrodeposition. Due to the recent interest in optical properties of metal micro- or nanorings[318] which are very attractive for sensing application[319] we tried to generate metal rings on submillimeter and micrometer GC beads. Different experimental conditions were tested in order to optimize the conditions for generating gold rings on these substrates. For an easy comparison, the discovered optimal conditions for the specific generation of JPs or ringed particles for sub-millimeter and micrometer GC beads are given in Table 3.3. The parameters reported for the synthesis of Janus particles are the one that were previously described in 3.6.2.2. For the synthesis of ringed particles, the experimental conditions were exactly the same except for the parameters reported in this table. Different factors are responsible for switching from gold Janus coatings to gold rings. First, the use of lower ionic strengths as well as a smaller C_{HAuCl4} / C_{GC} ratio should favor the ring formation, which is actually the case when looking at the conditions reported in Table 3.3. More importantly, a crucial parameter was the type of separator (see section 3.6.1.), since the yield of ring formation was found to dramatically decrease when using sintered glasses as separators instead of cation exchange membranes. This can be easily

understood based on the difference in convection rates in both configurations. As explained in section 3.6.1., sintered glass creates a stronger EOF, which induces convection and by this directs $AuCl_4^-$ ions to the cathodic pole. This decreases considerably the effect of the migration and favors the production of JPs instead of rings.

diameter	Janus particles	ringed particles
400 – 200 μm	C_{HAuCl4} = 1 mM C_{GC} = 5 mg mL^{-1} gel : ethyl cellulose separators : sintered glasses 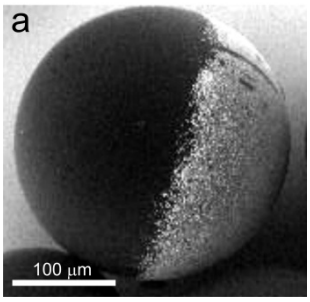	C_{HAuCl4} = 0.25 mM C_{GC} = 2.5 mg mL^{-1} gel : ethyl cellulose separators : cation exchange membrane 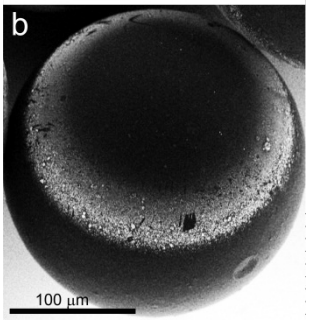
50 – 20 μm	C_{HAuCl4} = 1 mM C_{GC} = 1.2 mg mL^{-1} gel : agarose separators : sintered glasses 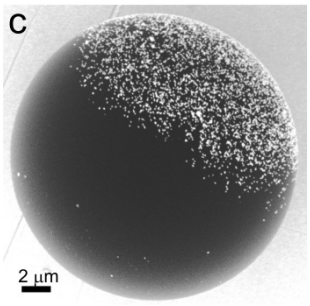	C_{HAuCl4} = 0.5 mM C_{GC} = 6.4 mg mL^{-1} gel : agarose separators : cation exchange membrane 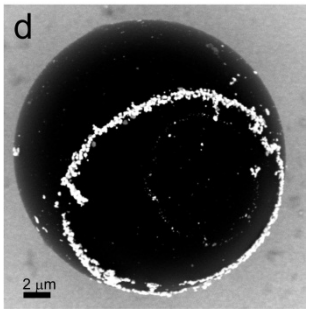

Table 3.3. Experimental conditions ($HAuCl_4$ concentration, C_{HAuCl4}; GC bead concentration, C_{GC}, gel type and used separators) for obtaining Janus particles or ringed particles, respectively, by bipolar electrodeposition of gold on GC particles of two different sizes. The corresponding structures are illustrated by SEM micrographs.

Another negatively charged metal complex, $PtCl_6^{2-}$, has been tested for the generation of ringed particles on 200-400 μm GC beads. A similar cell (PMMA/polypropylene cell with cation exchange membranes, see Figure 3.19b) than the one used for the generation of ringed gold particles (SEM picture b of Table 3.3) was used, the beads were trapped in an ethyl cellulose gel and exposed to a field of 42 kV.m^{-1}. As shown in Figure 3.45a, Pt rings were successfully obtained, which again confirms the mechanism requiring a negatively-charged species. Both SEM pictures of Figure 3.45 demonstrate that ringed particles can be obtained with relatively good yields when applying conditions described in Table 3.3. Nevertheless, it seems important to point out that the mechanism based on migration (Figure 3.41b) may be not the only mechanism responsible for the modification of the 20-40 μm GC particles, since in this case the used agarose gel may have a certain influence on

the final particle structure due to the undesired spontaneous reduction of tetrachloroaurate (previously discussed in section 3.6.2.2.).

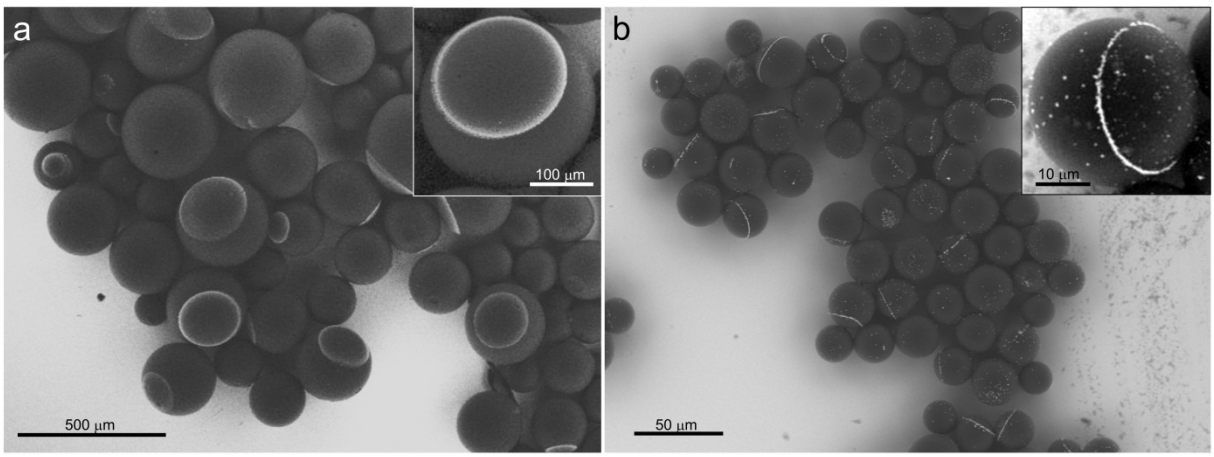

Figure 3.45. Ringed particles. a) SEM picture of GC beads with diameters ranging from 400 to 200 µm modified with a platinum ring. Inset: SEM picture a showing detailed view of one ringed particle. b) SEM picture of GC beads with diameters ranging from 50 to 20 µm modified with a gold ring. Inset: SEM picture showing a detailed view of one ringed particle.

To summarize, we have shown in this section that in the case where the mass transfer is controlled by migration, bipolar electrodeposition of negatively charged species can be very attractive for micro- and nanostructuration at different scales. This mechanism opens up many opportunities for the electrochemical design of very complex structures ranging from microstructured barcodes to optically-active nanostructures.

References

(1) Casagrande, C.; Veysié, M. *C. R. Acad. Sci. (Paris) Ser. II* **1988**, *306*, 1423.
(2) De Gennes, P. G. *Rev. Mod. Phys.* **1992**, *64*, 645.
(3) Perro, A.; Reculusa, S.; Ravaine, S.; Bourgeat-Lami, E.; Duguet, E. *J. Mater. Chem.* **2005**, *15*, 3745.
(4) Walther, A.; Muller, A. H. E. *Soft Matter* **2008**, *4*, 663.
(5) Markus B, L. *Curr. Opin. Coll. Interf. Sci.* **2009**, *14*, 356.
(6) Zhang, X. L.; Penfold, J.; Thomas, R. K.; Tucker, I. M.; Petkov, J. T.; Bent, J.; Cox, A.; Campbell, R. A. *Langmuir* **2011**, *27*, 11316.
(7) Basheva, E. S.; Kralchevsky, P. A.; Christov, N. C.; Danov, K. D.; Stoyanov, S. D.; Blijdenstein, T. B. J.; Kim, H.-J.; Pelan, E. G.; Lips, A. *Langmuir* **2011**, *27*, 2382.
(8) Caminade, A.-M.; Laurent, R.; Delavaux-Nicot, B.; Majoral, J.-P. *New J. Chem.* **2012**, *36*, 217.
(9) Liu, Y.; Zhang, G.; Niu, L.; Gan, L.; Liang, D. *J. Mater. Chem.* **2011**, *21*, 14864.
(10) Glotzer, S. C.; Solomon, M. J. *Nat. Mater.* **2007**, *6*, 557.
(11) Du, J.; O'Reilly, R. K. *Chem. Soc. Rev.* **2011**, *40*, 2402.
(12) Loget, G.; Kuhn, A. *J. Mater. Chem.* **2012**, *22*, 15429.
(13) Perro, A.; Duguet, E.; Lambert, O.; Taveau, J.-C.; Bourgeat-Lami, E.; Ravaine, S. *Angew. Chem.* **2009**, *121*, 367.
(14) Pawar, A. B.; Kretzschmar, I. *Macromol. Rapid Commun.* **2010**, *31*, 150.
(15) Kudera, S.; Carbone, L.; Carlino, E.; Cingolani, R.; Cozzoli, P. D.; Manna, L. *Physica E* **2007**, *37*, 128.
(16) Yoshida, M.; Lahann, J. *ACS Nano* **2008**, *2*, 1101.
(17) Cozzoli, P. D.; Pellegrino, T.; Manna, L. *Chem. Soc. Rev.* **2006**, *35*, 1195.
(18) Casavola, M.; Buonsanti, R.; Caputo, G.; Cozzoli, P. D. *Eur. J. Inorg. Chem.* **2008**, *2008*, 837.
(19) Yang, S.-M.; Kim, S.-H.; Lim, J.-M.; Yi, G.-R. *J. Mater. Chem.* **2008**, *18*, 2177.
(20) Teranishi, T.; Saruyama, M.; Kanehara, M. *Nanoscale* **2009**, *1*, 225.
(21) Wurm, F.; Kilbinger, A. F. M. *Angew. Chem. Int. Ed.* **2009**, *48*, 8412.
(22) Mao, Z.; Xu, H.; Wang, D. *Adv. Funct. Mater.* **2010**, *20*, 1053.
(23) Jiang, S.; Chen, Q.; Tripathy, M.; Luijten, E.; Schweizer, K. S.; Granick, S. *Adv. Mater.* **2010**, *22*, 1060.
(24) Niu, Z.; He, J.; Russell, T. P.; Wang, Q. *Angew. Chem. Int. Ed.* **2010**, *49*, 10052.
(25) Lee, K. J.; Yoon, J.; Lahann, J. *Curr. Opin. Coll. Interf. Sci.* **2010**, *16*, 195.
(26) Lattuada, M.; Hatton, T. A. *Nano Today* **2011**, *6*, 286.
(27) Xu, H.; Erhardt, R.; Abetz, V.; Müller, A. H. E.; Goedel, W. A. *Langmuir* **2001**, *17*, 6787.
(28) Binks, B. P.; Fletcher, P. D. I. *Langmuir* **2001**, *17*, 4708.
(29) Nonomura, Y.; Komura, S.; Tsujii, K. *Langmuir* **2004**, *20*, 11821.
(30) Aveyard, R. *Soft Matter* **2012**, *8*, 5233.
(31) Jiang, S.; Granick, S. *J. Chem. Phys.* **2007**, *127*, 161102.
(32) Hirose, Y. *J. Chem. Phys.* **2007**, *127*, 054707.
(33) Ruhland, T. M.; Gröschel, A. H.; Walther, A.; Müller, A. H. E. *Langmuir* **2011**, *27*, 9807.
(34) Park, B. J.; Brugarolas, T.; Lee, D. *Soft Matter* **2011**, *7*, 6413.
(35) Adams, D. J.; Adams, S.; Melrose, J.; Weaver, A. C. *Colloids Surf., A* **2008**, *317*, 360.
(36) Cheung, D. L.; Bon, S. A. F. *Soft Matter* **2009**, *5*, 3969.
(37) Glaser, N.; Adams, D. J.; Böker, A.; Krausch, G. *Langmuir* **2006**, *22*, 5227.
(38) Sahoo, J. K.; Tahir, M. N.; Hoshyargar, F.; Nakhjavan, B.; Branscheid, R.; Kolb, U.; Tremel, W. *Angew. Chem. Int. Ed.* **2011**, *50*, 12271.
(39) Takahara, Y. K.; Ikeda, S.; Ishino, S.; Tachi, K.; Ikeue, K.; Sakata, T.; Hasegawa, T.; Mori, H.; Matsumura, M.; Ohtani, B. *J. Am. Chem. Soc.* **2005**, *127*, 6271.
(40) Kim, J.-W.; Lee, D.; Shum, H. C.; Weitz, D. A. *Adv. Mater.* **2008**, *20*, 3239.
(41) Tanaka, T.; Okayama, M.; Minami, H.; Okubo, M. *Langmuir* **2010**, *26*, 11732.

(42) Liang, F.; Shen, K.; Qu, X.; Zhang, C.; Wang, Q.; Li, J.; Liu, J.; Yang, Z. *Angew. Chem.* **2011**, *123*, 2427.
(43) Cole-Hamilton, D. J. *Science* **2010**, *327*, 41.
(44) Crossley, S.; Faria, J.; Shen, M.; Resasco, D. E. *Science* **2010**, *327*, 68.
(45) Walther, A.; Hoffmann, M.; Müller, A. H. E. *Angew. Chem. Int. Ed.* **2008**, *47*, 711.
(46) Yan, L.-T.; Popp, N.; Ghosh, S.-K.; Bolˆker, A. *ACS Nano* **2010**, *4*, 913.
(47) Virgilio, N.; Favis, B. D. *Macromolecules* **2011**, *44*, 5850.
(48) Berger, S.; Ionov, L.; Synytska, A. *Adv. Funct. Mater.* **2011**, *21*, 2338.
(49) Kim, S.-H.; Lee, S. Y.; Yang, S.-M. *Angew. Chem. Int. Ed.* **2010**, *49*, 2535.
(50) Synytska, A.; Khanum, R.; Ionov, L.; Cherif, C.; Bellmann, C. *ACS Appl. Mater. Interfaces* **2011**, *3*, 1216.
(51) Alexeev, A.; Uspal, W. E.; Balazs, A. C. *ACS Nano* **2008**, *2*, 1117.
(52) Park, S.; Lim, J.-H.; Chung, S.-W.; Mirkin, C. A. *Science* **2004**, *303*, 348.
(53) Walther, A.; Drechsler, M.; Rosenfeldt, S.; Harnau, L.; Ballauff, M.; Abetz, V.; Müller, A. H. E. *J. Am. Chem. Soc.* **2009**, *131*, 4720.
(54) Vanakaras, A. G. *Langmuir* **2005**, *22*, 88.
(55) Hong, L.; Cacciuto, A.; Luijten, E.; Granick, S. *Nano Lett.* **2006**, *6*, 2510.
(56) Hong, L.; Cacciuto, A.; Luijten, E.; Granick, S. *Langmuir* **2008**, *24*, 621.
(57) Chen, Q.; Whitmer, J. K.; Jiang, S.; Bae, S. C.; Luijten, E.; Granick, S. *Science* **2011**, *331*, 199.
(58) Liu, Y.; Li, W.; Perez, T.; Gunton, J. D.; Brett, G. *Langmuir* **2011**, *28*, 3.
(59) Comiskey, B.; Albert, J. D.; Yoshizawa, H.; Jacobson, J. *Nature* **1998**, *394*, 253.
(60) Takei, H.; Shimizu, N. *Langmuir* **1997**, *13*, 1865.
(61) Crowley, J. M.; Sheridon, N. K.; Romano, L. *J. Electrostat.* **2002**, *55*, 247.
(62) Nisisako, T.; Torii, T.; Takahashi, T.; Takizawa, Y. *Adv. Mater.* **2006**, *18*, 1152.
(63) Kim, S.-H.; Jeon, S.-J.; Jeong, W. C.; Park, H. S.; Yang, S.-M. *Adv. Mater.* **2008**, *20*, 4129.
(64) Yin, S.-N.; Wang, C.-F.; Yu, Z.-Y.; Wang, J.; Liu, S.-S.; Chen, S. *Adv. Mater.* **2011**, *23*, 2915.
(65) Yu, Z.; Wang, C.-F.; Ling, L.; Chen, L.; Chen, S. *Angew. Chem. Int. Ed.* **2012**, *51*, 2375.
(66) Velev, O. D.; Gangwal, S.; Petsev, D. N. *Annu. Rep. Prog. Chem., Sect. C: Phys. Chem.* **2009**, *105*, 213.
(67) Bazant, M.; Squires, T. *Phys. Rev. Lett.* **2004**, *92*.
(68) Squires, T. M.; Bazant, M. Z. *J. Fluid Mech.* **2006**, *560*, 65.
(69) Gangwal, S.; Cayre, O. J.; Bazant, M. Z.; Velev, O. D. *Phys. Rev. Lett.* **2008**, *100*, 058302.
(70) Gangwal, S.; Cayre, O. J.; Velev, O. D. *Langmuir* **2008**, *24*, 13312.
(71) Smoukov, S. K.; Gangwal, S.; Marquez, M.; Velev, O. D. *Soft Matter* **2009**, *5*, 1285.
(72) Park, S.; Chung, S.-W.; Mirkin, C. A. *J. Am. Chem. Soc.* **2004**, *126*, 11772.
(73) Chang, S. T.; Paunov, V. N.; Petsev, D. N.; Velev, O. D. *Nat. Mater.* **2007**, *6*, 235.
(74) Calvo-Marzal, P.; Sattayasamitsathit, S.; Balasubramanian, S.; Windmiller, J. R.; Dao, C.; Wang, J. *Chem. Commun.* **2010**, *46*, 1623.
(75) Erb, R. M.; Jenness, N. J.; Clark, R. L.; Yellen, B. B. *Adv. Mater.* **2009**, *21*, 4825.
(76) Merkt, F. S.; et al. *New J. Phys.* **2006**, *8*, 216.
(77) Jiang, H.-R.; Yoshinaga, N.; Sano, M. *Phys. Rev. Lett.* **2010**, *105*, 268302.
(78) Kagan, D.; Laocharoensuk, R.; Zimmerman, M.; Clawson, C.; Balasubramanian, S.; Kang, D.; Bishop, D.; Sattayasamitsathit, S.; Zhang, L.; Wang, J. *Small* **2010**, *6*, 2741.
(79) Wu, J.; Balasubramanian, S.; Kagan, D.; Manesh, K. M.; Campuzano, S.; Wang, J. *Nat. Commun.* **2010**, *1*, 36.
(80) Balasubramanian, S.; Kagan, D.; Jack Hu, C.-M.; Campuzano, S.; Lobo-Castañon, M. J.; Lim, N.; Kang, D. Y.; Zimmerman, M.; Zhang, L.; Wang, J. *Angew. Chem. Int. Ed.* **2011**, *50*, 4023.
(81) Manesh, K. M.; Balasubramanian, S.; Wang, J. *Chem. Commun.* **2010**, *46*, 5704.
(82) Tierno, P.; Golestanian, R.; Pagonabarraga, I.; Sagués, F. *J. Phys. Chem. B* **2008**, *112*, 16525.
(83) Gao, W.; Sattayasamitsathit, S.; Manesh, K. M.; Weihs, D.; Wang, J. *J. Am. Chem. Soc.* **2010**, *132*, 14403.
(84) Pak, O. S.; Gao, W.; Wang, J.; Lauga, E. *Soft Matter* **2011**, *7*, 8169.

(85) Mano, N.; Heller, A. *J. Am. Chem. Soc.* **2005**, *127*, 11574.
(86) Stock, C.; Heureux, N.; Browne, W. R.; Feringa, B. L. *Chem. Eur. J.* **2008**, *14*, 3146.
(87) Wang, Y.; Hernandez, R. M.; Bartlett, D. J.; Bingham, J. M.; Kline, T. R.; Sen, A.; Mallouk, T. E. *Langmuir* **2006**, *22*, 10451.
(88) Gibbs, J. G.; Zhao, Y. P. *Appl. Phys. Lett.* **2009**, *94*, 163104.
(89) Fattah, Z.; Loget, G.; Lapeyre, V.; Garrigue, P.; Warakulwit, C.; Limtrakul, J.; Bouffier, L.; Kuhn, A. *Electrochim. Acta* **2011**, *56*, 10562.
(90) Wang, J. *ACS Nano* **2009**, *3*, 4.
(91) Mirkovic, T.; Zacharia, N. S.; Scholes, G. D.; Ozin, G. A. *ACS Nano* **2010**, *4*, 1782.
(92) Pumera, M. *Nanoscale* **2010**, *2*, 1643.
(93) Mallouk, T. E.; Sen, A. *Sci. Am.* **2009**, *300*, 74.
(94) Ebbens, S. J.; Howse, J. R. *Soft Matter* **2010**, *6*, 726.
(95) Wang, J.; Manesh, K. M. *Small* **2010**, *6*, 338.
(96) Manesh, K. M.; Cardona, M.; Yuan, R.; Clark, M.; Kagan, D.; Balasubramanian, S.; Wang, J. *ACS Nano* **2010**, *4*, 1799.
(97) Burdick, J.; Laocharoensuk, R.; Wheat, P. M.; Posner, J. D.; Wang, J. *J. Am. Chem. Soc.* **2008**, *130*, 8164.
(98) Gao, W.; Manesh, K. M.; Hua, J.; Sattayasamitsathit, S.; Wang, J. *Small* **2011**, *7*, 2047.
(99) Calvo-Marzal, P.; Manesh, K. M.; Kagan, D.; Balasubramanian, S.; Cardona, M.; Flechsig, G.-U.; Posner, J.; Wang, J. *Chem. Commun.* **2009**, 4509.
(100) Wang, Y.; Fei, S.-t.; Byun, Y.-M.; Lammert, P. E.; Crespi, V. H.; Sen, A.; Mallouk, T. E. *J. Am. Chem. Soc.* **2009**, *131*, 9926.
(101) Miño, G.; Mallouk, T.; Darnige, T.; Hoyos, M.; Dauchet, J.; Dunstan, J.; Soto, R.; Wang, Y.; Rousselet, A.; Clement, E. *Phys. Rev. Lett.* **2011**, *106*.
(102) Sundararajan, S.; Lammert, P. E.; Zudans, A. W.; Crespi, V. H.; Sen, A. *Nano Lett.* **2008**, *8*, 1271.
(103) Hong, Y.; Blackman, N.; Kopp, N.; Sen, A.; Velegol, D. *Phys. Rev. Lett.* **2007**, *99, 178103.*
(104) Zacharia, N. S.; Sadeq, Z. S.; Ozin, G. A. *Chem. Commun.* **2009**, 5856.
(105) Mirkovic, T.; Foo, M. L.; Arsenault, A. C.; Fournier-Bidoz, S.; Zacharia, N. S.; Ozin, G. A. *Nat. Nanotech.* **2007**, *2*, 565.
(106) Isojima, T.; Lattuada, M.; Vander Sande, J. B.; Hatton, T. A. *ACS Nano* **2008**, *2*, 1799.
(107) Himmelhaus, M.; Takei, H. *Sens. Actuat. B: Chem.* **2000**, *63*, 24.
(108) Anthony, S. M.; Hong, L.; Kim, M.; Granick, S. *Langmuir* **2006**, *22*, 9812.
(109) Anker, J. N.; Kopelman, R. *Appl. Phys. Lett.* **2003**, *82*, 1102.
(110) Anker, J. *J. Appl. Phys.* **2003**, *93*, 6698.
(111) Anker, J. N.; Behrend, C. J.; Huang, H.; Kopelman, R. *J. Magn. Magn. Mater.* **2005**, *293*, 655.
(112) Behrend, C. J.; Anker, J. N.; McNaughton, B. H.; Kopelman, R. *J. Magn. Magn. Mater.* **2005**, *293*, 663.
(113) McNaughton, B. H.; Agayan, R. R.; Wang, J. X.; Kopelman, R. *Sens. Actuat. B: Chem.* **2007**, *121*, 330.
(114) Choi, J.; Zhao, Y.; Zhang, D.; Chien, S.; Lo, Y. H. *Nano Lett.* **2003**, *3*, 995.
(115) Behrend, C. *Appl. Phys. Lett.* **2004**, *84*, 154.
(116) Behrend, C. J.; Anker, J. N.; McNaughton, B. H.; Brasuel, M.; Philbert, M. A.; Kopelman, R. *J. Phys. Chem. B* **2004**, *108*, 10408.
(117) Wang, H.; Halas, N. J. *Nano Lett.* **2006**, *6*, 2945.
(118) Koo, H. Y.; Yi, D. K.; Yoo, S. J.; Kim, D. Y. *Adv. Mater.* **2004**, *16*, 274.
(119) Pradhan, S.; Ghosh, D.; Chen, S. *ACS Appl. Mater. Interfaces* **2009**, *1*, 2060.
(120) Fu, X.; Liu, J.; Yang, H.; Sun, J.; Li, X.; Zhang, X.; Jia, Y. *Mater. Chem. Phys.* **2011**, *130*, 334.
(121) Seh, Z. W.; Liu, S.; Low, M.; Zhang, S.-Y.; Liu, Z.; Mlayah, A.; Han, M.-Y. *Adv. Mater.* **2012**, *24*, 2310.
(122) Hu, S.-H.; Gao, X. *J. Am. Chem. Soc.* **2010**, *132*, 7234.
(123) Xie, H.; She, Z.-G.; Wang, S.; Sharma, G.; Smith, J. W. *Langmuir* **2012**, *28*, 4459.

(124) Hu, S.-H.; Chen, S.-Y.; Gao, X. *ACS Nano* **2012**, *6*, 2558.
(125) Pang, M.; Hu, J.; Zeng, H. C. *J. Am. Chem. Soc.* **2010**, *132*, 10771.
(126) Ma, X.; Zhao, Y.; Jiang, X.; Liu, W.; Liu, S.; Tang, Z. *ChemPhysChem* **2012**, *13*, 2531.
(127) Petit, L.; Manaud, J.-P.; Mingotaud, C.; Ravaine, S.; Duguet, E. *Mater. Lett.* **2001**, *51*, 478.
(128) Pradhan, S.; Brown, L.; Konopelski, J.; Chen, S. *J. Nanopart. Res.* **2009**, *11*, 1895.
(129) Ling, X. Y.; Phang, I. Y.; Acikgoz, C.; Yilmaz, M. D.; Hempenius, M. A.; Vancso, G. J.; Huskens, J. *Angew. Chem. Int. Ed.* **2009**, *48*, 7677.
(130) Love, J. C.; Gates, B. D.; Wolfe, D. B.; Paul, K. E.; Whitesides, G. M. *Nano Lett.* **2002**, *2*, 891.
(131) Cayre, O.; Paunov, V. N.; Velev, O. D. *J. Mater. Chem.* **2003**, *13*, 2445.
(132) Yang, S.; Xu, J.; Wang, Z.; Zeng, H.; Lei, Y. *J. Mater. Chem.* **2011**, *21*, 11930.
(133) Dimitrov, A. S.; Nagayama, K. *Langmuir* **1996**, *12*, 1303.
(134) Cui, J.-Q.; Kretzschmar, I. *Langmuir* **2006**, *22*, 8281.
(135) Fujimoto, K.; Nakahama, K.; Shidara, M.; Kawaguchi, H. *Langmuir* **1999**, *15*, 4630.
(136) Park, B. J.; Furst, E. M. *Langmuir* **2010**, *26*, 10406.
(137) Anderson, K. D.; Luo, M.; Jakubiak, R.; Naik, R. R.; Bunning, T. J.; Tsukruk, V. V. *Chem. Mater.* **2010**, *22*, 3259.
(138) Gong, J.; Zu, X.; Li, Y.; Mu, W.; Deng, Y. *J. Mater. Chem.* **2011**, *21*, 2067.
(139) Wang, B.; Li, B.; Zhao, B.; Li, C. Y. *J. Am. Chem. Soc.* **2008**, *130*, 11594.
(140) McConnell, M. D.; Kraeutler, M. J.; Yang, S.; Composto, R. J. *Nano Lett.* **2010**, *10*, 603.
(141) Li, Z.; Lee, D.; Rubner, M. F.; Cohen, R. E. *Macromolecules* **2005**, *38*, 7876.
(142) Lu, Y.; Xiong, H.; Jiang, X.; Xia, Y.; Prentiss, M.; Whitesides, G. M. *J. Am. Chem. Soc.* **2003**, *125*, 12724.
(143) Chen, R. T.; Muir, B. W.; Such, G. K.; Postma, A.; McLean, K. M.; Caruso, F. *Chem. Commun.* **2010**, *46*, 5121.
(144) Nakahama, K.; Kawaguchi, H.; Fujimoto, K. *Langmuir* **2000**, *16*, 7882.
(145) Brugarolas, T.; Park, B. J.; Lee, M. H.; Lee, D. *Adv. Funct. Mater.* **2011**, *21*, 3924.
(146) Bae, C.; Moon, J.; Shin, H.; Kim, J.; Sung, M. M. *J. Am. Chem. Soc.* **2007**, *129*, 14232.
(147) Yin, Y.; Lu, Y.; Gates, B.; Xia, Y. *J. Am. Chem. Soc.* **2001**, *123*, 8718.
(148) Yin, Y.; Lu, Y.; Xia, Y. *J. Am. Chem. Soc.* **2001**, *123*, 771.
(149) Kline, T. R.; Tian, M.; Wang, J.; Sen, A.; Chan, M. W.; Mallouk, T. E. *Inorg. Chem.* **2006**, *45*, 7555.
(150) Fournier-Bidoz, S.; Arsenault, A. C.; Manners, I.; Ozin, G. A. *Chem. Commun.* **2005**, 441.
(151) Velev, O. D.; Lenhoff, A. M.; Kaler, E. W. *Science* **2000**, *287*, 2240.
(152) Millman, J. R.; Bhatt, K. H.; Prevo, B. G.; Velev, O. D. *Nat. Mater.* **2005**, *4*, 98.
(153) Fialkowski, M.; Bitner, A.; Grzybowski, B. A. *Nat. Mater.* **2005**, *4*, 93.
(154) Velev, O. D.; Prevo, B. G.; Bhatt, K. H. *Nature* **2003**, *426*, 515.
(155) Subramaniam, A. B.; Abkarian, M.; Stone, H. A. *Nat. Mater.* **2005**, *4*, 553.
(156) Shepherd, R. F.; Conrad, J. C.; Rhodes, S. K.; Link, D. R.; Marquez, M.; Weitz, D. A.; Lewis, J. A. *Langmuir* **2006**, *22*, 8618.
(157) Nie, Z.; Li, W.; Seo, M.; Xu, S.; Kumacheva, E. *J. Am. Chem. Soc.* **2006**, *128*, 9408.
(158) Nisisako, T.; Torii, T. *Lab. Chip* **2008**, *8*, 287.
(159) Maeda, K.; Onoe, H.; Takinoue, M.; Takeuchi, S. *Adv. Mater.* **2012**, *24*, 1340.
(160) Roh, K.-H.; Martin, D. C.; Lahann, J. *Nat. Mater.* **2005**, *4*, 759.
(161) Bhaskar, S.; Pollock, K. M.; Yoshida, M.; Lahann, J. *Small* **2010**, *6*, 404.
(162) Srivastava, Y. *Biomicrofluidics* **2009**, *3*, 012801.
(163) Dendukuri, D.; Doyle, P. S. *Adv. Mater.* **2009**, *21*, 4071.
(164) Sheridon, N. K., **1978**, US patent 4126854 (A).
(165) Sheridon, N. In *Flexible Flat Panel Displays*; John Wiley & Sons, Ltd, **2005**.
(166) Ho, C.-C.; Chen, W.-S.; Shie, T.-Y.; Lin, J.-N.; Kuo, C. *Langmuir* **2008**, *24*, 5663.
(167) He, J.; Perez, M. T.; Zhang, P.; Liu, Y.; Babu, T.; Gong, J.; Nie, Z. *J. Am. Chem. Soc.* **2012**, *134*, 3639.
(168) Gu, H.; Yang, Z.; Gao, J.; Chang, C. K.; Xu, B. *J. Am. Chem. Soc.* **2005**, *127*, 34.

(169) Li, D.; He, Y.; Wang, S. *J. Phys. Chem. C* **2009**, *113*, 12927.
(170) Suzuki, D.; Tsuji, S.; Kawaguchi, H. *J. Am. Chem. Soc.* **2007**, *129*, 8088.
(171) Liu, B.; Wei, W.; Qu, X.; Yang, Z. *Angew. Chem.* **2008**, *120*, 4037.
(172) Zhang, J.; Jin, J.; Zhao, H. *Langmuir* **2009**, *25*, 6431.
(173) He, Y.; Li, K. *J. Colloid Interf. Sci.* **2007**, *306*, 296.
(174) Zhang, J.; Wang, X.; Wu, D.; Liu, L.; Zhao, H. *Chem. Mater.* **2009**, *21*, 4012.
(175) Hong, L.; Jiang, S.; Granick, S. *Langmuir* **2006**, *22*, 9495.
(176) Jiang, S.; Schultz, M. J.; Chen, Q.; Moore, J. S.; Granick, S. *Langmuir* **2008**, *24*, 10073.
(177) Jiang, S.; Granick, S. *Langmuir* **2008**, *24*, 2438.
(178) Berger, S.; Synytska, A.; Ionov, L.; Eichhorn, K.-J.; Stamm, M. *Macromolecules* **2008**, *41*, 9669.
(179) Pardhy, N. P.; Budhlall, B. M. *Langmuir* **2010**, *26*, 13130.
(180) Perro, A.; Meunier, F.; Schmitt, V. r.; Ravaine, S. *Colloids Surf., A* **2009**, *332*, 57.
(181) Liu, B.; Zhang, C.; Liu, J.; Qu, X.; Yang, Z. *Chem. Commun.* **2009**, 3871.
(182) Kim, S.-H.; Yi, G.-R.; Kim, K. H.; Yang, S.-M. *Langmuir* **2008**, *24*, 2365.
(183) Zhang, S.; Li, Z.; Samarajeewa, S.; Sun, G.; Yang, C.; Wooley, K. L. *J. Am. Chem. Soc.* **2011**, *133*, 11046.
(184) Poncet-Legrand, C.; Petit, L.; Reculusa, S.; Mingotaud, C.; Duguet, E.; Ravaine, S. *Prog. Colloid Polym. Sci.* **2004**, *123*, 240.
(185) Lattuada, M.; Hatton, T. A. *J. Am. Chem. Soc.* **2007**, *129*, 12878.
(186) Bradley, M.; Rowe, J. *Soft Matter* **2009**, *5*, 3114.
(187) Nie, L.; Liu, S.; Shen, W.; Chen, D.; Jiang, M. *Angew. Chem. Int. Ed.* **2007**, *46*, 6321.
(188) Mao, J.; Qi, X.; Cao, X.; Lu, J.; Xu, Q.; Gu, H. *Chem. Commun.* **2011**, *47*, 4228.
(189) Mock, E. B.; De Bruyn, H.; Hawkett, B. S.; Gilbert, R. G.; Zukoski, C. F. *Langmuir* **2006**, *22*, 4037.
(190) Kim, J.-W.; Larsen, R. J.; Weitz, D. A. *J. Am. Chem. Soc.* **2006**, *128*, 14374.
(191) Mock, E. B.; Zukoski, C. F. *Langmuir* **2010**, *26*, 13747.
(192) Pfau, A.; Sander, R.; Kirsch, S. *Langmuir* **2002**, *18*, 2880.
(193) Kim, J. W.; Larsen, R. J.; Weitz, D. A. *Adv. Mater.* **2007**, *19*, 2005.
(194) Nagao, D.; Hashimoto, M.; Hayasaka, K.; Konno, M. *Macromol. Rapid Commun.* **2008**, *29*, 1484.
(195) Nagao, D.; van Kats, C. M.; Hayasaka, K.; Sugimoto, M.; Konno, M.; Imhof, A.; van Blaaderen, A. *Langmuir* **2010**, *26*, 5208.
(196) Reculusa, S. p.; Poncet-Legrand, C. l.; Perro, A.; Duguet, E.; Bourgeat-Lami, E.; Mingotaud, C.; Ravaine, S. *Chem. Mater.* **2005**, *17*, 3338.
(197) Perro, A.; Reculusa, S.; Pereira, F.; Delville, M.-H.; Mingotaud, C.; Duguet, E.; Bourgeat-Lami, E.; Ravaine, S. *Chem. Commun.* **2005**, 5542.
(198) Ge, J.; Hu, Y.; Zhang, T.; Yin, Y. *J. Am. Chem. Soc.* **2007**, *129*, 8974.
(199) Fujibayashi, T.; Tanaka, T.; Minami, H.; Okubo, M. *Colloid Polym. Sci.* **2010**, *288*, 879.
(200) Nagao, D.; Goto, K.; Ishii, H.; Konno, M. *Langmuir* **2011**, *27*, 13303.
(201) Rahman, M. M.; Montagne, F.; Fessi, H.; Elaissari, A. *Soft Matter* **2011**, *7*, 1483.
(202) Saito, N.; Kagari, Y.; Okubo, M. *Langmuir* **2006**, *22*, 9397.
(203) Ge, X.; Wang, M.; Ji, X.; Ge, X.; Liu, H. *Colloid Polym. Sci.* **2009**, *287*, 819.
(204) Tanaka, T.; Nakatsuru, R.; Kagari, Y.; Saito, N.; Okubo, M. *Langmuir* **2008**, *24*, 12267.
(205) Tanaka, T.; Okayama, M.; Kitayama, Y.; Kagawa, Y.; Okubo, M. *Langmuir* **2010**, *26*, 7843.
(206) Isojima, T.; Suh, S. K.; Vander Sande, J. B.; Hatton, T. A. *Langmuir* **2009**, *25*, 8292.
(207) Yabu, H.; Higuchi, T.; Ijiro, K.; Shimomura, M. *Chaos* **2005**, *15*, 047505.
(208) Higuchi, T.; Tajima, A.; Motoyoshi, K.; Yabu, H.; Shimomura, M. *Angew. Chem. Int. Ed.* **2008**, *47*, 8044.
(209) Voets, I. K.; de Keizer, A.; de Waard, P.; Frederik, P. M.; Bomans, P. H. H.; Schmalz, H.; Walther, A.; King, S. M.; Leermakers, F. A. M.; Cohen Stuart, M. A. *Angew. Chem. Int. Ed.* **2006**, *45*, 6673.

(210) Voets, I. K.; Fokkink, R.; Hellweg, T.; King, S. M.; Waard, P.; Keizer, A.; Cohen Stuart, M. A. *Soft Matter* **2009**, *5*, 999.
(211) Saito, R.; Fujita, A.; Ichimura, A.; Ishizu, K. *J. Polym. Sci. Pol. Chem.* **2000**, *38*, 2091.
(212) Erhardt, R.; Böker, A.; Zettl, H.; Kaya, H.; Pyckhout-Hintzen, W.; Krausch, G.; Abetz, V.; Müller, A. H. E. *Macromolecules* **2001**, *34*, 1069.
(213) Erhardt, R.; Zhang, M.; Böker, A.; Zettl, H.; Abetz, C.; Frederik, P.; Krausch, G.; Abetz, V.; Müller, A. H. E. *J. Am. Chem. Soc.* **2003**, *125*, 3260.
(214) Liu, Y.; Abetz, V.; Müller, A. H. E. *Macromolecules* **2003**, *36*, 7894.
(215) Walther, A.; André, X.; Drechsler, M.; Abetz, V.; Müller, A. H. E. *J. Am. Chem. Soc.* **2007**, *129*, 6187.
(216) Mulvaney, P.; Giersig, M.; Ung, T.; Liz-Marzán, L. M. *Adv. Mater.* **1997**, *9*, 570.
(217) Gu, H.; Zheng, R.; Zhang, X.; Xu, B. *J. Am. Chem. Soc.* **2004**, *126*, 5664.
(218) Grüening, B.; Holtschmidt, U.; Koerner, G.; Rossmy, G., **1987**, US patent 4715986.
(219) Liang, F.; Liu, J.; Zhang, C.; Qu, X.; Li, J.; Yang, Z. *Chem. Commun.* **2011**, *47*, 1231.
(220) Chen, T.; Chen, G.; Xing, S.; Wu, T.; Chen, H. *Chem. Mater.* **2010**, *22*, 3826.
(221) Chen, T.; Yang, M.; Wang, X.; Tan, L. H.; Chen, H. *J. Am. Chem. Soc.* **2008**, *130*, 11858.
(222) Tan, L. H.; Xing, S.; Chen, T.; Chen, G.; Huang, X.; Zhang, H.; Chen, H. *ACS Nano* **2009**, *3*, 3469.
(223) Habas, S. E.; Yang, P.; Mokari, T. *J. Am. Chem. Soc.* **2008**, *130*, 3294.
(224) Kudera, S.; Carbone, L.; Casula, M. F.; Cingolani, R.; Falqui, A.; Snoeck, E.; Parak, W. J.; Manna, L. *Nano Lett.* **2005**, *5*, 445.
(225) Deka, S.; Falqui, A.; Bertoni, G.; Sangregorio, C.; Poneti, G.; Morello, G.; Giorgi, M. D.; Giannini, C.; Cingolani, R.; Manna, L.; Cozzoli, P. D. *J. Am. Chem. Soc.* **2009**, *131*, 12817.
(226) Chakrabortty, S.; Yang, J. A.; Tan, Y. M.; Mishra, N.; Chan, Y. *Angew. Chem.* **2010**, *122*, 2950.
(227) Figuerola, A.; Franchini, I. R.; Fiore, A.; Mastria, R.; Falqui, A.; Bertoni, G.; Bals, S.; Van Tendeloo, G.; Kudera, S.; Cingolani, R.; Manna, L. *Adv. Mater.* **2009**, *21*, 550.
(228) Buonsanti, R.; Grillo, V.; Carlino, E.; Giannini, C.; Curri, M. L.; Innocenti, C.; Sangregorio, C.; Achterhold, K.; Parak, F. G.; Agostiano, A.; Cozzoli, P. D. *J. Am. Chem. Soc.* **2006**, *128*, 16953.
(229) Casavola, M.; Grillo, V.; Carlino, E.; Giannini, C.; Gozzo, F.; Fernandez Pinel, E.; Garcia, M. A.; Manna, L.; Cingolani, R.; Cozzoli, P. D. *Nano Lett.* **2007**, *7*, 1386.
(230) Cheng, C.; Yu, K. F.; Cai, Y.; Fung, K. K.; Wang, N. *J. Phys. Chem. C* **2007**, *111*, 16712.
(231) Vinod, T. P.; Yang, M.; Kim, J.; Kotov, N. A. *Langmuir* **2009**, *25*, 13545.
(232) Mao, J.; Cao, X.; Zhen, J.; Shao, H.; Gu, H.; Lu, J.; Ying, J. Y. *J. Mater. Chem.* **2011**, *21*, 11478.
(233) Wetz, F.; Soulantica, K.; Falqui, A.; Respaud, M.; Snoeck, E.; Chaudret, B. *Angew. Chem. Int. Ed.* **2007**, *46*, 7079.
(234) Mokari, T.; Rothenberg, E.; Popov, I.; Costi, R.; Banin, U. *Science* **2004**, *304*, 1787.
(235) Mokari, T.; Sztrum, C. G.; Salant, A.; Rabani, E.; Banin, U. *Nat. Mater.* **2005**, *4*, 855.
(236) Carbone, L.; Kudera, S.; Giannini, C.; Ciccarella, G.; Cingolani, R.; Cozzoli, P. D.; Manna, L. *J. Mater. Chem.* **2006**, *16*, 3952.
(237) Zhang, L.; Dou, Y.-H.; Gu, H.-C. *J. Colloid Interf. Sci.* **2006**, *297*, 660.
(238) Ridelman, Y.; Singh, G.; Popovitz-Biro, R.; Wolf, S. G.; Das, S.; Klajn, R. *Small* **2012**, *8*, 654.
(239) Choi, S.-H.; Kim, E.-G.; Hyeon, T. *J. Am. Chem. Soc.* **2006**, *128*, 2520.
(240) Yu, H.; Chen, M.; Rice, P. M.; Wang, S. X.; White, R. L.; Sun, S. *Nano Lett.* **2005**, *5*, 379.
(241) Shi, W.; Sahoo, Y.; Zeng, H.; Ding, Y.; Swihart, M. T.; Prasad, P. N. *Adv. Mater.* **2006**, *18*, 1889.
(242) Pellegrino, T.; Fiore, A.; Carlino, E.; Giannini, C.; Cozzoli, P. D.; Ciccarella, G.; Respaud, M.; Palmirotta, L.; Cingolani, R.; Manna, L. *J. Am. Chem. Soc.* **2006**, *128*, 6690.
(243) Wang, X.; Kong, X.; Yu, Y.; Zhang, H. *J. Phys. Chem. C* **2007**, *111*, 3836.
(244) Chaubey, G. S.; Nandwana, V.; Poudyal, N.; Rong, C.-b.; Liu, J. P. *Chem. Mater.* **2008**, *20*, 475.
(245) Gao, X.; Yu, L.; MacCuspie, R.; Matsui, H. *Adv. Mater.* **2005**, *17*, 426.
(246) Zhu, G.; Xu, Z. *J. Am. Chem. Soc.* **2011**, *133*, 148.
(247) Zhang, L.; Zhang, F.; Dong, W.-F.; Song, J.-F.; Huo, Q.-S.; Sun, H.-B. *Chem. Commun.* **2011**, *47*, 1225.
(248) Feyen, M.; Weidenthaler, C.; Schüth, F.; Lu, A.-H. *J. Am. Chem. Soc.* **2010**, *132*, 6791.

(249) Xing, S.; Feng, Y.; Tay, Y. Y.; Chen, T.; Xu, J.; Pan, M.; He, J.; Hng, H. H.; Yan, Q.; Chen, H. *J. Am. Chem. Soc.* **2010**, *132*, 9537.
(250) Duque, J. G.; Eukel, J. A.; Pasquali, M.; Schmidt, H. K. *J. Phys. Chem. C* **2009**, *113*, 18863.
(251) Duque, J. G.; Pasquali, M.; Schmidt, H. K. *J. Am. Chem. Soc.* **2008**, *130*, 15340.
(252) Reiche, H.; Dunn, W. W.; Bard, A. J. *J. Phys. Chem.* **1979**, *83*, 2248.
(253) Pacholski, C.; Kornowski, A.; Weller, H. *Angew. Chem. Int. Ed.* **2004**, *43*, 4774.
(254) Carbone, L.; Jakab, A.; Khalavka, Y.; Sönnichsen, C. *Nano Lett.* **2009**, *9*, 3710.
(255) Menagen, G.; Macdonald, J. E.; Shemesh, Y.; Popov, I.; Banin, U. *J. Am. Chem. Soc.* **2009**, *131*, 17406.
(256) Wang, P.; Huang, B.; Lou, Z.; Zhang, X.; Qin, X.; Dai, Y.; Zheng, Z.; Wang, X. *Chem. Eur. J.* **2010**, *16*, 538.
(257) Wang, P.; Huang, B.; Zhang, X.; Qin, X.; Dai, Y.; Wang, Z.; Lou, Z. *ChemCatChem* **2011**, *3*, 360.
(258) Choi, O.; Deng, K. K.; Kim, N.-J.; Ross Jr, L.; Surampalli, R. Y.; Hu, Z. *Water Res.* **2008**, *42*, 3066.
(259) Saunders, A. E.; Popov, I.; Banin, U. *Z. Anorg. Allg. Chem.* **2007**, *633*, 2414.
(260) Lagona, J.; Mukhopadhyay, P.; Chakrabarti, S.; Isaacs, L. *Angew. Chem. Int. Ed.* **2005**, *44*, 4844.
(261) An, Q.; Li, G.; Tao, C.; Li, Y.; Wu, Y.; Zhang, W. *Chem. Commun.* **2008**, 1989.
(262) Mahajan, S.; Lee, T.-C.; Biedermann, F.; Hugall, J. T.; Baumberg, J. J.; Scherman, O. A. *Phys. Chem. Chem. Phys.* **2010**, *12*, 10429.
(263) Lee, T.-C.; Scherman, O. A. *Chem. Commun.* **2010**, *46*, 2438.
(264) Lee, T.-C.; Scherman, O. A. *Chem. Eur. J.* **2012**, *18*, 1628.
(265) Taylor, R. W.; Lee, T.-C.; Scherman, O. A.; Esteban, R.; Aizpurua, J.; Huang, F. M.; Baumberg, J. J.; Mahajan, S. *ACS Nano* **2011**, *5*, 3878.
(266) de la Rica, R.; Velders, A. H. *Small* **2011**, *7*, 66.
(267) Premkumar, T.; Lee, Y.; Geckeler, K. E. *Chem. Eur. J.* **2010**, *16*, 11563.
(268) Lu, X.; Masson, E. *Langmuir* **2011**, *27*, 3051.
(269) Cao, M.; Lin, J.; Yang, H.; Cao, R. *Chem. Commun.* **2010**, *46*, 5088.
(270) Helveg, S.; Lopez-Cartes, C.; Sehested, J.; Hansen, P. L.; Clausen, B. S.; Rostrup-Nielsen, J. R.; Abild-Pedersen, F.; Norskov, J. K. *Nature* **2004**, *427*, 426.
(271) Rodríguez-Manzo, J. A.; Pham-Huu, C.; Banhart, F. *ACS Nano* **2011**, *5*, 1529.
(272) Girit, Ç. Ö.; Meyer, J. C.; Erni, R.; Rossell, M. D.; Kisielowski, C.; Yang, L.; Park, C.-H.; Crommie, M. F.; Cohen, M. L.; Louie, S. G.; Zettl, A. *Science* **2009**, *323*, 1705.
(273) Loget, G.; Lee, T.-C.; Taylor, R. W.; Mahajan, S.; Nicoletti, O.; Jones, S. T.; Coulston, R. J.; Lapeyre, V.; Garrigue, P.; Midgley, P. A.; Scherman, O. A.; Baumberg, J. J.; Kuhn, A. *Small,* **2012**, *8*, 2698.
(274) Jiao, D.; Zhao, N.; Scherman, O. A. *Chem. Commun.* **2010**, *46*, 2007.
(275) Ray, M.; Paria, S. *Ind. Eng. Chem. Res.* **2011**, *50*, 11601.
(276) Bottger, G. L.; Damsgard, C. V. *Solid State Commun.* **1971**, *9*, 1277.
(277) Blanco, E.; Quintana, C.; Hernández, P.; Hernández, L. *Electroanalysis* **2010**, *22*, 2123.
(278) Lee, J. W.; Samal, S.; Selvapalam, N.; Kim, H.-J.; Kim, K. *Acc. Chem. Res.* **2003**, *36*, 621.
(279) Warakulwit, C., PhD thesis, Bordeaux University and Kasetsart University, **2007**.
(280) Warakulwit, C.; Nguyen, T.; Majimel, J.; Delville, M.-H.; Lapeyre, V.; Garrigue, P.; Ravaine, V.; Limtrakul, J.; Kuhn, A. *Nano Lett.* **2008**, *8*, 500.
(281) Loget, G.; Roche, J.; Kuhn, A. *Adv. Mater.* **2012**, *24*, 5111.
(282) Loget, G.; Larcade, G.; Lapeyre, V.; Garrigue, P.; Warakulwit, C.; Limtrakul, J.; Delville, M.-H.; Ravaine, V.; Kuhn, A. *Electrochim. Acta* **2010**, *55*, 8116.
(283) Bard, A. J.; Faulkner, L. R. *Electrochemical Methods*; 2nd ed.; John Wiley & Sons, Inc., **2001**.
(284) Loget, G.; Lapeyre, V.; Garrigue, P.; Warakulwit, C.; Limtrakul, J.; Delville, M.-H.; Kuhn, A. *Chem. Mater.* **2011**, *23*, 2595.
(285) Wallace, G. G.; Spinks, G. M.; Kane-Maguire, L. A. P.; Teasdale, P. B. *Conductive Electroactive Polymers*; CRC Press, **2009**.
(286) Cosnier, S.; Karyakin, A. *Electro-polymerization*; Wiley-VCH, **2010**.

(287) McQuade, D. T.; Pullen, A. E.; Swager, T. M. *Chem. Rev.* **2000**, *100*, 2537.
(288) Sadki, S.; Schottland, P.; Brodie, N.; Sabouraud, G. *Chem. Soc. Rev.* **2000**, *29*, 283.
(289) Inoue, M. B.; Nebesny, K. W.; Fernando, Q.; Castillo-Ortega, M. M.; Inoue, M. *Synth. Met.* **1990**, *38*, 205.
(290) Loget, G.; Kuhn, A. **2011**, French patent FR2969508.
(291) Lashmore, D. S.; Beane, G. L.; Kelley, D. R.; Johnson, C. E., **1997**, US patent 5603815.
(292) Love, J. C.; Estroff, L. A.; Kriebel, J. K.; Nuzzo, R. G.; Whitesides, G. M. *Chem. Rev.* **2005**, *105*, 1103.
(293) Juris, A.; Balzani, V.; Barigelletti, F.; Campagna, S.; Belser, P.; von Zelewsky, A. *Coord. Chem. Rev.* **1988**, *84*, 85.
(294) Pinson, J.; Podvorica, F. *Chem. Soc. Rev.* **2005**, *34*, 429.
(295) Sun, Y.; Mayers, B.; Herricks, T.; Xia, Y. *Nano Lett.* **2003**, *3*, 955.
(296) Zhang, Q.; Li, N.; Goebl, J.; Lu, Z.; Yin, Y. *J. Am. Chem. Soc.* **2011**, *133*, 18931.
(297) Pletcher, D.; Walsh, F. *Industrial Electrochemistry*; 2nd ed.; Kluwer Academic Pub, **1990**.
(298) Therese, G. H. A.; Kamath, P. V. *Chem. Mater.* **2000**, *12*, 1195.
(299) Walcarius, A.; Mandler, D.; Cox, J. A.; Collinson, M.; Lev, O. *J. Mater. Chem.* **2005**, *15*, 3663.
(300) Shacham, R.; Avnir, D.; Mandler, D. *J. Sol-gel Sci. Techn.* **2004**, *31*, 329.
(301) Kurzawa, C.; Hengstenberg, A.; Schuhmann, W. *Anal. Chem.* **2002**, *74*, 355.
(302) Wang, B.; Li, B.; Wang, Z.; Xu, G.; Wang, Q.; Dong, S. *Anal. Chem.* **1999**, *71*, 1935.
(303) Arora, A.; Eijkel, J. C. T.; Morf, W. E.; Manz, A. *Anal. Chem.* **2001**, *73*, 3282.
(304) Lev, O.; Wu, Z.; Bharathi, S.; Glezer, V.; Modestov, A.; Gun, J.; Rabinovich, L.; Sampath, S. *Chem. Mater.* **1997**, *9*, 2354.
(305) Gratzel, M. *Nature* **2001**, *414*, 338.
(306) Walter, M. G.; Warren, E. L.; McKone, J. R.; Boettcher, S. W.; Mi, Q.; Santori, E. A.; Lewis, N. S. *Chem. Rev.* **2010**, *110*, 6446.
(307) Ohya, T.; Nakayama, A.; Ban, T.; Ohya, Y.; Takahashi, Y. *Chem. Mater.* **2002**, *14*, 3082.
(308) Sawatani, S.; Yoshida, T.; Ohya, T.; Ban, T.; Takahashi, Y.; Minoura, H. *Electrochem. Solid-State Lett.* **2005**, *8*, C69.
(309) Wessels, K.; Minnermann, M.; Rathousky, J.; Wark, M.; Oekermann, T. *J. Phys. Chem. C* **2008**, *112*, 15122.
(310) K.-H. Scherping; H.-J. Holsher; U. Reichelt; Reiter, U., **1992**, US patent 5114993.
(311) Szamocki, R.; Velichko, A.; Mücklich, F.; Reculusa, S.; Ravaine, S.; Neugebauer, S.; Schuhmann, W.; Hempelmann, R.; Kuhn, A. *Electrochem. Commun.* **2007**, *9*, 2121.
(312) Bon Saint Côme, Y.; Lalo, H.; Wang, Z.; Etienne, M.; Gajdzik, J.; Kohring, G.-W.; Walcarius, A.; Hempelmann, R.; Kuhn, A. *Langmuir* **2011**, *27*, 12737.
(313) Salaita, K.; Wang, Y.; Mirkin, C. A. *Nat. Nanotech.* **2007**, *2*, 145.
(314) Xia, Y.; Whitesides, G. M. *Angew. Chem. Int. Ed.* **1998**, *37*, 550.
(315) Menke, E. J.; Thompson, M. A.; Xiang, C.; Yang, L. C.; Penner, R. M. *Nat. Mater.* **2006**, *5*, 914.
(316) Heim, M.; Reculusa, S.; Ravaine, S.; Kuhn, A. *Adv. Funct. Mater.* **2012**, *22*, 446.
(317) Nishio, K.; Masuda, H. *Angew. Chem. Int. Ed.* **2011**, *50*, 1603.
(318) Aizpurua, J.; Hanarp, P.; Sutherland, D. S.; Käll, M.; Bryant, G. W.; García de Abajo, F. J. *Phys. Rev. Lett.* **2003**, *90*, 057401.
(319) Larsson, E. M.; Alegret, J.; Käll, M.; Sutherland, D. S. *Nano Lett.* **2007**, *7*, 1256.

Chapter 4

Bipolar electrochemical motors

4.1. Synthetic motors: concepts, fabrication and applications

4.1.1. Inspiration from nature

Nature offers wonderful examples of autonomous microsystems which operate at dimensions where viscosity effects predominate (at low Reynolds numbers) and Brownian motion is considerable. As examples at the micro-scale, we can cite eukaryote cells such as spermatozoa, which propel themselves generating a mechanical wave with their flagella. Some prokaryotic entities such as the bacteria *Escherichia coli* (*E.coli*) or *Salmonella* (Figure 4.1a) use the corkscrew motion of their flagella to direct themselves at extremely high speeds of up to 60 bodylengths s^{-1}. At a smaller scale, within the cell, one can see the latter flagella motion being driven by the action of a remarkable rotary nanomotor powered by the action of a proton flux.[1,2] Other biomolecular nanomotors are active in cells, for example kinesin and dynein travel along microtubule "tracks" in the cytoplasm to deliver required vesicles, organelles and other cargos at specific locations (Figure 4.1b).[3-5] Most of these motors are powered by the spontaneous reactions of energy rich biomolecules, such as the hydrolysis of the biological fuel adenosine triphosphate (ATP). Inspired by the remarkable performances of these systems, and encouraged by the visionary talk of Feynman,[6] biologists, chemists and physicists have developed in the last decades different strategies in order to try to compete with natural biomotors.[7-9]

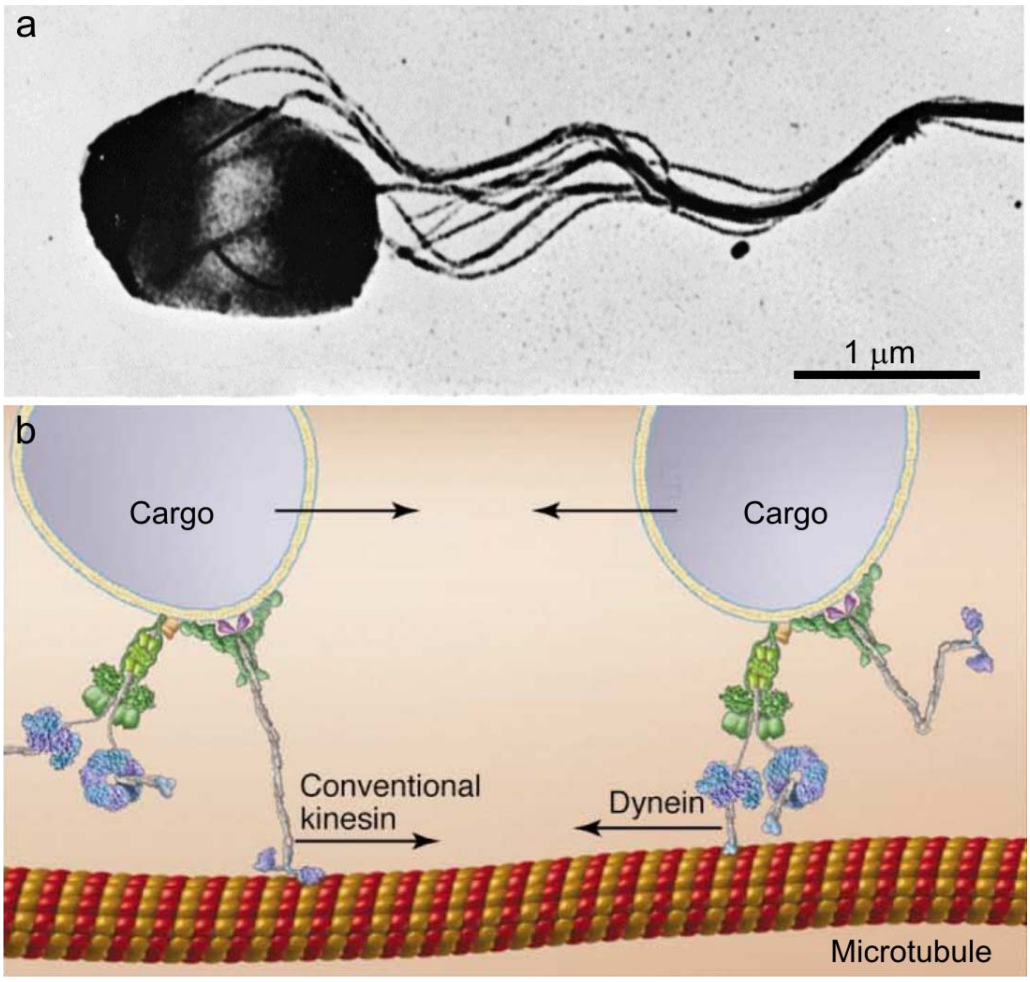

Figure 4.1. Examples of biomotors. a) TEM micrograph of a *Salmonella* bacterium. Adapted from reference (10). b) Scheme showing the cargo transport by kinesin and dynein along a microtubule. Adapted from reference (11).

A first approach consists in using directly the biosystems given by nature as active parts. Several publications from Whitesides' group illustrate this concept at the cell level.[12-14] Controlling the morphology of filamentous *E.coli* by making them grow in shaped microchambers results in specific motions.[13] Cargo transport and release was realized using flagella-propelled unicellular algae, which were steered by phototaxis within a microchannel.[14] Bacteria attached to the surface of particles can transfer their motion as demonstrated by Behkam *et al.*[15,16] At a smaller scale, a lot of effort has been devoted to the motion of nano- and microobjects using biomolecular nanomotors.[17-19] In this context, Montemagno used ATPase to rotate a biochemically bonded nickel nanorod in the presence of ATP.[20] The effect of viscosity on the rotation of a microbead attached to ATPase has also been reported.[21] Vogel's group presented the use of kinesin-modified surfaces for directing the ATP-powered motion of microtubules within miniaturized systems.[22-24] This system has recently been applied in biosensing,[25,26]cargo transport and release.[24,27] Even though such biological systems are

remarkably efficient, they have a very limited lifetime due to their rapid degradation in a wide range of experimental conditions. This major drawback has led to many efforts for conceiving more stable synthetic motors with comparable performances.

4.1.2. Chemically powered motion

Important developments in the area of synthetic molecular motors[28,29] using DNA or smaller molecules are currently in progress, but exceed the scope of this chapter. The most developed strategy is directly inspired by biological systems and is based on the use of a chemical fuel. This fuel induces motion, by reacting at a precise area on the motor.[30] Two main mechanisms, namely self-electrophoresis and bubble-propulsion have been discussed in this context. After a strong scientific debate,[31] the first one has been widely adopted for explaining the motion of bimetallic nanorods (also referred to as nanosubmarines)[32] in the presence of hydrogen peroxide. As shown in Figure 4.2a, these objects are usually synthetized by electroplating through alumina membranes containing cylindrical pores and are isolated after the dissolution of the membrane. They are typically several micrometers long and a few hundreds of nanometers wide (Figure 4.2c). Different metal combinations can be used with one metal being the cathodic pole, where H_2O_2 is reduced and the other one the anodic pole, where H_2O_2 is oxidized. The respective locations of the spontaneous and simultaneous reactions can be deduced from the mixed potential values of each metal in the fuel solution, as demonstrated by Mallouk *et al.*[31] The metal with the more positive mixed potential acts as the cathode and the other one as the anode. In the presence of the fuel, the nanorods are then bipolar electrodes but in this case the bipolarity is induced by the composition of the object and the solution and not by an external electric field. Classical rod compositions employ a good catalyst for H_2O_2 dismutation such as Pt[33] or Ni[34] as the cathodic pole and Au as the anodic pole. As illustrated in Figure 4.2b, the electron flow at the rod/solution interface is balanced by a proton flow in the electrical double layer, inducing the motion in an opposite direction.

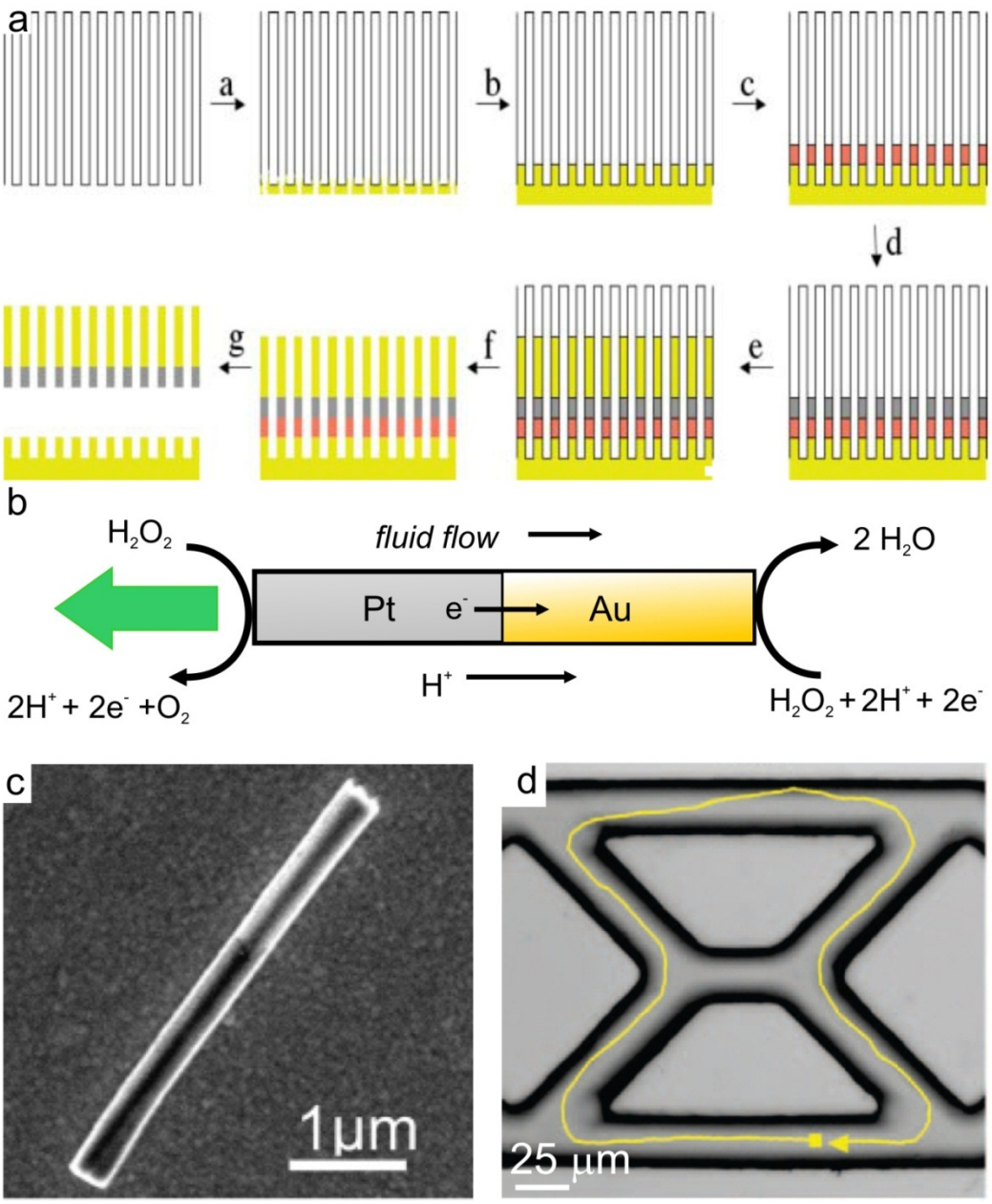

Figure 4.2. Self-electrophoretic swimmers. a) Synthetic procedure for obtaining Ni/Au nanorods. (a) Gold sputtering onto an alumina membrane. (b) Electrodeposition of gold plugs. (c) Electrodeposition of a sacrificial layer of copper. (d) Electrodeposition of a nickel segment. (e) Electrodeposition of a gold segment. (f) Selective dissolution of alumina. (g) Selective dissolution of copper. Adapted from reference (34). b) Scheme showing the self-electrophoresis mechanism on a Pt/Au nanorod. c) SEM micrograph showing a Ni/Au nanorods. Reprinted from reference (31). d) Optical micrograph showing the motion track of an Pt-CNT/Au/Ni/Au nanomotor which is steered around the central portion of a PDMS microstructure. Reprinted from reference (35).

A lot of work, mainly presented by the groups of Wang and Ozin, has been performed with the aim to enhance the speed of these objects by material engineering and tuning the medium composition. For example, the porosity of the Ni surface can be increased to boost the speed.[36] A shown strong speed

enhancements has also been demonstrated by the incorporation of carbon nanotubes (CNTs) into the Pt matrix,[37] the presence of Ag^+ ions[38] and hydrazine[37] in the solution and the use of an Au-Ag alloy instead of a pure Au.[39] Using this improved system, speeds in the order of ≈150 μm s^{-1}, equivalent to ≈75 bodylenght s^{-1} have been reached.[39] The speed responds to different stimuli[40] such as electrogenerated concentration gradients[41] and temperature.[42] Coupled with magnetically active parts, the nanorods can be steered using magnetic fields, as shown in Figure 4.2d.[43] Recently several applications for writing microstructures on surfaces,[44] transporting cargos,[45] delivering cargos in microfluidic channels[35,46] and sensing.[47,38] have been presented. Interestingly, Sen *et al.* have shown that these objects exhibit chemotaxis,[48] *i.e.* when exposed to a chemical gradient, they will drive to the fuel rich area, similarly to biological entities. Rotational motions have been reported for Ni/Au rods with one part attached to a substrate[34], Au rods with a non-centered Pt catalyst[49] and a sub-millimeter gold gear-like structure with platinum strips in the tooth regions.[50] Using a self-electrophoresis mechanism, Sen *et al.* recently reported the use of Pt/Cu rods powered by aqueous Br_2 or I_2.[51] Mano *et al.* designed biochemical swimmers which operate involving a similar mechanism. Composed of a carbon fiber "body" carrying at both extremities glucose oxidase and bilirubin oxidase respectively, they use biofuels such as glucose and O_2.[52] Sen's group recently reported the interesting concept of polymerization powered motors.[53] In this system a submicrometer-sized spherical Janus particle, half-coated with a Grubb's catalyst, is immersed into a solution containing the monomer fuel. The increase of the particle diffusion coefficient was attributed to the osmosis generated by the asymmetric polymerization.[53]

The bubble propulsion mechanism was first introduced by Whiteside *et al.*[54] They directed millimeter-sized floating objects on the surface of a solution of H_2O_2 by means of the hydrodynamic flow generated by the bubble formation and release on a Pt surface during the fuel decomposition.[54] This mechanism, which is independent from the ionic strength of the medium, constitutes a very interesting alternative to the previously discussed self-electrophoresis.[55] This concept has been then used at the micro- and submicroscale for moving Pt/SiO_2 Janus spheres,[56] stogmatocytes (bowl-shaped polymers) loaded with Pt NPs[57] and silica beads tethered with a synthetic manganese catalase.[58,59] A strong interest is currently focused on tubular micro-engines driven by bubble production (also referred in the literature as microbots,[60] microrockets[61] or microjets[62]). These objects are microsized tubes containing one outer surface that is inactive towards the fuel and a catalytically active inner surface. In the presence of the H_2O_2 fuel, O_2 bubbles nucleate and grow at the catalyst surface until they are expelled through the larger opening inducing the motion towards the opposite opening (Figure 4.3b).

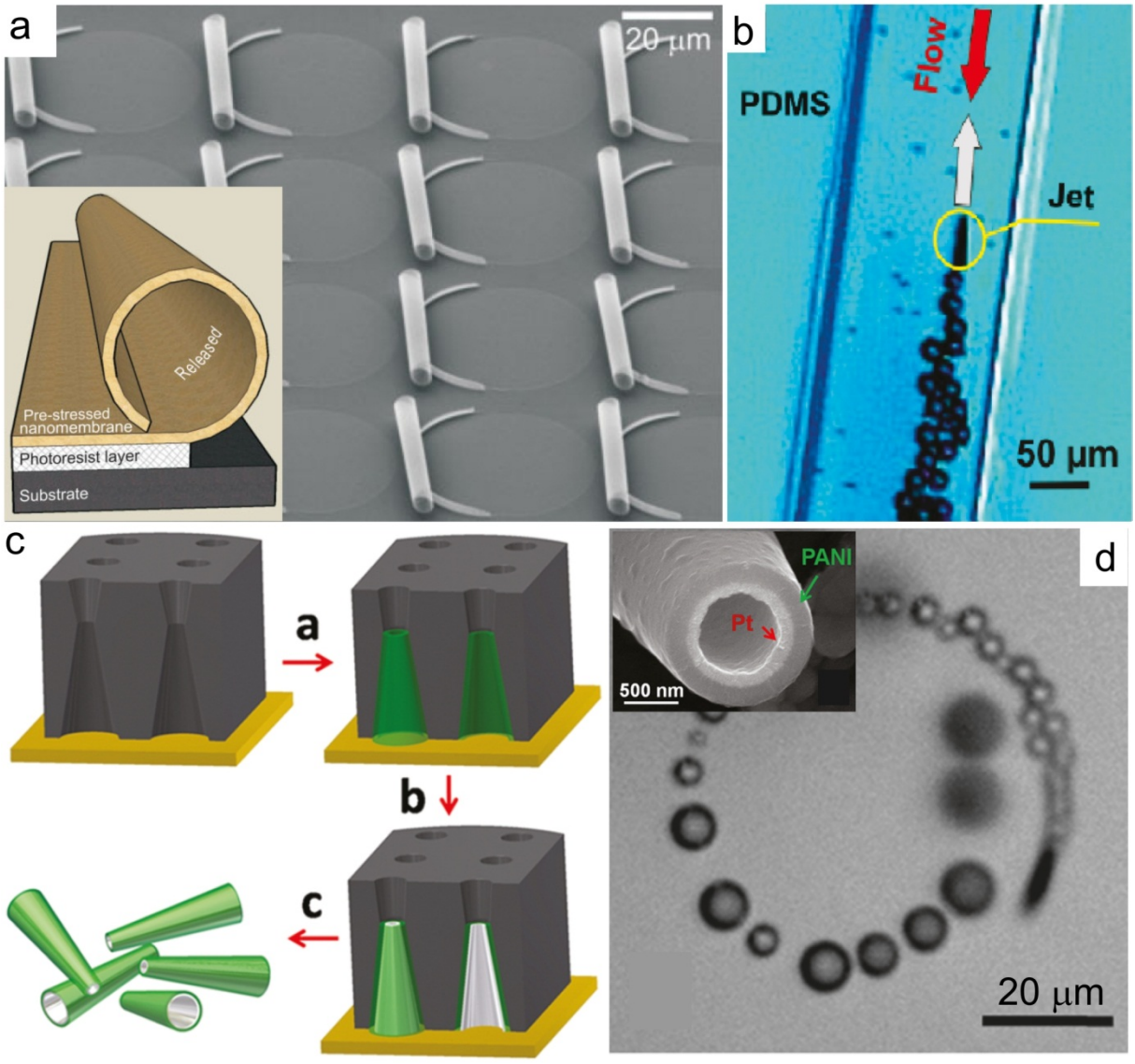

Figure 4.3. Bubble-propelled swimmers. a) SEM image of an array of rolled-up nanomembranes. Inset: scheme illustrating the roll-up process of a nanomembrane into a tube on photoresist. Reprinted from reference (61). b) Optical micrograph showing a rolled-up microengine flowing against the flow within a PDMS microchannel. Reprinted from reference (63). c) Preparation of bilayer PAni-Pt microtubes using polycarbonate membranes: (a) deposition of the PAni, (b) deposition of the Pt, and (c) dissolution of the membrane and release of the bilayer microtubes, reprinted from reference (64). d) Optical micrograph showing the circular motion of a tubular PAni-Pt microengine. Inset: SEM picture showing the smaller opening of a PAni-Pt microtubes. Reprinted from reference (64).

Schmidt's group developed the use of rolled-up nanotechnologies based on photolithographic methods for the synthesis of tubular miroengines.[61,65] First, a pre-stressed inorganic nanomembrane is deposited on a photoresist onto which other layers can be deposited (such as ferromagnetic ones) with the final one being the catalytically active layer. As shown in Figure 4.3a, the selective underetching of the sacrificial layer rolls-up the membrane, creating the final microswimmer shape.

Wang's group developed alternative strategies based on electrodeposition. The chemical etching of an Ag wire followed by the successive electrodeposition of metal layers can lead to tubular microengines after Ag dissolution and dicing.[66] As shown in Figure 4.3c, the successive electrodeposition of a conducting polymer, such as polypyrrole (PPy), poly(3,4-ethylenedioxythiophene) (PEDOT) or polyaniline (PAni), and the catalytic layer through the conical pores of a polycarbonate membrane can also lead to tubular microengines after removal of the template.[64,67] The catalyst is usually Pt but can also consist in a layer of an enzyme such as catalase.[68] Striking speeds up to 1400 bodylenghts s^{-1} have been recently reached at physiological temperature.[67] Coupled to a magnetic active layer, they showed an impressive degree of motion control in lab-on-chip microchannels (Figure 4.3b).[63] Their great potential for bioanalytics has been demonstrated[47] in applications such as dynamic isolation of cells,[69,60] nucleic acids,[70] proteins[71] and bacteria.[72] They have also been used for transporting,[63] assembling particles[73] and microdrilling biomaterials.[74] Recently, Zn-PAni tubular microengines have been propelled in strongly acidic media.[75]

4.1.3. Externally powered motion

However, the intrinsic problem of these approaches is the requirement of a fuel molecule. Indeed, typical media being strongly acidic or containing H_2O_2, they are not adapted for certain applications. Thus, alternative swimmers that can be used without fuel are attracting a lot of attention. In this context, the use of external electromagnetic fields seems to be an appealing approach. Some objects, namely surface walkers, require the use of a surface to break the spatial symmetry for generating a controlled motion. Doublets of paramagnetic beads,[76] superparamagnetic chains[77] and ferromagnetic nanowires[78] have been propelled in rotating magnetic fields using this approach. An increasing interest is focused on biomimetic approaches. Flagella like motion has been mimicked using centimeter[79] and micrometer-scaled (Figure 4.4)[80,81] rigid helical propellers in rotating magnetic fields. These objects are usually obtained by multistep laser writing[82] or vapor deposition techniques.[80] Propellers having a flexible magnetic tail have also been proposed. Wang's group developed flexible metal motors that can be steered by a rotating field. [83,84] Their synthesis was achieved by electrodeposition through alumina templates (similar to the bimetallic nanorods discussed previously) and a subsequent partial dissolution of the silver segment, which produces its flexibility.[83,84] Dreyfus *et al*. reproduced the spermatozoa flagella's motion to drive a red blood cell attached to a chain of magnetic particles in an alternating magnetic field.[85] Magnetic rigid helical motors have already been used for the transport and delivery of microparticles.[82]

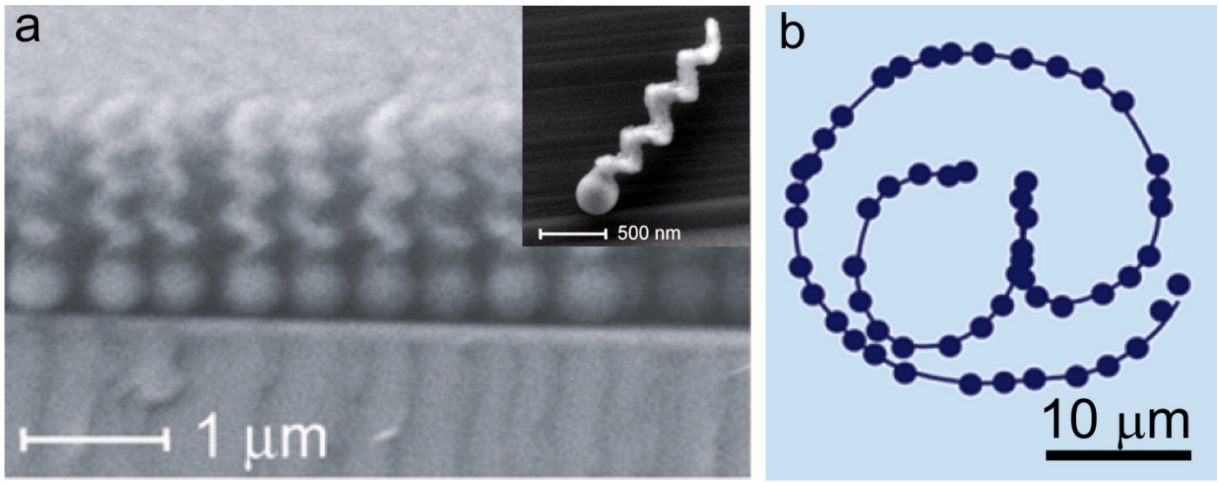

Figure 4.4. Magnetically-propelled swimmers. a) SEM image of a wafer section with a nanostructured film containing SiO_2 helical structures. Inset: detail on a SiO_2/magnetic helical structure. Adapted from reference (80). b) Trajectory of an individual nanoswimmer in solution that navigates along a preprogrammed track of the @ symbol. Reprinted from reference (80).

Electric field-driven motion is also a very promising area. Different electrokinetic phenomena are known to occur on particles when being exposed to an electric field, which can be used to induce object motion.[86] In uniform *d.c.* fields, well-known electrophoresis makes charged particles migrate towards the electrode of opposite charge. In uniform *a.c.* fields, diodes can be propelled in a controlled way, like first demonstrated by Velev *et al*.[87] As depicted in Figure 4.5a, the current rectification within the diode induces an electroosmotic ion flux on its electric double layer that propels the diode in the direction of either the cathode or the anode, depending on its surface charge. This phenomenon was used to drive translational (Figure 4.5b)[87,88] and rotational motions (Figure 4.5c)[87]. The interaction of the induced dipole of a particle with the gradient of a *d.c.* or *a.c.* field generates a dielectrophoretic force.[86,89] The force intensity and direction depends on the particle size as well as the dielectric properties of the particle and the surrounding medium. This leads to the attraction or repulsion of the particle from the region of highest electric field intensity.[89] It has been used for sorting of nanotubes,[90] cell separation,[91] colloidal crystal assembly[92] and many other applications.[89] Electrowetting can also be used to move objects. Takei *et al.* recently used this phenomenon to rotate a millimeter-sized capillary motor floating on a liquid drop.[93] Finally, as previously discussed in section 3.2.2.2., also Janus particles can be moved in *a.c.* fields.[94]

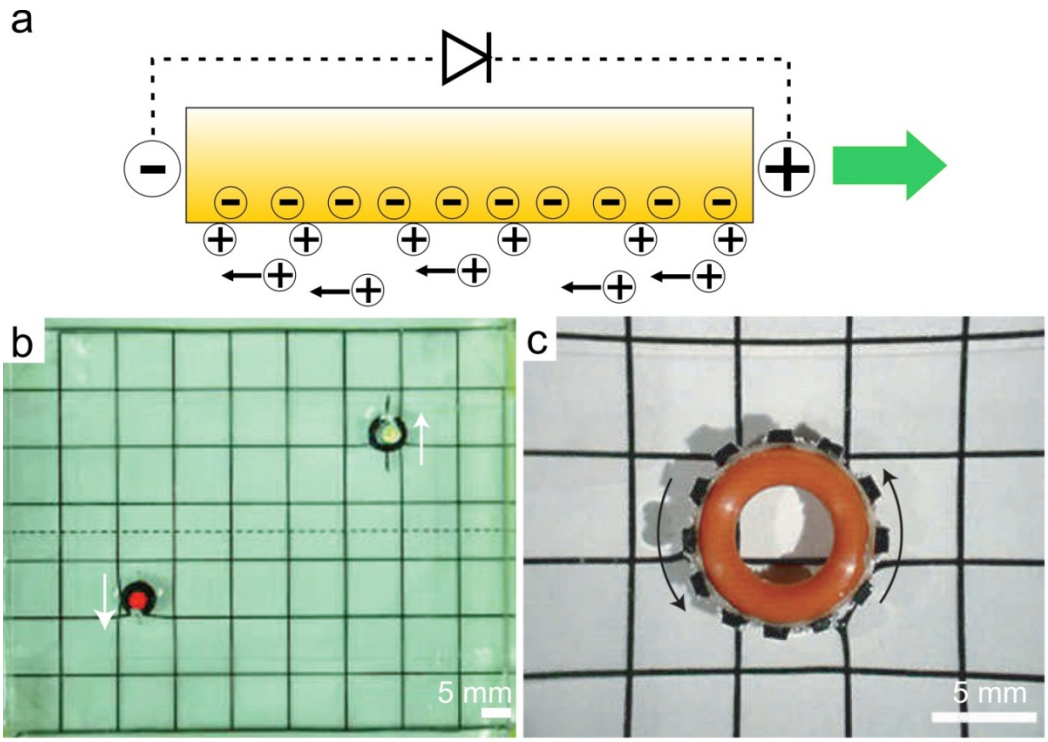

Figure 4.5. Diodes propelled in *a.c.* electric fields. a) Scheme illustrating the origin of the motion of diodes in an *a.c.* electric field. b) Two LEDs floating on the solution surface light up and move towards the top or bottom depending on the orientation of their anodes (marked with white paint).Reprinted from reference(87). c) Floating rotor ring with diodes attached to its periphery spins around when an external *a.c.* field is applied. Reprinted from reference (87).

While all the presented examples show the motion of objects differing in various characteristics, they have in common that one relevant parameter is asymmetric. Asymmetry is either incorporated in the structure of the swimmer, indeed bacteria (Figure 4.1a), magnetic swimmers (Figure 4.4) and microjets (Figure 4.3) are asymmetric in shape, and bimetallic nanorods (Figure 4.2) and diodes (Figure 4.5) are asymmetric in composition. Asymmetry can also be introduced by an electric like for example in the case of dielectrophoresis. With this, asymmetry appears to be crucial for the generation of a controlled motion. In order to understand the importance of asymmetry for the controlled motion of an object isolated from the influence of other parameters we propose the scheme shown in Figure 4.6. There we consider the model system of an isotropic particle which is submitted to the driving forces $\overrightarrow{F_{drive}}$ inducing the object's motion. $\overrightarrow{F_{drive}}$ can be generated, for example, by the release of a bubble. In the situation shown in Figure 4.6a, the forces acts at points of action which are distributed statistically over the particle surface, whereas in Figure 4.6b, the points of action are asymmetrically distributed over the particle by being localized only on one hemisphere. In each case, the object's motion is directed by $\overrightarrow{F_{net}}$, which results from the addition of all $\overrightarrow{F_{drive}}$ vectors. In Figure 4.6a, the vectors $\overrightarrow{F_{drive}}$ cancel each other out and no net motion results. In Figure

4.6b, in contrast, the asymmetric distribution of $\overrightarrow{F_{drive}}$ provokes that $\overrightarrow{F_{net}} > 0$ and a net motion is induced, perpendicular to the equatorial plane of asymmetry. In a real scenario, the simultaneous application of $\overrightarrow{F_{drive}}$ is less likely than a successive application, provoking a displacement from the center of mass and resulting in an erratic or Brownian motion (Figure 4.6a). In an analogous manner, oscillations around the motion axis can be provoked for the swimmer in Figure 4.6b. The morphological or chemical asymmetries are usually introduced to micromotors by means of synthetic techniques, often multistep procedures which require a complex equipment. In this context, the reactivity asymmetry offered by bipolar electrochemistry is a very appealing approach for motion generation that we will present in the following.

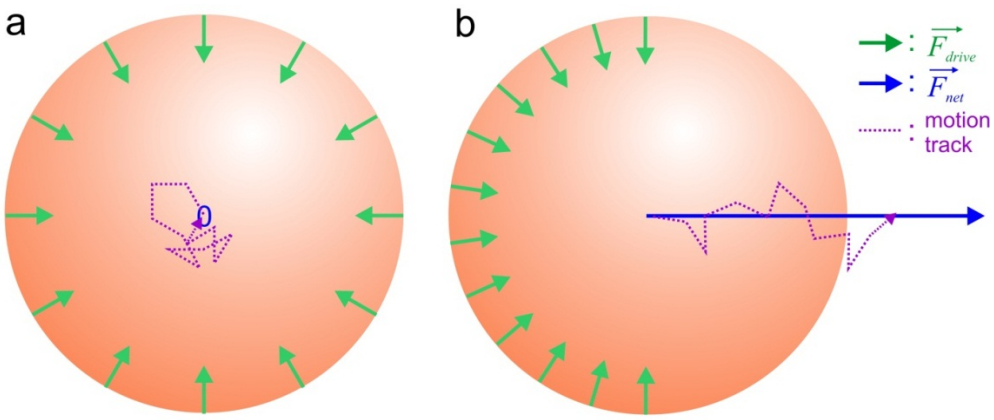

Figure 4.6. Asymmetry controls particle motion. a) Scheme representing the net force $\overrightarrow{F_{net}}$ and the motion track of a particle resulting from the driving forces $\overrightarrow{F_{drive}}$ being statistically distributed over the surface of an isotropic particle. b) Scheme representing the net force $\overrightarrow{F_{net}}$ and the motion track of a particle resulting from the driving forces $\overrightarrow{F_{drive}}$ being asymmetrically distributed over one hemisphere of an isotropic particle.

4.2. Patchy motors synthetized by bipolar electrochemistry

As described in Chapter 3, bipolar electrodeposition is a very attractive approach for the synthesis of Janus and patchy particles. The highly asymmetric structures that can be obtained are appealing objects for a use as synthetic motors, as we discuss in the following.

4.2.1. Magnetically-controlled motion

CMTs with a Ni patch at one extremity have been synthesized using the CABED process (section 3.1.2.1.). These asymmetric structures, recovered at the capillary outlet after the modification, were suspended in a water droplet on a transparent glass slide that was positioned in front of the objective of a transmission optical microscope. Using this set-up, the motion of isolated Ni/CMTs has

been observed and recorded. The challenge of this lies in following the object simultaneously in the x, y and z direction, with the additional problem that not the entire object is in the same focal plane. The effect of an external magnetic field was studied and we observed that the presence of a permanent magnet in close proximity to the droplet orientates the asymmetric object with the Ni "head" towards the magnet position. A circular motion of the magnet around the microscope objective induced the object rotation around its normal axis.[95] This is demonstrated by a series of optical micrographs in Figure 4.7, showing the controlled counterclockwise rotation of a Ni/CMT particle in the rotating magnetic field. Triggering a well-controlled rotation of the object would be difficult using homogeneously modified tubes, but can be easily carried out with the present objects due to their asymmetric nature.

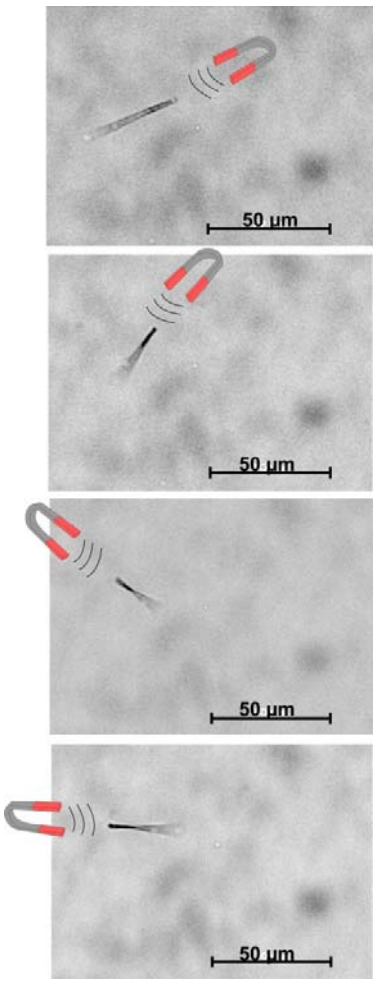

Figure 4.7. Series of optical micrographs showing the manipulation of a nickel modified CMT suspended in water by applying a counterclockwise rotating magnetic field. Reprinted from reference (95).

This proof-of-principle experiment shows that bipolar electrodeposition can be used to fabricate magnetic microswimmers. As this is a straightforward process, bipolar electrodeposition can strongly

compete with other usual synthetic procedure employed to produce magnetic swimmers (vapor deposition or laser writing, see section 4.1.3.). The versatility offered by this technique is also an advantage. Indeed, the strategy of using a Ni patch was chosen, but several other routes could have been taken. As an example, the incorporation of magnetic NPs within an electrodeposited matrix (see section 3.6.5.) could also be possible. This concept could also be adapted to sort conducting, semiconducting, and insulating carbon tubes. As the latter ones will not be modified with metal, whereas the two first categories of species will undergo a potential-dependent metal modification, they can be separated easily from a bulk mixture using a magnetic field and eventually post-purified, by acidic dissolution of the magnetic patch.

4.2.2. Chemically controlled motion

Platinum is a well-known catalyst for the decomposition of the hydrogen peroxide:

$$H_2O_2(l) \xrightarrow{Pt} H_2O(l) + ½\ O_2(g) \quad (4.1)$$

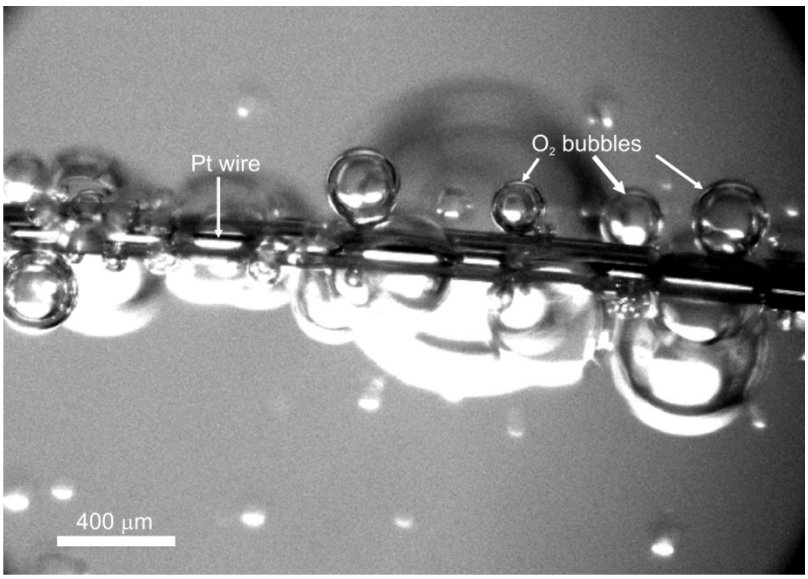

Figure 4.8. Optical micrograph showing the production of O_2 bubbles at the surface of a Pt wire immersed into a 30 wt.% aqueous solution of hydrogen peroxide.

An evidence of its reactivity is given by the intense spontaneous production of O_2 bubbles at the Pt surface when observed while being immersed into an H_2O_2 solution, (Figure 4.8). Due to this chemical activity, Pt has been intensively used in order to power swimmers at different sizes by a bubble propulsion mechanism (see section 4.1.2.). This propulsion mechanism is here explored using Pt/CMTs with centered and off-centered deposits. The procedure employed for obtaining such particles has been described in section 3.6.2.1. We first tested their ability to decompose hydrogen

peroxide. The production of O_2 bubbles was immediately observed as soon as the Pt/CMT hybrids were in contact with the reactant solution. The bubble generation can be tuned by the hydrogen peroxide content.

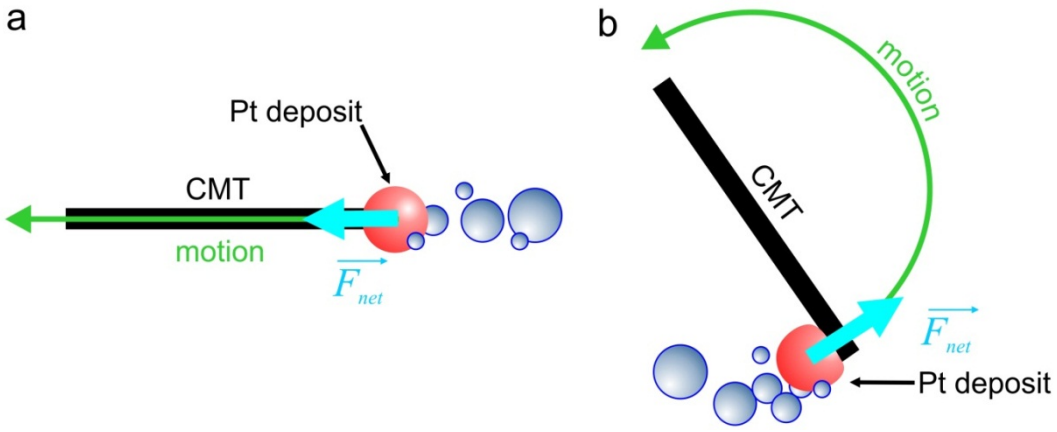

Figure 4.9. Schematic illustrations of the propulsion mechanism of Pt modified carbon tubes. a) Centered Pt deposit. b) Non-centered Pt deposit.

Figure 4.9a and b gives a schematic representation of the propulsion mechanisms causing the motions of CMT with a centered Pt deposit and an non-centered Pt deposit, respectively. At a CMT functionalized with a symmetric Pt particle at one extremity, the local mechanical perturbations due to the O_2 bubble formation and release generate a driving force $\overrightarrow{F_{net}}$ opposite to the direction of the translation motion.[56] In this ideal situation, a translation parallel to the longitudinal axis of the CMT in direction of its unmodified end results. In the case of an CMT with a non-centered deposit, $\overrightarrow{F_{net}}$ is parallel to the normal axis of the CMT, acting at its modified end and drives the rotation of the object.[49] The experimental observation of the movement of modified CMTs was achieved using the following procedure. One drop of the suspension was dried on a glass slide and the CMT-Pt objects were observed with the transmission optical microscope. 5 µl of a solution of 30 wt.% hydrogen peroxide in water was then added onto the CMTs. The imaging is experimentally very challenging for several reasons. *i*) The generation of a large quantity of bubbles is necessary to move the microhybrid, but these bubbles disturb the optical resolution by changing the nature of the local environment of the CMT. *ii*) The propulsion usually takes place in a three dimensional system, (x,y,z), and focusing with the optical microscope is only possible in the x,y plane. *iii*) The rate of bubble formation and the CMT acceleration do proceed with different time scales and it is therefore very frequent that the CMT moves out of the focal plane of the microscope. However, using the described protocol, several videos of propelled swimmers could be recorded, as shown in Figure 4.10 and Figure 4.11.

Figure 4.10 shows an optical picture of a CMT during motion. The four dioxygen bubbles were formed successively from right to left, resulting in an efficient propulsion of the carbon tube towards the bottom-left corner of the image. As mentioned above, this linear mode of motion can be explained by a CMT morphology with a centered Pt deposit and the related propulsion mechanism which is shown in Figure 4.9a.

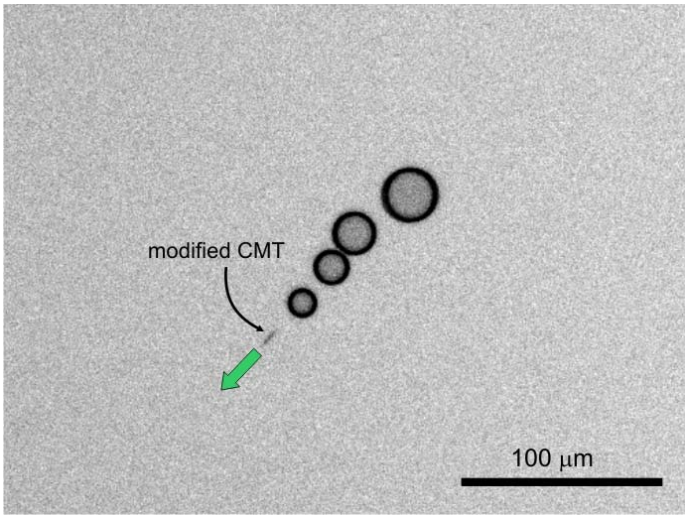

Figure 4.10. Linear motion of a microswimmer leaving a bubble train behind, as observed with the optical microscope. Reprinted from reference (96).

In addition to this linear mode of motion, rotation has also been observed. Figure 4.11 shows a selection of six optical images of a particular CMT performing a counterclockwise turn. These data are extracted from a large set of images in which the microhybrid is spinning several times. A time interval of 2.01 ±0.14 s/turn was estimated from 10 full turns which allows calculating an angular speed ω = 29.9 ± 2.1 rpm corresponding to a frequency $f \approx$0.50 Hz. The sequence of images in Figure 4.11 is in good agreement with the rotational motion of a CMT with a non-centered Pt deposit, depicted in Figure 4.9b. Therein, the CMT is rotating in the opposite direction with respect to the bubble evolution.

Whereas the majority of the literature approaches used for the generation of chemical microswimmers are multistep procedures, bipolar electrodeposition is straightforward and well adapted to generate such objects. Especially for rotational motion, complex synthetic procedures have usually to be employed to generate the appropriate particles.[49,50,97] In the presented study, it was possible to generate swimmers that can perform both, rotational and linear motion as a function of the position of the Pt cluster with respect to the CMT longitudinal axis. Moreover, due to the process versatility, other strategies might be explored in order to generate bubble-propelled microswimmers. For example, the encapsulation of Pt nanoparticles or enzymes (such as catalase)

within porous matrices (see section 3.6.5.) could be alternatives to the direct deposition of Pt. Tuning the porosity of Pt by introducing surfactants[98] in the bipolar electrodeposition mixture can also be considered as a way to enhance the bubble production rate, and thus the swimmer speed.[36]

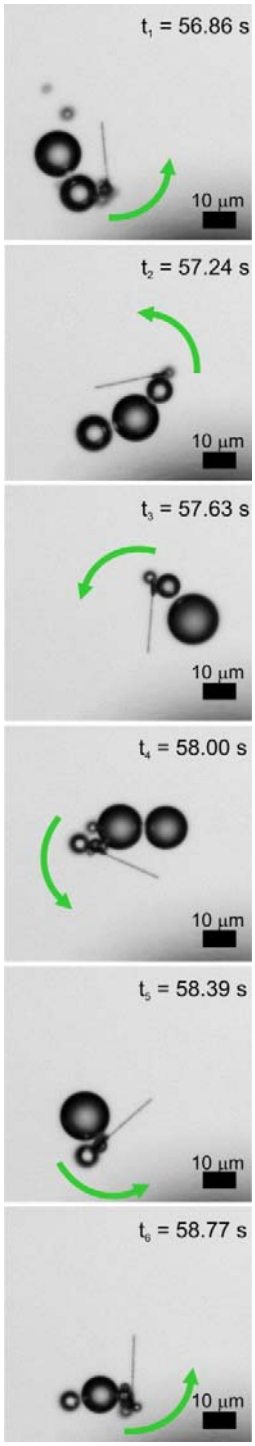

Figure 4.11. Series of optical micrographs of a counterclockwise rotating microswimmer. Reprinted from reference (96).

4.3. Bubble induced motion on chemically isotropic objects

As discussed previously in section 4.1. and experimentally illustrated by the two previous sections, the key concept for the propulsion of particles is asymmetry (see Figure 4.6). The great majority of the techniques used for generating controlled motion of particles requires the use of intrinsically asymmetric swimmers. Because bipolar electrochemistry directly provides a chemical break of symmetry, which can be induced on any kind of conducting object, it is an appealing alternative to the existing propulsion mechanisms.[99] We will now present its direct use for the propulsion of isotropic objects.

4.3.1. Translation

As shown in section 3.6.4., water splitting can be carried out at both extremities of a bipolar object. In an acidic aqueous solution, the following reactions take place (Figure 4.12a):

$$2\ H^+(l) + 2\ e^- \rightarrow H_2(g) \quad E^0 = 0\ V\ vs\ NHE \tag{4.2}$$

$$2\ H_2O(l) \rightarrow O_2(g) + 4\ H^+(l) + 4\ e^- \quad E^0 = 1.23\ V\ vs\ NHE \tag{4.3}$$

At the cathodic and anodic pole of the object, gas bubbles are produced that can be visualized with the optical microscope, as presented by Figure 4.12b which shows a 1 mm sized metallic bead located in a 1.6 kV m^{-1} electric field. To maintain electroneutrality at the bipolar electrode, the electron production and consumption must be equal at both sides. As a result, considering reactions (4.2) and (4.3), the produced H_2 volume (left side) is twice the produced O_2 volume (right side). In analogy with bubble-powered nanomotors (see section 4.1.2. and 4.2.2.) this asymmetric bubble production is responsible for a directional motion. Figure 4.12c shows a conductive microswimmer observed with the transmission microscope that is propelled by using this mechanism. The 285 µm sized bead is moving towards the cathode in a polydimethylsiloxane (PDMS) microchannel shown in Figure 4.13a (see appendix 3 for details about its fabrication) at a speed v = 20 µm s^{-1}, which corresponds to one bodylength every 14.2 s.

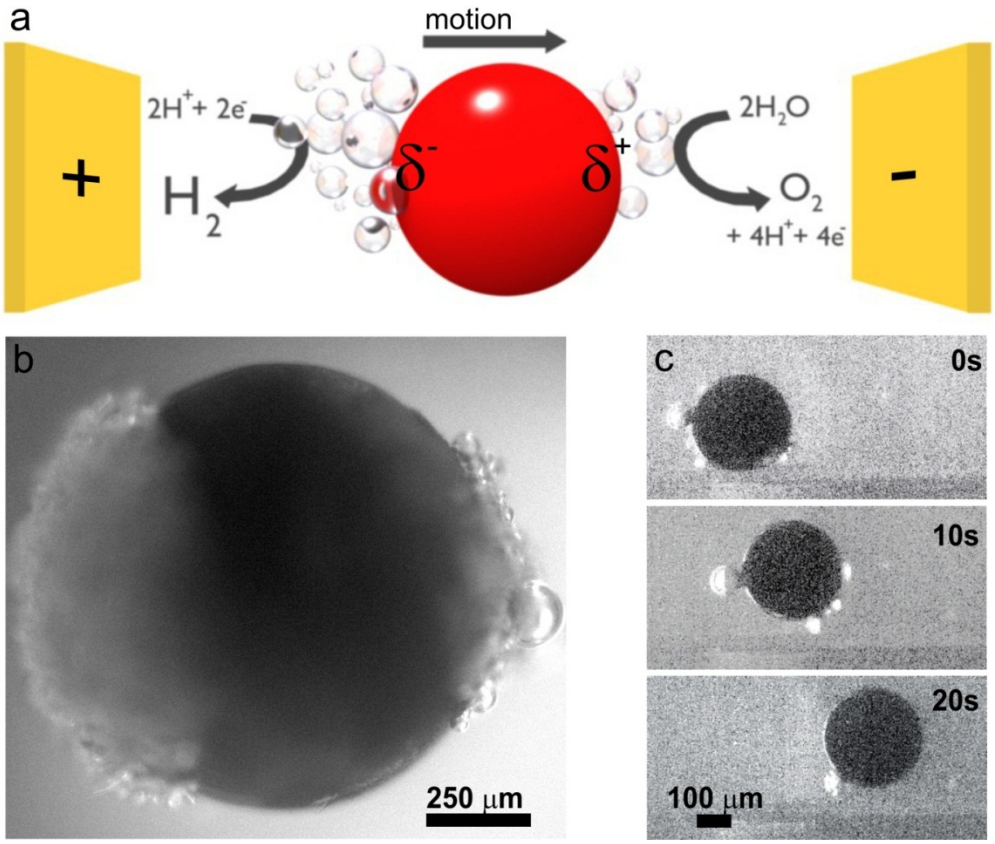

Figure 4.12. Competing bubble production. a) Scheme of water splitting, induced by bipolar electrochemistry. b) Optical micrograph of a 1 mm stainless steel spherical bead exposed to a 1.6 kV m^{-1} electric field in aqueous 24 mM H_2SO_4. The left part of the bead is the cathodic pole where H_2 bubbles are produced and the right part is the anodic pole where O_2 bubbles are produced. c) Series of optical micrographs showing the translational motion generated on a 285 μm glassy carbon sphere in a PDMS microchannel exposed to a 5.3 kV m^{-1} electric field in aqueous 7 mM H_2SO_4. Reprinted from reference (99).

As the produced O_2 bubbles hinder this motion, one can increase the speed by suppressing this reaction, like illustrated in Figure 4.14a. The lower redox potential of the hydroquinone (HQ)/benzoquinone (BQ) redox couple, compared to the one of H_2O/O_2 (reaction 4.3), makes it an ideal couple for suppressing the O_2 production. In an aqueous HQ solution the following reactions occur at the cathodic and anodic poles of the bipolar object, respectively:

$$2\ H^+(l) + 2\ e^- \rightarrow H_2(g) \quad E^0 = 0\ V\ vs\ NHE \tag{4.2}$$

$$HQ(l) \rightarrow BQ(g) + 2\ H^+(l) + 2\ e^- \quad E^0 = 0.7\ V\ vs\ NHE \tag{4.4}$$

In this case the bubble formation takes place only at the cathodic side of the object, leading to a higher speed (Figure 4.14a). In the experiment that is reported in Figure 4.14b the motion of a metal bead (d = 1 mm) was recorded using a digital camera placed at the top of the cell depicted in Figure

4.13b. The bipolar electrode is propelled over a distance of 1.5 cm with a speed v = 512 µm s^{-1} (about 1 bodylength every 2 s) in an electric field of 1.3 kV m^{-1}. The polarization potential difference ΔV that is generated between the two sides of the bead is 1.3 V, a value that is in agreement with the thermodynamic value ΔV_{min} corresponding to the combination of both reactions (see section 1.2.). These coupled redox reactions can be used to move the object under various pH conditions, because the potential of proton reduction and HQ oxidation will shift by 60 mV per pH unit in the same direction, which means that the overall polarization, needed to drive the two reactions simultaneously, will remain the same, no matter which pH.

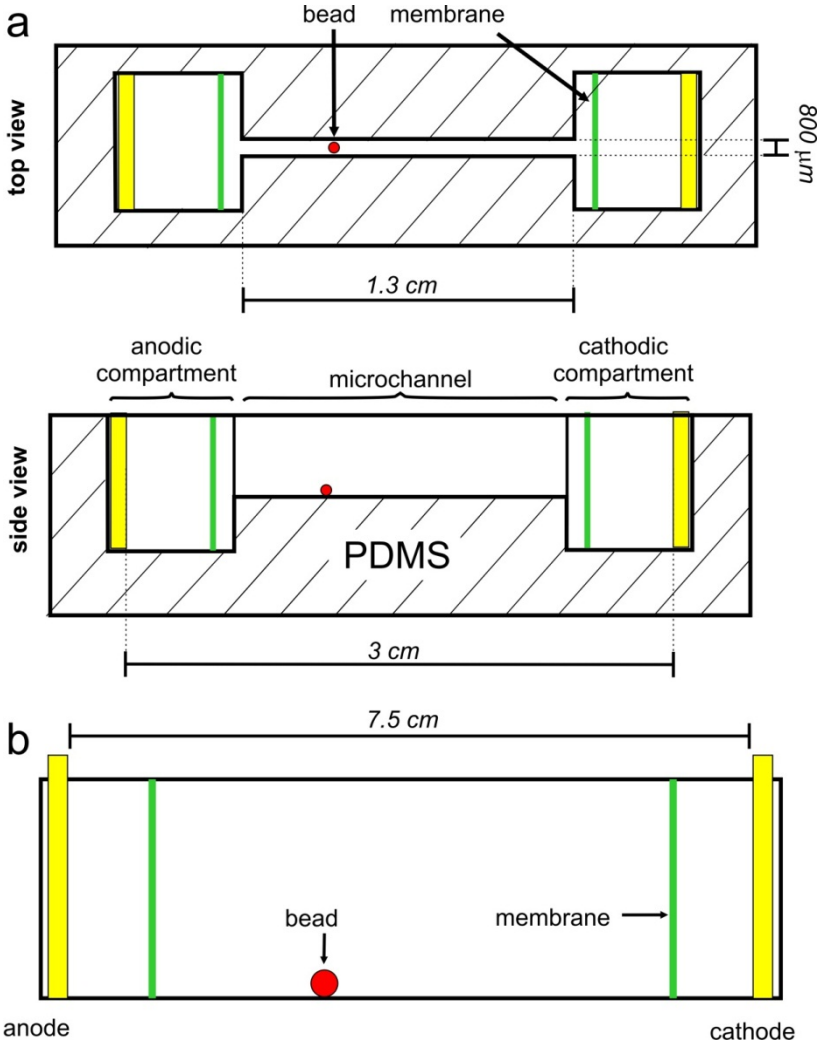

Figure 4.13. Description of the electrochemical cells. a) Cell used for the propulsion of micrometer-sized GC beads. b) Side view of the setup used for the propulsion of 1 mm stainless steel beads.

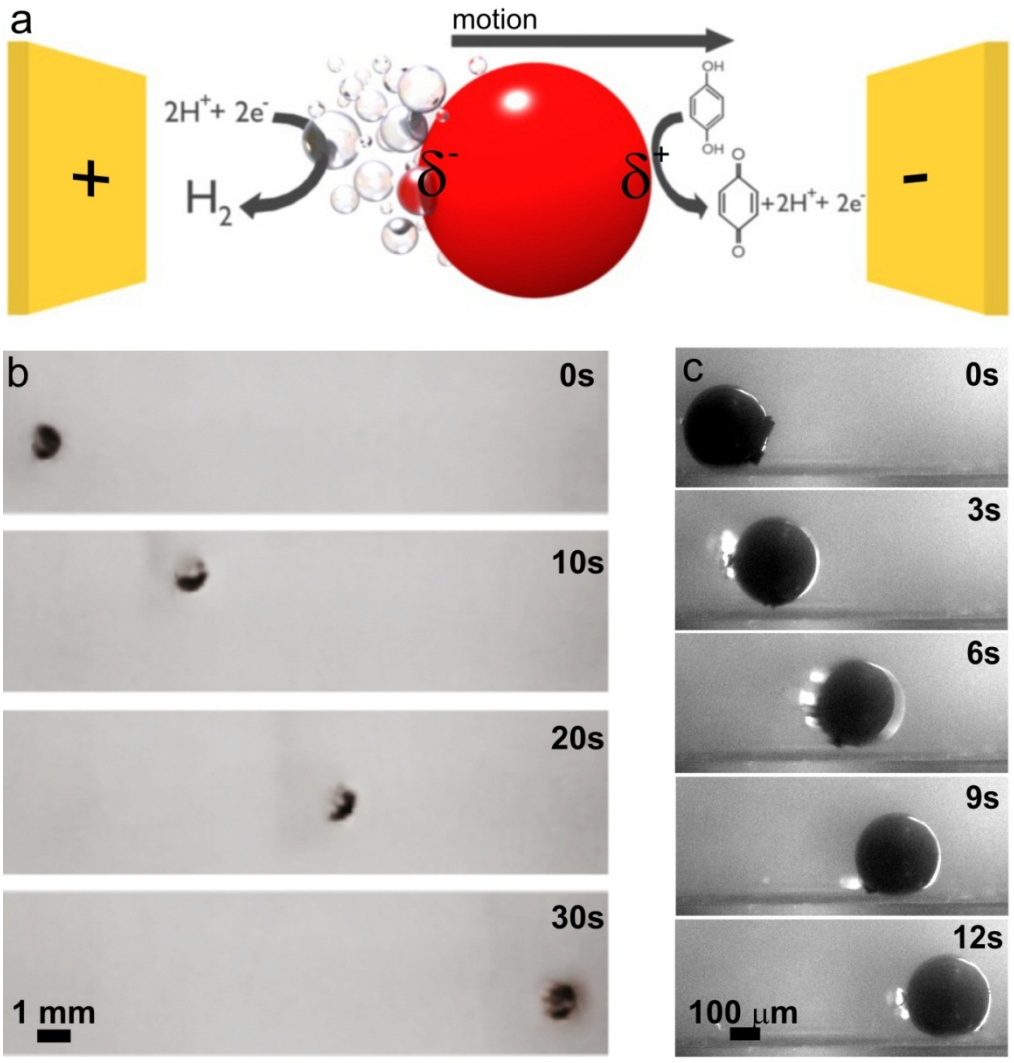

Figure 4.14. Quenching of O_2 bubble production. a) Scheme of proton reduction and HQ oxidation. b) Translational motion generated on a 1 mm stainless steel bead exposed to a 1.3 kV m^{-1} electric field in 24 mM HCl and 48 mM HQ. c) Translational motion generated with a 275 µm GC sphere in a PDMS microchannel with a 4.3 kV m^{-1} electric field in an aqueous solution of 7 mM HCl and 14 mM HQ. Reprinted from reference (99).

For micrometer-sized objects, as in the experiment reported Figure 4.14c, a higher electric field is required to induce a ΔV of the same order of magnitude. An electric field of 4.3 kV m^{-1} was applied in the cell reported in Figure 4.13a, which corresponds to a ΔV of 1.18 V across the 275 µm-sized GC bead. We used in this case GC to illustrate that it is a quite general phenomenon that not only occurs on one type of conducting material. On the basis of the data of Figure 4.14a, the bead velocity is v = 62 µm s^{-1}, or 1 bodylength every 4.4 s. Watching the imperfections on the bead surface, one can easily note that the bead is rolling inside the microchannel while moving. These imperfections are certainly also responsible, like surface roughness in general, for the bubble nucleation and release. No attempts were made to control this parameter, except that a surfactant (GOJO NXT) has been

added to the solution to decrease the size and the adherence of the bubbles to the surface. This leads to a more homogeneous release and thus also to a more regular motion of the objects. It becomes also clear from the observations that the motion is due to the hydrodynamics produced by the local bubble release as a consequence of the bipolar reaction, and not due to other electrokinetic phenomena. In addition, a control experiment carried out using an isolating glass bead did not lead to any movement. From this, one can conclude that under the present conditions, electroosmotic flow (EOF) is not playing a significant role; however, it might become important when going to higher electric fields or for objects of smaller dimensions. The difference of measured velocity in the two experiments is mainly due to three parameters, that is, the difference in the generated ΔV values, the difference of hydrochloric (HCl) acid and HQ concentrations, which influences the reaction kinetics and thermodynamic parameters, and the different composition of the objects. This latter point is crucial, because different materials have different overpotentials/activation energies for carrying out a certain redox reaction. In particular it is more difficult to reduce protons on the carbon beads compared with the metal beads. Therefore, one can expect that in the latter case the local current that results in H_2 production will be higher compared to the one on carbon. This means that for the same external driving voltage more bubbles will be produced per time unit on the metal bead, leading *in fine* to more efficient propulsion and thus a higher speed. This shows that the speed of the objects can be controlled by using different experimental parameters. The concept has nevertheless some limits in terms of particle size. First of all when the objects become too small (typically in the micrometer or submicrometer range), viscosity effects become very important and therefore momentum-based propulsion is increasingly difficult. The friction that the particle has to overcome in order to move is amplified, due to the disadvantageous evolution of the surface to volume ratio. Second, the particles are more and more subjected to Brownian motion and therefore more force/energy has to be applied to fight against this. Finally, the external driving force, necessary in our experiment to generate a sufficient polarization, scales inversely with the particle diameter (Equation 1.4). This means that for moving smaller objects one needs larger fields, which is somewhat counterintuitive, because usually bigger objects need a bigger external driving force.

These experiments showed that bipolar electrodeposition can directly induce a controlled motion of conductive objects by a bubble-propulsion mechanism. Control experiments showed that this motion is not due to one of the usual propulsion mechanisms, it is therefore a new concept for chemical locomotion. The advantage of this mechanism compared to most of the existing ones (see section 4.1) resides in the fact that theoretically every kind of conducting object can be propelled without the need of any synthetic procedure for breaking the symmetry of the system.

4.3.2. Rotation

Besides allowing translations, the described concept can be adapted to generate rotational motion. We designed two kinds of bipolar electrochemical rotors, the first one rotating in a horizontal plane (Figure 4.15) and the second one in a vertical plane (Figure 4.18). The schemes of the rotors are represented in the insets of Figure 4.15 and Figure 4.18a. The rotors were made by cutting polycarbonate sheets doped with carbon particles. To concentrate the bubble production on specific sites, the rotor surface has been shielded with an insulating polymer (blue parts in Figure 4.15 and Figure 4.18a), except the extremities (red parts in Figure 4.15 and Figure 4.18a). Glass parts were made by melting glass capillaries and adjusting them to the desired shapes. In the center of the cross, a small glass cup was fixed and positioned on top of a very thin glass stick axis. The motions were recorded by a digital camera. Figure 4.16b shows the rotation of a horizontal rotor powered by bipolar electrochemistry-induced water splitting.

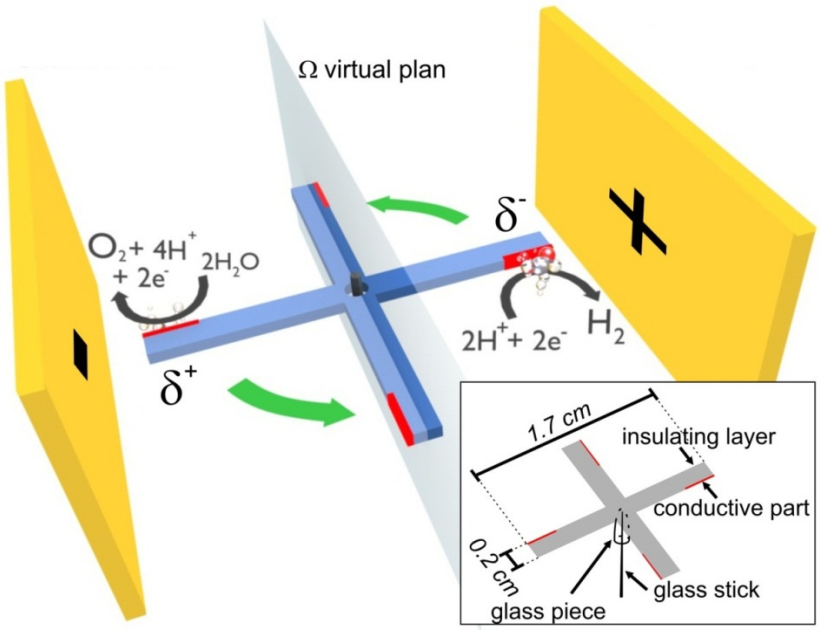

Figure 4.15. Scheme of a horizontal rotor powered by bipolar electrochemistry-induced water splitting; red areas represent the conductive parts exposed to the solution, whereas the blue areas have been shielded with an insulating polymer. Inset: description and dimensions of the horizontal rotor, the rotor was placed in the middle of the cell shown in Figure 4.13b. Reprinted from reference (99).

Bubble production on the rotor blades can be observed with the naked eye (Figure 4.16b) or by optical microscopy, as shown in Figure 4.16a. The water-splitting reactions are induced at the extremities of the object by imposing an electric field $\mathscr{E}$ = 0.5 kV m^{-1}, corresponding to a ΔV of 8.5 V. While rotating, the electroactive parts of the cross invert their polarization, when passing the virtual

plane Ω (Figure 4.15) which is parallel to the external electrodes and includes the rotor axis. The conducting parts of the cross are positioned in such a way that an anticlockwise motion is generated. An average angular speed ω = 1.9° s^{-1} has been calculated, which correspond to 0.32 rpm. However, this speed is not completely constant in time as can be seen on the graph presented in Figure 4.17b. This can be understood by considering the theoretical polarization of the object as a function of time.

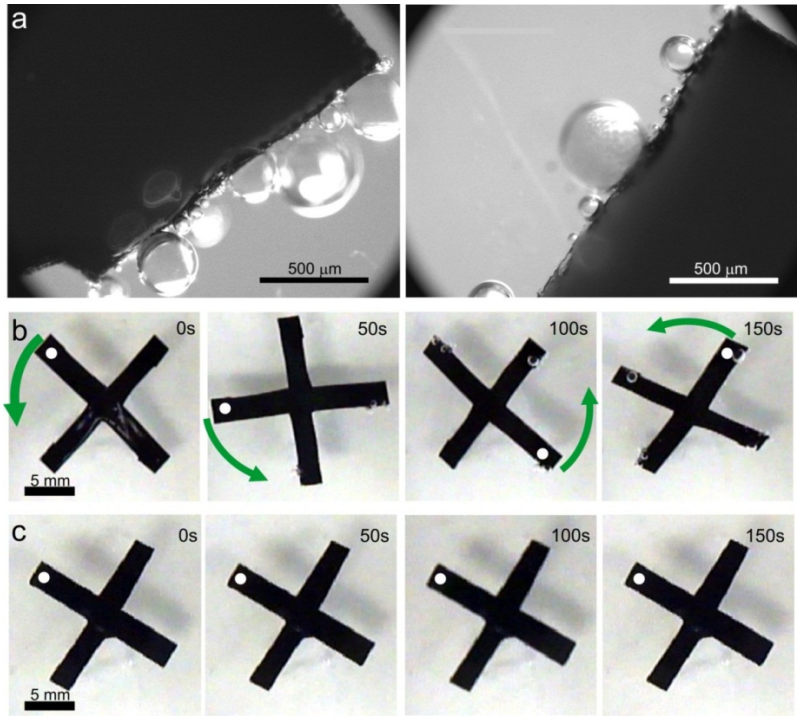

Figure 4.16. Horizontal bipolar rotor. a) Optical micrographs showing the production of H_2 bubbles at the cathodic blade (left) and the production of O_2 bubbles at the anodic blade (right) of the rotor. b) Series of photographs showing the rotational motion of a horizontal bipolar rotor in an electric field of 0.5 kV m^{-1} in 50 mM HCl. In order to help visualization, one white spot has been made on a blade. c) Series of photographs showing an insulating polypropylene cross in an electric field of 0.5 kV m^{-1} in 50 mM HCl. In order to help visualization, one white spot has been made on a blade.

Figure 4.17a illustrates that when the cross is exposed to the external electric field, the polarization voltage of the rotor arm 1 can be expressed as:

$$\Delta V = \mathscr{E} d \cos\phi \tag{4.5}$$

and the one of the arm 2 as:

$$\Delta V = \mathscr{E} d \sin\phi \tag{4.6}$$

Therefore, the overall polarization voltage, which is the driving force for propulsion, can be expressed as the sum of 4.5 and 4.6:

$$\Delta V = \mathscr{E} d(\sin\phi + \cos\phi) \tag{4.7}$$

This induces an acceleration of the rotor, and will lead to a maximum speed with a theoretical shift of 90° with respect to the maximum of the driving force. The experimentally obtained variation in speed is qualitatively in agreement with this theoretical function (see Figure 4.17c). In the beginning of the experiment there is indeed a good correlation between the theoretical maximum of the driving force, which appears at an angle of ϕ = 45°, and the maximum of experimental rotor speed which is located around 140°. The further velocity oscillations are slightly shifted with respect to the theoretically expected values, most likely because the size of the bubbles and the time when they detach from the blade is subject to random fluctuations. A control experiment with a completely insulated cross, shown in Figure 4.16c, resulted in no motion, demonstrating that the rotation is exclusively due to bipolar electrochemistry.

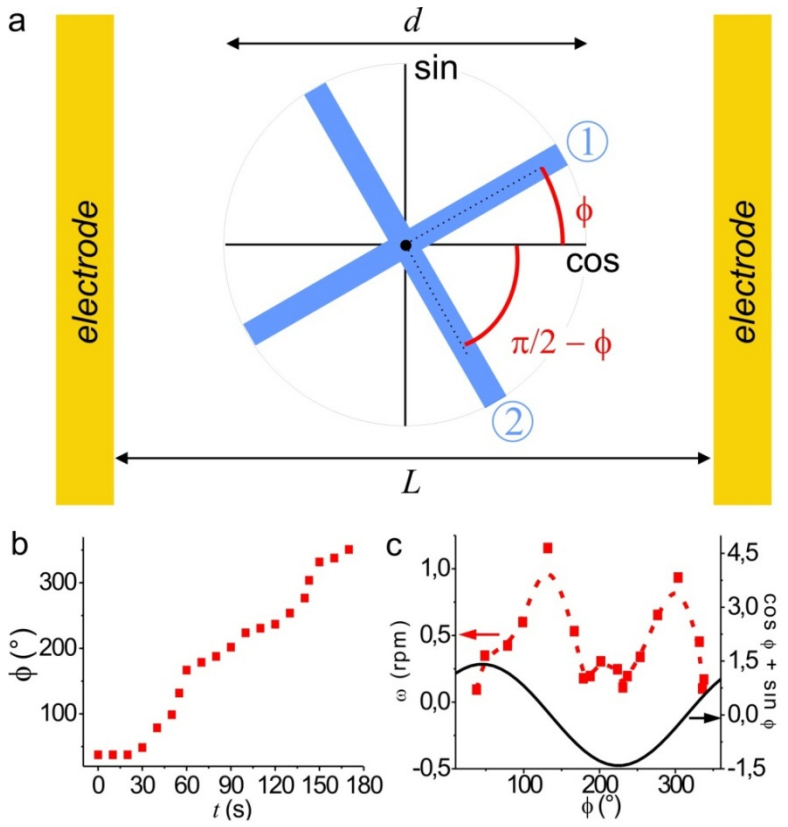

Figure 4.17. Polarization and rotation. a) Scheme illustrating the variation of driving force for the whole object as a function of the angle ϕ with respect to the external electrodes. L is the distance between the electrodes and d the rotor diameter. b) Graph showing the evolution of the rotation angle ϕ as a function of time t. c) Graph showing the evolution of the experimental rotor speed ω (red curve), as well as the theoretical variation of driving force (black curve) as a function of the rotation angle ϕ. Reprinted from reference (99).

A vertical rotor can also be designed and is a very good option to enhance the rotational speed, as this configuration takes advantage of the buoyancy of the bubbles generated below the rotor blade. In general, when gas is released from the object, and while the resulting bubble is still attached to the object, the expansion of the gas bubble in the liquid exerts a force on the object, which pushes the latter one in the opposite direction. In the particular case of the vertical rotor, the gas bubbles are sticking to the rotor blade and are located below the rotor blade because the rotor has been designed on purpose in that manner. This means that in addition to the above mentioned force, the buoyancy of the gas exerts a second type of force on the rotor blade (Figure 4.18a, left side), leading in principle to a higher speed. However, if the bubbles adhere too strongly to the blade they will slow down the motion once they are dragged downwards (right side of the rotor). Therefore, one has to make sure that they will detach from the rotor when the blade is in the vertical position, essentially by the addition of small amounts of surfactant. The speed can be further optimized by suppressing again the O_2 evolution, occurring at the opposite blade, by adding HQ, because generated O_2 bubbles might stick to the blade, and in this case the buoyancy slows down the rotation, as the forces are orientated in the wrong direction. A beneficial side-effect of using HQ, which leads to a higher velocity, is an increase of the H_2 bubble production at the cathodic pole for the same external electric field, because a lower ΔV_{min} is required for the combination of these two redox reactions (see section 1.2.). Figure 4.18b shows the motion of a vertical rotor experiencing a ΔV of 8.5 V. The motion seems to be slightly more homogeneous in time (Figure 4.18c) than for the horizontal configuration and the extrapolated average angular speed is 4.2° s^{-1} (0.70 rpm), more than two times higher compared to the previous speed. Although in this case the rotor is submitted to a sigmoidal variation of the driving force (Figure 4.17a), the angular speed is leveled out by the buoyancy effect, specific to this setup.

These experiments showed that bipolar electrochemistry can be directly used for the rotation of objects. The induced motion is not homogeneous in time, on the one hand due to the random detachment of the bubbles from the object and on the other hand due to intrinsic variations in polarization of the rotors. In the latter case an increase of the number of rotor blades can make this kind of variations smoother. The angular speed can be tuned by changing different parameters such as the solution composition and the electric field strength. One can imagine that this kind of rotors could be used for producing additional mechanical energy in a setup where electric fields are used anyway, such as in electrolysis reactors.[99]

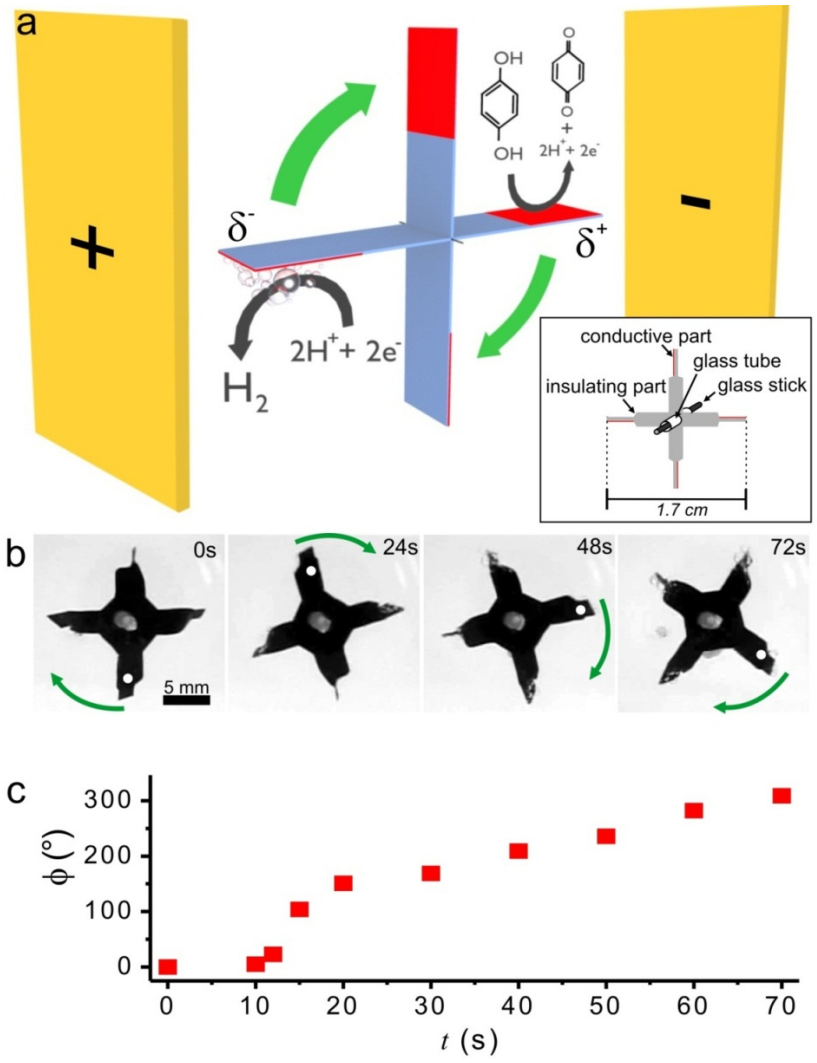

Figure 4.18. Vertical rotor. a) Scheme of a vertical bipolar rotor powered by the reduction of protons coupled with HQ oxidation. Inset: description and dimensions of the vertical rotor. b) Series of photographs showing the rotational motion of a vertical bipolar rotor, in an electric field of 0.5 kV m^{-1} with 50 mM HCl and 100 mM HQ. c) Graph showing the evolution of the rotation angle ϕ as a function of time *t*. Reprinted from reference (99).

4.3.3. Levitation

The translation motion presented in section 4.3.1. has been achieved in an horizontal plane. We will now discuss the vertical ascension of bipolar electrodes using a similar bubble propulsion mechanism. For these experiments U-shaped glass capillaries (Figure 4.20a), that were made by manual shaping of Pasteur pipettes with a Bunsen burner were used as cells. A few drops of surfactant were added to 10 mL of an aqueous solution containing HCl (25 mM) and HQ (48 mM). The solution was carefully injected into the cell to prevent the formation of air bubbles. The cell was maintained with its arms in a vertical position and the GC bead (with a diameter around 1 mm) was then inserted into one arm of the cell. Due to the slightly conical shape of the capillary the bead dropped until it was stopped by the surrounding capillary walls. Movies showing the BE motion were recorded using a digital camera.

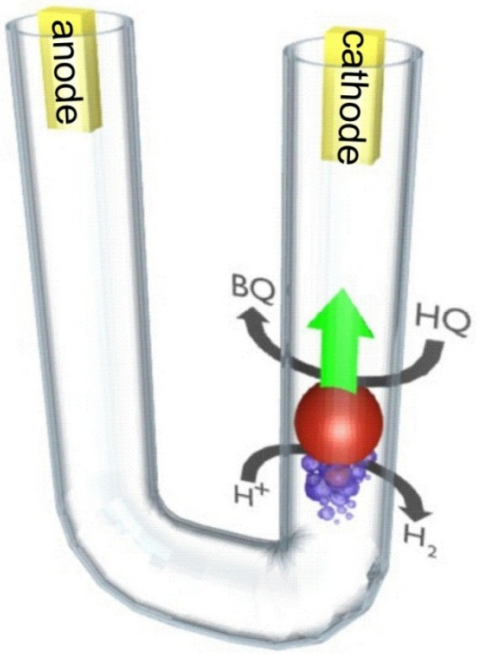

Figure 4.19. Scheme of the levitation mechanism for a conducting bead in a U-shaped cell.

Like previously, the proton reduction (reaction 4.2) at the cathodic pole of the object, coupled with the HQ oxidation (reaction 4.4) at the anodic pole induces the asymmetric production of bubbles at the object surface. If the external electrodes, localized at the capillary entrances, are polarized in such a way that the H_2 flow is generated underneath the bead, this bipolar mechanism can lead to the levitation of a conducting bead as illustrated in Figure 4.19. GC has been chosen as the swimmer material because of its low density (1.4 g cm^{-3}) compared to many other conducting materials. This decreases the force needed to overcome gravity for an object with a given volume. Figure 4.20b

shows the motion of a GC bead with a diameter around 1 mm (mass = 0.7 mg) in a glass capillary. The applied voltage being 270 V with a distance of 11.5 cm between the two feeder electrodes, the overall electric field $\mathscr{E}$ is 23.5 V cm^{-1}. One can calculate that this corresponds to a polarization voltage ΔV of 2.3 V between the top and the bottom part of the bead. This value, that is more than three times higher than the theoretical value 0.7 V, needed for inducing reactions (4.2) and (4.4) at both extremities of the object in standard conditions, shows that these two reactions are highly favored. The resulting bubble production leading to the bead levitation can be clearly observed at the bottom of the bead in Figure 4.20b. Stopping the electric field directly induces a dropping of the bead, but a new ascension can be triggered by re-applying the electric field.

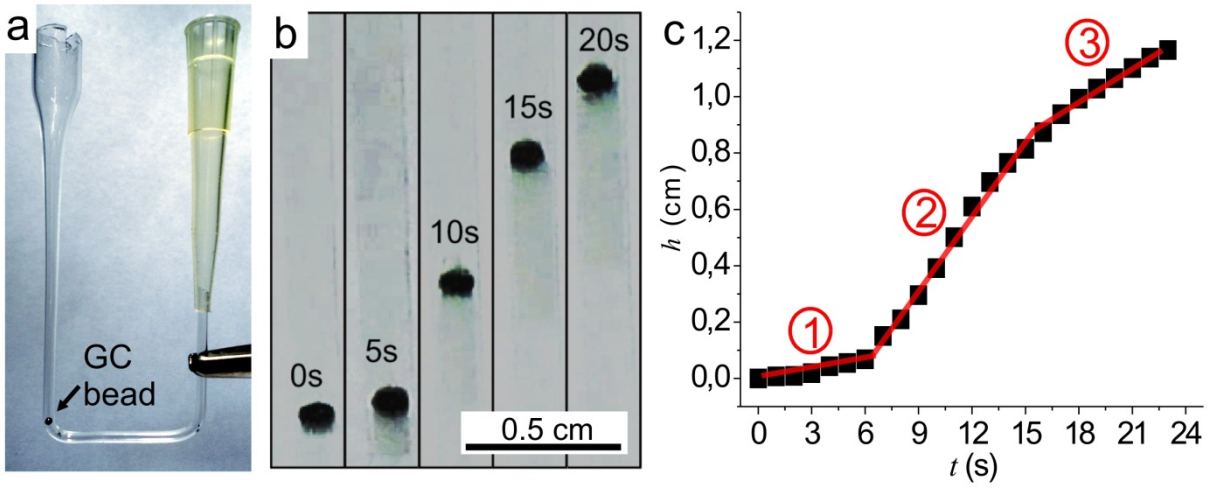

Figure 4.20. Levitation of a GC bead. a) Photograph showing a typical U-shaped cell used for the levitation experiments, the diameter of the GC bead is about 1 mm. b) Series of optical micrographs showing the rise of a carbon bead in a glass capillary. c) Graph showing the height h evolution as a function of time t. Reprinted from reference (100).

The graph presented in Figure 4.20c shows the evolution of the bead height during the rising period. This profile can be divided into three distinct parts from which the speed v can be extracted based on the curve slope. In the first part of the curve, the bead does not move significantly (v = 0.1 mm s^{-1}). This part corresponds to the period of bubble accumulation underneath the bead for the generation of a sufficiently high buoyancy force to overcome gravity. After this initial phase, at around t = 6 s, the height evolution starts to be linear for 8 s with v = 0.9 mm s^{-1}. Finally, because the shape of the cell arm is slightly conical, some space between the bead and the glass walls becomes available for bubbles to escape from below the bead, which induces a decrease of the speed during the third phase (v = 0.4 mm s^{-1}). One can easily imagine using this approach of bipolar electrode levitation for stirring, cleaning or unblocking microchannels.

4.3.3.1. Yo-Yo motion

Based on the observation, that the swimmer motion can be controlled by changing the capillary shape, we will demonstrate in the following that a Yo-Yo type motion can be generated on purpose when using a conical capillary. For these experiments a well pronounced conical shape was intentionally given to the cell arms.

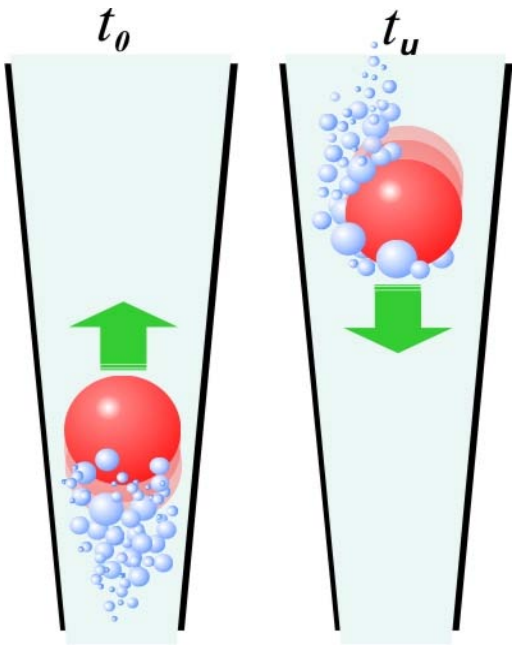

Figure 4.21. Scheme of the Yo-Yo motion mechanism induced by a cone-shaped capillary. Reprinted from reference (100).

Figure 4.21 describes the origin of the Yo-Yo motion. At the initial time t_0, the capillary cross-section at the bead location forces the H_2 bubbles to stay below the bead, resulting in a levitation of the bead in the same manner like previously described. Because the capillary cross-section gradually increases during the particle elevation, the amount of bubbles that are able to escape from underneath the bead increases simultaneously. The ascension continues until the extreme case, at $t = t_u$, where the bead is located in a part of the capillary with a cross-section that is sufficiently large so that a majority of the produced H_2 can escape. This stops the bead rising and finally leads to its fall. The dropping occurs until the bead reaches, at $t = t_d$, a capillary cross-section small enough to trap enough bubbles underneath, inducing another ascension. In theory, this cycle can be repeated indefinitely. Figure 4.22a and b show the evolution of the bead position as a function of time, the applied electric field being 27 V cm^{-1}. Until t = 22 s, the elevation profile is similar to the one observed in Figure 4.20. At t = 21 s in Figure 4.22a, the H_2 flow escaping from under the bead is clearly observable. After the bead reaches h = 1.6 cm at t_{u1} = 22 s, the H_2 production that occurs under the

bead is not sufficient to maintain the elevation, which causes a drop of the bead over about one bodylength before the capillary cross-section is again small enough to induce another elevation period at t_{d1} = 26 s. This up and down cycle can be observed several times in a row, describing a signal that is sinusoidal in a first order approximation. The signal amplitude A, calculated as the average amplitude of the four falling segments from t_{un} to t_{dn} and the three ascensions from t_{dn} to t_{un+1} is A = 1.5 mm (≈1.5 bodylengths). The period calculated as the average time between t_{un} and t_{un+1} is T = 10.7 s which results in an oscillation frequency f = 0.09 Hz. Since the amplitude and frequency characteristics depend strongly on the capillary shape, the applied electric field, the density of the bead as well as the viscosity of the medium, they can be easily tuned by playing with these parameters. Such a system might be used for designing devices like miniaturized microchannel viscosimeters or self-regulating valves and pumps.

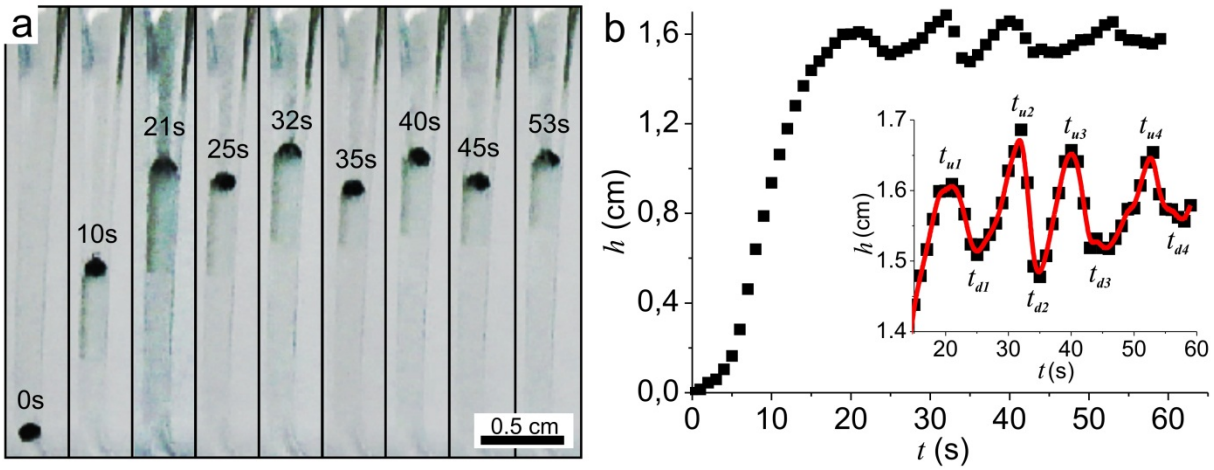

Figure 4.22. Height profile during the Yo-Yo motion. a) Series of optical micrographs showing the Yo-Yo motion of a GC bead in the glass capillary. b) Graph showing the height h of the bead as a function of time t. Inset: zoom of the Yo-Yo height profile. Reprinted from reference (100).

4.3.3.2. Cargo lifter

We will demonstrate in the following that the conductive bead can be used as a lifting motor moving through the capillary with a cargo attached to it. This cargo consisted in a piece of polymer attached to the bead via a very thin polymer wire with a tiny drop of glue. The wire extremity was coated with black nail varnish in order to facilitate its visualization. The GC bead is the only conductive part and the total mass of the object is 0.9 mg. Figure 4.23 shows the cargo lifting with an electric field $\mathscr{E}$ = 23 V cm^{-1}. The motion which drives the cargo over 2.7 cm is very clearly due to the bubbles being generated only underneath the GC bead motor and not at the cargo or at the wire surface, because of their insulating character. The height profile presents the same characteristics as the one obtained

without cargo in Figure 4.20. The whole object moves with a maximum speed v = 2 mm s^{-1}. This value, which is more than two times higher than the one obtained previously without cargo (section 4.3.3.) for a comparable electric field and bead size, is due to the capillary shape. Indeed, in the present case the conical character is much less pronounced than in the first case, generating a higher driving force, thus a faster motion. This proof-of-concept experiment shows for the first time, that cargo lifting in fluid channels is possible using bipolar electrochemistry, and this phenomenon might be used as an alternative concept for moving particles in microfluidic systems. The towing speed of the cargo can be controlled by the applied external voltage, the length of the bipolar motor and most importantly the distance between the motor and the capillary walls.

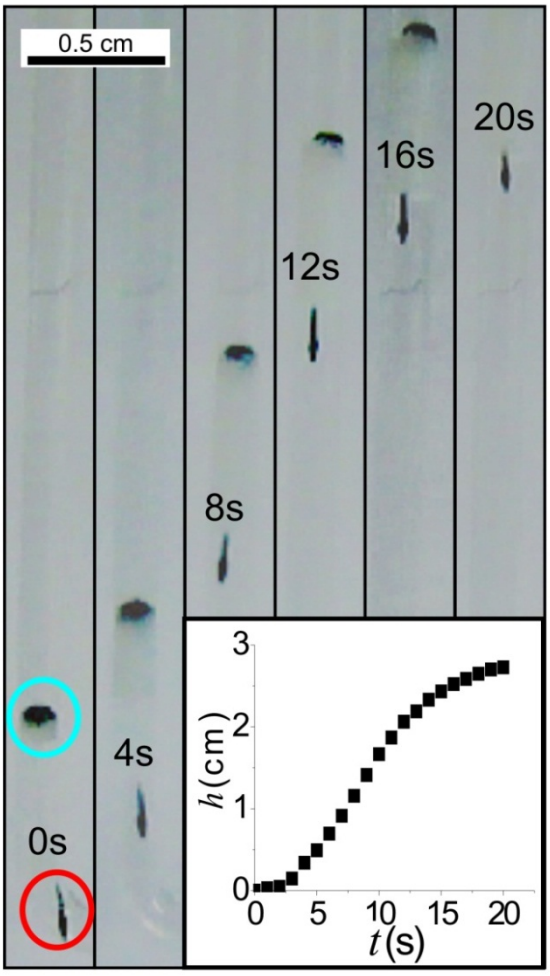

Figure 4.23. Series of optical micrographs showing the cargo lifter composed of the cargo (red circle) and the bipolar motor (blue circle). Inset: height position h of the cargo as a function of time t. Reprinted from reference (100).

4.4. Integrated light emission from bipolar motors

Tracking moving objects in real time is a challenge and therefore intensive effort has been made to design particles with specific optical, in many cases fluorescent, properties. For example, the observation of most of the microswimmers presented en section 4.1. requires efficient microscopy set-ups[37] or a functionalization of the swimmers with a fluorophore[80] in order to monitor them while moving. In this context it would be very helpful if the swimmer could act at the same time as an autonomous light source with the photon emission being intrinsically coupled to the motion. Here we will present an original approach, where the moving object is simultaneously emitting light, produced by electrogenerated chemiluminescence (ECL). In this section, bipolar electrochemistry is not only the asymmetric driving force for the particle propulsion but is also responsible for the light emission, combining in a synergetic way both redox reactions on the same object.

Like in the previous sections, the motion is here induced by the produced H_2 bubbles due to the reduction of water at the GC anodic pole, which proceeds according to the following equation at a neutral pH:

$$H_2O(l) + e^- \rightarrow ½\ H_2(g) + OH^-(l) \qquad (4.8)$$

Because of charge neutrality during bipolar electrochemistry, in the previous sections water or a sacrificial reductant such as hydroquinone was simultaneously oxidized at the anodic pole, generating oxidation products such as O_2 (reaction 4.3) or benzoquinone (reaction 4.4). These unavoidable anodic processes were not useful in the context of propulsion, and can therefore be replaced by electrochemical reactions leading to ECL emission. As discussed in section 2.2.3.3., ECL is an electrochemical process which produces light. The ECL mechanism of the reaction of TPrA with $Ru(bpy)_3^{2+}$ is an active area of investigation and it depends on several experimental parameters like the surface hydrophobicity,[101] the electrode material, the concentration ratio, the pH or the presence of surfactant.[102] All the reported mechanisms involve the following oxidation reactions:

$$TPrA(l) \rightarrow TPrA^{\cdot+}(l) + e^- \qquad (4.9)$$

$$Ru(bpy)_3^{2+}(l) \rightarrow Ru(bpy)_3^{3+}(l) + e^- \qquad (4.10)$$

The generated reactive radical cation $TPrA^{\cdot+}$ fastly undergoes reaction of deprotonation forming a highly reactive reducing agent $TPrA^{\cdot}$. $TPrA^{\cdot}$ and $TPrA^{\cdot+}$ react with ruthenium complexes to generate the excited state $Ru(bpy)_3^{2+*}$producing the ECL.[103] As depicted in Figure 4.24, the asymmetric electroactivity induced by bipolar electrochemistry can induce the synergetic reduction of H_2O at the

cathodic pole and oxidation of the ECL reagents at the anodic pole of the BE which should theoretically generate simultaneously motion and light emission of the bipolar swimmer.

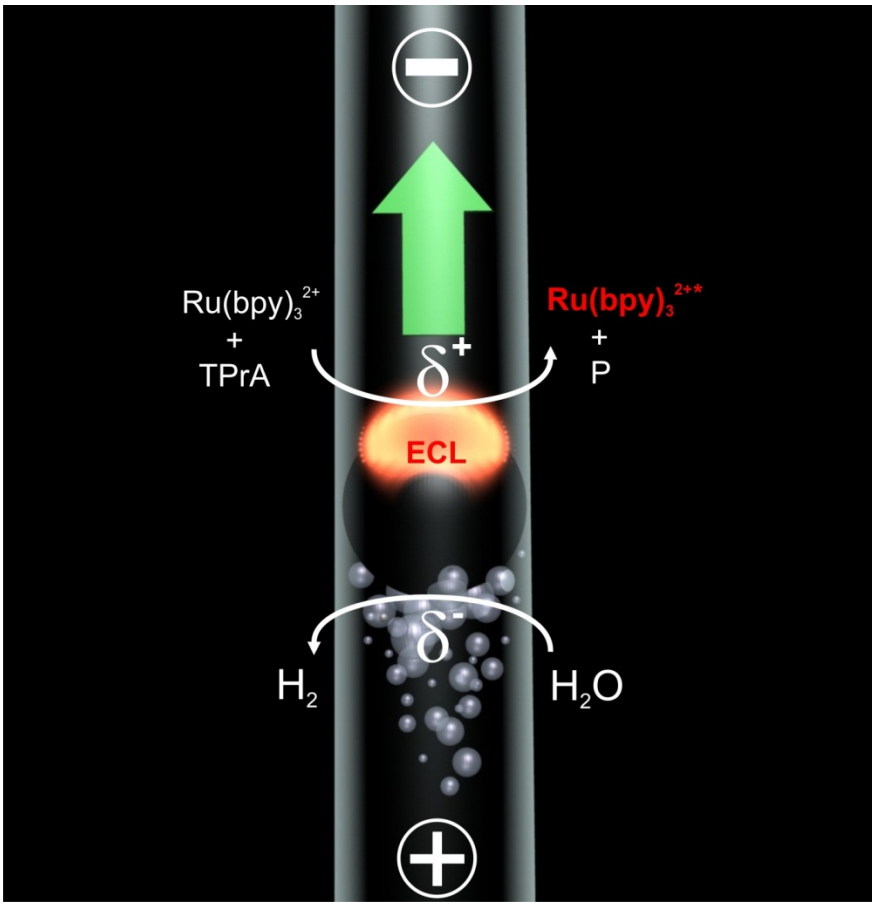

Figure 4.24. Scheme showing the synergetic reduction of H_2O at the cathodic pole and oxidation of the ECL reagents at the anodic pole which induces simultaneous motion and light emission. P corresponds to a side-product of the tripropylamine radicals formed during the ECL process.

In order to estimate the ΔV_{min} which is required to generate simultaneously the gas bubbles and ECL, the corresponding redox reactions have been first characterized by cyclic voltammetry with a normal working electrode composed of the swimmer material, as described in section 1.2. This electrochemical measurement has been combined with a simultaneous monitoring of the ECL intensity by using a photomultiplier tube. Typical voltammetric and ECL responses are presented in Figure 4.25.

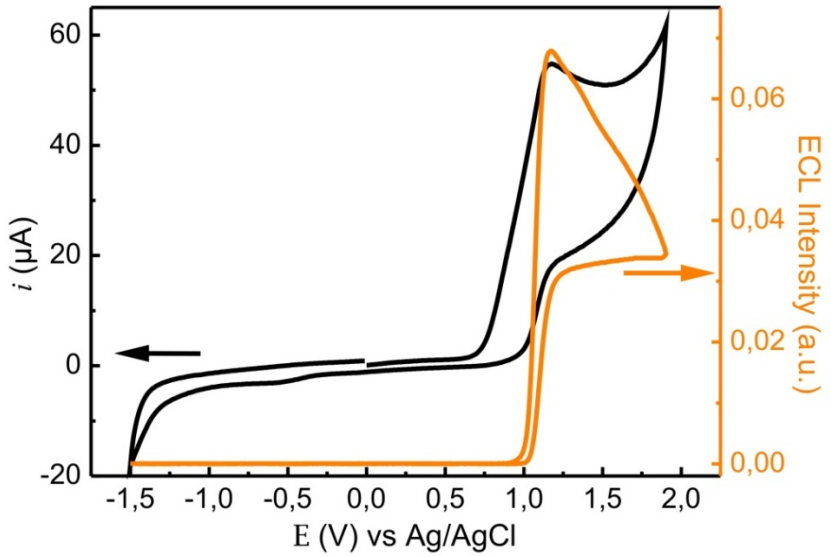

Figure 4.25. Cyclic voltammogram (black) and ECL emission (orange) of 0.5 mM $Ru(bpy)_3^{2+}$ in the presence of 100 mM TPrA with 100 mM phosphate buffer saline (pH = 7.4) on a home-made glassy carbon working electrode at a scan rate of 100 mV s^{-1}.

From these curves, the potential values for which the different redox reactions are occurring at the swimmer surface can be easily extracted. Water reduction (reaction 4.8) takes place at - 1.1 V *vs* Ag/AgCl and ECL emission occurs at 1 V *vs* Ag/AgCl. Based on these experimentally determined values, one can conclude that the coupling of water reduction and ECL emission at the reactive poles of a BE is possible only if the polarization potential ΔV between both extremities of the BE is at least equal to ΔV_{min} = 2.1 V. Equation (1.4) thus states that for a BE having a diameter d of about 1 mm, the electric field $\mathscr{E}$ has to be, in a first order approximation, at least equal to 21 V cm^{-1}.

The bipolar electrochemistry experiments were achieved using a similar protocol like for the levitation presented in section 4.3.3. A phosphate buffer saline (PBS) solution containing 0.5 mM of tris(2.2'-bipyridyl)dichlororuthenium(II) hexahydrate, 100 mM TPrA and a few drops of surfactant were injected into a U-shaped cell (Figure 4.20a). A GC bead with a diameter $d \approx 1$ mm was inserted into one arm of the cell. The electrodes were inserted into the top part of the cell and were polarized in such a way that the H_2 flow is generated underneath the bead, as illustrated in Figure 4.24. The ECL was recorded using a digital camera (Sony, Cyber-shot). The distance between both electrodes was 9.8 cm and the applied voltage was equal to 250 V, corresponding to a global electric field of $\mathscr{E}$ = 25.5 V cm^{-1}. The value is above the previously calculated theoretical threshold value of 21 V cm^{-1} and therefore leads to the synergetic levitation/ECL emission of the GC bead under these conditions, as demonstrated by Figure 4.26.

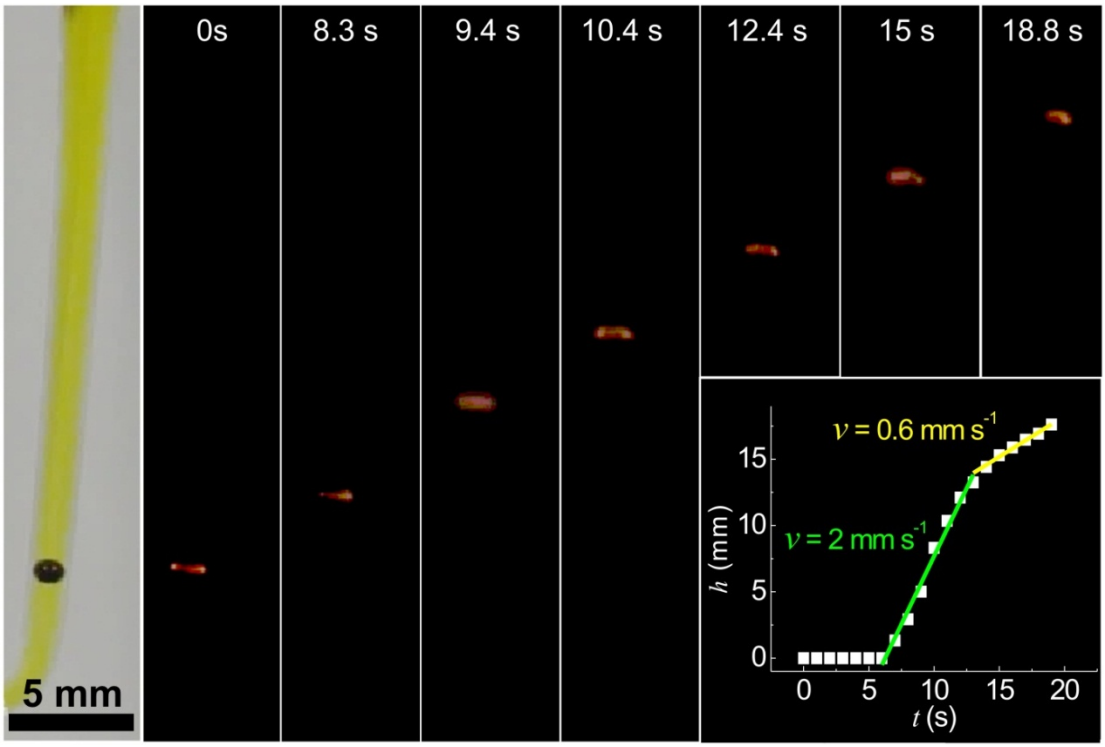

Figure 4.26. Series of optical pictures showing the levitation of a glassy carbon bead emitting ECL at different times. The left image presents the bead position under white light and the other images where taken in the dark. Inset: plot showing the height evolution h as a function of time t.

The left picture of Figure 4.26, obtained under ambient light, shows the GC bead in the capillary. The bead is spherical, but appears slightly stretched along its equatorial axis due to an optical effect of the cylindrical capillary. The light was then turned off and the electric field applied. The ECL generated at the anodic pole of the BE, as presented in Figure 4.26, was extremely bright and could be instantaneously observed with the naked eyes. The initial time t = 0 s is defined as the time when the camera has been focused on the ECL signal, allowing its correct visualization. After 6 s, the levitation starts due to H_2 bubble production underneath the bead, a phenomenon that could be clearly observed when the ambient light was turned on during the bead motion. The inset of Figure 4.26 shows the height evolution of the ECL bead as a function of time. h was defined as the distance between the equatorial axis of the immobilized bead on the left picture and the center of the ECL emitting area during the motion. As it was the case for the levitation without ECL (section 4.3.3.), this curve can be divided into three distinct parts. In the first part of the curve, the bead does not move. This part corresponds to the period of bubble accumulation underneath the bead for the generation of a sufficiently high buoyancy to overcome gravity. After this initial phase, the height evolution is linear for 7 s at a speed v = 2 mm s^{-1} or ≈2 bodylengths per second. Finally, because the shape of the cell arm is slightly conical (see left picture of Figure 4.26), the space between the bead and the glass walls becomes larger when the bead rises, thus allowing the bubbles to escape from below the bead,

which leads to a decrease of the speed during the third phase (v = 0.6 mm s^{-1}). The levitation, as well as the ECL emission can be stopped by switching off the electric field. The height evolution and the levitation speed is comparable to the ones reported without ECL (see section 4.3.3.2.), showing that the ECL mechanism does not influence the bead propulsion. According to Figure 4.24, one would expect the ECL profile to follow the shape of the anodic pole, leading to a lightened hemisphere at the top of the bead. This is actually the case at certain moments of the experiment, but during the run one can also observe an ECL shape looking rather like a ring. In order to understand these changes we further investigated parameters affecting the ECL profile at GC beads in more details.

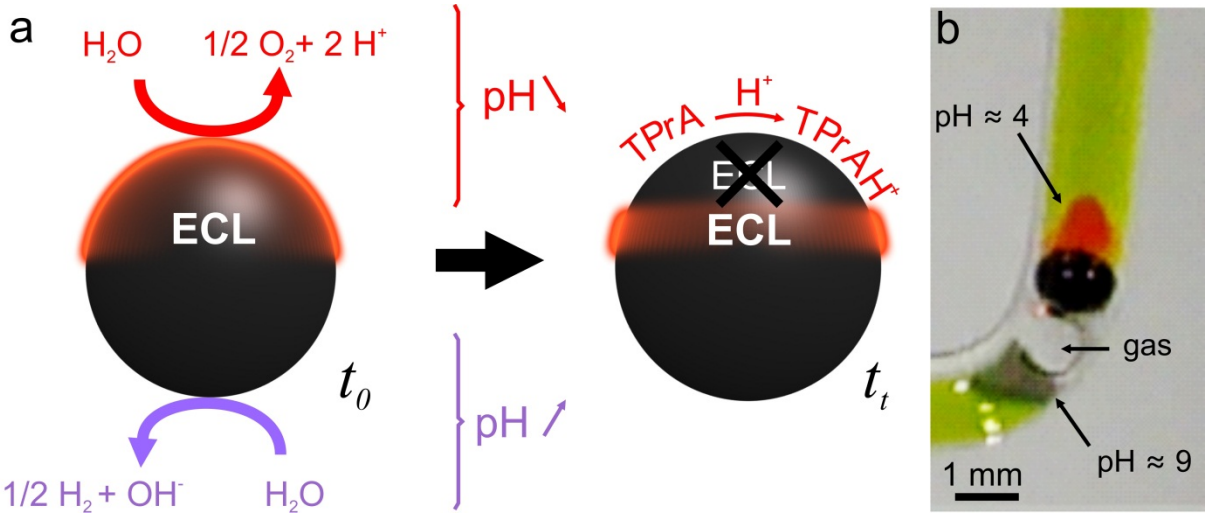

Figure 4.27. pH control of the ECL shape. a) Mechanism responsible for the shape of the ECL-emitting region on the bead. b) Optical micrograph of a GC bead in the U-shaped cell filled with 100 mM PBS containing 0.5 mM $Ru(bpy)_3^{2+}$, 100 mM TPrA and a universal pH indicator under the influence of a 25.5 V cm^{-1} external electric field.

pH is a crucial parameter for the ECL mechanism to occur. Indeed, ECL is known to be effective at pH > 5.5, with a maximum intensity at pH 7.5. TPrA is insoluble at higher pH and is protonated at lower pH (as well as $TPrA^{\cdot+}$) which inhibits the ECL mechanism.[104] This is the reason for using PBS buffer in the reported experiments, ensuring a constant pH value of 7.4 under normal conditions. But, depending on the applied potential, water may also be oxidized at the anodic hemisphere of the bead following reaction 4.3. The oxidation wave corresponding to this reaction can be observed on Figure 4.25. It starts at more anodic potential than the ECL reactions, around 1.5 V *vs.* Ag/AgCl. The theoretical polarization voltage required for achieving simultaneously water reduction (reaction 4.8) at the cathodic pole and ECL emission and water oxidation (reaction 4.3) at the anodic pole corresponds then to $1.5 + 1.1 = 2.6$ V. This value fits with the value of ΔV applied for Figure 4.26. This suggests that water oxidation occurs at the very top of the bead where the polarization potential is the highest, inducing therefore a local pH decrease.

To check such a pH variation, experiments were performed in the presence of a pH indicator. A GC bead was submitted to the same electric field than previously. The medium was also identical except that no surfactant was added and a few drops of a universal pH indicator were added to the solution. Figure 4.27b shows clearly that, during these experiments, pH variations are occurring at the reactive poles of the BE. Indeed, one can observe that water reduction which produces the H_2 gas bubble also induces an expected pH increase (reaction 4.8) up to a value about 9. It is worth noting that in this particular case, the absence of surfactant caused the H_2 accumulation, producing the bubble that can be seen at the bottom of the bead. At the top of the bead, the pH reaches a value of 4, confirming that water oxidation (reaction 4.3) also takes place at the anodic pole. This experiment confirmed that ECL reactions are in competition with water oxidation at the anodic pole of the bead. As depicted in Figure 4.27a, this reaction directly influences the ECL process since it induces locally a pH decrease, leading to TPrA protonation, which finally causes the ECL quenching at the top part of the bead, thus creating an ECL ring instead of the hemispherical shape.

To precisely capture the ECL profile around the GC bead during bipolar electrochemistry, additional experiments were performed with the BE placed in front of a microscope (objective x5) equipped with a CCD camera. To avoid bead motion, which is useless for these experiments, they were also carried out in the absence of surfactant. We investigated the influence of parameters such as applied voltage and buffer capacity which directly affect the pH gradient around the bead and thus the ECL profile. Surprisingly, ECL has been observed at global electric fields as low as 6.2 V cm^{-1}. This is due to the fact that, in this particular case, the bead is touching the capillary walls, leaving only a very thin layer of liquid between the bead and the walls. The configuration present here is intermediate between the classical case of open bipolar electrochemistry and the closed bipolar electrochemistry, presented in section 1.5. The electrical resistance of the liquid thin layer is much higher than the resistance of the solution in the rest of the capillary, leading to a locally increased potential drop that can drive the two redox reactions. During these experiments, the desired voltage was applied, directly generating the initial ECL shape. As shown in Figure 4.28, the ECL-emitting region does not expand into the solution surrounding the bead. It is confined to the bead surface by the high TPrA concentration which limits the thickness of the ECL reaction layer. This initial shape changes rapidly to a transient state (typically after a few seconds). Two representative times are now considered, as they correspond to the two characteristic ECL shapes. The first one is the initial time t_0 which corresponds to the initial ECL shape obtained once the desired voltage is reached. The second, t_t, corresponds to the transient shape. The images obtained at t_0 and t_t for two buffer concentrations for applied voltages E_{imp} of 60 V, 75 V and 100 V are shown on Figure 4.28.

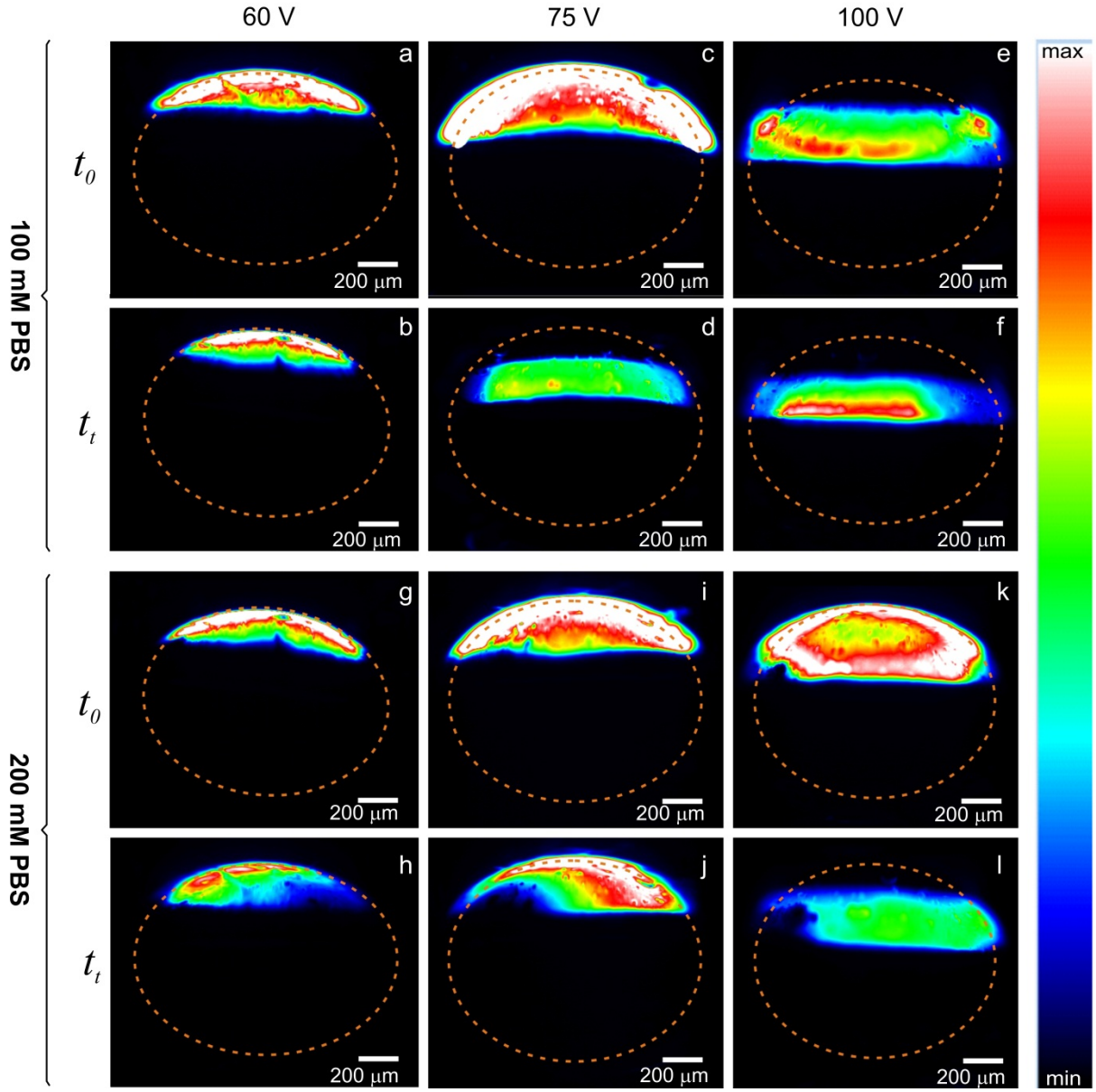

Figure 4.28. CCD pictures showing the ECL intensity profiles on a GC bead in a U-cell filled with PBS containing 0.5 mM $Ru(bpy)_3^{2+}$ and 100 mM TPrA, at $t = t_0$ applying 60 V, 75 V and 100 V between the feeder electrodes. The six top pictures were obtained using a PBS concentration of 100 mM and the six bottom ones with a PBS concentration of 200 mM.

As expected, the direct consequence of the increase of the potential between the feeder electrodes is a shift of the ECL boundary towards the equatorial axis of the bead. Indeed, the region where the potential is anodic enough to generate ECL expands towards the middle of the bead. As shown by Figure 4.28a, c, g and i, hemispherical ECL shapes are generated at the initial stage t_0 with experimental conditions such as 100 mM PBS and E_{imp} = 60 V or 75 V. With 60 V, this shape remains roughly the same during the whole experiment but with 75 V, it changes quickly to an ECL ring that is shown in Figure 4.28d. Such a behavior can be rationalized by means of the mechanism previously

discussed and illustrated in Figure 4.27a. At 60 V, the driving force is not sufficient to generate a pH change at the top of the bead, so the ECL shape remains hemispherical. On the contrary, an external voltage of 75 V is high enough to induce proton formation at a sufficient rate to decrease the pH after a given time (t_t) at the anodic pole when using a 100 mM PBS solution. Therefore the formation of an electrogenerated pH gradient limits the ECL region to a ring shape. This general trend is confirmed by Figure 4.28e which shows that when applying 100 V the ring is instantaneously generated at t_0. The influence of the buffer capacity on these experiments was also investigated. At higher buffer capacity (200 mM PBS), the ECL shape remains hemispherical up to a voltage of 75 V even after a few seconds (Figure 4.28j). Under these conditions, no ECL ring was observed because the buffer capacity is strong enough to avoid TPrA protonation, promoting ECL emission all over the anodic pole. Also at this buffer concentration, the initial ECL (at t_0) shape using 100 V is hemispherical (Figure 4.28k), which was not the case at 100 mM PBS (Figure 4.28e), confirming once again a pH-based mechanism.

These experiments demonstrate clearly that the control of the ECL shape on a BE in these static experiments can be fine-tuned using easily controllable parameters such as electric field or buffer concentration. In this case, the ECL ring corresponds ideally to the area of the anodic pole where the polarization potential is strong enough to generate ECL emission, but where the water oxidation rate is not efficient enough to protonate TPrA or its radicals. In the case of swimmer motion the situation becomes more complicated, because proton diffusion, convection due to bubble formation and motion of the bipolar swimmer have a strong impact on the concentration gradients of the involved species and thus on the final ECL shape. Nevertheless, the mechanism inducing the ECL profile changes from hemispherical to ring shapes can be rationalized in terms of local pH variations, which occur in the vicinity of the swimmer during its motion.

This work presents the first synergetic action of bipolar electrochemistry in terms of simultaneous propulsion and ECL generation, leading *in fine* to the first example of a swimmer which is intrinsically coupled with a chemical light source. In the reported experiments, ECL provides a direct monitoring of the object motion, which is very useful when dealing with autonomous swimmers. The versatility of bipolar electrochemistry coupled to ECL allows imagining using the same principle with other types of swimmers and at smaller scales. It therefore opens up the door to a new class of dynamic experiments with multifunctional objects. For instance, dynamic detection in a sample solution by using ECL as an analytic output signal. Finally, such an ECL swimmer resembles biological systems and may be considered as an artificial analogue of bioluminescent fishes or marine creatures.

4.5. Dynamic bipolar self-regeneration

The previously presented motion was based on bubble propulsion. In this section, we demonstrate that bipolar electrochemistry can also be used to propel macroscopic or microscopic metallic objects by a completely different mechanism called dynamic self-regeneration process. This original approach consists in the simultaneous combination of deposition and dissolution of an electroactive material. The deposition occurs at the cathodic pole of the object and the dissolution at the opposite pole, which leads to a linear motion of the object (Figure 4.29). A deposition/dissolution mechanism has also been previously employed by Bradley's team in the context of spatially coupled bipolar electrochemistry (SCBE) for creating electrical contacts between copper particles[105] (see section 2.2.4.), but never before for the propulsion of objects.

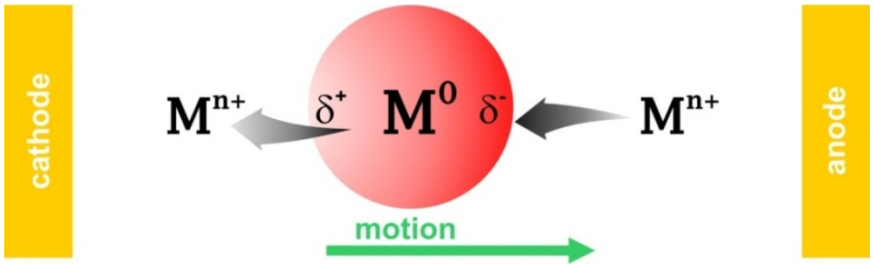

Figure 4.29. Dynamic bipolar self-regeneration principle.

In our experiments, metal objects in the form of zinc dendrites were positioned within capillaries previously filled with an aqueous $ZnSO_4$ solution. When an external electric field is applied across the capillary, the two following reactions proceed:

$$Zn^{2+}(l) + 2\ e^- \rightarrow Zn^0(s) \quad E^0 = -0.76\ V\ vs\ NHE \tag{4.11}$$

at the cathodic pole of the zinc object and

$$Zn^0(s) \rightarrow Zn^{2+}(l) + 2\ e^- \quad E^0 = -0.76\ V\ vs\ NHE \tag{4.12}$$

at the anodic pole. Since one and the same redox couple (Zn^{2+}/Zn^0) is involved in the bipolar process on both sides of the object, ΔV_{min} is almost equal to zero (see section 1.2.) and theoretically the application of low electric fields should be sufficient for triggering reactions 4.11 and 4.12.

As a proof of principle, first experiments were carried out at a macroscopic level. Under the employed experimental conditions zinc grows electrochemically following a dendritic morphology[106] as it can be seen on the SEM micrographs of Figure 4.30. This property was used to generate freestanding zinc dendrites. Therefore, as depicted in Figure 4.30b, zinc was electrodeposited at the extremity of a metallic wire inside a glass tube (inner diameter: 0.6 mm) filled with a 0.1 M $ZnSO_4$

solution. As soon as a Zn deposit of a few millimeters length was obtained, the zinc dendrites were disconnected from the zinc cathode by carefully pulling the wire out of the capillary in order to isolate the freestanding dendrite. This is the most difficult step of the procedure since in the majority of the cases the dendrite is also pulled out together with the wire. Finally, a potential difference of 125 V between two external electrodes separated by 10 cm was imposed, leading to an electric field with a value of 1.25 kV m^{-1}. As discussed above, a smaller electric field could be imposed for triggering reactions 4.11 and 4.12 but the latter $\mathscr{E}$ value was set in order to reach sufficient speeds.

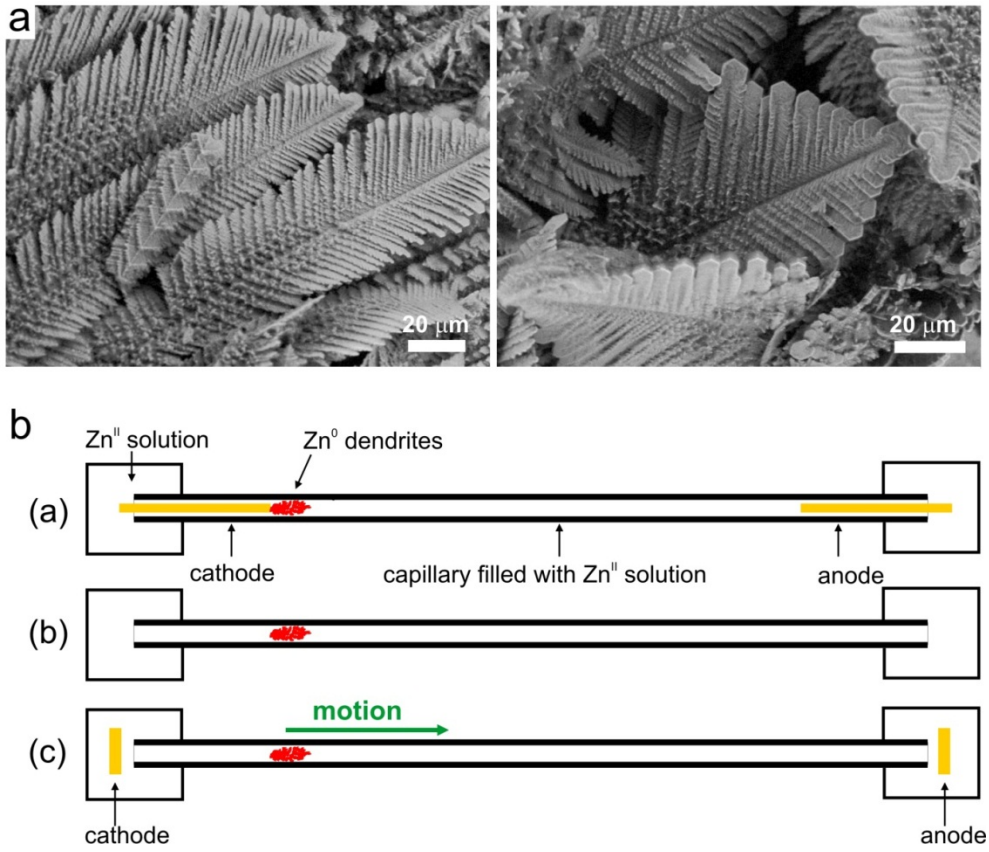

Figure 4.30. Electrodeposited zinc dendrites. a) SEM pictures of electrodeposited zinc dendrites. The scale bars equal 20 μm. b) experimental process: (a) dendrite growth; (b) dendrite detachment; (c) dynamic bipolar self-regeneration.

Figure 4.31 shows a series of optical micrographs recorded at different times during the experiment. The object dissolution at its anodic pole according to 4.12 and its simultaneous regeneration at its cathodic pole according to 4.11, leads to a visible motion (from left to right) with a speed $v \approx 60\ \mu m\ s^{-1}$. This value represents an average speed, calculated using the distance covered by the object during the full run. It seems hardly convertible to bodylenght s^{-1}, because due to the nonhomogeneous density of the object, its length permanently changes during the bipolar regeneration.

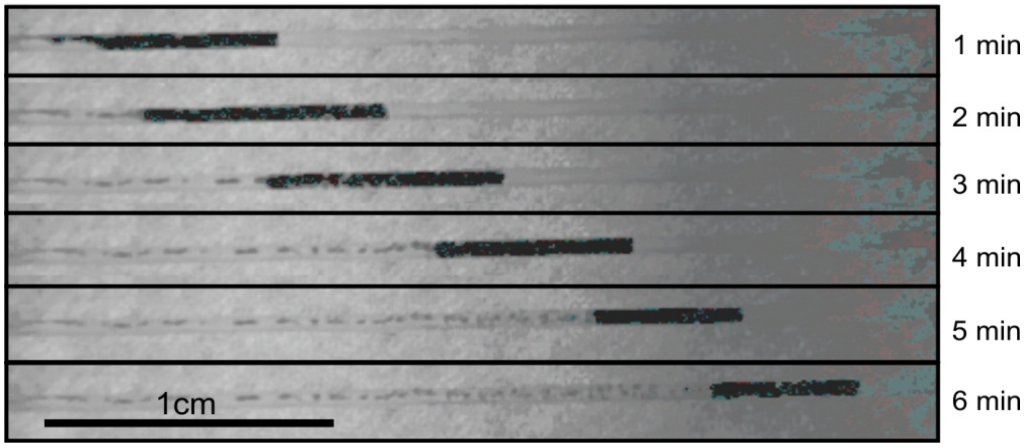

Figure 4.31. Pictures of a zinc macroswimmer in a glass tube filled with a $ZnSO_4$ solution under the influence of an external electrical field, recorded at various times during the experiment. Reprinted from reference (107).

As expect, turning off the electric field stopped the motion. In these pictures, depending on the local pH conditions, the presence of a thin zinc oxide layer behind the moving object can be noticed, this suggests that the technique might be used for printing surfaces with a conducting or semiconducting "ink" which could be engineered by adjusting the swimmer composition.

The presented experiment encouraged us to perform analogous experiments at a microscopic scale. As in the previous experiments, a zinc dendrite was isolated in a capillary (inner diameter: 100 µm) filled with a $ZnSO_4$ solution whose pH was adjusted by the addition of a small amount of acid in order to prevent zinc oxide formation during the experiment. The swimmer was then exposed to an external electric field of 7 kV m^{-1}, which propelled it with a speed $v \approx 80$ µm s^{-1} (Figure 4.32).

The change of the swimmer morphology clearly shows that the motion was induced by the dynamic bipolar self-regeneration process and not by electrokinetic phenomena. Electroosmotic flow becomes relevant at the micrometer scale, but was oriented in the opposite direction of the movement and therefore cannot explain it. We verified that inert particles indeed moved in the direction of the electroosmotic flow. The dendrite could be propelled for several minutes over distances in the centimeter range. The travelled distance can be increased by using a longer experimental time, and the speed can also be controlled by tuning the electric field value. The observed movement was restricted to one dimension, due to the use of a capillary, but we also performed similar experiments under open conditions (no capillary), in which however the objects were more difficult to follow under the microscope.

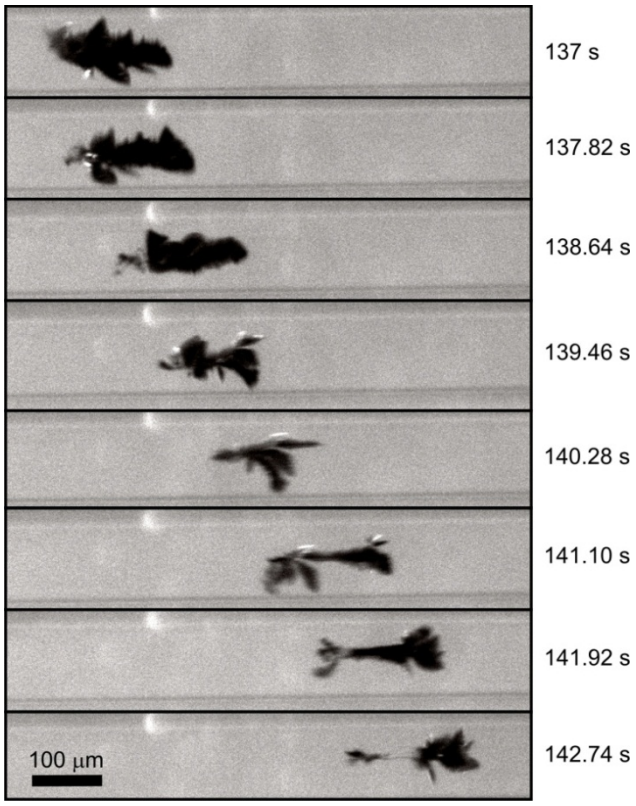

Figure 4.32. Optical micrographs of a zinc dendrite in a glass capillary filled with a zinc sulfate solution at pH ≈5 under the influence of an external electric field at various times during the experiment. Reprinted from reference (107).

It seems important to note that the object is constantly reconstructing itself during the run, rendering its atomic composition at the end different from that in the beginning. This raises the philosophic question whether the object keeps its identity after replacement of all its components, as it is discussed in the paradox of the ship of Theseus.[108] The notion of "motion", "propulsion" and "swimmer" can then be critically regarded and one can think of describing these experiments as the propagation of a kind of chemical wave.

The process can be generalized to other metals, as we made similar observations using copper. In the future, dynamic bipolar self-regeneration could potentially be used for wireless localized deposition, fabrication of electrical microcontacts or surface patterning, since the process is very robust with respect to changes in experimental conditions.

References

(1) Berg, H. C. *Annu. Rev. Biochem.* **2003**, *72*, 19.
(2) Berg, H. C. *Curr. Biol.* **2008**, *18*, R689.
(3) Schliwa, M.; Woehlke, G. *Nature* **2003**, *422*, 759.
(4) Lipowsky, R.; Chai, Y.; Klumpp, S.; Liepelt, S.; Müller, M. J. I. *Physica A* **2006**, *372*, 34.
(5) Kon, T.; Oyama, T.; Shimo-Kon, R.; Imamula, K.; Shima, T.; Sutoh, K.; Kurisu, G. *Nature* **2012**, *484*, 345.
(6) Feynman, R. P. *Eng. Sci. (California Institute of technology)* **1960**, *23*, 22.
(7) Wang, J. *ACS Nano* **2009**, *3*, 4.
(8) Ozin, G. A.; Manners, I.; Fournier-Bidoz, S.; Arsenault, A. *Adv. Mater.* **2005**, *17*, 3011.
(9) Ebbens, S. J.; Howse, J. R. *Soft Matter* **2010**, *6*, 726.
(10) http://www.bmb.leeds.ac.uk/illingworth/6form/index.htm.
(11) Vale, R. D. *Cell* **2003**, *112*, 467.
(12) DiLuzio, W. R.; Turner, L.; Mayer, M.; Garstecki, P.; Weibel, D. B.; Berg, H. C.; Whitesides, G. M. *Nature* **2005**, *435*, 1271.
(13) Takeuchi, S.; DiLuzio, W. R.; Weibel, D. B.; Whitesides, G. M. *Nano Lett.* **2005**, *5*, 1819.
(14) Weibel, D. B.; Garstecki, P.; Ryan, D.; DiLuzio, W. R.; Mayer, M.; Seto, J. E.; Whitesides, G. M. *Proc. Natl. Acad. Sci. USA* **2005**, *102*, 11963.
(15) Behkam, B.; Sitti, M. *App. Phys. Lett.* **2007**, *90*, 023902.
(16) Behkam, B.; Sitti, M. *App. Phys. Lett.* **2008**, *93*, 223901.
(17) van den Heuvel, M. G. L.; Dekker, C. *Science* **2007**, *317*, 333.
(18) Hess, H.; Bachand, G. D.; Vogel, V. *Chem. Eur. J.* **2004**, *10*, 2110.
(19) Goel, A.; Vogel, V. *Nat. Nanotech.* **2008**, *3*, 465.
(20) Soong, R. K.; Bachand, G. D.; Neves, H. P.; Olkhovets, A. G.; Craighead, H. G.; Montemagno, C. D. *Science* **2000**, *290*, 1555.
(21) Yamaguchi, S.; Matsumoto, S.; Ishizuka, K.; Iko, Y.; Tabata, K. V.; Arata, H. F.; Fujita, H.; Noji, H.; Hamachi, I. *Chem. Eur. J.* **2008**, *14*, 1891.
(22) Hess, H.; Clemmens, J.; Qin, D.; Howard, J.; Vogel, V. *Nano Lett.* **2001**, *1*, 235.
(23) Clemmens, J.; Hess, H.; Doot, R.; Matzke, C. M.; Bachand, G. D.; Vogel, V. *Lab. Chip* **2004**, *4*, 83.
(24) Schmidt, C.; Vogel, V. *Lab. Chip* **2010**, *10*, 2195.
(25) Fischer, T.; Agarwal, A.; Hess, H. *Nat. Nanotech.* **2009**, *4*, 162.
(26) Rios, L.; Bachand, G. D. *Lab. Chip* **2009**, *9*, 1005.
(27) Hiyama, S.; Moritani, Y.; Gojo, R.; Takeuchi, S.; Sutoh, K. *Lab. Chip* **2010**, *10*, 2741.
(28) von Delius, M.; Leigh, D. A. *Chem. Soc. Rev.* **2011**, *40*, 3656.
(29) Sykes, E. C. H. *Angew. Chem. Int. Ed.* **2012**, *51*, 4277.
(30) Paxton, W. F.; Sundararajan, S.; Mallouk, T. E.; Sen, A. *Angew. Chem. Int. Ed.* **2006**, *45*, 5420.
(31) Wang, Y.; Hernandez, R. M.; Bartlett, D. J.; Bingham, J. M.; Kline, T. R.; Sen, A.; Mallouk, T. E. *Langmuir* **2006**, *22*, 10451.
(32) Pumera, M. *Nanoscale* **2010**, *2*, 1643.
(33) Paxton, W. F.; Kistler, K. C.; Olmeda, C. C.; Sen, A.; St. Angelo, S. K.; Cao, Y.; Mallouk, T. E.; Lammert, P. E.; Crespi, V. H. *J. Am. Chem. Soc.* **2004**, *126*, 13424.
(34) Fournier-Bidoz, S.; Arsenault, A. C.; Manners, I.; Ozin, G. A. *Chem. Commun.* **2005**, 441.
(35) Burdick, J.; Laocharoensuk, R.; Wheat, P. M.; Posner, J. D.; Wang, J. *J. Am. Chem. Chem. Soc.* **2008**, *130*, 8164.
(36) Zacharia, N. S.; Sadeq, Z. S.; Ozin, G. A. *Chem. Commun.* **2009**, 5856.
(37) Laocharoensuk, R.; Burdick, J.; Wang, J. *ACS Nano* **2008**, *2*, 1069.
(38) Kagan, D.; Calvo-Marzal, P.; Balasubramanian, S.; Sattayasamitsathit, S.; Manesh, K. M.; Flechsig, G.-U.; Wang, J. *J. Am. Chem. Soc.* **2009**, *131*, 12082.
(39) Demirok, U. K.; Laocharoensuk, R.; Manesh, K. M.; Wang, J. *Angew. Chem.* **2008**, *120*, 9489.

(40) Wang, J.; Manesh, K. M. *Small* **2010**, *6*, 338.
(41) Calvo-Marzal, P.; Manesh, K. M.; Kagan, D.; Balasubramanian, S.; Cardona, M.; Flechsig, G.-U.; Posner, J.; Wang, J. *Chem. Commun.* **2009**, 4509.
(42) Balasubramanian, S.; Kagan, D.; Manesh, K. M.; Calvo-Marzal, P.; Flechsig, G.-U.; Wang, J. *Small* **2009**, *5*, 1569.
(43) Kline, T. R.; Paxton, W. F.; Mallouk, T. E.; Sen, A. *Angew. Chem. Int. Ed.* **2005**, *44*, 744.
(44) Manesh, K. M.; Balasubramanian, S.; Wang, J. *Chem. Commun.* **2010**, *46*, 5704.
(45) Sundararajan, S.; Lammert, P. E.; Zudans, A. W.; Crespi, V. H.; Sen, A. *Nano Lett.* **2008**, *8*, 1271.
(46) Wang, J. *Lab. Chip* **2012**, *12*, 1944.
(47) Campuzano, S.; Kagan, D.; Orozco, J.; Wang, J. *Analyst* **2011**, *136*, 4621.
(48) Hong, Y.; Blackman, N. M. K.; Kopp, N. D.; Sen, A.; Velegol, D. *Phys. Rev. Lett.* **2007**, *99*, 178103.
(49) Qin, L.; Banholzer, M. J.; Xu, X.; Huang, L.; Mirkin, C. A. *J. Am. Chem. Soc.* **2007**, *129*, 14870.
(50) Catchmark, J. M.; Subramanian, S.; Sen, A. *Small* **2005**, *1*, 202.
(51) Liu, R.; Sen, A. *J. Am. Chem. Soc.* **2011**, *133*, 20064.
(52) Mano, N.; Heller, A. *J. Am. Chem. Soc.* **2005**, *127*, 11574.
(53) Pavlick, R. A.; Sengupta, S.; McFadden, T.; Zhang, H.; Sen, A. *Angew. Chem. Int. Ed.* **2011**, *50*, 9374.
(54) Ismagilov, R. F.; Schwartz, A.; Bowden, N.; Whitesides, G. M. *Angew. Chem.* **2002**, *114*, 674.
(55) Huang, G.; Wang, J.; Mei, Y. *J. Mater. Chem.* **2012**, *22*, 6519.
(56) Gibbs, J. G.; Zhao, Y. P. *App. Phys. Lett.* **2009**, *94*, 163104.
(57) Wilson, D. A.; Nolte, R. J. M.; van Hest, J. C. M. *Nat. Chem.* **2012**, *4*, 268.
(58) Vicario, J.; Eelkema, R.; Browne, W. R.; Meetsma, A.; Crois, R. M. L.; Feringa, B. L. *Chem. Commun.* **2005**, 3936.
(59) Pantarotto, D.; Browne, W. R.; Feringa, B. L. *Chem. Commun.* **2008**, 1533.
(60) Sanchez, S.; Solovev, A. A.; Schulze, S.; Schmidt, O. G. *Chem. Commun.* **2011**, *47*, 698.
(61) Mei, Y.; Huang, G.; Solovev, A. A.; Ureña, E. B.; Mönch, I.; Ding, F.; Reindl, T.; Fu, R. K. Y.; Chu, P. K.; Schmidt, O. G. *Adv. Mater.* **2008**, *20*, 4085.
(62) Sanchez, S.; Ananth, A. N.; Fomin, V. M.; Viehrig, M.; Schmidt, O. G. *J. Am. Chem. Soc.* **2011**, *133*, 14860.
(63) Sanchez, S.; Solovev, A. A.; Harazim, S. M.; Schmidt, O. G. *J. Am. Chem. Soc.* **2011**, *133*, 701.
(64) Gao, W.; Sattayasamitsathit, S.; Orozco, J.; Wang, J. *J. Am. Chem. Soc.* **2011**, *133*, 11862.
(65) Mei, Y.; Solovev, A. A.; Sanchez, S.; Schmidt, O. G. *Chem. Soc. Rev.* **2011**, *40*, 2109.
(66) Manesh, K. M.; Cardona, M.; Yuan, R.; Clark, M.; Kagan, D.; Balasubramanian, S.; Wang, J. *ACS Nano* **2010**, *4*, 1799.
(67) Gao, W.; Sattayasamitsathit, S.; Uygun, A.; Pei, A.; Ponedal, A.; Wang, J. *Nanoscale* **2012**, *4*, 2447.
(68) Sanchez, S.; Solovev, A. A.; Mei, Y.; Schmidt, O. G. *J. Am. Chem. Soc.* **2010**, *132*, 13144.
(69) Balasubramanian, S.; Kagan, D.; Jack Hu, C.-M.; Campuzano, S.; Lobo-Castañon, M. J.; Lim, N.; Kang, D. Y.; Zimmerman, M.; Zhang, L.; Wang, J. *Angew. Chem. Int. Ed.* **2011**, *50*, 4161.
(70) Kagan, D.; Campuzano, S.; Balasubramanian, S.; Kuralay, F.; Flechsig, G.-U.; Wang, J. *Nano Lett.* **2011**, *11*, 2083.
(71) Orozco, J.; Campuzano, S.; Kagan, D.; Zhou, M.; Gao, W.; Wang, J. *Anal. Chem.* **2011**, *83*, 7962.
(72) Campuzano, S.; Orozco, J.; Kagan, D.; Guix, M.; Gao, W.; Sattayasamitsathit, S.; Claussen, J. C.; Merkoçi, A.; Wang, J. *Nano Lett.* **2012**, *12*, 396.
(73) Solovev, A. A.; Sanchez, S.; Pumera, M.; Mei, Y. F.; Schmidt, O. G. *Adv. Funct. Mater.* **2010**, *20*, 2430.
(74) Solovev, A. A.; Xi, W.; Gracias, D. H.; Harazim, S. M.; Deneke, C.; Sanchez, S.; Schmidt, O. G. *ACS Nano* **2012**, *6*, 1751.
(75) Gao, W.; Uygun, A.; Wang, J. *J. Am. Chem. Soc.* **2012**, *134*, 897.

(76) Tierno, P.; Golestanian, R.; Pagonabarraga, I.; Sagués, F. *J. Phys. Chem. B* **2008**, *112*, 16525.
(77) Sing, C. E.; Schmid, L.; Schneider, M. F.; Franke, T.; Alexander-Katz, A. *Proc. Natl. Acad. Sci. USA* **2009**.
(78) Zhang, L.; Petit, T.; Lu, Y.; Kratochvil, B. E.; Peyer, K. E.; Pei, R.; Lou, J.; Nelson, B. J. *ACS Nano* **2010**, *4*, 6228.
(79) Ishiyama, K.; Sendoh, M.; Yamazaki, A.; Arai, K. I. *Sens. Actuat. A: Phys.* **2001**, *91*, 141.
(80) Ghosh, A.; Fischer, P. *Nano Lett.* **2009**, *9*, 2243.
(81) Zhang, L.; Peyer, K. E.; Nelson, B. J. *Lab. Chip* **2010**, *10*, 2203.
(82) Tottori, S.; Zhang, L.; Qiu, F.; Krawczyk, K. K.; Franco-Obregón, A.; Nelson, B. J. *Adv. Mater.* **2012**, *24*, 811.
(83) Gao, W.; Sattayasamitsathit, S.; Manesh, K. M.; Weihs, D.; Wang, J. *J. Am. Chem. Soc.* **2010**, *132*, 14403.
(84) Pak, O. S.; Gao, W.; Wang, J.; Lauga, E. *Soft Matter* **2011**, *7*, 8169.
(85) Dreyfus, R.; Baudry, J.; Roper, M. L.; Fermigier, M.; Stone, H. A.; Bibette, J. *Nature* **2005**, *437*, 862.
(86) Velev, O. D.; Gangwal, S.; Petsev, D. N. *Annu. Rep. Prog. Chem., Sect. C: Phys. Chem.* **2009**, *105*, 213.
(87) Chang, S. T.; Paunov, V. N.; Petsev, D. N.; Velev, O. D. *Nat. Mater.* **2007**, *6*, 235.
(88) Calvo-Marzal, P.; Sattayasamitsathit, S.; Balasubramanian, S.; Windmiller, J. R.; Dao, C.; Wang, J. *Chem. Commun.* **2010**, *46*, 1623.
(89) Zhang, C.; Khoshmanesh, K.; Mitchell, A.; Kalantar-zadeh, K. *Anal. Bioanal. Chem.* **2010**, *396*, 401.
(90) Krupke, R.; Hennrich, F.; Löhneysen, H. v.; Kappes, M. M. *Science* **2003**, *301*, 344.
(91) Pohl, H. A.; Hawk, I. *Science* **1966**, *152*, 647.
(92) Zhang, K.-Q.; Liu, X. Y. *Nature* **2004**, *429*, 739.
(93) Takei, A.; Matsumoto, K.; Shomoyama, I. *Lab. Chip* **2010**, *10*, 1781.
(94) Gangwal, S.; Cayre, O. J.; Bazant, M. Z.; Velev, O. D. *Phys. Rev. Lett.* **2008**, *100*, 058302.
(95) Loget, G.; Larcade, G.; Lapeyre, V.; Garrigue, P.; Warakulwit, C.; Limtrakul, J.; Delville, M.-H.; Ravaine, V.; Kuhn, A. *Electrochim. Acta* **2010**, *55*, 8116.
(96) Fattah, Z.; Loget, G.; Lapeyre, V.; Garrigue, P.; Warakulwit, C.; Limtrakul, J.; Bouffier, L.; Kuhn, A. *Electrochim. Acta* **2011**, *56*, 10562.
(97) Wang, Y.; Fei, S.; Byun, Y.-M.; Lammert, P. E.; Crespi, V. H.; Sen, A.; Mallouk, T. E. *J. Am. Chem. Soc.* **2009**, *131*, 9926.
(98) Attard, G. S.; Bartlett, P. N.; Coleman, N. R. B.; Elliott, J. M.; Owen, J. R.; Wang, J. H. *Science* **1997**, *278*, 838.
(99) Loget, G.; Kuhn, A. *Nat. Commun.* **2011**, *2*, 535.
(100) Loget, G.; Kuhn, A. *Lab. Chip* **2012**, *12*, 1967.
(101) Zu, Y.; Bard, A. J. *Anal. Chem.* **2001**, *73*, 3960.
(102) Workman, S.; Richter, M. M. *Anal. Chem.* **2000**, *72*, 5556.
(103) Miao, W.; Choi, J.-P.; Bard, A. J. *J. Am. Chem. Soc.* **2002**, *124*, 14478.
(104) Leland, J. K.; Powell, M. J. *J. Electrochem. Soc.* **1990**, *137*, 3127.
(105) Bradley, J.-C.; Babu, S.; Carroll, B.; Mittal, A. *J. Electroanal. Chem.* **2002**, *522*, 75.
(106) Argoul, F.; Kuhn, A. *J. Electroanal. Chem.* **1993**, *359*, 81.
(107) Loget, G.; Kuhn, A. *J. Am. Chem. Soc.* **2010**, *132*, 15918.
(108) Rea, M. C. *Phys. Review* **1995**, *104*, 525.

Chapter 5

Conclusion and perspectives

5.1. Conclusion

In the frame of the present PhD thesis we studied and employed the asymmetric reactivity that can be generated on the surface of electrically conducting objects when exposing them to electric fields. This phenomenon of bipolar electrochemistry has been introduced theoretically in the first chapter with experimental results obtained on macroscopic bipolar electrodes. Historical aspects of bipolar electrochemistry and its recent applications have been presented in Chapter 2.

The bulk synthesis of asymmetric particles, so-called “Janus particles” is of great scientific interest, and was the main topic of Chapter 3. The common routes employed in the literature for generating such objects require an interface, as it has been illustrated by our example of the electron beam induced breaking of symmetry. This technique has been used to generate snowman-like silver/silver bromide dimers. Since such procedures are occurring only in a two dimensional reaction spaces, they often lead to weak production rates. As a consequence, we proposed bipolar electrochemistry for the bulk generation of Janus particles.

First, capillary-assisted bipolar electrodeposition, a technology based on the use of a capillary electrophoresis set-up, which allows reaching electric fields in the order of 100 kV m^{-1}, has been used. Micrometer long carbon tubes could be modified at one extremity with different metals such as gold, copper or nickel. By employing electric field pulses, these carbon tubes could be modified with the same metal at both extremities. It was also shown that simultaneous to a metal reduction occurring at the cathodic pole of the carbon tube, a conducting polymer (polypyrrole) can be electrodeposited at the anodic pole, which leads to metal/carbon tube/conducting polymer hybrid structures.

A strong drawback of this technique lies in the use of a capillary, which limits the reaction volume. In order to solve this problem, a new technology has been developed which allows the modification of much higher volumes with electric fields of the same order of magnitude. This process could be used for obtaining asymmetric carbon tube/metal (gold, platinum) structures. By using a gelling agent in order to stop the motion of isotropic carbon particles during the modification, carbon/metal (gold, silver) Janus beads with different sizes have also been produced with this process. The selective functionalization of the gold layer of the carbon/gold Janus microbeads has been demonstrated using a thiolated fluorophore.

Bipolar electrodeposition is not limited to the formation of a combination of conductive materials. The substrate where the modification happens must be conductive enough to be polarized by the electric field, but materials such as semi-conductors and insulators can be deposited. We used our technology for the formation of silver nanowire/silver chloride structures by a mechanism involving the localized precipitation of the silver halide compound. Depositions triggered by local pH changes around a bipolar electrode have also been used to generate Janus beads (carbon/silica, carbon/silicone, carbon/titanate and carbon/electrophoretic deposition paint). The titanate coating can be converted into crystalline titanium dioxide by annealing. The encapsulation properties of these materials have been used to entrap mineral dyes, organic fluorophores and metal nanoparticles for the generation of bicolored and fluorescent Janus objects.

When mass-transfer is controlled by migration, bipolar electrodeposition of a negatively charged species can lead to the formation of very attractive microstructures such as metal rings on spherical bipolar electrodes. This phenomenon has been studied by theoretical simulations and experiments at different scales. It has finally been used to generate barcode structures on gold beads as well as platinum and gold rings on carbon microbeads.

Asymmetry is a crucial parameter for the generation of controlled motion. The use of bipolar electrochemistry for the development of miniaturized motors has been developed in the fourth chapter of this thesis. A first strategy consists in using the asymmetric particles generated by bipolar electrodeposition and employing them directly as micromotors. In this context, carbon tube/nickel particles could be turned in rotating magnetic fields and carbon tube/platinum particles could be propelled using the oxygen generation occurring at the platinum surface when exposed to hydrogen peroxide solutions.

Since bipolar electrochemistry intrinsically allows a break of symmetry, it can be used also as a direct trigger of motion for isotropic particles. Based on a bubble propulsion mechanism, we showed that water splitting reactions, induced at the reactive poles of a bipolar electrode can induce translational

motion of millimeter and micrometer-sized conducting objects. The speed can be strongly enhanced in the presence of a sacrificial reductant such as hydroquinone.

By using this concept, the rotation of centimeter-sized objects could also be achieved. Furthermore, bubble accumulation under a swimmer can be used for the levitation of bipolar electrodes and cargo-lifting in fluid channels. It was also demonstrated that such a motion can be coupled to electrochemiluminescence at the anodic pole.

Finally, we developed a motion mechanism based on the simultaneous deposition/dissolution of a bipolar electrode. In this case, a zinc dendrite can be dynamically self-regenerated in a capillary filled with a zinc sulfate solution.

5.2. Perspectives

5.2.1. Material science and micromotors

Many perspectives for the use of bipolar electrochemistry in material science can be imagined. Considering all the applications of Janus particles described in section 3.2., pushing the limits of bipolar electrodeposition, in terms of available material combinations, the size of particles and the obtainable yields, is of strong interest from an academic as well as an industrial point of view. Various other materials besides those described in the present thesis can be considered for deposition. The list is extremely long since theoretically all electrodeposable materials can be also deposited by bipolar electrochemistry, ranging from insulating organic thin films to complex metal alloys. Controlling the morphology and the porosity of the deposits should also be possible by adjusting the experimental conditions and/or using additives such as surfactants or colloids. Asymmetric modification of particles with monolayers by using underpotential deposition or a covalent grafting of organic molecules or biomolecules on nanoparticules is also of strong interest, since it could offer wonderful tools for self-assembly and sensing. As described in Figure 5.1, much more complex structures than simple Janus particles could be obtained by varying the reactor structure, the number of feeder electrodes, their position in the cell and the type of imposed electric field. Convection can be introduced into the reactor in such a way that the particles are moving during their polarization. If the experiment is long enough, each point of the particle surface can temporarily be a part of the cathodic pole, which could be an interesting alternative approach for the generation of core-shell particles. Electrodeposition is not the only way for modifying or structuring materials. Processes such as anodization or dealloying could be used to create objects with an anisotropy in structure or porosity, which might be very interesting for optical or sensor applications.

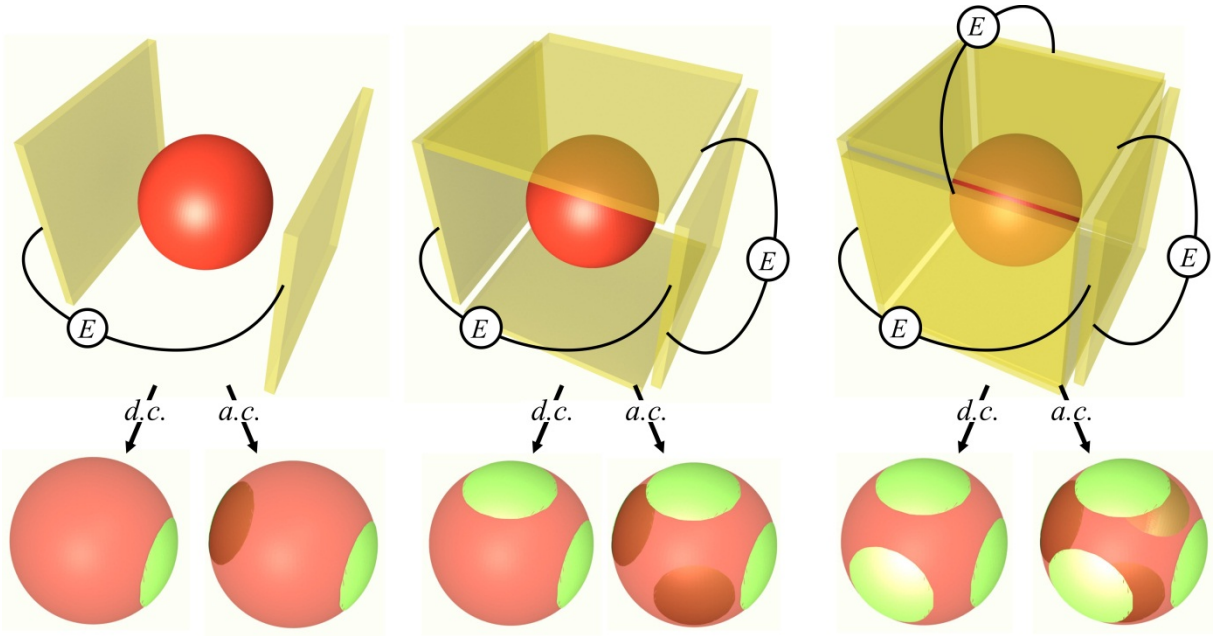

Figure 5.1. Scheme showing the fabrication of a series of patchy particles by bipolar electrodeposition.

The possibilities with respect to the field of micromotors are also very promising. A first challenge concerning bubble-propulsion and dynamic self-regeneration will be to decrease the microswimmer size (and, as a consequence, using higher electric fields). This will allow to test these mechanisms at low Reynold numbers, in the presence of significant Brownian motion and with competing electrokinetic phenomena. In the case of the levitation experiment discussed in section 4.3.3., the bubbles were confined under the bipolar electrode by the cell walls, but one could also imagine a swimmer structure which can trap the bubbles, to make it levitate without any contact with the cell walls. By engineering the swimmer shape, a three-dimensional motion based on these mechanisms may also be envisioned. Furthermore, an electrochemically-triggered cargo release, induced by an electric field pulse or reversal could be considered. Beyond the academic interest, these mechanisms have to be tested for practical applications such as cargo delivery in a lab on chip device, or unclogging of fluid channels. Finally, the behavior of the metal swimmer in the bipolar self-regeneration is also very interesting from an intellectual point of view. The trajectory of the swimmer could be studied in different environments such as a microchannel with a Y-junctions or in a labyrinth.

5.2.2. Bipolar electrodeposition beyond the frontiers of material science

Bipolar electrochemistry can also contribute to many other fields. In particular, it can serve as a tool for the investigation of electrical properties of diverse substrates. Conductivity measurements on molecules or supramolecular assemblies is of major importance for many domains ranging from molecular electronics to biology. In the last few decades, a strong scientific debate on the charge transfer through DNA emerged.[1,2] DNA conductivity is a crucial parameter, which certainly plays a major role in biological processes and could be exploited for medical applications[3] and nanoelectronics. Many complicated approaches based on the use of conductive AFM,[4] scanning tunneling microscopy (STM),[5] nanogap junctions[6] or low-energy electron point source microscope[7] have been employed in order to investigate DNA conductivity. In this context, bipolar electrochemistry might be used as a straightforward technique for studying DNA conductivity.

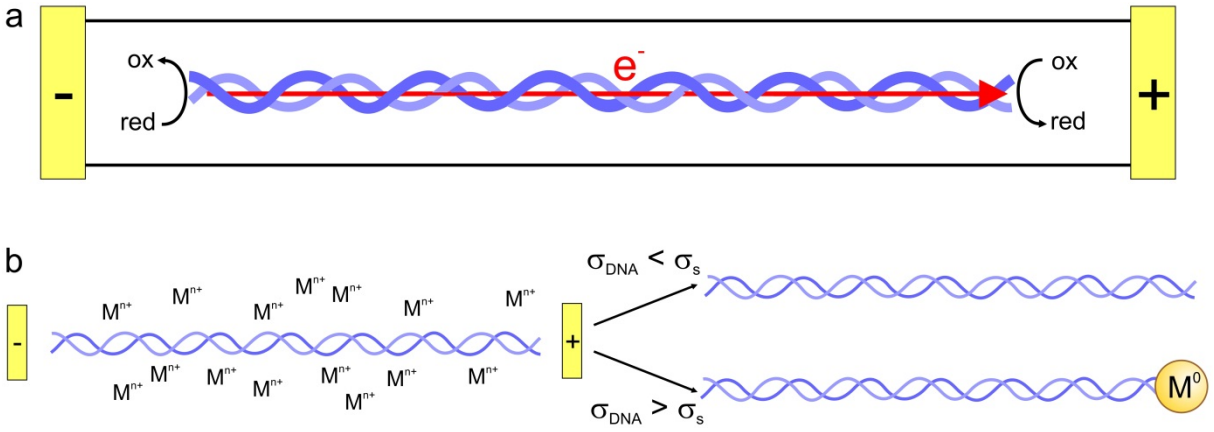

Figure 5.2. Bipolar electrochemistry with double stranded DNA. a) Scheme showing double stranded DNA acting as a bipolar electrode. b) Scheme showing the possible results of DNA polarization (with $\Delta V > \Delta V_{min}$), depending on the conductivity of DNA with respect to its environment.

One crucial property for a substrate to act as a bipolar electrode is to have a better conductivity than the surrounding medium (see section 1.3.). This condition can be used to estimate the conductivity of certain objects, for instance DNA. If DNA is polarized and the following conditions are fulfilled: *i)* $\Delta V > \Delta V_{min}$ and *ii)* DNA conductivity σ_{DNA} is superior to the conductivity of the surrounding medium σ_s, then DNA should behave as a bipolar electrode and undergo reduction and oxidation reactions at its reactive poles, as shown in Figure 5.2a. One can then use the experiment depicted in Figure 5.2b in order to estimate DNA conductivity. The polarization of DNA in the presence of metal cations M^{n+} should lead to the deposition of a metal cluster at its cathodic pole only if $\sigma_{DNA} > \sigma_s$. In the following, we present preliminary results concerning DNA modification by bipolar electrodeposition.

In order to prove this concept, preliminary experiments were carried out. A commercially available and long double stranded DNA was chosen in order to facilitate its polarization and its visualization by TEM. A TEM picture of the DNA, which was not submitted to the electric field, is presented in Figure 5.3a. Regarding the width of the middle strand that is in the order of 100 nm, it seems clear that this DNA can pack into bundles (the width of a single DNA strand is about 2 nm). The polarization experiments were carried out in the capillary electrophoresis set-up (see section 3.5.1.). Nickel sulfate was chosen among other metal salts due to its low reduction potential. No aggregation phenomenon was observed when the salt was added to a solution of DNA. A similar procedure like the one used for single point modification of CMTs with Ni (section 3.5.2.1.) was used. Taking into account the length of one double stranded DNA, one can calculate that ΔV = 2.1 V, which shows that the thermodynamic condition $\Delta V > \Delta V_{min}$ is fulfilled (ΔV_{min} = 1.49 V for Ni deposition, see section 3.5.2.1.). The electric field was applied for 1 to 2 min, during which the DNA motion could be followed by UV-detection.

Figure 5.3b and c show TEM pictures of the DNA strands collected at the capillary outlet after the polarization. One can see that after its journey through the capillary, the strands are generally less curved than before the experiments (Figure 5.3a), which can be related to a stretching during the experiment. The widths of the strands, which are present in the middle of Figure 5.3b and c are around 4 nm, which seems compatible with the widths of double stranded DNA, when taking into account the TEM resolution. It is very clear that a spherical cluster, much darker than the rest of the object, is present at the extremities of the strands. This shape, as well as the color contrast between the DNA “body” and the cluster “head”, suggests strongly the presence of a nickel metal nanoparticle at the extremity of the DNA. Unfortunately, imaging the other extremity of the DNA strands was not possible due to their lengths and experimental difficulties.

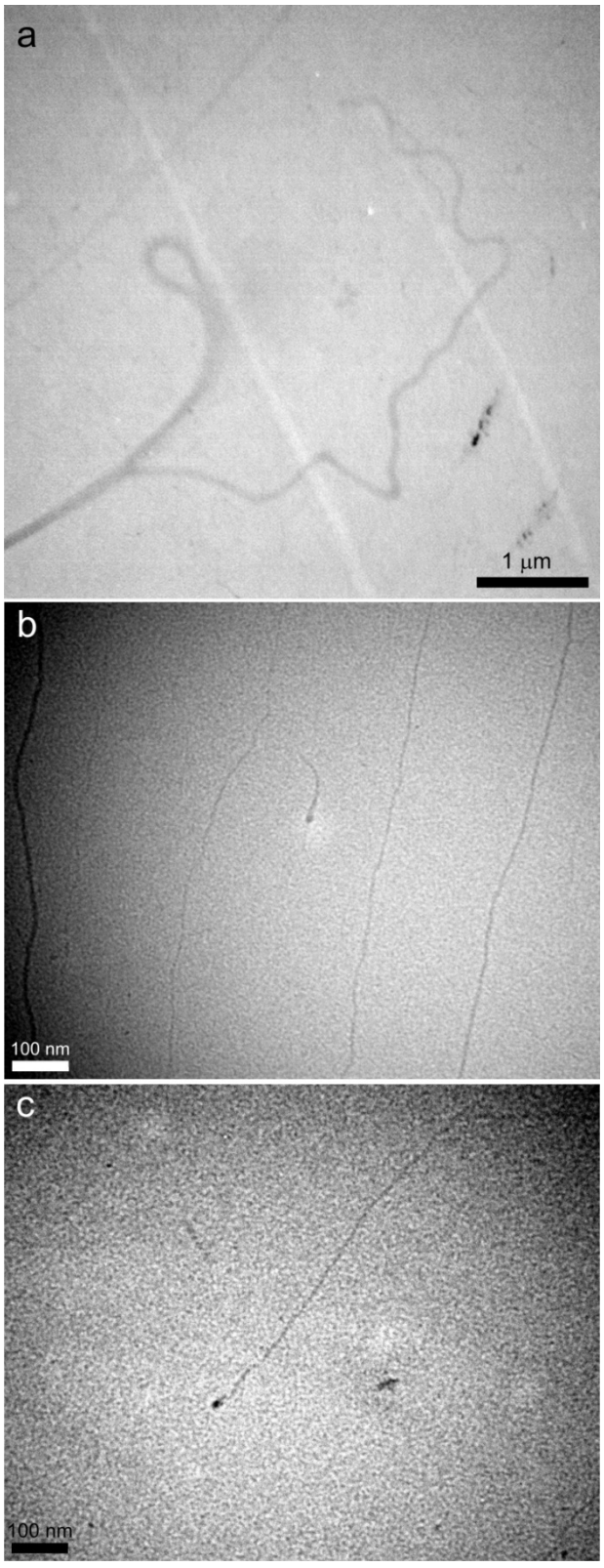

Figure 5.3. Bipolar electrochemistry on DNA. a) TEM picture showing DNA prior to its exposure to the electric field. b,c) TEM pictures showing DNA after its polarization using capillary electrophoresis in the presence of $NiSO_4$.

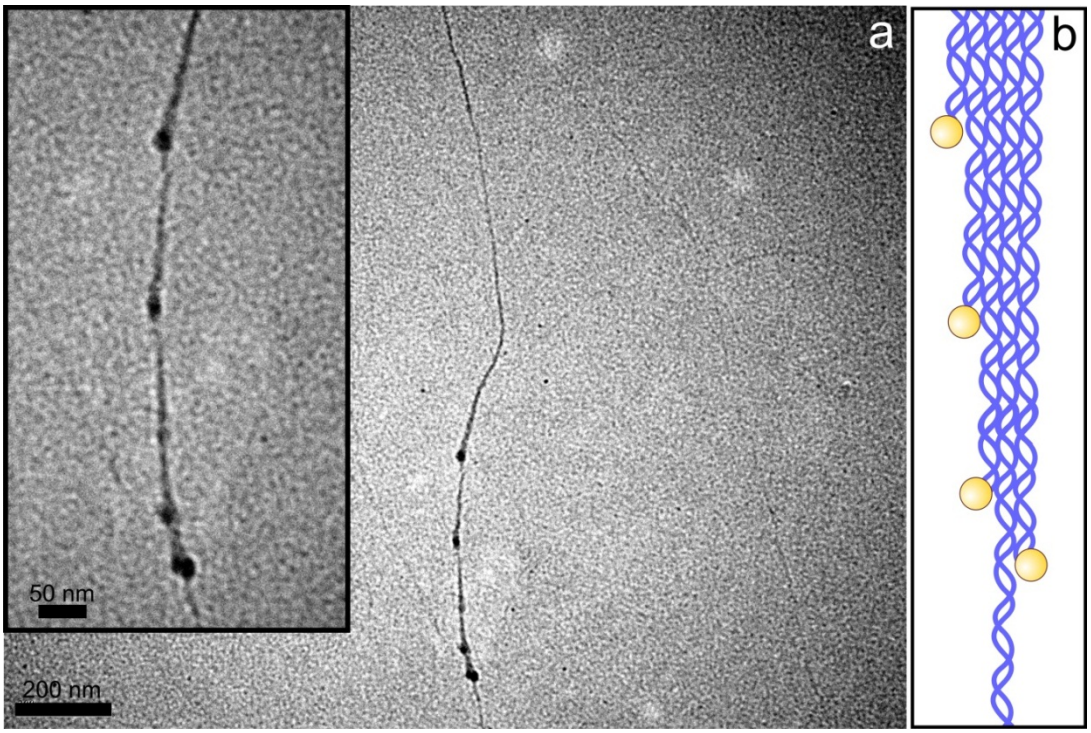

Figure 5.4. DNA bundles. a) TEM pictures showing the DNA after its polarization in a capillary electrophoresis set-up in the presence of $NiSO_4$. Inset: TEM picture showing a detailed view of the nanoparticles. b) Scheme showing a DNA bundle with several metal nanoparticles at the extremities of the double strands.

Another type of morphology that can be observed after the modification is shown in Figure 5.4a. In this figure, a DNA strand containing 4 nanoparticles is presented. In the detailed view presented in the inset of this figure, one can clearly see the DNA width decreasing from the top of the picture (≈10 nm) to the bottom (≈4 nm). This seems to indicate the presence of a bundle of double strands, confirmed by the fact that this DNA can arrange itself into such structures, as observed in Figure 5.3a. The existence of several nickel nanoparticles at these spots can be explained by the bipolar electrodeposition of the metal at each end of an individual double strand of the bundle, resulting in the structure depicted in Figure 5.4b.

These preliminary results are really promising, since they suggest that DNA can be modified by bipolar electrochemistry. Besides being a concrete proof that charge-transfer can occur along these DNA strands, these experiments might be used to probe its conductivity by varying the ionic strength of the solution. The so-generated metal/DNA objects are also unprecedented tools that can be used for nanotechnology. However, these results are still at an early stage and more experiments are needed in order to get the definite proof that DNA can be modified by bipolar electrochemistry. The use of spectroscopy, intercalators or DNA strands with mismatches[8] constitute short and medium term perspectives for confirming these results.

References

(1) Turro, N. J.; Barton, J. K. *J. Biol. Inorg. Chem.* **1998**, *3*, 201.
(2) Genereux, J. C.; Barton, J. K. *Chem. Rev.* **2009**, *110*, 1642.
(3) Boal, A. K.; Genereux, J. C.; Sontz, P. A.; Gralnick, J. A.; Newman, D. K.; Barton, J. K. *Proc. Natl. Acad. Sci. USA* **2009**, *106*, 15237.
(4) Cohen, H.; Nogues, C.; Ullien, D.; Daube, S.; Naaman, R.; Porath, D. *Farad. Disc.* **2006**, *131*, 367.
(5) van Zalinge, H.; Schiffrin, D. J.; Bates, A. D.; Starikov, E. B.; Wenzel, W.; Nichols, R. J. *Angew. Chem. Int. Ed.* **2006**, *45*, 5499.
(6) Roy, S.; Vedala, H.; Roy, A. D.; Kim, D.-H.; Doud, M.; Mathee, K.; Shin, H.-K.; Shimamoto, N.; Prasad, V.; Choi, W. *Nano Lett.* **2007**, *8*, 26.
(7) Fink, H.-W.; Schonenberger, C. *Nature* **1999**, *398*, 407.
(8) Slinker, J. D.; Muren, N. B.; Renfrew, S. E.; Barton, J. K. *Nat. Chem.* **2011**, *3*, 228.

Appendix

1. Preparation of CB[*n*]-capped AgBr nanoparticles

CB[7] and CB[5] were synthesized,[1] separated and purified[2] according to already published procedures by our collaborators at the University of Cambridge. The bromide-free CB[7] was purified according to reported procedures by Kim et *al.*[1] The typical procedure for preparing CB[5]-capped AgBr NPs using a ratio of $n_{AgNO3}/n_{CB[5]}$ = 1 consisted in mixing 0.36 mL of a 16 mM aqueous CB[5] solution and 0.48 mL of a 12 mM aqueous $AgNO_3$ solution in a vial. A typical procedure for preparing CB[7]-capped AgBr NPs consisted in mixing 0.36 mL of a 8 mM aqueous CB[7] solution and 0.48 mL of a 6 mM aqueous $AgNO_3$ solution in a vial. The vials were then placed in the dark for ≈24 h. White solutions with orange reflectivity were obtained (Figure 3.7c). Decreasing the CB[5]-$AgNO_3$ concentrations by a factor of 4 was found to lead to the same results.

2. Preparation of uncapped AgBr and AgCl particles

AgBr and AgCl were respectively prepared by precipitating 0.5 mL of an 11.7 mM aqueous $AgNO_3$ solution with 0.36 ml of 24 mM HCl, and 0.16 mL of a 6 mM $AgNO_3$ aqueous solution with 0.12 mL of 6 mM NaBr during ≈24 h in the dark. Although the majority of the precipitate settled at the bottom of the vials, the supernatant contained a sufficient amount of NPs that were transferred and observed on the TEM grids (Figure 3.9d).

3. PDMS preparation and molding

A PDMS kit containing the pre-polymer and a curing agent (RTV-615, Momentive Performance Materials) was used. The pre-polymer and the curing agent were inserted together in a centrifuge tube with a respective 9 to 1 mass ratio and mixed intensively. This mixture was then centrifuged for releasing air bubbles. As shown in Figure A.1, the mold was usually constituted of a vessel (preferentially hydrophobic and flexible) and a PTFE or a rubber shape for the superior part. The

mixture containing the pre-polymer and the curing agent was added slowly to the mold to prevent the formation of air bubbles. The whole system was then baked at 90 °C for several hours and the final shape was recovered after removal of the other parts.

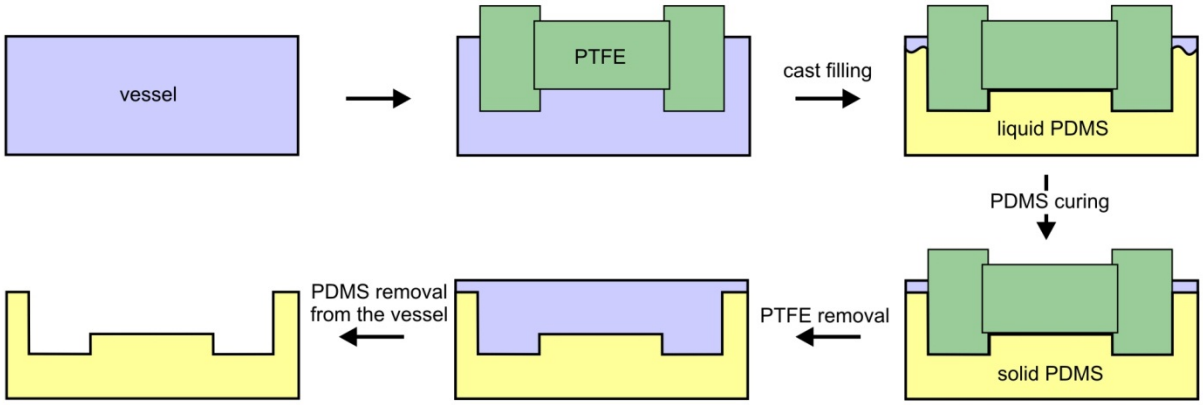

Figure A.1. Scheme showing the PDMS molding procedure.

4. Synthesis of spherical gold nanoparticles

AuNPs were synthesized following the Turkevich protocol.[3] 50 mL of an aqueous solution of 0.5 mM $HAuCl_4$ was heated in an Erlenmeyer flask under magnetic stirring. When boiling is reached, 0.7 mL of an aqueous solution of 0.1 M sodium citrate was added to the mixture. After a few minutes the color changed from purple to red indicating the presence of metallic gold nanocolloids. When a stable color was obtained, the solution was cooled down to room temperature. A suspension droplet was placed on the TEM grid and was sucked from bellow with a paper tissue. The grid was then rinsed three times with mQ water following the same procedure. As it is shown by Figure 3.39a, TEM imaging revealed roughly spherical AuNPs with sizes ranging from 10 nm to 25 nm.

5. Theoretical prediction of the hot spots on a spherical bipolar electrode

In order to qualitatively illustrate the two different situations corresponding to the bipolar electrodeposition of anionic or cationic metal precursors, simulations involving a competition between transport and reduction kinetics were performed. Simulations were obtained with the commercially available program Comsol Multiphysics 3.4, which allows the resolution of the partial differential equations based on finite elements. In our study, we consider a simple monoelectronic and fast redox couple undergoing the reduction reaction 1.6. Initially, exclusively the oxidized form is present in the solution (1 mM). The mass transport depends on diffusion (D = 1 10^{-5} cm^2 s^{-1}) and

migration. The bead boundary condition was programmed using the Butler-Volmer formalism to evaluate the flux towards it. Figure A.2 shows the concentration gradients of the reductant, generated by the reduction of the oxidant at the reactive areas of the BE using $\mathscr{E}$ = 1 kV m^{-1} at *t* = 10 s after the electric field was on. In this model the reductant is neutral (unaffected by migration). Figure A.2a shows the simulated concentration profile of the reduced species around the 2D projection of the BE in a system containing a positively charged (+1) oxidant. One can clearly see in this case that the oxidant is reduced over the whole cathodic pole surface. When the oxidant is negatively charged (-1), as it is the case in Figure A.2b, the reduced species concentration gradient is totally different. The maximum concentrations are clearly localized at two spots on the BE projection, these two spots corresponding to the position of the boundary between the areas where $\Delta V_x > \Delta V_{min}$ and $\Delta V_x < \Delta V_{min}$. Because for electrodeposition, the reduced species does not diffuses but stays on the BE surface, these gradient profiles are not representative of the one of the practical experiments, nevertheless, these simulations show very clearly the BE hot-spots and qualitatively confirm our hypothesis schematically depicted in Figure 3.41.

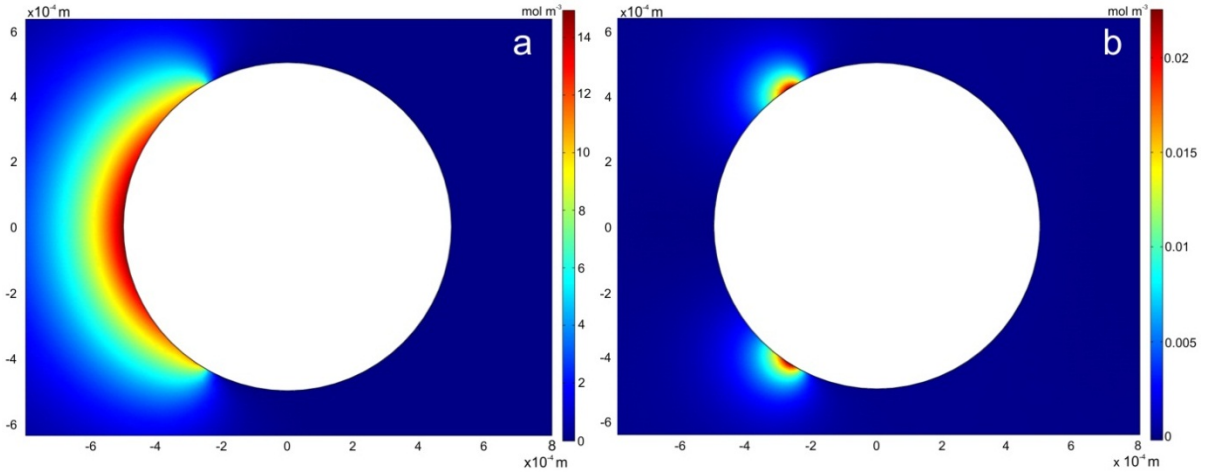

Figure A.2. Simulated concentration profiles of a reduced species around the 2D projection of a spherical bipolar electrode at 10 s after the electric field was applied. a) Simulated concentration profile of a reduced species, the oxidant being positively charged (this case corresponds to the situation depicted in Figure 3.41a). b) Simulated concentration profile of a reduced species, the oxidant being negatively charged (this case corresponds to the situation depicted in Figure 3.41a).

6. Collaborations

The following co-workers contributed in collaborations in different projects of this thesis. The majority of the work has been performed at the University of Bordeaux and if not, the co-worker affiliation is specified.

Pr. Alexander Kuhn contributed in all the parts as the supervisor of this thesis.

Pr. Jeremy J. Baumberg, Dr. Oren A. Scherman, Dr. Roger J. Coulston and Samuel T. Jones, from the University of Cambridge (England) contributed to section 3.4.

Dr. Tung-Chun Lee reproduced the experiments presented in section 3.4. at the Melville Laboratory for Polymer Synthesis (University of Cambridge).

Dr. Sumeet Mahajan and Richard W. Taylor, from the University of Cambridge, performed the Raman spectroscopy measurements presented in section 3.4.

Dr. Olivia Nicoletti, from the University of Cambridge, performed the STEM-EDX and HAADF analysis presented in section 3.4.

The AFM picture presented in section 3.4. was realized in collaboration with Patrick Garrigue.

Pr. Jumras Limtrakul and Dr. Chompunuch Warakulwit from the Kasetsart University (Thailand) synthetized and provided the carbon microtubes used in section 3.5. and 3.6.

Dr. Marie-Hélène Delville (ICMCB) recorded the EDX spectra presented in section 3.5.3.

Dr. Jérome Roche performed to the modification of the 200-400 μm GC beads presented in sections 3.6.2.2. and 3.7.

Dr. Dodzi Zigah collaborated to the selective molecular grafting on spherical Janus particles presented in section 3.6.2.2. and performed the simulations presented in appendix 5.

The X-ray spectrum presented in section 3.6.4.2. was recorded by Eric Lebraud (ICMCB).

Dr. Stephane Arbault contributed in the recording of the photographs shown in Figure 3.43 and Figure 3.44.

Guillaume Larcade contributed to section 4.2.1.

Dr. Laurent Bouffier collaborated in section 4.2.2.

Zahra Fattah recorded the movies from which the pictures of Figure 4.10. and 4.11. were extracted.

Section 4.4. was realized in collaboration with Pr. Neso Sojic.

Milica Sentic performed the cyclic voltammetry of figure 4.25, recorded the movie from which the pictures of Figure 4.26. were extracted and the CCD pictures presented in Figure 4.28.

Véronique Lapeyre contributed in the recording of the TEM pictures presented in section 5.2.

All these collaborators are warmly acknowledged for their inputs and support.

7. List of publications resulting from this thesis

Material science

1 Loget, G.; Larcade, G.; Lapeyre, V.; Garrigue, P.; Warakulwit, C.; Limtrakul, J.; Delville, M.-H.; Ravaine, V.; Kuhn, A.
Single point electrodeposition of nickel for the dissymmetric decoration of carbon tubes.
Electrochim. Acta **2010**, *55*, 8116.

2 Fattah, Z.; Loget, G.; Lapeyre, V.; Garrigue, P.; Warakulwit, C.; Limtrakul, J.; Bouffier, L.; Kuhn, A.
Straightforward single-step generation of microswimmers by bipolar electrochemistry.
Electrochim. Acta **2011**, *56*, 10562.

3 Loget, G.; Lapeyre, V.; Garrigue, P.; Warakulwit, C.; Limtrakul, J.; Delville, M.-H.; Kuhn, A.
A versatile procedure for the synthesis of Janus-type carbon tubes.
Chem. Mater. **2011**, *23*, 2595.

4 Loget, G.; Kuhn, A.
Bulk synthesis of Janus objects and asymmetric patchy particles.
J. Mater. Chem. **2012**, *22*, 15429.

5 Loget, G.; Lee, T.-C.; Taylor, R. W.; Mahajan, S.; Nicoletti, O.; Jones, S. T.; Coulston, R. J.; Lapeyre, V.; Garrigue, P.; Midgley, P. A.; Scherman, O. A.; Baumberg, J. J.; Kuhn, A.
Direct visualization of symmetry breaking during Janus nanoparticles formation.
Small **2012**, 8, 2698.

6 Loget, G.; Roche, J.; Kuhn, A.
True bulk synthesis of Janus objects by bipolar electrochemistry.
Adv. Mater. **2012**, 24, 5111.

7 Kumsapaya, C.; Bakaï, M.-F.; Loget, G.; Goudeau B.; Warakulwit C.; Limtrakul J.; Kuhn, A.; Zigah, D.
Janus beads obtained by grafting of organic layers via bipolar electrochemistry.
Submitted.

Dynamic systems

8 Loget, G.; Kuhn, A.
Propulsion of microobjects by dynamic bipolar self-regeneration.
J. Am. Chem. Soc. **2010**, *132*, 15918.

9 Loget, G.; Kuhn, A.
Electric field-induced chemical locomotion of conducting objects.
Nat. Commun. **2011**, *2*, 535.

10 Loget, G.; Kuhn, A.
Bipolar electrochemistry for cargo-lifting in fluid channels
Lab. Chip **2012**, 12, 1967.

11 Sentic, M.; Loget, G.; Manojlovic, D.; Kuhn, A.; Sojic, N.
Light-emitting electrochemical swimmers.
Angew. Chem. Int. Ed. **2012**, in press, DOI: 10.1002/anie.201206227.

Combination of both fields

12 Loget, G.; Kuhn, A.
Shaping and exploring the micro- and nanoworld using bipolar electrochemistry.
Anal. Bioanal. Chem. **2011**, *400*, 1691.

13 Kuhn, A.; Loget, G.
Bipolar electrochemistry, an emerging tool in nanoscience.
G.I.T. Laboratory Journal **2011**, *5-6*, 19.

14 Loget, G.; Kuhn, A.
L'électrochimie bipolaire, un nouvel outil pour la chimie analytique et les nanosciences.
Techniques de l'Ingénieur **2011**, RE 208

References

(1) Kim, J.; Jung, I.-S.; Kim, S.-Y.; Lee, E.; Kang, J.-K.; Sakamoto, S.; Yamaguchi, K.; Kim, K. *J. Am. Chem. Soc.* **2000**, *122*, 540.
(2) Jiao, D.; Zhao, N.; Scherman, O. A. *Chem. Commun.* **2010**, *46*, 2007.
(3) Kimling, J.; Maier, M.; Okenve, B.; Kotaidis, V.; Ballot, H.; Plech, A. *J. Phys. Chem. B* **2006**, *110*, 15700.